Synthesis, characterisation and application of inherently conducting polymer nanoparticles

Orawan Ngamna
University of Wollongong

SYNTHESIS, CHARACTERISATION AND APPLICATION OF INHERENTLY CONDUCTING POLYMER NANOPARTICLES

A thesis submitted in fulfilment of the requirements for the award of the degree

DOCTOR OF PHILOSOPHY

from the

UNIVERSITY OF WOLLONGONG

by

ORAWAN NGAMNA, B.Sc.(Food Technology)

INTELLIGENT POLYMER RESEARCH INSTITUTE

DEPARTMENT OF CHEMISTRY

February 2006

This work is dedicated to my dad and mom, Mr. Surin and Mrs Pratin Ngamna for their unconditional love and support.

CERTIFICATION

I, Orawan Ngamna, declare that this thesis, submitted in fulfilment of the requirements for the award of Doctor of Philosophy, in the Department of Chemistry, University of Wollongong, is wholly my own work unless otherwise referenced or acknowledged. The document has not been submitted for qualifications at any other academic institution.

Orawan Ngamna

February 2006

ACKNOWLEDGEMENTS

Firstly I would like to thank my family: dad, mom, P'Nong and Ekkapol for giving me life as well as unconditional love and support.

Thanks also to Unilever Thai Holdings Ltd. for financial support during my Master's degree. P'Noo (PYT) and Rene (RL) who encouraged and supported me to undertake further study and to pursue a PhD as well as P'Tee, P'Pensri, K. Adisai (AMV) and all friends in Unilever are really appreciated.

My life in IPRI would not be possible without the great help and support from both of my supervisors- Prof. Gordon G. Wallace and Dr. Simon E. Moulton. I appreciate the time that Simon has given to my work and thesis, and also his encouragements throughout my time in IPRI. Gordon is an absolutely exceptional professor who cares not only about the research outcome, but also for the well-being of every one under his reign, and is always understanding and helpful. I have never felt left behind or unappreciated whilst working in his 'Evil Empire'. Thanks to Peter (and Uncle Pete's magic toys), Dr. Chee, Violeta (for the nice TEM and AFM images) and Elvis, who always has something to do for other people in IPRI. Thanks to all those involved in collaborative works: Siree, Aoife and Jenny. Thanks to P'Yingpit, Maria, Fatemeh, Vahid, Brianna, Carol, Kerry, Aoife, Su Ryon, Changkee and Eve for all of their encouragements and for always making my work in the lab and my personal life fruitful. My gratitude to Leon, Bjørn, Chee, Peter, Toni and George for comments/proof reading my final thesis chapters. Last but not least, I would like to thank Ngae for being such an unbelievable friend throughout both good and tough times and always be there for me.

Finally, I would like to thank Prof. Gordon Wallace again for giving me the IPRI scholarship throughout my PhD studies.

PUBLICATIONS

1. S.E. Moulton*, P.C. Innis, L.A.P. Kane-Maguire, O. Ngamna, and G.G. Wallace, "Polymerisation and characterisation of conducting polyaniline nanoparticle dispersions", *Current Applied Physics*, 2004, **4** (2-4), 402-406.

2. A. Morrin, O. Ngamna, A.J. Killard, S.E. Moulton, M.R. Smyth*, and G.G. Wallace*, "An Amperometric Enzyme Biosensor Fabricated from Polyaniline Nanoparticles", *Electroanalysis*, 2005, **17** (5-6), 423-430.

3. O. Ngamna, A. Morrin, S.E. Moulton, A.J. Killard, M.R. Smyth, and G.G. Wallace*, "An HRP based biosensor using sulphonated polyaniline**"**, *Synthetic Metals*, 2005, **153** (1-3), 185-188.

4. A. Morrin, F. Wilbeer, O. Ngamna, S.E. Moulton, A.J. Killard, G.G. Wallace, and M.R. Smyth*, "Novel biosensor fabrication methodology based on processable conducting polyaniline nanoparticles", *Electrochemistry Communications*, 2005, **7** (3), 317-322.

5. J.M. Pringle*, O. Ngamna, J. Chen, G.G. Wallace, M. Forsyth and D.R. MacFarlane, "Conducting Polymer Nanoparticles Synthesized in an Ionic Liquid by Chemical Polymerisation", *Synthetic Metals*, in press.

6. O. Ngamna, S.E. Moulton and G.G. Wallace, “Incorporation of Dye into Conducting Polyaniline Nanoparticles”, *Polymer*, accepted.

TABLE OF CONTENTS

Chapter 2 – Instrumental and Characterisation Techniques

PART II – Synthesis and Characterisation of Conducting Polymer Nanoparticles

Chapter 3 – Synthesis and Characterisation of Polyaniline Nanoparticles

ABBREVIATIONS

μ	micro
μ	viscosity
λ	wavelength
k_B	Boltzman's constant
γ	surface tension
Ω	Ohm
ν	frequency
ºC	degree Celsius
Θ	angle
η	refractive index
σ	conductivity
ρ	resistivity
υ	scan rate
A	ampere
Å	angstrom
A^-	anion
A_i	acivity of species i
ABTS	2,2'-azino-bis(3-ethylbenzthiazoline-6-sulphonic acid)
AFM	atomic force microscopy
Ag/AgCl	silver/silver chloride reference electrode
Ag/Ag^+	silver/silver ion reference electrode
APS	ammonium peroxydisulphate

BSA	bovine serum albumin
BFEE	boron-fluoride ethyl ether
C	Cunningham slip correction factor
ca.	approximately
CB	Carbolan Blue
CCD	charge-coupled device
cm	centrimeter
cm^{-1}	wave number
CMC	critical micelle concentration
CV	cyclic voltammetry
d	diameter
Da	dalton
D_{AB}	diffusion coefficient
DBSA	dodecylbenzene sulphonic acid
DLS	dynamic light scattering
E	potential
E^0	standard reduction potential
EB	emeraldine base
emiTFSA	1-ethyl-3-methylimidazolium-bis(trifluoromethane-sulfonyl)amide
ES	emeraldine salt
F	Faraday constant
g	gram
GC	glassy carbon

HCSA	camphorsulphonic acid
HPLC	high performance liquid chromatography
HRP	horseradish peroxidase
h	hour
ICP	inherently conducting polymer
IL	ionic liquid
ITO	indium tin oxide
k	thousand
L	litre
LB	leucoemeraldine base
m	metre
M	molar
MAS	2-methoxyaniline-5-sulphonic acid
mg	milligram
min	minute
ml	millilitre
mM	millimolar
MoAb	monoclonal antibody
mS	millisiemen
Mw	molecular weight
nm	nanometre
OCP	open circuit potential
PANI	polyaniline
PB	perniganiline base

PBS	phosphate buffer saline
PEI	poly(ethyleneimine)
PLL	poly(L-lysine)
PMAS	poly(2-methoxyaniline-5-sulphonic acid)
PPy	polypyrrole
PS	perniganiline salt
PSS	poly(sodium 4-styrene sulfonate)
Pt	platinum
PTh	polythiophene
PTTh	polyterthiophene
PVA	poly(vinyl alcohol)
PVP	poly(4-vinylpyridine)
PVS	polyvinylsulphonate
Py	pyrrole
r	radius
RM	rapid mixing
RMS	root mean square
rpm	round per minute
S	siemen
SCE	saturated calomel electrode
SDS	sodium dodecylsulfate
SEM	scanning electron microscopy
SHE	standard hydrogen electrode
SPM	scanning probe microscopy

T	temperature
TBAP	tetrabutylammonium perchlorate
TEM	transmission electron microscopy
Th	thiophene
TTh	terthiophene
V	volt
vs.	versus
w/v	weight by volume
w/w	weight by weight

ABSTRACT

Synthesis of inherently conducting polymers (ICPs) nanoparticles is an option to improve the processability and conductivity of ICPs. In this thesis, the synthesis and application of ICPs nanoparticles has been demonstrated. Various polymerisation methods, such as emulsion polymerisation, use of steric stabiliser and synthesis in ionic liquid (IL) media, have been used to synthesise polymer nanoparticles. These synthesis methods render the ICPs nanoparticles stable as dispersions which are more processable and contain peculiar and fascinating properties superior to their bulk counterparts. These nanoparticles are further applied as mediators for biosensors. They have been fabricated into sensors using electrodeposition, evaporative casting, or ink-jet printing methods. Electrodeposition method results in formation of ultra thin nanostructured polymeric films that enhance sensor performance. Evaporative casting method is an easy one-step method, but precision is hard to achieve and dense films with rough morphology are formed. Ink-jet printing can be used to produce precise and accurate patterns and also this approach is amenable to mass production.

Polyaniline (PANI) nanoparticles; *nano*PANI-dodecylbenzene sulphonic acid (DBSA) have been synthesised using emulsion polymerisation (Chapter 3). The *nano*PANI-DBSA obtained has a conductivity of 34±7 S/cm with particle size in the range of 10±2 nm. The *nano*PANI-DBSA has been used as a mediator layer in biosensor applications as demonstrated in Chapter 7. These nanoparticles were fabricated onto the conductive electrode using an electrodeposition method with subsequent immobilisation of the enzyme horseradish peroxidase (HRP). Sensor performance was examined using

amperometric method and HRP/hydrogen peroxide (H_2O_2) configuration as a model system. The nanodomain of the *nano*PANI-DBSA particles contributed to highly ordered nanostructure patterning on the electrode surface. This uniform surface showed improved enzyme deposition characteristics, a lower background signal and better sensor performance at a lower HRP loading when compared to the sensors fabricated from electropolymerisation of the bulk monomer.

*Nano*PANI-DBSA particles aggregate at high concentrations; hence they are not amenable to ink-jet printing. *s*PANI-DBSA was prepared from centrifugation of the *nano*PANI-DBSA dispersions and used as a material for ink-jet printing. HRP was pre-mixed with the *s*PANI-DBSA nanodispersions before fabrication onto ITO-coated mylar using ink-jet printing. The print quality from the *s*PANI-DBSA nanodispersions was inconsistent and the catalytic signal of this biosensor was very low. These resulted in no further ink-jet printing work for this material.

The PANI-DBSA-rapid mixing (RM) nanodispersions were synthesised using a RM method. These dispersions contained nanometre size PANI particles dispersed in aqueous media. These nanoparticles have been successfully printed using ink-jet printing as outline in Chapter 9. This work has demonstrated the ink-jet printability of conducting polymer nanoparticles and their use as working electrodes for biosensors. The sensor response from these ink-jet printed PANI-DBSA-RM was higher than the sensor response from evaporative casting of poly(2-methoxyaniline-5-sulphonic acid) (PMAS) in Chapter 8.

The addition of functional group into PANI nanoparticles was also investigated. Carbolan Blue (CB) dye was incorporated into the PANI backbone using emulsion polymerisation method as demonstrated in Chapter 4. The dye was proved to have strong interaction with PANI backbone using Raman spectroscopy and centrifugation test. The

distinct solution colour after a reduction process could lead the PANI-DBSA-CB to be a potential candidate of the material for electrochromic devices.

Synthesis of polypyrrole (PPy) nanoparticles is demonstrated in Chapter 5. Poly(vinyl alcohol) (PVA) was used as the steric stabiliser to produce PPy-DS-PVA nanoparticles. These nanoparticles were well dispersed in water with particle size in the order of 52±5 nm. Aggregation was obvious in concentrated solutions and leaded to poor ink-jet printed quality of the PPy-DS-PVA nanoparticles.

The water soluble polymer, PMAS, was also used to fabricate biosensors using evaporative casting method in Chapter 8 and ink-jet printing in Chapter 9. In chapter 8, its solubility enabled PMAS to pre-mix with the HRP enzyme prior to complexing with the polycations poly(L-lysine) hydrochloride (PLL) and subsequently casting onto ITO coated mylar substrate. This biosensor format has proven ability to easily fabricate the conducting polymer nanoparticles by one-step evaporative casting. The optimised sensors exhibited good sensor response, high selectivity and very good long-term stability. The ink-jet printed films from PMAS and PLL solutions (Chapter 9) showed better electroactivity compared to the evaporative cast films which could lead to better sensor performance. However, the problem of PLL blocking the print head resulted in the discontinuation of its use.

The polyterthiophene (PTTh) aqueous dispersed nanoparticles were also successfully synthesised in the presence of surfactant (DBSA) and in ionic liquid; 1-ethyl-3-methylimidazolium bis(trifluoromethane-sulfonyl)amide (emiTFSA) as demonstrated in Chapter 6. The dispersion of PTTh-DBSA nanoparticles has shown poor colloidal stability and poor electroactivity. Although the PTTh nanoparticles synthesised in emiTFSA needed

2-3 minutes sonication to be dispersed in water, they have shown good electrochemistry and being test in another study in our laboratories for its use in photovoltaic devices.

These processable ICPs nanoparticles are promising materials for biosensor applications, electrochromic devices and solar cells. Assembly of these nanoparticles on to conductive substrates leads to highly ordered nanostructured ICPs on the surface and improves the biosensor performances. Also these nanoparticles prove their ability to be processable in mass production scale.

1.1 Inherently Conducting Polymers (ICPs)

The evolution of conducting polymers began in the mid-1970s, with the discovery of polysulphur nitride [$(SN)_x$], which becomes superconducting at low temperatures. Two years later, a linear conjugated organic polymer, polyacetylene, was shown to have metallic properties[1]. Three discoverers of high conductivity iodine doped-polyacetylene: Alan MacDiarmid, Alan Heeger and Hideki Shirakawa were awarded the Nobel Prize for Chemistry in 2000[2]. The level of publications related to the synthesis of new types of conducting polymers or modifications to the existing conducting polymers in the past 25 years has increased rapidly[2]. This increased interest is a result of the potential application of conducting polymers in plastic electronics and for providing new functional materials[3]. The main characteristic of a conducting polymer is a conjugated backbone that can be subjected to oxidation or reduction by electron acceptors or donors. Metals conduct electricity via mobile electrons in the conduction band that travel across atoms in the lattice, while in organic materials conductivity occurs by mobility of the delocalised π-electrons along the polymer chain[4]. Polyaniline (PANI), polythiophene (PTh) and polypyrrole (PPy) are examples of typical inherently conducting polymers (ICPs)[2] (Figure 1.1).

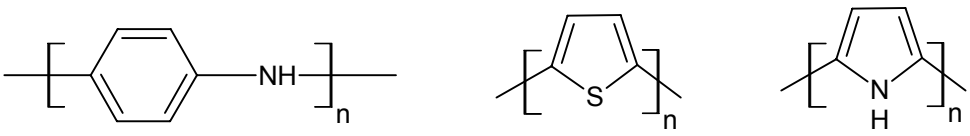

(a) (b) (c)

Figure 1.1 The structures of ICPs (a) polyaniline, (b) polythiophene and (c) polypyrrole.

The treatment of a conjugated polymer with an oxidant leads to inclusion of a molecular dopant (A^-) and a concomitant increase in electron mobility and electrical conductivity (e.g. Figure 1.2[1,2]).

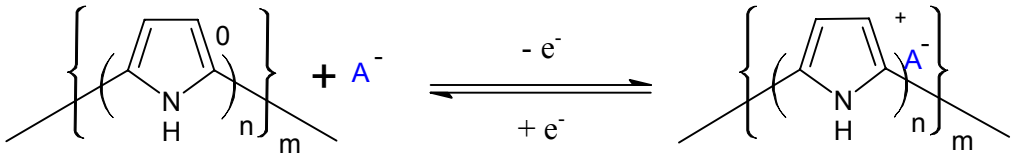

Figure 1.2 Doping and dedoping process of PPy. n is the number of monomer units per unit positive charge; A^- is a counterion (molecular dopant) incorporated during synthesis, m determines molecular weight.

The molecular dopant incorporated into the conducting polymer during synthesis has a profound effect on processability and conductivity[5]. The dopant also determines the chemical/biological properties of the conducting polymer. For example, the incorporation of oligonucleotides into PPy has been used to produce biosensors[6]; light harvesting porphyrins molecules have been incorporated in PTTh for the development of photovoltaic devices[7]; and biological moieties have been successfully incorporated into PPy to improve performance when used as a novel platform for mammalion cell culturing[8].

The electrical conductivity range of several conducting polymers are comparable to conventional metals and semiconductors as shown in Figure 1.3[4]. The main limitations of conducting polymers include poor processability, both in melt and solution processing[9], and poor environmental stability[3]. Therefore numerous studies have been aimed at improving their processability[10], stability[3,9,11,12] and conductivity[9,13,14]. Synthesis of conducting polymer nanoparticles is one method to improve these properties. Emulsion polymerisation[9,14-18] or the use of steric stabilisers[19-33] results in formation of nanoparticles. Such nanoparticles are of interest in various applications such as sensor technologies[34], transparent EMI shielding, antistatic coatings, display devices and electrochromics[9].

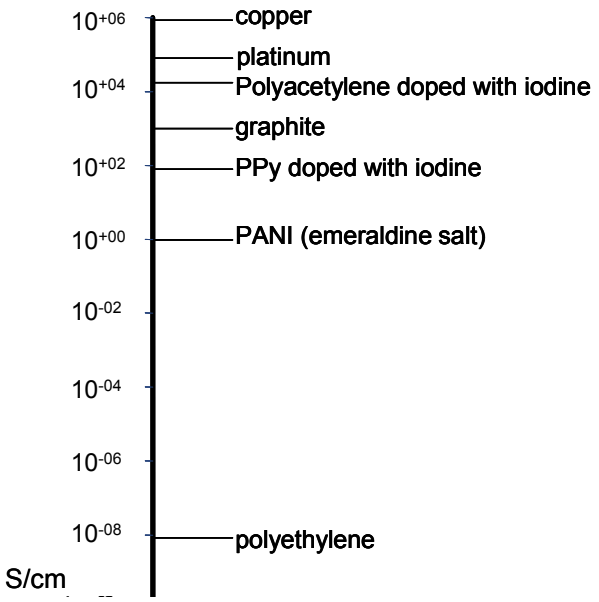

Figure 1.3 Conductivity chart for metals and various conducting polymers.

1.1.1 Polyaniline (PANI)

Polyaniline (Figure 1.1a) has been the most extensively studied ICP over the past decade, due to its reversible redox and pH switching properties, ease of synthesis and wide range of potential applications[2]. Its polymeric structure (Figure 1.4) is different from the other ICPs such as PTh (Figure 1.1b) and PPy (Figure 1.1c), and leads to three oxidation states, each with its own distinctive colour[2]. The fully reduced leucoemeraldine base (LB) form is colourless or pale yellow, protonated emeraldine salt (ES) form is bright green, and the fully oxidised pernigraniline base (PB) form is dark blue[35,36].

Polyaniline has a very strong pH sensitivity, which is based on a reversible acid-base reaction[36]. The only electrically conducting form of PANI, the ES form, can be obtained either by protonation of half oxidised emeraldine base (EB) or by oxidation of LB. It is noteworthy that the protonation does not affect the oxidation state of PANI[36]. The structures and transition states of PANI are shown in Figure 1.4.

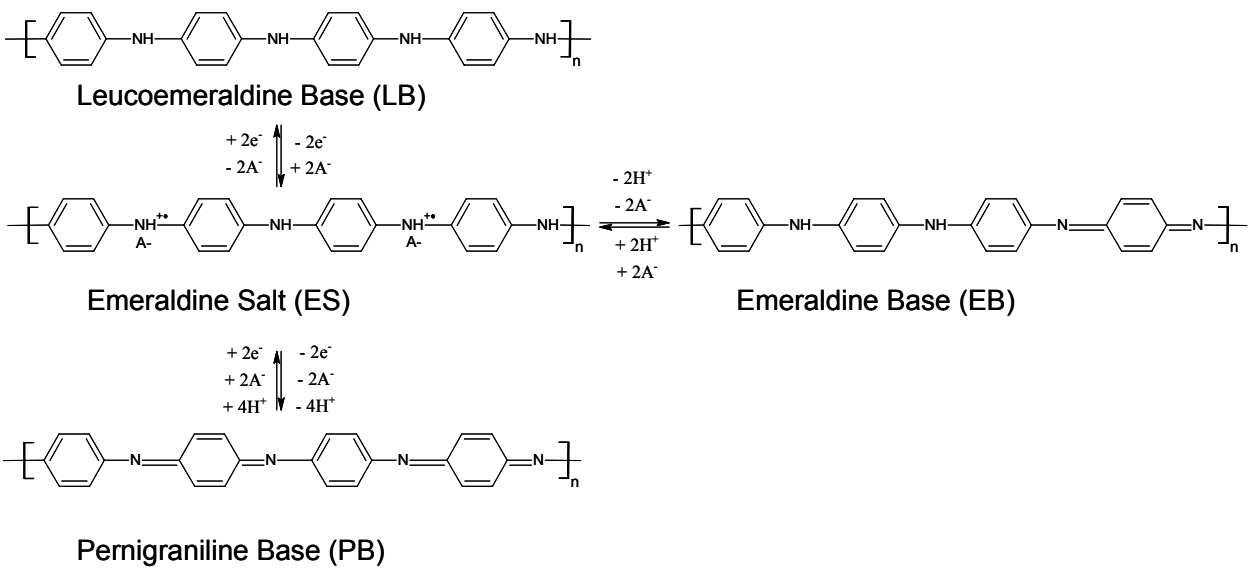

Figure 1.4 The redox mechanism of PANI and its pH dependent transition between the ES and EB form.

Aniline can be polymerised electrochemically or by chemical oxidation in acidic solution[2]. In Figure 1.5, the mechanism of chemical polymerisation is depicted and the rate-determining step is considered to be the formation of the radical cation of aniline by oxidation[2] (Figure 1.5 a[1]). The radical cation has resonance structures as shown in Figure 1.5 b[1]. After formation of the radical cation the chemical polymerisation involves radical coupling, chain propagation, and reduction of pernigraniline salt (PS) to emeraldine salt (ES) as shown in Figure 1.5 c, d and e, respectively[2,35].

(a) Oxidation of monomer

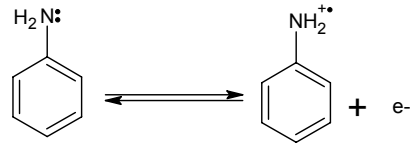

(b) Resonance formation

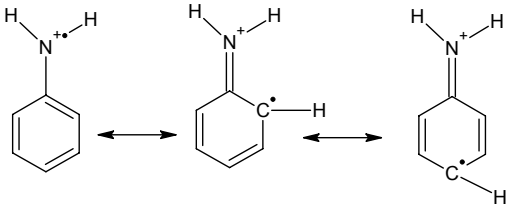

(c) Radical coupling

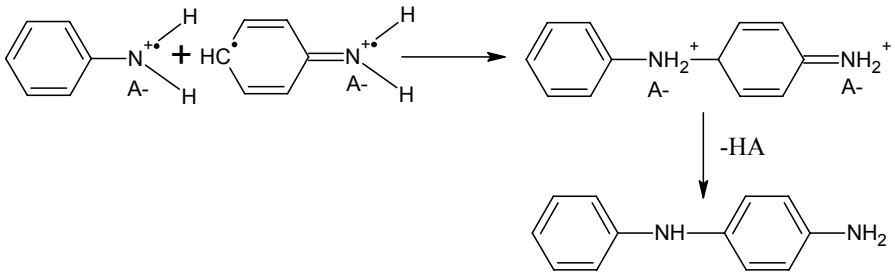

(d) Chain propagation

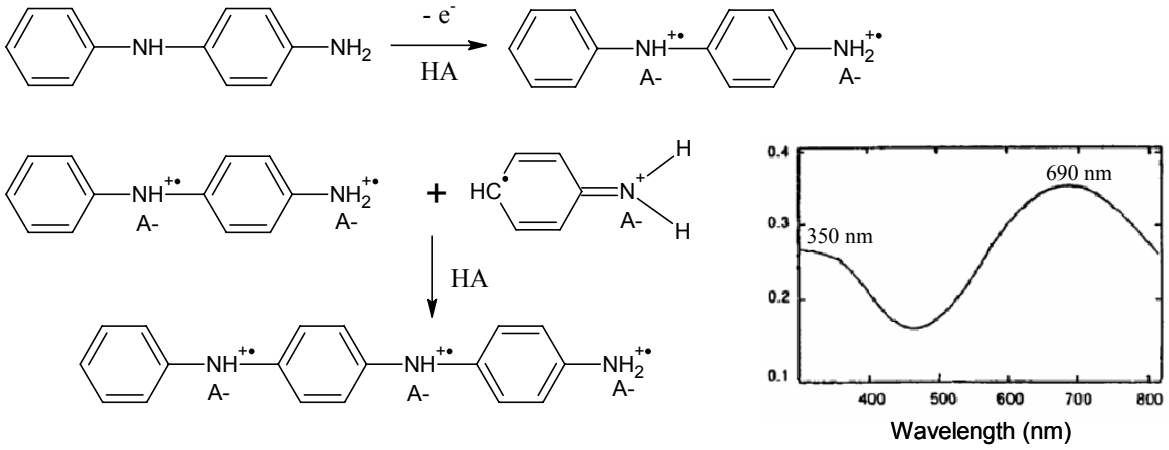

(e) Reduction of PS to ES

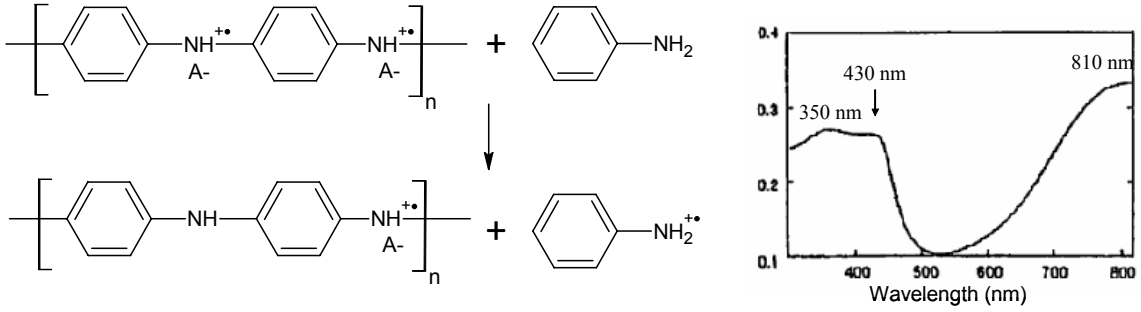

Figure 1.5 Mechanism of formation of PANI synthesised by chemical oxidative polymerisation and corresponding UV-visible spectra of (d) perniganiline salt and (e) emeraldine salt form.

The initial product of chemical polymerisation has been shown to be the fully oxidised PS form of PANI which is due to high oxidising power of ammonium persulfate

(1.94 V vs. SHE)[2]. Stejskal *et al*[35] and Haba *et al*[37] used a spectroscopic study to confirm the change to the PS form of PANI. A deep blue colour was observed and the UV-visible spectra indicated the presence of the protonated pernigraniline structure in its dication diradical form with the polaron peak appearing at about 690 nm[35,37] (Figure 1.5 d). When the oxidant is all consumed, PS oxidises the aniline monomer to the radical cation and PS itself returns to ES[2] (confirmed by green colour and UV-visible spectrum[35] shown in Figure 1.5 e). The three absorption peaks in the UV-visible spectrum of the emeraldine salt form can be assigned as the transitions from π band to π* band (350 nm), π*-polaron band (430 nm) and polaron band (810 nm)[38].

The two distinct redox processes of PANI can also be observed using cyclic voltammetry as shown in Figure 1.6[2]. The most conductive form of the polyaniline is the ES form which occurs between about 0.2 V and 0.6 V vs. Ag/AgCl. The fully undoped form (leucoemeraldine), which occurs at less positive potentials, and fully oxidised form (pernigraniline), which occurs at higher potentials, are much less conductive[2]. If the PANI polymer is exposed to potentials greater than the second oxidation process, a third voltammetric response appears at around 0.5 V which is due to oxidation/reduction of a degradation product such as *p*-benzoquinone and hydroquinone[2,39].

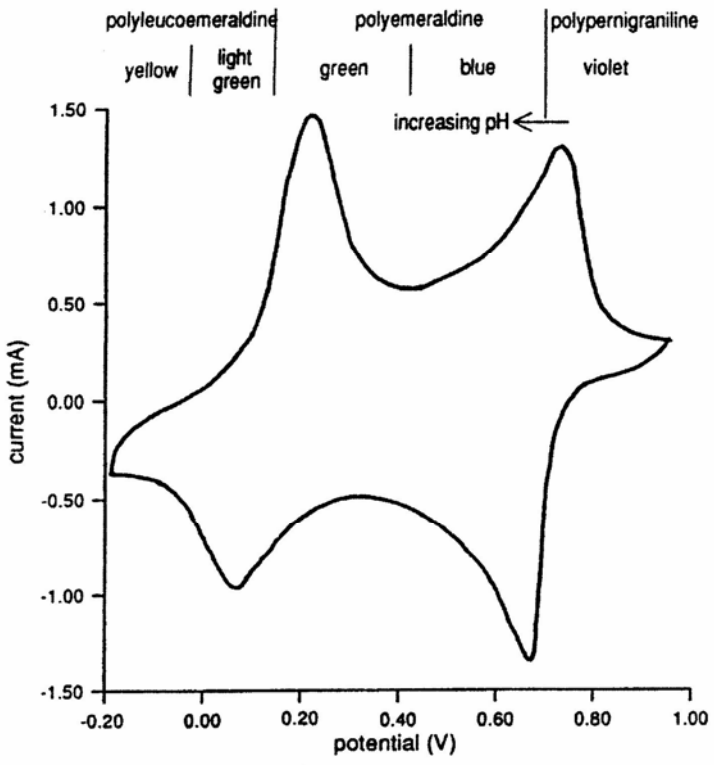

Figure 1.6 Cyclic voltammogram of polyaniline (HCl) on a glassy carbon electrode in 1 M $HCl_{(aq)}$ electrolyte (pH 0) at 50 mV/s scan rate. The potentials at which structure and colour changes occur are shown. The second oxidation peak shifts to a less positive potential with increasing pH[2].

Chemical properties, conductivity and colour of the PANI vary with the oxidation states and/or degree of protonation, and can be controlled by application of a potential or an acid or base. These chromatic changes have led to the use of PANI for display devices, redox and pH indicators and other applications[2].

1.1.2 Poly(2-methoxyaniline-5-sulphonic acid)

The application of PANI has been limited due to its infusibility and modest solubility in common organic solvents; hence lack of processability[2,20,22]. In order to improve processability, synthesis of polymer from functionalised monomers has been employed to improve solubility[2]. Alkyl- and alkoxy groups can be substituted onto the

aniline monomer that is subsequently used to produce a polymer with markedly improved solubility in organic solvent. Sulphonic acid and phosphonic acid are also utilised to generate self-doped PANI. A fully sulphonated polymer related to PANI, poly(2-methoxyaniline-5-sulphonic acid) (PMAS) (Figure 1.7), can be prepared from sulphonic acid and methoxy group substituted monomer[2].

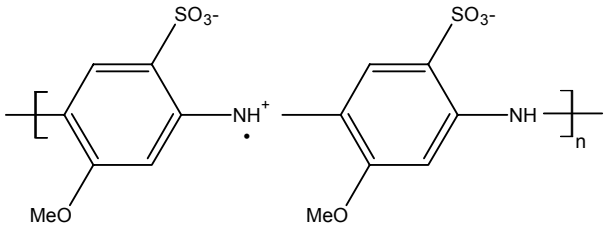

Figure 1.7 PMAS structure.

Introduction of the sulphonate group has a dramatic effect on the polymerisation process as its electron-withdrawing effect lowers the electron density on the amino groups of PANI, which consequently lowers the molecular weight and conductivity of the polymer produced[40]. In order to solve this problem an electron-donating methoxy group is substituted onto the aniline ring. The 2-methoxyaniline-5-sulphonic acid (MAS) monomer can be chemically synthesised under normal atmospheric pressure using aqueous solution of ammonium peroxydisulphate (APS) as the oxidant in the presence of ammonia or pyridine (to assist with monomer solubility in water)[2,41]. The polymer can be obtained in up to 90% isolated yield with molecular weight of approximately 10,000 Da and conductivity of 0.04 S/cm. The monomer can also be electropolymerised and the polymer obtained has similar conductivity to the chemical synthesis but a slightly higher average molecular weight of 15,000 Da[42].

Although these polymers have lower conductivity and molecular weight than the parent PANI, their solubility and redox activity over a broad range of pH make them good

candidates for sensor and biosensor applications[2,43]. In some cases, they have been found to be redox active in solutions up to pH 14[43]. Chiroptical properties can be induced in PMAS and this could potentially be used as a chiral ion exchange material for enantiomeric separations[44,45].

Zhou *et al*[42] synthesised PMAS using a flow-through electropolymerisation set up. The UV-visible spectrum of PMAS solution obtained using this method exhibited the characteristic polymer absorption peak at 475 nm (Figure 1.8) and increase of this peak with polymerisation time.

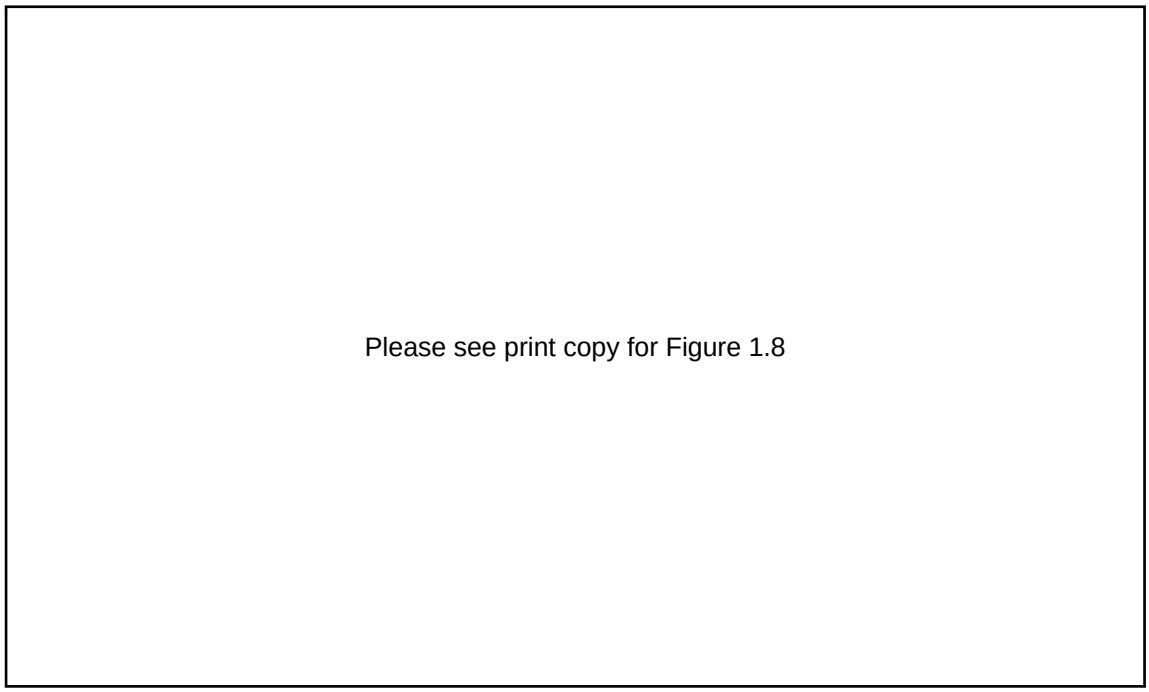

Figure 1.8 UV-visible spectra of PMAS electrochemically synthesised at 0.3 to 0.5 V and 100 ml/min flow rate from solution containing 0.5 M MAS monomer at pH 4.1 with synthesis time marked on curve. Catholyte solution was about pH 10-11. Reproduced from Ref [46].

Tallman and Wallace[46] investigated electroactivity of PMAS-poly(4-vinylpyridine) (PVP) by casting an ethanol slurry of the PMAS-PVP complex on a platinum (Pt) electrode.

Cyclic voltammograms were subsequently obtained in 0.1 M HCl as shown in Figure 1.9. The CV reveals the two main redox waves characteristic of a PANI with slightly broad middle peak (C) around 0.5 V indicating the presence of an over-oxidation product when the potential is taken to 0.8 V and beyond. Only one reduction peak was observed on the reverse scan[46].

Please see print copy for Figure 1.9

Figure1.9 Cyclic voltammogram of a PMAS-PVP film deposited on a Pt electrode, in 0.1 M HCl at 20 mV/s scan rate and $E_{initial}$ = 0.0 V. Reproduced from Ref [47].

1.1.3 Polypyrrole

Polypyrrole (PPy) has been intensively studied due to its mechanical and electrochemical stability, relatively good conductivity and ease of synthesis. The character of the polymer is determined largely by the anion present during the polymerisation which dopes the polymer as it forms[47]. It can be synthesised by electrochemical polymerisation[26-28,30,47-54], chemical polymerisation[25,32,55-62] and enzyme-catalysed polymerisation[63]. Generally, electrochemical synthesis produces continuous films deposited on the working electrode whereas chemical synthesis produces powders and enzymatic polymerisation gives aqueous dispersions[2]. The oxidation mechanism is presented in Figure 1.10[2,64].

Step 1. Monomer Oxidation

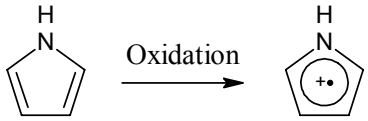

Resonance forms

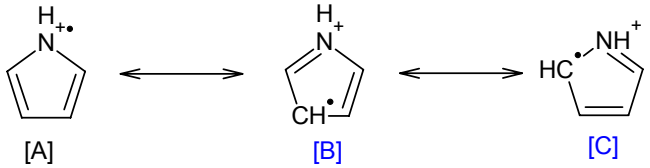

Step 2. Radical-Radical Coupling and Deprotonation

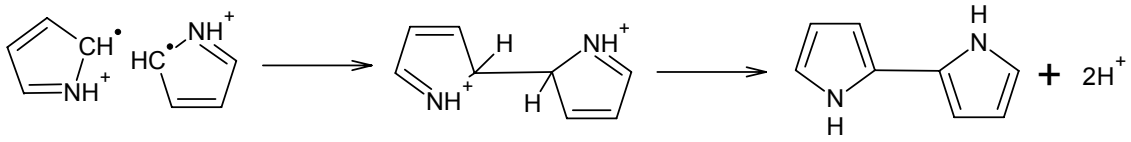

Step 3. Chain Propagation

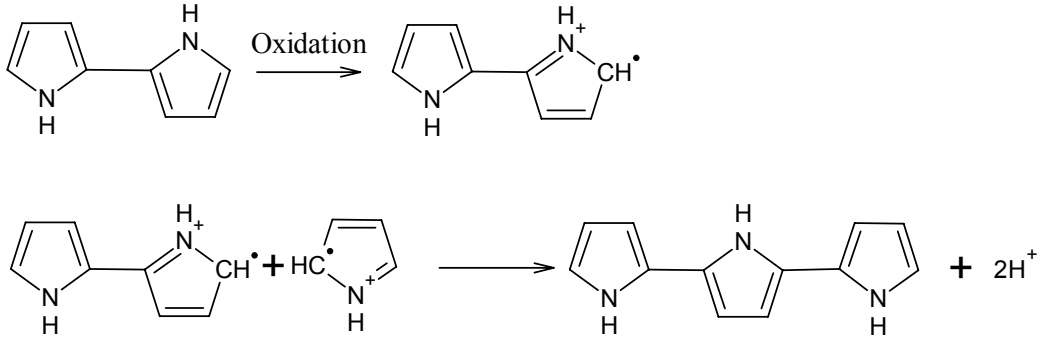

Figure 1.10 Synthesis of PPy.

Polymerisation of pyrrole can be carried out in neutral aqueous solution (with no acid required) which is a significant advantage over PANI synthesis in terms of flexibility and compatibility with biomolecules[2]. A wide range of dopants have been incorporated in PPy including enzymes[63,65], hyaluronic acid[66] and proteins[67]. PPy has been used widely in a range of applications such as substrates to support cellular growth[8,66], biosensors[65,67-69]and actuators[52].

Enzyme-catalysed polymerisation of PPy using horseradish peroxidase (HRP) was demonstrated by Nabid and Entezami[63]. The UV-visible spectra (Figure 1.11) reveal the formation of PPy after addition of the oxidant, hydrogen peroxide (H_2O_2). The absorption peak at 279 nm corresponded to the polyelectrolyte, poly(sodium 4-styrene sulfonate) (PSS), whereas the peak at 450 is assigned to π-π* transition and the polaron band near the IR region is characteristic of an oxidised PPy[63] (Figure 1.11 b).

Please see print copy for Figure 1.11

Figure 1.11 UV-visible spectra of the mixture reaction Py/PSS: (a) before and (b) after the addition of H_2O_2[63].

Skaarup *et al*[51] electrochemically synthesised PPy-dodecylbenzene sulphonate (DBS) and studied its electroactivity. Its CV in 0.05 M potassium chloride (KCl) is shown in Figure 1.12. The cathodic sweep is dominated by a sharp reduction peak at about -0.6 V (vs. SCE) whereas the broader anodic peak centered about -0.5 V is attributed to the expulsion of potassium ion (K^+). The smaller and broader peak at 0.2 to 0.5 V was tentatively assigned to the uptake of small anions (e.g. Cl^-) from the cycling electrolyte[51].

Please see print copy for Figure 1.12

Figure 1.12 Cyclic voltammogram (2nd cycle) of PPy-DBS film deposited on Pt wire in 0.05 M KCl at 50 mV/s scan rate[51].

1.1.4 Polythiophene

Polythiophene (PTh) is another conducting polymer which has been extensively studied in the past 20 years due to its high stability and ease of manipulating the structure and consequently the optical properties, electrical properties and conductivity[70]. Thiophene monomer is a five membered heterocyclic molecule as shown in Figure 1.13, and its oxidation polymerisation is similar to that of PPy (Figure 1.10).

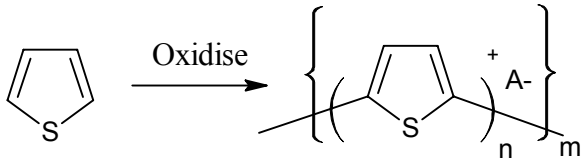

Figure 1.13 Oxidative polymerisation of thiophene monomer to PTh. n is the number of monomer units per unit positive charge; A^- is a counterion (molecular dopant) incorporated during synthesis, m determines molecular weight.

The application of PTh has been limited due to poor solubility, which arises from its rigid backbone[71]. It also requires a higher oxidation potential for polymerisation than the other ICPs described. There are numerous chemical methods being explored to modify the thiophene monomer by substitution of functional groups at the 3-(β) position. The addition

of functional groups generally aims at improving processability by lowering oxidation potential and making more soluble materials, as well as improving function of the polymer through addition of reactive groups.

The regioregular structure of this polymer plays a very important role in the improvement of the electronic and photonic properties of PTh as reviewed by many authors[2,70,72]. This kind of structure is formed when two thiophene rings are coupled at 2- and 5- positions which results in the 2,5' or head-to-tail (HT) coupling[72]. A coplanar arrangement structure and more effective electron hopping processes could be expected resulting in improved conductivity. Poly(3-alkylthiophene) was one of the earliest discovered and most extensively studied substituted thiophene polymers[70,72,73]. More research aiming to synthesis soluble PTh by modification of the monomer side chain group has been performed. Incorporation of carboxylic acid groups[74], increasing alkyl-chain length of the substituent[71] and addition of sulfonate moieties[75-78] have all been investigated with a view to improve solubility. All those methods are generally based on complex chemical synthesis of the monomers. Subsequent polymerisation has been achieved chemically[73,74,79-89], electrochemically[90-108] or using either approach[78,109-112]. However, simpler methods have been used in order to make soluble polymers, such as combinatorial synthesis of the polymer with a water dispersible polyelectrolyte such as polystyrenesulfonic acid (PSS)[88], or using poly(vinyl alcohol) (PVA) as a steric stabiliser[113] or dodecylbenzene sulphonic acid (DBSA) as a micellar media[89].

Zhang *et al*[114] studied the effect of the potential applied during electropolymerisation of terthiophene in boron-fluoride ethyl ether (BFEE). With applied potentials higher than 0.8 V, irregularly linked α,β-linkages were formed. UV-visible spectra reveal different absorption peaks for polymers synthesised at different oxidation

potentials (Figure 1.14)[114]. The absorption peaks at around 400-480 nm are assigned to the π-π* transition associated with the conjugated chain length of the polymer. This peak shifts to higher wavelength as the applied potential shifts from 0.65 to 0.75 V indicating that more effective conjugated chain lengths were obtained at higher potentials. However, the peak shifts to lower wavelength when the applied oxidation potential was increased to 0.85 V. This may be attributed to the mislinked thiophene rings leading to a decrease in the effective conjugated chain lengths[114].

Please see print copy for Figure 1.14

Figure 1.14 The UV-visible spectra of (A) terthiophene monomer in hexane and (B)-(D) the neutral polyterthiophene (PTTh) films synthesised at 0.65, 0.75 and 0.85 V, respectively[114].

The cyclic voltammogram of the polythiophene (PTTh) synthesised in BFEE at 0.75 V (Figure 1.15) displays a broad anodic peak at about 0.9 to 1.1 V due to polymer oxidation and a cathodic peak at about 0.1 to 0.3 V due to polymer reduction[114].

PTh and its derivatives have been used in photovoltaic devices[77,90,100,115], sensors[86,116,117], diodes[85], light-emitting displays (LEDs)[83] and for mild steel protection[118].

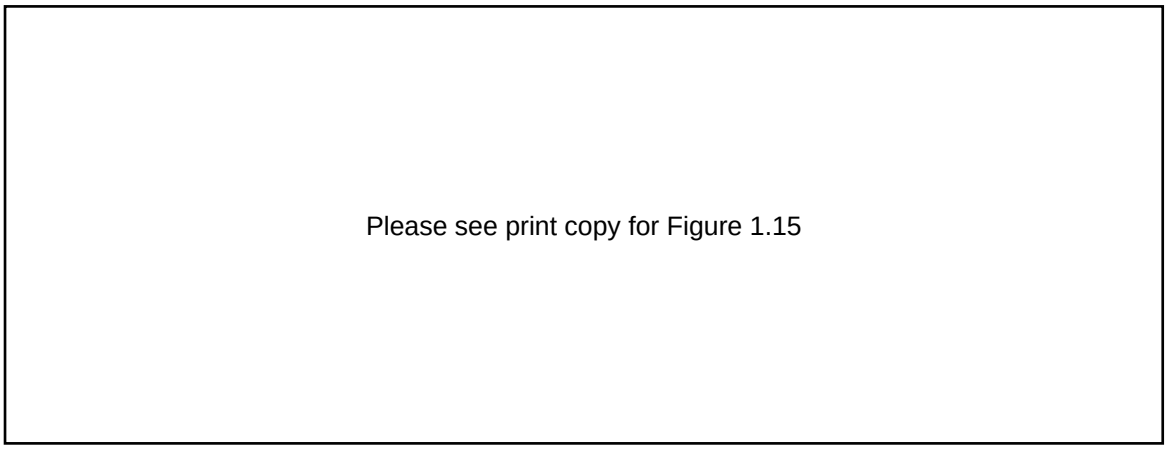

Figure 1.15 The CVs of PTTh in BFEE, cycle 1, 3, 100, 200, 500, 1000 and 1200 are recorded at 40 mV/s scan rate[114].

1.2 Conducting Polymer Nanoparticles

Nanostructures are defined as structures that have at least one dimension between 1 and 100 nm. They have received much interest as a result of their peculiar and fascinating properties often superior to their bulk counterparts[119]. The nanoparticle domain has been dominated by inorganic materials as these materials are well characterised and utilised in the development of electronic devices. The combination of the nanoparticle and ICPs has been developed to achieve new synergistic properties of the composites and a number of researchers have turned their attention to the synthesis and characterisation of ICP nanocomponents in recent years[120]. These studies have included making composite structures with existing nanoparticles and nanostructures[121-125] as well as attempts to synthesise true ICP nanostructures[9,14,89].

Conducting polymer nanostructures are a very important class of electrochemically active materials and they are highly desirable for applications ranging from chemical and

biological sensing, micro-electronic devices and interconnects, energy conversion and storage (photovoltaic cells, batteries and capacitors, and hydrogen storage devices), catalysis, optical emission, data storage, electrochromics, and even anti-corrosion[2,126].

For example, in sensor applications, Huang *et al*[34] have shown that chemical sensors prepared from nanostructured PANI have greater sensitivity and faster response relative to their conventional bulk counterpart, due to higher effective surface area and shorter penetration depth for target molecules. Moreover, Xia and Wang[16] described the advantages of PANI nanoparticles as;

(i) special electrical, optical, opto-electrical properties due to smaller size,

(ii) decrease of the particle size provides better dispersion stability and more uniform PANI dispersions, which is helpful in producing uniform, transparent conducting polymer thin films and thus in overcoming the problem of processability,

(iii) decrease in particle size can promote more effective doping, strengthen inter- or intrachain interaction and enhance the degree of crystallinity, and

(iv) conducting polymer blends with low percolation thresholds can be prepared using PANI nanoparticles.

Conducting polymer nanowires/-rods/-fibers and particles can be synthesised using various methods such as interfacial polymerisation[34,127], rapid mixing polymerisation[128], and emulsion/inverse microemulsion polymerisation using surfactants[9,14-18] or steric stabilisers[20-24]. Physical templates, molecular templates and nanocomposites are also methods used for production of ICP nanostructures as reviewed by Wallace and Innis[120]. In this thesis, emulsion polymerisation and the use of steric stabiliser were the methods of choice used to synthesis the ICP nanoparticles.

1.2.1 Emulsion polymerisation

Surfactants are amphiphilic compounds containing polar (hydrophilic) head and non-polar (hydrophobic) tails[129]. In solution, a micelle is formed as the surfactants form aggregates in which the hydrophobic tail are oriented towards the interior of the micelle, leaving the hydrophilic groups in contact with the aqueous medium[130].

The critical micelle concentration is the threshold surfactant concentration at which micellisation begins[131]. The CMC of the system can be determined by observation of a property of the solution that displays a discontinuity in slope when plotted against increasing surfactant concentration (Figure 1.16)[131]. In emulsion polymerisation, the surfactant concentration used needs to be higher than the CMC. Below the CMC, anionic surfactants behave as strong electrolytes[131].

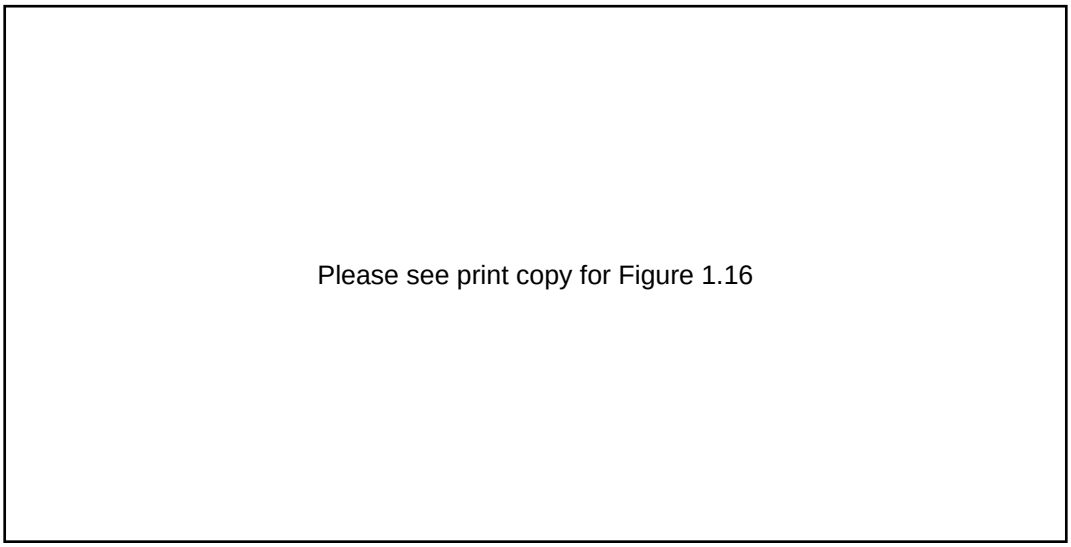

Figure 1.16 Schematic illustration of variation of solution properties with surfactant concentration. The shadowing indicates that the CMC is not necessarily sharply defined[131].

Typically, micelles tend to be approximately spherical at the concentration above the CMC; at higher concentrations (approximately higher than 40%) and under appropriate conditions these spherical micelles may adopt a cylindrical, ellipsoidal, or laminar form (Figure 1.17). Systems containing these non-spherical forms tend to have high viscosity[130,132].

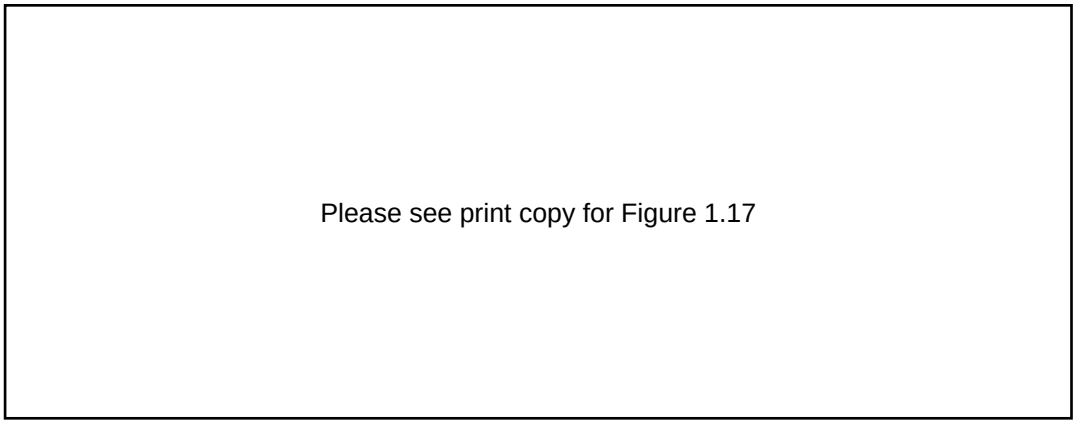

Figure 1.17 Some types of micellar structure: (a) spherical, (b) disc-like, (c) cylindrical, (d) lamellar, and (e) spherical vesicle. The head groups are shown as filled circles[132].

In emulsion polymerisation of ICPs, the monomer assembles itself into micelles. The location of the monomer in the micelles is important as it can dictate the reaction mechanism and properties of the final product[9]. The semipolar amines (aniline monomer) locate at the palisade layer (the region between the hydrophilic groups and the first few carbon atoms of the hydrophobic group) of the micelle, with the polar group at the micellar surface and the nonpolar hydrocarbon groups in the micellar[133]. The proposed mechanism for synthesis of PANI-dedecylbenzene sulphonic acid (DBSA), as determined by Han *et al*[9], is shown in Figure 1.18. Anilinium cations (phenyl-NH_3^+) sit between the individual DBSA molecules near the shell of a micelle, complexed with sulfonate ion. When polymerisation

proceeds, anilinium cations are polymerised within the micelle together with DBSA and forms the PANI (ES)[9].

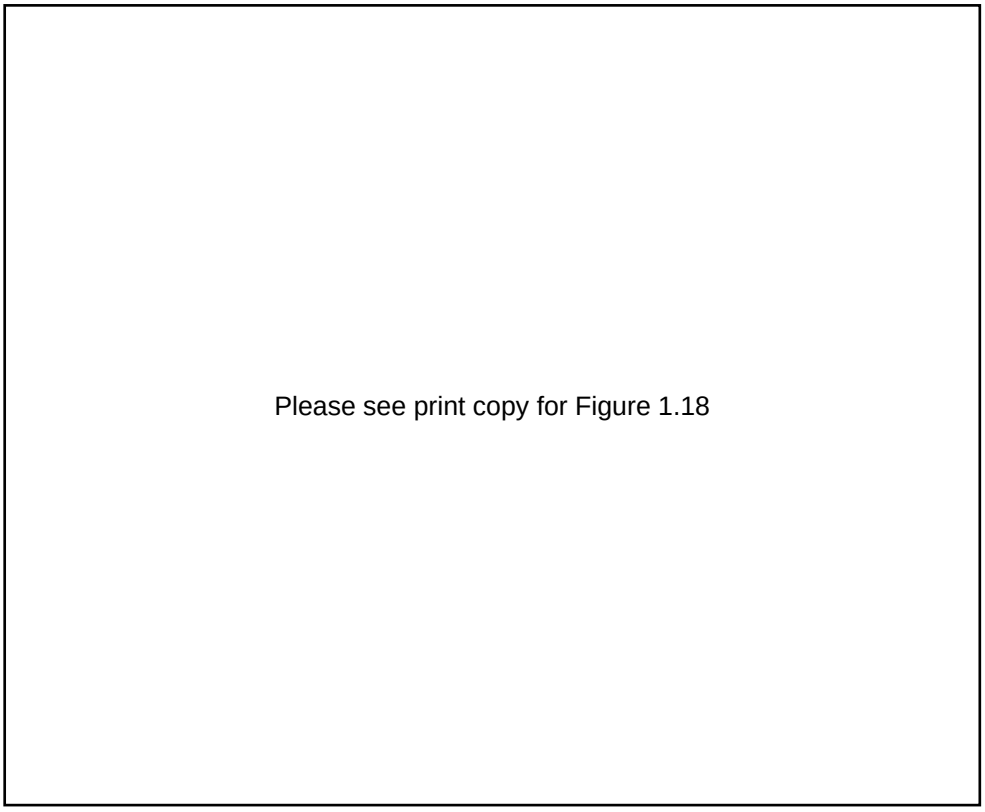

Figure 1.18 Reaction scheme of PANI preparation in the DBSA micellar system[9].

1.2.2 Use of steric stabilisers

Apart from making ICP nanodispersions using the emulsion polymerisation method, a combination of surfactants and steric stabilisers has also been used in nanoparticles synthesis. Many stabilisers such as poly(styrene sulphonic acid)[25], poly(vinyl alcohol) (PVA)[26-30], poly(N-vinyl pyrrolidone)[23,31], poly(ethylene glycol)[32] and hydroxypropylcellulose have been used[31,33].

In a typical dispersion polymerisation process, the monomer is miscible in the reaction medium, and upon monomer oxidation the polymer formed is insoluble and precipitates out of the solution. When polymerisation proceeds in the presence of a steric stabiliser, which is soluble in the reaction medium, macroscopic precipitation of the polymer can be prevented and submicrometer particles stabilised in solution are obtained[134].

The ICPs are believed to be in the 'core' which is surrounded by an outer layer of adsorbed, solvated water-soluble stabilisers[25] as shown in Figure 1.19. The outer layer stabilises the particles against coagulation by masking van der Waals attraction between the particles, hence imparting stability to the dispersion[131]. The colloidal stability of such ICP particles is strongly dependent on the nature of the stabilisers[134].

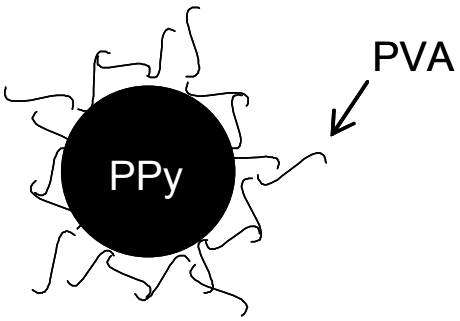

Figure 1.19 Schematic representation of PPy colloids stabilised by steric stabilisers.

1.3 Polymer-modified Amperometric Biosensors

Polymer-modified amperometric biosensors are bioactive modified electrodes in which the specificity and selectivity of a bioreaction culminate in a current response proportional to the analyte concentration. Biomolecules can be entrapped in conducting polymer films by electrochemical polymerisation of the conducting polymer in the presence of the biomolecules[135-141]. However, to avoid the extreme conditions such as high acidity

which arise during polymerisation, the biomolecules can be subsequently immobilised on the polymeric films by the means of electrochemical[142-144], evaporative casting[145] and dip-coating[146].

Enzymes and other biomolecules immobilised on modified electrodes catalyse biospecific redox reactions and the resulting electroactive species can be detected at the electrode. This approach leads to detection of many electroactive molecules of biological interest. These sensors are popular for several reasons. The polymers can be applied to an electrode surface in different thickness resulting in the possibility to increase the concentration of response-modifying species such as electron transfer mediators and enzymes[147]. The three-dimensional distribution of mediators is preferable to monolayer coatings for the design of biosensors, due to the larger catalytic response of polymer coating owing to the volume effect[145]. Moreover, the electroactive film can be used to provide a favorable microenvironment in which an enzyme reaction can proceed efficiently and also can protect the electrode from fouling by nonspecific protein adsorption and exclude interference species[148].

1.3.1 Horseradish peroxidase and hydrogen peroxide system

Horseradish peroxidase (HRP) is a haemoprotein enzyme isolated from horseradish[149] and a well-documented enzyme that has been immobilised onto various supports for use in biosensors[150]. HRP based biosensors are important in many fields of analyses and its sensitivity can be significantly improved by using mediators[151]. Conducting polymer with immobilised HRP electrode has been used to detect H_2O_2 electrochemically via an enzyme-catalysed mechanism[138,139,145,152-154], integrated with glucose oxidase or putrescine oxidase in bi-enzyme systems to detect glucose[135,136,140,151,155]

or putrescine[156], and used as antigen-labelled enzymes to detect specific antibodies[142-144]. In this thesis, HRP has been used to detect hydrogen peroxide (H_2O_2) as a model system to demonstrate the application of ICP nanodispersions as mediators for biosensors.

The HRP-catalysed reduction of peroxides can occur in the presence of redox species which are either electron donors or hydrogen donors[136]. The direct oxidation of H_2O_2 requires a relatively high working electrode potential (about 0.6 V vs. SCE). At this high potential, interference species such as urate, acetaminophen and ascorbic acid can also be electrochemically oxidised and produce an interfering response[136,154]. Hydrogen peroxide can be detected enzymatically at low applied potentials by employing peroxidases as bioelectrocatalysts for its electrochemical reduction[136]. HRP is often combined with ICPs and is used for the fabrication of H_2O_2 sensors because direct electron transfer from ICPs to oxidised HRP (compound I and II in Figure 1.20) is possible[153].

Please see print copy for Figure 1.20

Figure 1.20 The Pt/PANI-PVS/HRP biosensor reaction scheme. Ferric HRP resting state (Fe^{III}), oxyferryl HRP-I ($Fe^{\bullet+IV}$ =O), Hydroxylferryl HRP-II ($Fe^{\bullet\bullet IV}$-OH) and polyleucoemeraldine/polyleucoemeraldine radical cation redox couple ($PANI^{0/+}$), participate in the peroxidase ping-pong mechanism[138].

In Figure 1.20, $PANI^0$ participates in the biosensing process by converting HRP-I to HRP via a two-electron reduction step. The $PANI^+$ is then reduced at the electrode which is held at a suitable constant potential. The magnitude of the reduction depends on the bulk concentration of the substrate (H_2O_2)[142-144,153].

1.3.2 Fabrication methods

Sensor detection limit can be lowered by fabrication of ultrathin and coherent layers of the conducting polymers[2]. ICPs can be fabricated as sensors by various methods such as electropolymerisation of the monomers[69,157], evaporative casting[158-161] and electrodeposition[162] of the preformed polymer, and matrix-assisted pulsed laser evaporation (MAPLE)[163]. Other methods such as screen printing[164,165] and ink-jet printing[166-173] are currently being used to fabricate conducting polymer devices. These approaches enable rapid sensor production and are amenable to scale up.

1.3.2.1 Electrodeposition

Electrochemical fabrication of ICPs has been used widely[135-141,153]. Various electrochemical methods can be used to produce ICPs biosensors such as potentiostatic[137,141,174,175], galvanostatic[136,139,176-179] and potentiodynamic[153,180-182]. The advantages of the electrodeposition method are (i) the thickness and characteristics of the sensing film, and hence the rate of response of the biosensor, can be controlled by choosing appropriate electrochemical synthesis conditions[153], and (ii) the electrochemical reaction is localised at the electrode surface allowing precise modification of micro-electrodes and/or surfaces with complex geometries[138,148]. One drawback of the electrodeposition method is that the electrode can only be processed one at a time; hence it is not a practical method for mass production.

1.3.2.2 Evaporative casting

Evaporative casting[155,159] is a an easy one-step method for producing polymer films containing the entrapped biomolecule. Using this method allows the amount of biomolecule to be controlled; hence eliminating waste. Moreover, this method provides better accessibility of the polymer to the biomolecules as the biomolecules are not just adsorbed on the polymer surface but entrapped within the polymer matrix encouraging polymer and biomolecules interaction throughout the films[159].

1.3.2.3 Ink-jet printing

Ink-jet printing is a recent advance in film formation and has been used in the ceramic industry for printing the binder onto substrates as well as printing ceramic suspensions[183-185]. It has also been used to print conducting polymers for fabrication of transistors[166,167,186], diodes[171,187], organic light-emitting devices (OLEDs)[188], RC filter circuits[168,189], capacitors[170] and biosensors[173].

Ink-jet printing is a non-contact printing method and the high speed printing ability makes it amenable for mass production. Precise and accurate printing patterns can be controlled using computer software[167]. Furthermore, different materials can be printed simultaneously via different nozzles[166], and only picolitre volumes are consumed per printed drop[188].

The most commonly used operating systems in ink-jet printing are thermal and piezoelectric methods[190]. In thermal ink-jet printing, the heat (~300 °C) generated from a short voltage pulse inside the ink cartridge causes the solvent to evaporate. The transition from liquid to vapour causes expansion of the ink which is then forced to be jetted from the nozzle[191]. The time from bubble formation to collapse takes place in less than 10 μs[190].

Ballarin[169] and Setti *et al*[173] used a thermal ink-jet printing system to fabricate conducting polymer films. Films were characterised and shown to possess the same properties as spin-coated films demonstrating that thermal printing did not alter the material properties[169]. Thermal ink-jet printing was also applied to fabrication of ICPs for biosensor application but low sensor performance was obtained[173].

For piezoelectric ink-jet printing, the special ceramic material inside the print head becomes deformed by the electric field. The deformation causes the ink volume to change and the pressure generated forces the ink jet through the nozzle[190,191]. The piezoelectric method has been used in various studies to fabricate ICPs for transistors[166,167,192], diodes[171] and capacitors[170]. This method has also been used to print ceramic suspensions[184,185], gold or silver conductive tracks[193,194] and refractive lenses[195]. As the conducting polymer and biomolecules can be degraded or denatured at high temperature, the piezoelectric method was used in this thesis. Epson C45 was chosen as it uses the piezoelectric method and also is low cost and available in the market.

1.4 Structure of the Thesis and the Aim of the Chapter

Part I-General introduction and characterisation techniques

This part gives general introduction of the related topics and also the detail of characterisation techniques used in the thesis.

Part II-Synthesis and characterisation of conducting polymer nanodispersions

This section deals with synthesis and characterisation of the ICP nanodispersions in aqueous media. Three ICPs are synthesised; namely PANI, PPy and PTTh. Different

methods used to produce and characterise the nanodispersions are discussed in this section. Some dispersions described here were further used for biosensing applications in part III.

Chapter 3 describes the production of PANI nanodispersions in aqueous media. Details of synthesis and characterisation of various PANI nanodispersions are given. The *nano*PANI-DBSA was successfully synthesised using emulsion polymerisation and further used as the mediator for biosensing applications in Chapter 7. The *nano*PANI-DBSA was also further processed to attain the supernatant of *nano*PANI-DBSA (sPANI-DBSA) for ink-jet printing (Chapter 9). The PANI-DBSA-rapid mixing (PANI-DBSA-RM) polymer was synthesised using the modified rapid-mixing method from Huang *et al*[128] and also used as the ink-jet printing material in Chapter 9.

The ability to incorporate functional molecules into the PANI nanoparticles was investigated using Carbolan Blue dye as the model compound as outlined in Chapter 4.

The work in Chapter 5 describes production of high concentration PPy nanodispersions for ink-jet printing. The steric stabiliser poly (vinyl alcohol) (PVA), in combination with a surfactant, was used to synthesise the PPy-SDS-PVA nanodispersions. The nanodispersions were characterised using various techniques. This work was a collaborative venture between the Department of Chemistry, Kasetsart University, Thailand and the Intelligent Polymer Research Insititute (IPRI), University of Wollongong.

In Chapter 6, synthesis of PTTh nanodispersions in aqueous media was investigated using emulsion polymerisation with the aid of organic solvents. The characterisation of the polymer obtained shows poor electroactivity; hence an alternative method was investigated. In the second approach, PTTh nanodispersions were synthesised in ionic liquid using gold chloride as the oxidant. The nanodispersions from the latter method showed improved electroactivity which rendered them to be useful material for solar cells. This work was a

collaborative venture with the Department of Materials Engineering, Faculty of Engineering, Monash University.

Part III-Applications of conducting polymer nanodispersions

In order to implement the application of the nanodispersions as a mediator for biosensors, various methods were used to fabricate the polymer onto the electrode substrates. The HRP/H_2O_2 configuration was used as a model for biosensing application.

In Chapter 7, the electrodeposition method was used to deposit the *nano*PANI-DBSA dispersion which was synthesised in Chapter 3. The uniform, highly ordered, nanometric structured polyaniline film was formed on a glassy carbon electrode. This work was a collaborative venture with Dublin City University (DCU), Ireland and the performance of the sensors was compared to previous works from electropolymerisation of the bulk monomer carried out by DCU.

The water soluble polymer-PMAS was used to fabricate some biosensors in Chapter 8. Following from the work of Tatsuma *et al*[159], water insoluble PMAS was prepared by complexing with poly(L-lysine) (PLL). In the present work, insoluble films on ITO-coated mylar electrode substrates were formed using an easy one-step casting of the PMAS-HRP-PLL mixture. The sensors were characterised using various methods.

The ink-jet printing method was introduced in Chapter 9 to utilise the polymeric materials as mediators for biosensing applications. Different nanodispersions, synthesised as nanoparticles in concentrated solution form (as reported in Chapters 3 and 5), and PMAS were used as the printing materials. Flexible electrode substrates were investigated for their properties. The possibility of achieving ink-jet printed biosensors by using the desktop printer was the objective of this work.

1.5 References

1. Syed, A.A. and Dinesan, M.K., *Talanta*, 1991. **38**(8): p. 815-837.
2. Wallace, G.G., Spinks, G.M., Kane-Maguire, L.A.P., and Teasdale, P.R., *Conductive electroactive polymers : intelligent materials systems*. 2nd ed. 2002, Boca Raton, FL: CRC Press. , and references cited therein.
3. Henderson, A.M.J., Saunders, J.M., Mrkic, J., Kent, P., Gore, J., and Saunders, B.R., *Journal of Materials Chemistry*: p. 3037-3042.
4. Malhotra, B.D. and Singhal, R., *Pramana-Journal of Physics*, 2003. **61**(2): p. 331-343, and references cited therein.
5. Dahman, S.J., *Polymer Engineering and Science*, 1999. **39**(11): p. 2181-2188.
6. Wu, Y.Z., Moulton, S.E., Too, C.O., Wallace, G.G., and Zhou, D.Z., *Analyst*, 2004. **129**(7): p. 585-588.
7. Chen, J., Officer, D.L., Pringle, J.M., MacFarlane, D.R., Too, C.O., and Wallace, G.G., *Electrochemical and Solid State Letters*, 2005. **8**(10): p. A528-A530.
8. Garner, B., Hodgson, A.J., Wallace, G.G., and Underwood, P.A., *Journal of Materials Science-Materials in Medicine*, 1999. **10**(1): p. 19-27.
9. Han, M.G., Cho, S.K., Oh, S.G., and Im, S.S., *Synthetic Metals*, 2002. **126**(1): p. 53-60.
10. Yuan, W.-L., O'Rear, E.A., Cho, G., Funkhouser, G.P., and Glatzhofer, D.T., *Thin Solid Films*, 2001. **385**(1-2): p. 96-108.
11. Haba, Y., Segal, E., Narkis, M., Titelman, G.I., and Siegmann, A., *Synthetic Metals*, 2000. **110**(3): p. 189-193.
12. Jeon, B.H., Kim, S., Choi, M.H., and Chung, I.J., *Synthetic Metals*, 1999. **104**: p. 95-100.
13. Mandal, B.M., *Bulletin of Materials Science*, 1998. **21**(2): p. 161-165.
14. Kim, B.J., Oh, S.G., Han, M.G., and Im, S.S., *Synthetic Metals*, 2001. **122**(2): p. 297-304.
15. Yu, L., Lee, J.I., Shin, K.W., Park, C.E., and Holze, R., *Journal of Applied Polymer Science*, 2003. **88**(6): p. 1550-1555.
16. Xia, H.S. and Wang, Q., *Journal of Nanoparticle Research*, 2001. **3**(5-6): p. 401-411.
17. Kim, D., Choi, J., Kim, J.Y., Han, Y.K., and Sohn, D., *Macromolecules*, 2002. **35**(13): p. 5314-5316.
18. Madathil, R., Parkesh, R., Ponrathnam, S., and Largo, M.C.J., *Macromolecules*, 2004. **37**(6): p. 2002-2003.
19. Armes, S.P., Miller, J.F., and Vincent, B., *Journal of Colloid and Interface Science*, 1987. **118**(2): p. 410-416.
20. Gangopadhyay, R., De, A., and Ghosh, G., *Synthetic Metals*, 2001. **123**(1): p. 21-31.
21. Ghosh, P., Siddhanta, S.K., Haque, S.R., and Chakrabarti, A., *Synthetic Metals*, 2001. **123**(1): p. 83-89.
22. Somani, P.R., *Materials Chemistry and Physics*, 2002. **77**(1): p. 81-85.
23. Stejskal, J. and Sapurina, I., *Journal of Colloid and Interface Science*, 2004. **274**(2): p. 489-495.
24. Dorey, S., Vasilev, C., Vidal, L., Labbe, C., and Gospodinova, N., *Polymer*, 2005. **46**(4): p. 1309-1315.

25. Cairns, D.B., Armes, S.P., and Bremer, L.G.B., *Langmuir*, 1999. **15**(23): p. 8052-8058.
26. Eisazadeh, H., Gilmore, K.J., Hodgson, A.J., Spinks, G., and Wallace, G.G., *Colloids Surfaces A: Physicochemical Engineering Aspects*, 1995. **103**: p. 281-288.
27. Aboutanos, V., Barisci, J.N., Innis, P.C., and Wallace, G.G., *Colloids and Surfaces a-Physicochemical and Engineering Aspects*, 1998. **137**(1-3): p. 295-300.
28. Sahmetlioglu, E., Yuruk, H., Toppare, L., Cianga, I., and Yagci, Y., *Polymer International*, 2004. **53**(12): p. 2138-2144.
29. Mirmohseni, A. and Wallace, G.G., *Polymer*, 2003. **44**(12): p. 3523-3528.
30. Bhat, N.V., Gadre, A.P., and Bambole, V.A., *Journal of Applied Polymer Science*, 2001. **80**(13): p. 2511-2517.
31. Riede, A., Helmstedt, M., Riede, V., and Stejskal, J., *Langmuir*, 1998. **14**(23): p. 6767-6771.
32. Lee, E.S., Park, J.H., Wallace, G.G., and Bae, Y.H., *Polymer International*, 2004. **53**(4): p. 400-405.
33. Chattopadhyay, D., Chakraborty, M., and Mandal, B.M., *Polymer International*, 2001. **50**(5): p. 538-544.
34. Huang, J.X., Virji, S., Weiller, B.H., and Kaner, R.B., *Journal of the American Chemical Society*, 2003. **125**(2): p. 314-315.
35. Stejskal, J., Kratochvil, P., and Jenkins, A.D., *Collection of Czechoslovak Chemical Communications*, 1995. **60**: p. 1747-1755.
36. Lindfors, T. and Ivaska, A., *Journal of Electroanalytical Chemistry*, 2002. **535**(1-2): p. 65-74.
37. Haba, Y., Segal, E., Narkis, M., Titelman, G.I., and Siegmann, A., *Synthetic Metals*, 1999. **106**(1): p. 59-66.
38. Xia, Y., Wiesinger, J.M., MacDiarmid, A.G., and Epstein, A.J., *Chemistry of Materials*, 1995. **7**(3): p. 443-445.
39. Chen, W.C., Wen, T.C., and Gopalan, A., *Synthetic Metals*, 2002. **128**(2): p. 179-189.
40. Guo, R., Barisci, J.N., Innis, P.C., Too, C.O., Wallace, G.G., and Zhou, D., *Synthetic Metals*, 2000. **114**(3): p. 267-272.
41. Shimizu, S., Saitoh, T., Uzawa, M., Yuasa, M., Yano, K., Maruyama, T., and Watanabe, K., *Synthetic Metals*, 1997. **85**(1-3): p. 1337-1338.
42. Zhou, D.Z., Innis, P.C., Wallace, G.G., Shimizu, S., and Maeda, S.I., *Synthetic Metals*, 2000. **114**(3): p. 287-293.
43. Mazeikiene, R., Niaura, G., and Malinauskas, A., *Synthetic Metals*, 2003. **139**(1): p. 89-94.
44. Reece, D.A., *Development of Conducting Polymers for Separations*, PhD Thesis, University of Wollongong, 2003.
45. Pornputtkul, Y., *Development of Chiral Conducting Polymers for Asymmetric Electrosynthesis*, PhD Thesis, University of Wollongong, 2005.
46. Tallman, D.E. and Wallace, G.G., *Synthetic Metals*, 1997. **90**(1): p. 13-18, and references cited therein.
47. Visy, C., Krivan, E., and Peintler, G., *Journal of Electroanalytical Chemistry*, 1999. **462**(1): p. 1-11.
48. John, R., John, M.J., Wallace, G.G., and Zhao, H., *Use of Surfactants in the Oxidative Synthesis of Conductive, Electroactive Polymers*, in *Electrochemistry in*

Colloids and Dispersions, R.A. Mackay and J. Texter, Editors. 1992, VCH Publishers, Inc.: New York.
49. Dall'Antonia, L.H., Vidotti, M.E., de Torresi, S.I.C., and Torresi, R.M., *Electroanalysis*, 2002. **14**(22): p. 1577-1586.
50. Cui, X.Y., Lee, V.A., Raphael, Y., Wiler, J.A., Hetke, J.F., Anderson, D.J., and Martin, D.C., *Journal of Biomedical Materials Research*, 2001. **56**(2): p. 261-272.
51. Skaarup, S., Bay, L., Vidanapathirana, K., Thybo, S., Tofte, P., and West, K., *Solid State Ionics*, 2003. **159**(1-2): p. 143-147, and references cited therein.
52. Takashima, W., Pandey, S.S., and Kaneto, K., *Sensors and Actuators B-Chemical*, 2003. **89**(1-2): p. 48-52.
53. Sarac, A.S., Sonmez, G., and Cebeci, F.C., *Journal of Applied Electrochemistry*, 2003. **33**(3-4): p. 295-301.
54. Skompska, M. and Vorotyntsev, M.A., *Journal of Solid State Electrochemistry*, 2004. **8**(6): p. 360-368.
55. Son, Y., Choi, J.S., Jang, K.S., Suh, J.S., Oh, E.J., Joo, J., and Cho, J.H., *Synthetic Metals*, 1997. **84**(1-3): p. 175-176.
56. Torres-Gomez, G. and Gomez-Romero, P., *Synthetic Metals*, 1998. **98**(2): p. 95-102.
57. Simmons, M.R., Chaloner, P.A., Armes, S.P., Greaves, S.J., and Watts, J.F., *Langmuir*, 1998. **14**(3): p. 611-618.
58. Mandal, T.K. and Mandal, B.M., *Journal of Polymer Science Part a-Polymer Chemistry*, 1999. **37**(19): p. 3723-3729.
59. Lascelles, S.F., McCarthy, G.P., Butterworth, M.D., and Armes, S.P., *Colloid and Polymer Science*, 1998. **276**(10): p. 893-902.
60. Saunders, B.R., Saunders, J.M., Mrkic, J., and Dunlop, E.H., *Pccp Physical Chemistry Chemical Physics*, 1999. **1**(7): p. 1563-1568.
61. Wang, Z.X., Roberge, C., Wan, Y., Dao, L.H., Guidoin, R., and Zhang, Z., *Journal of Biomedical Materials Research Part A*, 2003. **66A**(4): p. 738-746.
62. Jang, J. and Oh, J.H., *Langmuir*, 2004. **20**(20): p. 8419-8422.
63. Nabid, M.R. and Entezami, A.A., *Journal of Applied Polymer Science*, 2004. **94**(1): p. 254-258, and references cited therein.
64. Steckhan, E., *Electrochemistry*. 1988, Berlin ; New York: Springer-Verlag.
65. Korri-Youssoufi, H. and Yassar, A., *Biomacromolecules*, 2001. **2**(1): p. 58-64.
66. Cen, L., Neoh, K.G., Li, Y., and Kang, E.T., *Biomacromolecules*, 2004. **5**: p. 2238-2246.
67. Hernandez, R.M., Richter, L., Semancik, S., Stranick, S., and Mallouk, T.E., *Chemistry of Materials*, 2004. **16**(18): p. 3431-3438.
68. Kurzawa, C., Hengstenberg, A., and Schuhmann, W., *Analytical Chemistry*, 2002. **74**(2): p. 355-361.
69. Tian, F.M., Xu, B., Zhu, L.D., and Zhu, G.Y., *Analytica Chimica Acta*, 2001. **443**(1): p. 9-16.
70. Chan, H.S.O. and Ng, S.C., *Progress in Polymer Science*, 1998. **23**(7): p. 1167-1231.
71. Ahn, S.H., Czae, M.Z., Kim, E.R., Lee, H., Han, S.H., Noh, J., and Hara, M., *Macromolecules*, 2001. **34**(8): p. 2522-2527.
72. McCullough, R.D. and Ewbank, P.C., *Regioregular, Head-to-tail Coupled Poly(3-alkylthiophene) and Its Derivatives*, in *Handbook of Conducting Polymers*, T.A.

Skotheim, R.L. Elsenbaumer, and J.R. Reynolds, Editors. 1998, M. Dekker: New York. p. p. 225-258.
73. McCullough, R.D., Lowe, R.D., Jayaraman, M., and Anderson, D.L., *Journal of Organic Chemistry*, 1993. **58**: p. 904-912.
74. Kim, B.S., Chen, L., Gong, J.P., and Osada, Y., *Macromolecules*, 1999. **32**(12): p. 3964-3969.
75. Diaz-Quijada, G.A., Pinto, B.M., and Holdcroft, S., *Macromolecules*, 1996. **29**(16): p. 5416-5421.
76. Chayer, M., Faid, K., and Leclerc, M., *Chemistry of Materials*, 1997. **9**(12): p. 2902-2905.
77. Rud, J.A., Lovell, L.S., Senn, J.W., Qiao, Q.Q., and McLeskey, J.T., *Journal of Materials Science*, 2005. **40**(6): p. 1455-1458.
78. Zotti, G., Zecchin, S., Schiavon, G., and Groenendaal, L., *Macromolecular Chemistry and Physics*, 2002. **203**(13): p. 1958-1964.
79. Olinga, T.E., Destri, S., Botta, C., Porzio, W., and Consonni, R., *Macromolecules*, 1998. **31**(4): p. 1070-1078.
80. Ranieri, N., Ruggeri, G., and Ciardelli, F., *Polymer International*, 1999. **48**(11): p. 1091-1098.
81. Andreani, F., Salatelli, E., Lanzi, M., Bertinelli, F., Fichera, A.M., and Gazzano, M., *Polymer*, 2000. **41**(9): p. 3147-3157.
82. Cirpan, A., Alkan, S., Toppare, L., Cianga, I., and Yagci, Y., *Journal of Materials Science*, 2002. **37**(9): p. 1767-1775.
83. Jin, S.H., Yoo, B.U., Kang, S.Y., Gal, Y.S., and Moon, D.K., *Optical Materials*, 2002. **21**(1-3): p. 153-157.
84. Brustolin, F., Goldoni, F., Meijer, E.W., and Sommerdijk, N., *Macromolecules*, 2002. **35**(3): p. 1054-1059.
85. Saxena, V. and Santhanam, K.S.V., *Current Applied Physics*, 2003. **3**(2-3): p. 227-233.
86. Ho, H.A. and Leclerc, M., *Journal of the American Chemical Society*, 2003. **125**(15): p. 4412-4413.
87. Sersen, F., Cik, G., and Veis, P., *Journal of Applied Polymer Science*, 2003. **88**(9): p. 2215-2223.
88. Louwet, F., Groenendaal, L., Dhaen, J., Manca, J., Van Luppen, J., Verdonck, E., and Leenders, L., *Synthetic Metals*, 2003. **135**(1-3): p. 115-117.
89. Choi, J.W., Han, M.G., Kim, S.Y., Oh, S.G., and Im, S.S., *Synthetic Metals*, 2004. **141**(3): p. 293-299.
90. Yohannes, T., Solomon, T., and Inganas, O., *Synthetic Metals*, 1996. **82**(3): p. 215-220.
91. Welzel, H.-P., Kossmehl, G., Boettcher, H., Engelmann, G., and Hunnius, W.-D., *Macromolecules*, 1997. **30**(24): p. 7419-7426.
92. Li, G.T., Kossmehl, G., Welzel, H.P., Engelman, G., Hunnius, W.D., Plieth, W., and Zhu, H.S., *Macromolecular Chemistry and Physics*, 1998. **199**(10): p. 2255-2266.
93. Sakmeche, N., Aeiyach, S., Aaron, J.J., Jouini, M., Lacroix, J.C., and Lacaze, P.C., *Langmuir*, 1999. **15**(7): p. 2566-2574.
94. Marchand, G., Pilard, J.F., Fabre, B., Rault-Berthelot, J., and Simonet, J., *New Journal of Chemistry*, 1999. **23**(8): p. 869-875.

95. Zhu, S.S., Kingsborough, R.P., and Swager, T.M., *Journal of Materials Chemistry*, 1999. **9**(9): p. 2123-2131.
96. Clot, O., Wolf, M.O., and Patrick, B.O., *Journal of the American Chemical Society*, 2000. **122**(42): p. 10456-10457.
97. Sakmeche, N., Aaron, J.J., Aeiyach, S., and Lacaze, P.C., *Electrochimica Acta*, 2000. **45**(12): p. 1921-1931.
98. Li, G.T., Kossmehl, G., Kautek, W., Plieth, W., Zhu, H.S., Chan, N.S.O., and Ng, S.C., *Macromolecular Chemistry and Physics*, 2000. **201**(1): p. 21-30.
99. Haegel, F.H., Schlupen, J., Schultze, J.W., Winkels, S., and Stromberg, C., *Electrochimica Acta*, 2001. **46**(26-27): p. 3973-3984.
100. Too, C.O., Wallace, G.G., Burrell, A.K., Collis, G.E., Officer, D.L., Boge, E.W., Brodie, S.G., and Evans, E.J., *Synthetic Metals*, 2001. **123**(1): p. 53-60.
101. Fall, M., Assogba, L., Aaron, J.J., and Dieng, M.M., *Synthetic Metals*, 2001. **123**(3): p. 365-372.
102. Fall, M., Dieng, M.M., Aaron, J.J., Aeiyach, S., and Lacaze, P.C., *Synthetic Metals*, 2001. **118**(1-3): p. 149-155.
103. Sotzing, G.A. and Lee, K.H., *Macromolecules*, 2002. **35**(19): p. 7281-7286.
104. Chen, J., Burrell, A.K., Collis, G.E., Officer, D.L., Swiegers, G.F., Too, C.O., and Wallace, G.G., *Electrochimica Acta*, 2002. **47**(17): p. 2715-2724.
105. Ko, H.C., Park, S., Paik, W., and Lee, H., *Synthetic Metals*, 2002. **132**(1): p. 15-20.
106. Alkan, S., Cutler, C.A., and Reynolds, J.R., *Advanced Functional Materials*, 2003. **13**(4): p. 331-336.
107. Sadki, S. and Chevrot, C., *Electrochimica Acta*, 2003. **48**(6): p. 733-739.
108. Li, C. and Imae, T., *Macromolecules*, 2004. **37**(7): p. 2411-2416.
109. Kang, B.S., Kim, D.H., Jung, T.S., Jang, E.K., Pak, Y., Shin, S.C., Park, D.S., and Shim, Y.B., *Synthetic Metals*, 1999. **105**(1): p. 9-12.
110. Kim, D.H., Park, D.S., Shim, Y.B., and Shin, S.C., *Journal of Organometallic Chemistry*, 2000. **608**(1-2): p. 133-138.
111. Iarossi, D., Mucci, A., Parenti, F., Schenetti, L., Seeber, R., Zanardi, C., Forni, A., and Tonelli, M., *Chemistry-a European Journal*, 2001. **7**(3): p. 676-685.
112. Skabara, P.J., Serebryakov, I.M., Perepichka, I.F., Sariciftci, N.S., Neugebauer, H., and Cravino, A., *Macromolecules*, 2001. **34**(7): p. 2232-2241.
113. de Souza, J.M. and Pereira, E.C., *Synthetic Metals*, 2001. **118**(1-3): p. 167-170.
114. Zhang, D.H., Qin, J.G., and Xue, G., *Synthetic Metals*, 1999. **100**(3): p. 285-289.
115. Qiao, Q.Q. and McLeskey, J.T., *Applied Physics Letters*, 2005. **86**(15): p. 53501-53501.
116. Chan, H.S.O., Gan, L.M., Chi, H., and Toh, C.S., *Journal of Electroanalytical Chemistry*, 1994. **379**: p. 293-300.
117. Vedrine, C., Fabiano, S., and Tran-Minh, C., *Talanta*, 2003. **59**(3): p. 535-544.
118. Tuken, T., Yazici, B., and Erbil, M., *Progress in Organic Coatings*, 2004. **51**(3): p. 205-212.
119. Xia, Y.N., Yang, P.D., Sun, Y.G., Wu, Y.Y., Mayers, B., Gates, B., Yin, Y.D., Kim, F., and Yan, Y.Q., *Advanced Materials*, 2003. **15**(5): p. 353-389.
120. Wallace, G.G. and Innis, P.C., *Journal of Nanoscience and Nanotechnology*, 2002. **2**(5): p. 441-451, and reference cited therein.
121. Sih, B.C. and Wolf, M.O., *Chemical Communications*, 2005(27): p. 3375-3384.
122. Abdou, M.S.A. and Holdcroft, S., *Synthetic Metals*, 1993. **60**: p. 93-96.

123. Kinyanjui, J.M., Hanks, J., Hatchett, D.W., Smith, A., and Josowicz, M., *Journal of the Electrochemical Society*, 2004. **151**(12): p. D113-D120.
124. Lee, M., Kim, B.W., Nam, J.D., Lee, Y., Son, Y., and Seo, S.J., *Molecular Crystals and Liquid Crystals*, 2003. **407**: p. 397-402.
125. Zhai, L. and McCullough, R.D., *Journal of Materials Chemistry*, 2004. **14**: p. 141-143.
126. Liu, J., Lin, Y.H., Liang, L., Voigt, J.A., Huber, D.L., Tian, Z.R., Coker, E., McKenzie, B., and McDermott, M.J., *Chemistry-a European Journal*, 2003. **9**(3): p. 605-611.
127. Huang, J.X. and Kaner, R.B., *Journal of the American Chemical Society*, 2004. **126**(3): p. 851-855.
128. Huang, J.X. and Kaner, R.B., *Angewandte Chemie-International Edition*, 2004. **43**(43): p. 5817-5821.
129. Huang, H.L. and Lee, W.M.G., *Chemosphere*, 2001. **44**(5): p. 963-972.
130. Shaw, D.J., *Introduction to Colloid and Surface Chemistry*. 1991, Oxford: Butterworth-Heinemann Ltd. 87-88.
131. Hiemenz, P.C. and Rajagopalan, R., *Principles of Colloid and Surface Chemistry*. 3rd , rev. and expanded / Paul C. Hiemenz, Raj Rajagopalan ed. 1997, New York: Marcel Dekker. p.359, 605.
132. Everett, D.H., *Basic Principles of Colloid Science*. 1988, London: Royal Society of Chemistry. 153-155.
133. Moroi, Y., *Micelles : Theoretical and Applied Aspects*. 1992, New York: Plenum Press. p.179.
134. Chehimi, M.M., Azioune, A., Bousalem, S., Slimane, A.B., and Yassar, A., *Synthesis, Characterization, and Biomedical Applications of Conducting Polymer Particles*, in *Colloidal Polymers : Synthesis and Characterization*, A. Elaissari, Editor. 2003, M. Dekker: New York. p. 251.
135. De Benedetto, G.E., Palmisano, F., and Zambonin, P.G., *Biosensors and Bioelectronics*, 1996. **11**(10): p. 1001-1008.
136. Tian, F.M. and Zhu, G.Y., *Analytica Chimica Acta*, 2002. **451**(2): p. 251-258.
137. Singh, S., Chaubey, A., and Malhotra, B.D., *Analytica Chimica Acta*, 2004. **502**(2): p. 229-234.
138. Gaspar, S., Habermuller, K., Csoregi, E., and Schuhmann, W., *Sensors and Actuators B-Chemical*, 2001. **72**(1): p. 63-68.
139. Thanachasai, S., Rokutanzono, S., Yoshida, S., and Watanabe, T., *Analytical Sciences*, 2002. **18**(7): p. 773-777.
140. Gao, M., Dai, L.M., and Wallace, G.G., *Electroanalysis*, 2003. **15**(13): p. 1089-1094.
141. Cen, L., Neoh, K.G., and Kang, E.T., *Langmuir*, 2002. **18**(22): p. 8633-8640.
142. Killard, A.J., Zhang, S.Q., Zhao, H.J., John, R., Iwuoha, E.I., and Smyth, M.R., *Analytica Chimica Acta*, 1999. **400**: p. 109-119.
143. Killard, A.J., Micheli, L., Grennan, K., Franek, M., Kolar, V., Moscone, D., Palchetti, I., and Smyth, M.R., *Analytica Chimica Acta*, 2001. **427**(2): p. 173-180.
144. Grennan, K., Strachan, G., Porter, A.J., Killard, A.J., and Smyth, M.R., *Analytica Chimica Acta*, 2003. **500**(1-2): p. 287-298.
145. Yang, R., Ruan, C.M., Dai, W.L., Deng, J.Q., and Kong, J.L., *Electrochimica Acta*, 1999. **44**(10): p. 1585-1596.

146. Caramori, S.S. and Fernandes, K.F., *Process Biochemistry*, 2004. **39**(7): p. 883-888.
147. Iwuoha, E.I. and Smyth, M.R., *Polymer-Based Amperometric Biosensors*, in *Electroactive polymer electrochemistry*, M.E.G. Lyons, Editor. 1994, Plenum Press: New York. p. 289.
148. Bartlett, P.N. and Cooper, J., *Applications of Electroactive Polymers in Bioelectrochemistry and Bioelectronics*, in *Electroactive Polymer Electrochemistry*, M.E.G. Lyons, Editor. 1994, Plenum Press: New York. p. 246.
149. Childs, R.E. and Bardsley, W.G., *Biochemical Journal*, 1975. **145**: p. 93-103.
150. Fernandes, K.F., Lima, C.S., Pinho, H., and Collins, C.H., *Process Biochemistry*, 2003. **38**(9): p. 1379-1384, and references cited therein.
151. Mulchandani, A. and Pan, S.T., *Analytical Biochemistry*, 1999. **267**(1): p. 141-147.
152. Tatsuma, T., Ariyama, K., and Oyama, N., *Analytica Chimica Acta*, 1996. **318**(3): p. 297-301.
153. Iwuoha, E.I., de Villaverde, D.S., Garcia, N.P., Smyth, M.R., and Pingarron, J.M., *Biosensors & Bioelectronics*, 1997. **12**(8): p. 749-761, and references cited therein.
154. Darder, M., Takada, K., Pariente, F., Lorenzo, E., and Abruna, H.D., *Analytical Chemistry*, 1999. **71**(24): p. 5530-5537.
155. Yabuki, S., Mizutani, F., and Hirata, Y., *Electroanalysis*, 2001. **13**(5): p. 380-383.
156. Saby, C., Nguyen, T.V., and Luong, J.H.T., *Electroanalysis*, 2004. **16**(4): p. 260-267.
157. Thanachasai, S., Yoshida, S., and Watanabe, T., *Analytical Sciences*, 2003. **19**(5): p. 665-669.
158. Su, X.D., Ng, H.T., Dai, C.C., O'Shea, S.J., and Sam, F.Y.L., *Analyst*, 2000. **125**(12): p. 2268-2273.
159. Tatsuma, T., Ogawa, T., Sato, R., and Oyama, R., *Journal of Electroanalytical Chemistry*, 2001. **501**(1-2): p. 180-185.
160. Morrin, A., Wilbeer, F., Ngamna, O., Moulton, S.E., Killard, A.J., Wallace, G.G., and Smyth, M.R., *Electrochemistry Communications*, 2005. **7**(3): p. 317-322.
161. Ngamna, O., Morrin, A., Moulton, S.E., Killard, A.J., Smyth, M.R., and Wallace, G.G., *Synthetic Metals*.
162. Morrin, A., Ngamna, O., Killard, A.J., Moulton, S.E., Smyth, M.R., and Wallace, G.G., *Electroanalysis*, 2005. **17**(5-6): p. 423-430.
163. Pique, A., Wu, P., Ringeisen, B.R., Bubb, D.M., Melinger, J.S., McGill, R.A., and Chrisey, D.B., *Applied Surface Science*, 2002. **186**(1-4): p. 408-415.
164. Jin, G., Norrish, J., Too, C., and Wallace, G., *Current Applied Physics*, 2004. **4**(2-4): p. 366-369.
165. Bao, Z., Feng, Y., Dodabalapur, A., Raju, V.R., and Lovinger, A.J., *Chemistry of Materials*, 1997. **9**(6): p. 1299-1301.
166. Sirringhaus, H., Kawase, T., Friend, R.H., Shimoda, T., Inbasekaran, M., Wu, W., and Woo, E.P., *Science*, 2000. **290**(5499): p. 2123-2126.
167. Kawase, T., Shimoda, T., Newsome, C., Sirringhaus, H., and Friend, R.H., *Thin Solid Films*, 2003. **438-439**: p. 279-287.
168. Chen, B., Cui, T., Liu, Y., and Varahramyan, K., *Solid-State Electronics*, 2003. **47**(5): p. 841-847.
169. Ballarin, B., Fraleoni-Morgera, A., Frascaro, D., Marazzita, S., Piana, C., and Setti, L., *Synthetic Metals*, 2004. **146**(2): p. 201-205.

170. Liu, Y., Cui, T., and Varahramyan, K., *Solid-State Electronics*, 2003. **47**(9): p. 1543-1548.
171. Liu, Y. and Cui, T., *Macromolecular Rapid Communications*, 2005. **26**(4): p. 289.
172. Tekin, E., Gans, B.-J.d., and Schubert, U.S., *Journal of Materials Chemistry*, 2004. **14**(17): p. 2627.
173. Setti, L., Fraleoni-Morgera, A., Ballarin, B., Filippini, A., Frascaro, D., and Piana, C., *Biosensors & Bioelectronics*, 2005. **20**(10): p. 2019-2026.
174. Bender, S. and Sadik, O.A., *Environmental Science & Technology*, 1998. **32**(6): p. 788-797.
175. Lu, W., Zhou, D.Z., and Wallace, G.G., *Analytical Communications*, 1998. **35**(8): p. 245-248.
176. Khan, G.F. and Wernet, W., *Thin Solid Films*, 1997. **300**(1-2): p. 265-271.
177. Gooding, J.J., Wasiowych, C., Barnett, D., Hibbert, D.B., Barisci, J.N., and Wallace, G.G., *Biosensors and Bioelectronics*, 2004. **20**(2): p. 260-268.
178. Campbell, T.E., Hodgson, A.J., and Wallace, G.G., *Electroanalysis*, 1999. **11**(4): p. 215-222.
179. Garner, B., Georgevich, A., Hodgson, A.J., Liu, L., and Wallace, G.G., *Journal of Biomedical Materials Research*, 1999. **44**(2): p. 121-129.
180. Cho, W.J. and Huang, H.J., *Analytical Chemistry*, 1998. **70**(18): p. 3946-3951.
181. Morrin, A., Guzman, A., Killard, A.J., Pingarron, J.M., and Smyth, M.R., *Biosensors & Bioelectronics*, 2003. **18**(5-6): p. 715-720.
182. Do, J.-S. and Chang, W.-B., *Sensors and Actuators B: Chemical*, 2004. **101**(1-2): p. 97-106.
183. Reis, N., Ainsley, C., and Derby, B., *Journal of the American Ceramic Society*, 2005. **88**(4): p. 802-808.
184. Reis, N., Ainsley, C., and Derby, B., *Journal of Applied Physics*, 2005. **97**(9): p. 94903-94903.
185. Zhao, X., Evans, J.R.G., Edirisinghe, M.J., and Song, J.H., *Journal of Materials Science*, 2002. **37**(10): p. 1987-1992.
186. Ling, M.M. and Bao, Z., *Chemistry of Materials*, 2004. **16**(23): p. 4824-4840.
187. Gans, B.-J.d. and Schubert, U.S., *Langmuir*, 2004. **20**(18): p. 7789-7793.
188. Yoshioka, Y., Calvert, P.D., and Jabbour, G.E., *Macromolecular Rapid Communications*, 2005. **26**(4): p. 238-246.
189. Cui, T.H., Liu, Y., Chen, B., Zhu, M., and Varahramyan, K., *Solid-State Electronics*, 2005. **49**(5): p. 853-859.
190. Le, H.P., *Journal of Imaging Science and Technology*, 1998. **42**(1): p. 49-62.
191. Baydo, R. and Groscup, A., *Technical*, 2001: p. 10-14.
192. Plotner, M., Wegener, T., Richter, S., Howitz, S., and Fischer, W.-J., *Synthetic Metals*, 2004. **147**(1-3): p. 299-303.
193. Nur, H.M., Song, J.H., Evans, J.R.G., and Edirisinghe, M.J., *Journal of Materials Science: Materials in Electronics*, 2002. **13**(4): p. 213-219.
194. Liu, Z., Su, Y., and Varahramyan, K., *Thin Solid Films*, 2005. **478**(1-2): p. 275-279.
195. Biehl, S., Danzebrink, R., Oliveira, P., and Aegerter, M.A., *Journal of Sol-Gel Science and Technology*, 1998. **13**(1 - 3): p. 177-182.

2.1 Spectroscopy

2.1.1 Ultraviolet-visible (UV-visible) spectroscopy

UV-visible spectroscopy is the most common technique used to characterise inherently conducting polymers (ICPs) such as polyaniline (PANI)[1-3], poly(2-methoxyaniline-5-sulphonic acid) PMAS[4], polypyrrole (PPy)[5] and polythiophene (PTh)[6] both during and post polymerisation. The characteristic peak positions indicate the different forms of the polymer[1,2], oxidation states[3,5], doping level[3] and conjugation length of the polymer backbone[6].

Typical spectra are recorded over the region of the electromagnetic spectrum (λ in the range of 200-380 nm) relating to π-π^* molecular transitions in ICPs. Wavelength in the visible region from 380-800 nm relate to polaron/bipolaron transitions and wavelength over than 800 nm in near infrared region relate to conformations information of the polymer molecules.

In this thesis, UV-visible spectroscopy has been used to study different forms of ICPs during chemical synthesis, pH and redox switching process, degree of doping and conjugation length of the ICPs nanoparticles.

2.1.2 Raman spectroscopy

In Raman spectroscopy, the sample is irradiated by intense laser beams in the UV-visible region which has frequency ν_0. The scattered light is observed and it consists of Rayleigh and Raman scattering. Rayleigh scattering is strong and has the same frequency as the incident beam (ν_0). Raman scattering is very weak (~ 10^{-5} of the incident beam) and has frequencies $\nu_0 \pm \nu_m$ where ν_m is a vibrational frequency of a molecule. Thus, the vibrational

frequency (ν_m) as a shift from the incident beam (ν_0) is measured[7]. The Raman spectrum is the plot of an optical intensity of Raman scattering versus vibrational frequency (cm^{-1}).

A Raman spectrometer consists of four major components which are excitation source, sample illumination and collection system, wavelength selector, and detection and computer control/processing systems[7]. In this thesis, the integrated Raman system HR800 from Jobin Yvon Horiba with the HeNe 20 mW laser source[8] was used as shown in Figure 2.1.

In this system (Figure 2.1), the laser is totally reflected by the notch filter towards the sample under the microscope. The Raman signal collected by the microscope objective in back scattering configuration follows the same way back. The reflection on the sample of the laser line (Rayleigh scattering) is redirected onto the notch filter rejecting the excitation wavelength of the laser while permitting the Raman scattering to pass through the notch filter towards the confocal hole and entrance slit of the spectrograph. Raman shifted light is passed to a dispersive grating under the entrance optic of the instrument and forming a spectrum image on the CCD (charge-coupled device) detector[8].

The vibration frequencies of the conjugated bonds along the ICPs backbone can be observed using Raman spectroscopy. The Raman frequencies shifts were used to investigate oxidation states[9-14], conductivity[15] and degradation products from thermal treatment[11] or electrochemical oxidation[16] of PANI, PPy and PTh. In this thesis, Raman spectroscopy has been used to investigate oxidation states and conduction bands of ICPs nanoparticles, and interaction between incorporated dye molecules and PANI back bone.

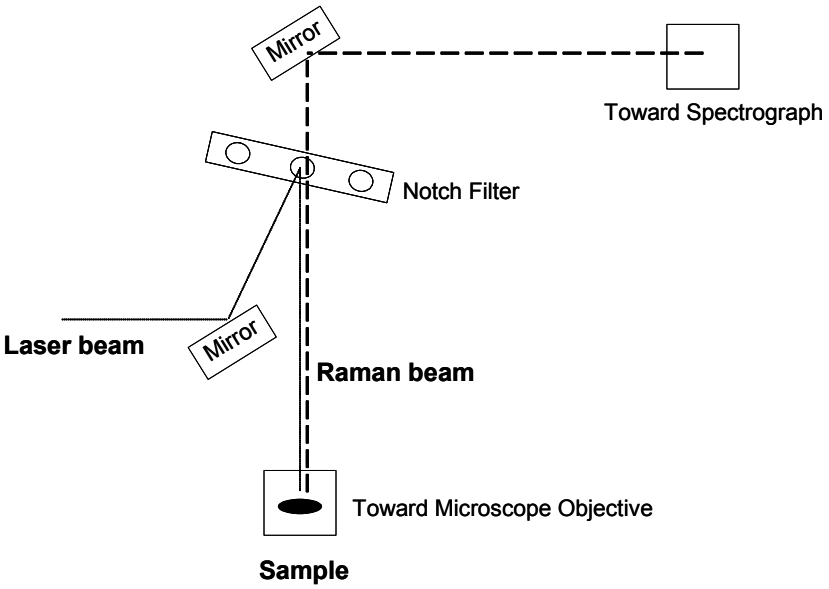

Figure 2.1 Schematic illustration of the HR800 integrated Raman system.

2.2 Microscopic and Light Scattering Methods

2.2.1 Transmission electron microscopy (TEM)

With TEM free electrons are discharged from an electron gun passing through an objective, intermediate and projector lens to act on the atomic nuclei of the specimen. The resultant beam contains some of the original free electrons and some that have been changed in energy or direction. The image formed is projected onto a fluorescent screen and then transmitted to a photographic plate, or CCD camera film. Since different parts of the specimen absorb electrons differentially, the projected beam of electrons on the fluorescent screen shows bright areas where the sample has absorbed least, and darker where the sample has absorbed more electrons[17]. A vacuum system is used to provide stability and contamination-free chamber[18].

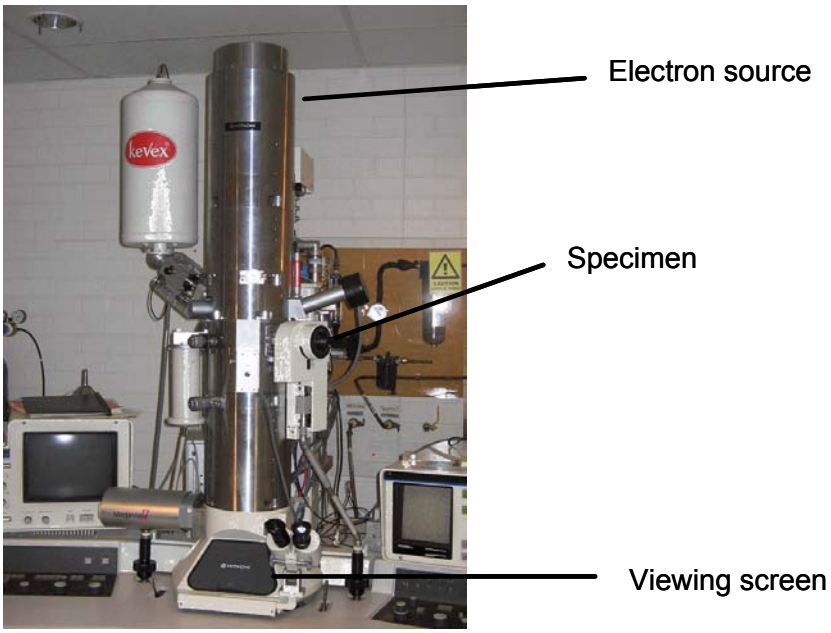

Figure 2.2 Transmission electron microscope Hitachi H7000[19].

Specimen thickness is very important in TEM as it leads to optimum visibility. The specimen must be thin enough for electrons to pass through and thick enough to absorb electrons preferentially[17]. For solution-based samples, evaporative castings of the diluted samples are cast onto carbon coated copper TEM grids and allowed to dry. The solid samples can be prepared as thin films using various equipment such as Reichert Ultracut E Ultramicrotome, Reichert Ultracut E Cryo-Ultramicrotome Struers Tenupol or focused ion beam[19]. The dried film or thin specimen is held on the grids and fitted into the microscope holder. In most instruments the holder is intended for a screen or grid with approximately 200 openings per inch with a grid diameter of 3 mm common. In some cases, supporting films no thicker than 20-50 nm can be used[17].

The specimen represents only a small portion of the sample and the selection of a representative specimen is crucial. Typically a low resolution image is obtained initially to

observe the true nature of the sample followed by a higher resolution image at various representative points to observed the smaller features[17].

The high resolving power of the TEM results from the ability to focus an extremely short wavelength of electron beams (less than 1 nm[17]). A resolution of 0.4 nm at 50 kV and 0.3 nm at 100 kV is attainable for TEM. Typical electron energy used in this thesis is 100 kV.

TEM is used to observe morphology of ICPs nanoparticles or nanocomposites[20-23]. However, any alteration of the sample material can affect the result and needs to be critically assessed in any image result[24]. In this thesis, TEM is used to study particle size and morphology of segregated particle from very dilute solution. Therefore the results of particle size from TEM are different from dynamic light scattering method which measures the size of particles in more concentrated solution as outlined in the following section (2.2.3).

2.2.2 Atomic force microscopy (AFM)

The AFM is a scanning probe microscopy (SPM) technique which has proven to be a powerful tool for obtaining information on the packing order of molecules adsorbed on a surface[25]. Atomic force microscopy is used to characterise the topography of ICP films. The surface morphology[23], roughness and thickness[25] of the film can be attained. The film thickness measurement is performed by carefully scratching the film in the representative area. The AFM probe scans over the prepared scratches to the sample edge and moves across to the plain substrate as shown in Figure 2.3. The cross-section analysis is subsequently performed over the scratched area and the film thickness is the difference in vertical distance (Figure 2.3).

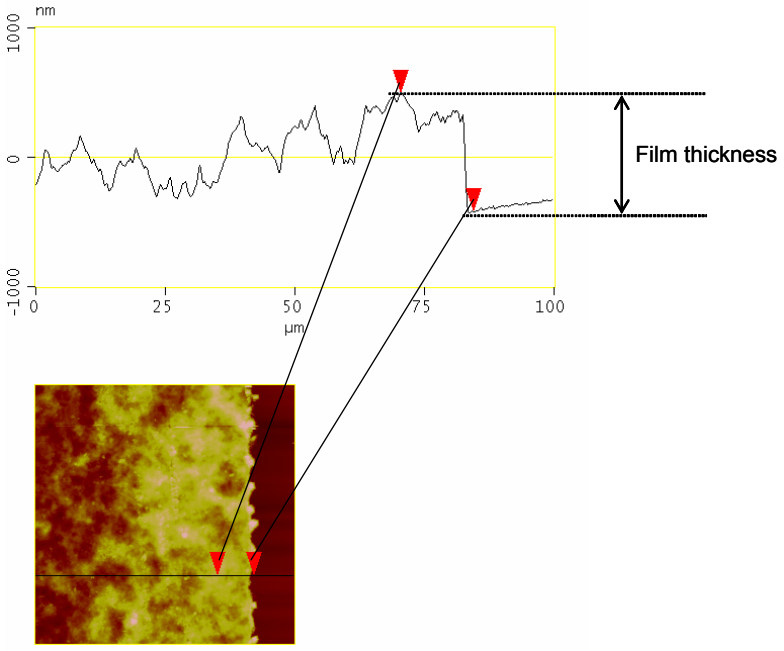

Figure 2.3 Example of PMAS-HRP-PLL film thickness measurement using AFM cross section analysis.

Atomic force microscopy can be operated in ambient condition and in solution, and on conducting or non-conducting surfaces[24]. A flexible cantilever with a tip mounted to it (Figure 2.4) scans over the sample surface while keeping the force constant between the tip and the surface[24]. The surface topography is monitored by the deflection of a laser beam focused on the back of the tip. As the tip flexes up and down the laser deflections are recorded by the photodiode array which translates these diffractions into topographic features. Typically, pyramidal silicon nitride tips, which have a radius of curvature on the order of 10 nm, are used.

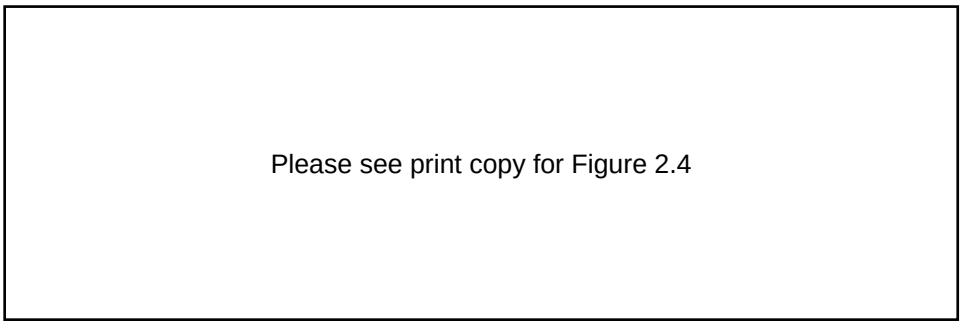

Figure 2.4 Atomic force microscopy apparatus principle. Cantilever movement on a substrate under controlled constant force or other parameters[24].

The most common modes of operation are contact and tapping mode. In contact mode, the tip is in perpetual contact with the sample and the detected net force is the sum of the attractive and repulsive force between the tip and the sample[24,26]. This method is suitable for smooth surfaces. In tapping mode, the sample topography is mapped by lightly tapping the surface with an oscillating probe tip. The cantilever's oscillation amplitude changes with sample surface topography, and the topography image is obtained by monitoring these changes. The tapping mode eliminates lateral forces that can damage soft samples and reduce image resolution therefore it allows routine imaging of samples once considered impossible to image in contact mode[27].

Resolution of AFM is in the range of atomic dimension, i.e., 10 Å = 1 nm but it is highly dependent on the characteristics of the sample such as surface texture and the degree of hydration, as well as sample preparation. A sharp clean tip as well as a clean and defect free substrate are required for high resolution imaging[24].

In this work, AFM has been used to study morphology of the ICPs film, determine film surface roughness and measure film thickness.

2.2.3 Light scattering

The light scattering method can be used to measure particle size. An example of light scattering is shown in Figure 2.5 where the laser beam with intensity (I_0) passes straight through the sample, but some is scattered by the particles within the sample[28].

Pleae see print copy for Figure 2.5

Figure 2.5 Light scattering and backscatter detection of the sample[28].

The scattered light with its intensity –I(θ) is dependent on the scatter angle (θ), wavelength of the incident light (λ), the particle diameter (d) and the refractive index in relation to the medium (η) in which the particles reside[29]. As a particle scatters light in all directions, it is possible to place the detector in any position and it will still detect the scattering. The particle sizes reported in this thesis were measured using a Malvern Nano-ZS Zetasizer which employs a backscattering detection system. Backscatter detection (Figure 2.5) can reduce the effect of multiple scattering, where the scattered light from one particle is itself scattered by other particles and allows higher concentrations to be measured. Moreover, contaminants such as dust particles are typically large compared to the particle size of the sample, and mainly scatter in the forward direction; hence this method can reduce the effect of dust[28].

According to Mie theory and Rayleigh's approximation, for homogeneous spherical particles which is much smaller than λ, I(θ) is proportional to d^6 with weak scattering at

large angles whereas, for the larger particle, I(θ) increases in proportion to d^2 and strongly scatters at small angles[29,30].

In the dynamic light scattering (DLS) method, the particle size is determined by illuminating the particles with a laser and analysing the intensity fluctuation in the scattered light over a period of time. The particles in solution are constantly moving due to Brownian motion[28]. Particle movement plays an important role for this analysis since based on the Stokes-Einstein equation (2.1)[30], large particles move slower than the small particles. Temperature and viscosity of the solution have to be measured and taken into account when calculating the particle size as they influence particle movement.

$$D_{AB} = C k_B T / 9.425 \mu d \qquad (2.1)$$

where D_{AB} is Diffusion coefficient (m^2/s)

C is Cunningham slip correction factor

k_B is Boltzman's constant, 1.380622 X 10^{-23} JK^{-1}

T is temperature (K)

μ is viscosity (Pa.s)

A digital correlator measures the degree of similarity between two intensity-I(θ) signals over period of time is established. The rate of decay for the correlation will be faster for small particles as they move quicker than large particles as shown in Figure 2.6[28].

Please see print copy for Figure 2.6

Figure 2.6 Correlation of different particle sizes[28].

The correlation function is calculated to produce a primary intensity size distribution. The Intensity distribution can be converted, using Mie theory, to a Volume distribution and then to a Number distribution with increasing in systematic error. Therefore, the Volume and Number distribution should be treated with some caution. The difference in Intensity, Volume and Number distribution are presented in Figure 2.7[28].

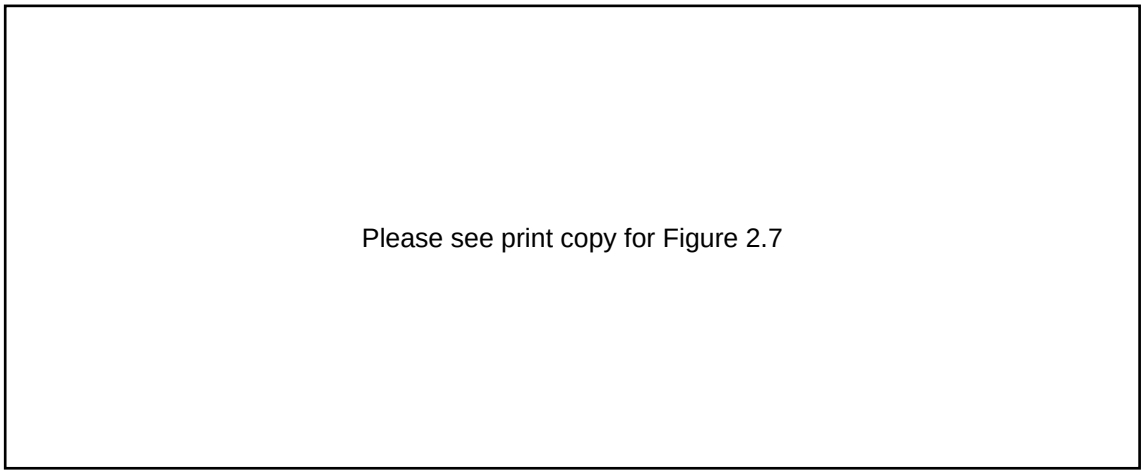

Figure 2.7 The difference of particle size presentation by: (a) Number, (b) Volume, and (c) Intensity particle size distribution[28].

Consider a sample that contains only two sizes of particles (5 nm and 50 nm) but with equal numbers of each size particle. The first graph shows the Number distribution and the two peaks are of the same size as there are equal number of particles. The second graph shows the Volume distribution with the peak for the 50 nm particle being 1000 times larger than the peak for the 5 nm. This is because the volume of a 50 nm particle is 1000 times larger than the 5 nm particle based on volume of sphere ($4\pi r^3/3$). The third graph shows the Intensity distribution and the peak for 50 nm is 1,000,000 times larger than the peak for 5 nm which is according to Rayleigh's approximation[28] that $I(\theta)$ is proportional to d^6.

The Volume distribution plot indicates the distribution of particle size based on scattering intensity; whereby larger particles scatter at larger intensity. The Volume distribution plot is normally skewed to show greater percentage of larger particle sizes due to the volume effect as aforementioned (Figure 2.7 b) and this result alone can mislead the researcher into believing their solution contains a majority of larger particles.

To obtain a clear understanding of the total solution particle size distribution then Number distribution plot must also be taken into account. This plot is based on the relationship volume of sphere is proportional to r^3 of the particle and adjusts the particle size distribution accordingly. The Number plot gives the researcher an insight into the amount of each particle size in a sample as a percentage value (Figure 2.7 a).

Using DLS, it is clear that the particle size needs to be reported carefully. The Number distribution tells the real number of the particle of each size therefore it can be used to present the size of the particles in the sample. However, in some applications such as ink-jet printing (Chapter 9); where small amounts of large particles (larger than 1000 nm) can block the print head; the Volume distribution result is significant as it indicates the effect of the large particles.

Dynamic light scattering method has been used to determine the particle size of ICPs nanodispersions[31-34] and pigment based inks[35]. The particle size data from this method is measured in concentrated solutions. Under these conditions some aggregation would be expected and the results could be different from these obtained using the TEM method.

2.3 Electrochemical Techniques

2.3.1 Open circuit potential

Open circuit potential (OCP) is an important parameter in various electrochemical processes such as corrosion of metals, photoelectronic effects in semiconducting materials and secondary batteries. The OCP usually reflects the complex discharging phenomena that are associated with the pseudo-capacitor effect of chemisorbed electroactive intermediates in the electrode process[36]. Hence this process relates to the concentration of electroactive species (*A*i) involved in the electron transfer processs which is based on the Nernst equation[37,38].

For example of the two half-reactions

$$aA + ne^- \rightleftharpoons cC \qquad E^0_+ \tag{2.2}$$

$$dD + ne^- \rightleftharpoons bB \qquad E^0_- \tag{2.3}$$

The OCP of this reaction is tentatively assigned as;

$$OCP = E^0_+ - E^0_- - \frac{RT}{nF} \ln \frac{[A_C{}^c A_D{}^d]}{[A_A{}^a A_B{}^b]} \tag{2.4}$$

$$OCP = E^0 - \frac{RT}{nF} \ln \frac{[A_C{}^c A_D{}^d]}{[A_A{}^a A_B{}^b]} \tag{2.5}$$

where E^0 = standard reduction potential = $E^0_+ + E^0_-$

R = gas constant (8.314 J/K.mol)

T = temperature (K)

n = number of electrons in the half-reaction

F = Faraday constant (9.648 X 10^4 C/mol)

*A*i = activity of species i

a, b, c and d = coefficients of the reactants and products in the reaction

The technique is based on the potentiometric method whereby the potential is measured when an equilibrium situation of anodic and cathodic reactions are proceeding equal rate. Consequently, the net current flow is zero and the OCP is the potential corresponding to this zero current[36]. The cell consists of a working electrode and a reference electrode which are connected to a multimeter. In this thesis, the OCP of the solution in which chemical polymerisation was carried out was measured as a function of time. From equation 2.2, when the concentrations of reactants and products reach equilibrium, the constant OCP is obtained which indicates the completion of the reaction. Thus the rate and the completion of polymerisation process can be observed[36,39].

2.3.2 Cyclic voltammetry (CV)

Cyclic voltammetry is a versatile electrochemical technique and is often the first experiment performed in an electrochemical study. It is used to investigate the redox properties of the sample and evaluate electron transfer kinetics. The potential is applied across the electrode-solution interface from $E_{initial}$ at t_0, and reversed when it reaches E_{final} at t_1 back to $E_{initial}$ at t_2 as shown in Figure 2.8 and can be continued for any number of cycles. By this method the product of the electron transfer reaction that occurred in the forward scan can be probed again in the reverse scan[38,40].

Please see print copy for Figure 2.8

Figure 2.8 Potential-time excitation signal for cyclic voltammetry.

Cyclic voltammogram is obtained when the potential is applied across the working electrode in an unstirred solution and the current is measured during the potential scan as an example shown in Figure 2.9[40].

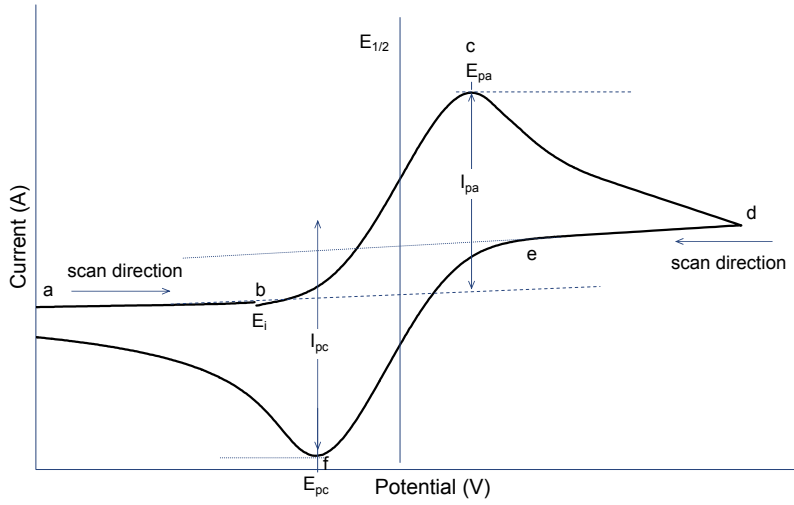

Figure 2.9 Example of cyclic voltammogram. Scan started at E_i from negative to positive potential.

The CV in Figure 2.9 shows a redox couple where the anodic peak appears at E_{pa} and the cathodic peak at E_{pc}. During the scan, the applied potential becomes sufficiently

positive at point 'b' to cause oxidation of reduced species at the electrode surface to occur. The anodic current increases until a maximum at E_{pa} (point 'c') where the surface concentration of reduced species approaches zero and the oxidised species is accumulated at the electrode. The anodic current decayed beyond point 'c' as the solution surrounding the electrode is depleted of reduced species due to its conversion to oxidised species. The applied potential started increasing negative at point 'd' and also the depletion of oxidised species. The cathodic current increases and maximised at E_{pc} (point 'f') where the oxidised species is completely reduced on the electrode surface.

In this work CV has been used to study electroactivity[6,41-43] and degradation products[44] of ICPs films and dispersions, and also the electron transfer process of the polymeric films[45,46].

2.3.3 DC amperometry

DC amperometry involves application of a constant potential and measurement of current.

According to Faraday's law: $Q = nFN$ (2.6)

where Q is the number of coulombs passed

n is the number of electrons involved in the reaction

F is the Faraday constant = 9.65×10^4

N is the number of moles

The instantaneous current I is given by $I = dQ/dt$, therefore

$I = nFdN/dt$ (2.7)

where dN/dt is termed as the oxidation or reduction rate of the redox active species at the working electrode.

The reaction rate depends on both the electron transfer rate at the electrode surface and the rate of mass transport of the redox active species in solution[40].

Amperometric detection has limited selectivity which can be manipulated by adjusting the operation potential. Amperometric sensors are unable to discriminate against species that are more easily reduced/oxidised than the desired species[47].

Practically, the current increases when the redox active species is added to the system (Figure 2.10).

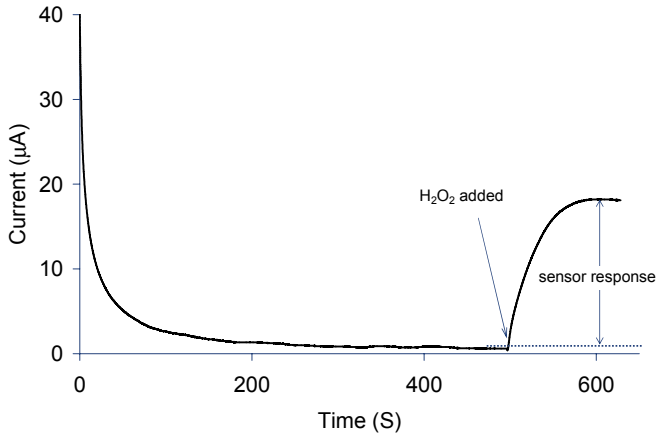

Figure 2.10 Typical response obtained from PMAS-HRP-PLL biosensors using DC amperometry.

DC amperometry has been widely used to generate responses for polymer-modified biosensors. Conducting polymers are often used as the mediators in biosensing technology and various analytes such as hydrogen peroxide[48], glucose[46,49], cholesterol[50] and urea[51] can be detected. In this thesis, DC amperometry has been used to evaluate the polymer-modified biosensors performance.

2.4 Conductivity Measurement

To determine conductivity, a potential difference is applied across a sample material and the current flow is measured. George Simon Ohm observed that at a constant temperature the potential drop across a conducting material was proportional to the electric current flowing through it. This relationship is know as Ohm's law which is expressed as[52]

$$I = V/R \tag{2.8}$$

where I is the current flowing (A-amperes)

V is the voltage applied across the conductor (V-volts)

R is the resistance of the conductor (Ω-ohms)

The R is related to the length (l) and cross sectional area (a) of material of interest by the intrinsic resistivity of material (ρ)[52].

$$R = \rho l/a \tag{2.9}$$

Thus the total resistance depends on the resistivity and the dimension of the material and has the unit as ohm metre, Ω m.

Conductivity of materials (σ) is defined as the reciprocal of the resisitivity, ρ[52].

$$\sigma = 1/\rho \tag{2.10}$$

therefore

$$\sigma = l/\rho a \tag{2.11}$$

In conductivity measurements, it was assumed that the probe leads and the contacts have zero resistance and no thermally generated voltages or uncompensated contact potentials. For the square probe configuration as shown in Figure 2.11, van der Pauw has developed the formulation for conductivity calculation as in equation 2.20[53].

$$\sigma = \frac{\ln 2 \; i}{\pi d \; V} \qquad (2.12)$$

where i = current passing through two adjacent contacts

d = sample thickness

V = voltage drop which is measured across the other two contacts (Figure 2.11)

Conductivity measurements are performed on either cast films or pressed pellets of the dried ICPs nanoparticles in this thesis.

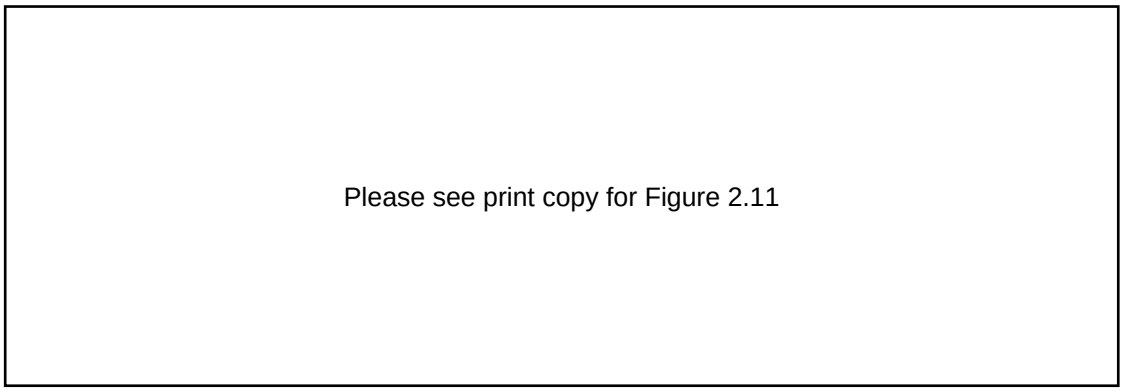

Figure 2.11 van der Pauw configuration for the measurement of conductivity[53].

2.5 Contact Angle Measurement

Contact angle measurement is the most frequently used and most accessible technique for solid surface tension measurement. Solid surface tension relates to the hydrophilicity/hydrophobicity. The higher the solid surface tension the more hydrophilic the surface is. At the basis of the contact angle measurement there is the equilibrium at the three-phase boundary as shown in Figure 2.12[54].

Please see print copy for Figure 2.12

Figure 2.12 Schematic illustration the three-phase boundary and contact angle (Θ) of the liquid drop on the solid surface[54]

The drop of liquid that is put on the surface will adopt a shape under the pressure of different surface/interfacial tensions, until reaching equilibrium. The equation of interfacial equilibrium was stated by Thomas Young[54] as

$$\gamma_{sv} - \gamma_{sl} = \gamma_{lv} \cos\Theta \qquad (2.13)$$

where γ_{ij} = the interfacial between phases i and j, subscripts s, l and v refer to solid, liquid and vapour, respectively

Θ = the equilibrium (Young) contact angle

In the sessile drop experiment, a droplet of a properly purified liquid is put on the solid surface by mean of a syringe or a micropipette. The droplet is generally observed by a low magnification microscope[54].

Wetting usually means that the contact angle between a liquid and a solid is zero or so close to zero that the liquid spreads over the solid surface easily. From Young equation, for the case of a finite contact angle, and the spreading coefficient $S_{l/s}$,

$$S_{l/s} = \gamma_{sv} - \gamma_{lv} - \gamma_{sl} \qquad (2.14)$$

should wetting occur.

Spreading occurs if γ_{lv} and γ_{sl} is made smaller by adding a surfactant to the liquid phase that is absorbed at both solid-liquid and the liquid-air interfaces and therefore lower these interfacial tensions[55].

Azioune *et al*[56] used contact angle measurements to determine relative hydrophilicity/hydrophobicity of the PPy/human serum albumin surface. In this thesis, this technique has been used to provide hydrophilicity/hydrophobicity information of the conductive substrates as well as to investigate wettability of the ICPs nanodispersions used in ink-jet printing.

2.6 References

1. Stejskal, J., Kratochvil, P., and Jenkins, A.D., *Collection of Czechoslovak Chemical Communications*, 1995. **60**: p. 1747-1755.
2. Haba, Y., Segal, E., Narkis, M., Titelman, G.I., and Siegmann, A., *Synthetic Metals*, 1999. **106**(1): p. 59-66.
3. Xia, Y., Wiesinger, J.M., MacDiarmid, A.G., and Epstein, A.J., *Chemistry of Materials*, 1995. **7**(3): p. 443-445.
4. Zhou, D.Z., Innis, P.C., Wallace, G.G., Shimizu, S., and Maeda, S.I., *Synthetic Metals*, 2000. **114**(3): p. 287-293.
5. Nabid, M.R. and Entezami, A.A., *Journal of Applied Polymer Science*, 2004. **94**(1): p. 254-258, and references cited therein.
6. Zhang, D.H., Qin, J.G., and Xue, G., *Synthetic Metals*, 1999. **100**(3): p. 285-289.
7. Ferraro, J.R., *Introductory Raman spectroscopy*. 2nd ed. 2003, Amsterdam ; Boston: Academic Press. pp.3-97.
8. *HR 800 User Manual*: Jobin Yvon Horiba.
9. Boyer, M.I., Quillard, S., Rebourt, E., Louarn, G., Buisson, J.P., Monkman, A., and Lefrant, S., *Journal of Physical Chemistry B*, 1998. **102**(38): p. 7382-7392.
10. Boyer, M.I., Quillard, S., Louarn, G., Froyer, G., and Lefrant, S., *Journal of Physical Chemistry B*, 2000. **104**(38): p. 8952-8961.
11. do Nascimento, G.M., da Silva, J.E.P., de Torresi, S.I.C., and Temperini, M.L.A., *Macromolecules*, 2002. **35**(1): p. 121-125.
12. Han, G.Y., Shi, G.Q., Qu, L.T., Yuan, J.Y., Chen, F.E., and Wu, P.Y., *Polymer International*, 2004. **53**(10): p. 1554-1560.
13. Bazzaoui, E.A., Levi, G., Aeiyach, S., Aubard, J., Marsault, J.P., and Lacaze, P.C., *journal of physical chemistry*, 1995. **99**(17): p. 6628-6634.
14. Fu, M., Shi, G., Chen, F., and Hong, X., *Physical Chemistry Chemical Physics*, 2002. **4**: p. 2685-2690.
15. Liu, Y.-C. and Hwang, B.-J., *Synthetic Metals*, 2000. **113**(1-2): p. 203-207.
16. Ghosh, S., Bowmaker, G.A., Cooney, R.P., and Seakins, J.M., *Synthetic Metals*, 1998. **95**(1): p. 63-67.
17. Rochow, T.G., *Introduction to microscopy by means of light, electrons, X rays, or acoustics*. 2nd ed. 1994, New York: Plenum Press. pp.265-326.
18. *Handbook of microscopy : applications in materials science, solid-state physics and chemistry*. 1997, Weinheim, Germany: VCH Verlagsgesellschaft. p.250.
19. http://srv.emunit.unsw.edu.au/TEM.htm. accessed on 16 November 2005.
20. Han, M.G., Cho, S.K., Oh, S.G., and Im, S.S., *Synthetic Metals*, 2002. **126**(1): p. 53-60.
21. Percy, M.J., Barthet, C., Lobb, J.C., Khan, M.A., Lascelles, S.F., Vamvakaki, M., and Armes, S.P., *Langmuir*, 2000. **16**(17): p. 6913-6920.
22. Gangopadhyay, R., De, A., and Ghosh, G., *Synthetic Metals*, 2001. **123**(1): p. 21-31.
23. Dorey, S., Vasilev, C., Vidal, L., Labbe, C., and Gospodinova, N., *Polymer*, 2005. **46**(4): p. 1309-1315.
24. Birdi, K.S., *Scanning probe microscopes : applications in science and technology*. 2003, Boca Raton, FL: CRC Press. pp.16-49.

25. Benesch, J., Askendal, A., and Tengvall, P., *Journal of Colloid and Interface Science*, 2002. **249**(1): p. 84-90.
26. *http://www.veeco.com/html/product_bymarket_proddetail.asp?productID=178&MarketID=4&Title=AFM%2F%20SPMs%2F%20NSOM*. accessed on 15 November 2005.
27. *http://www.veeco.com/Polymer/polymer_sample.asp*. accessed on 15 November 2005.
28. *Zetasizer nano series user manual*. 2003, Worcestershire: Malvern Instruments Ltd. 2003. 13.1-14.5.
29. Wedd, M.M., *Determination of Particle Size Distributions Using Laser Diffraction*. 2003.
30. Seville, J., Tuzn, U., and Clift, R., *The processing of particulate solids*. 1997, London: Blackie Academic & Professional. pp.1-98.
31. Blinova, N.V., Sapurina, I., Klimovic, J., and Stejskal, J., *Polymer Degradation and Stability*, 2005. **88**(3): p. 428-434.
32. Stejskal, J. and Sapurina, I., *Journal of Colloid and Interface Science*, 2004. **274**(2): p. 489-495.
33. Cassignol, C., Cavarero, M., Boudet, A., and Ricard, A., *Polymer*, 1999. **40**(5): p. 1139-1151.
34. Aboutanos, V., Barisci, J.N., Innis, P.C., and Wallace, G.G., *Colloids Surfaces A: Physicochemical Engineering Aspects*, 1998. **137**: p. 295-300.
35. Magdassi, S. and Ben Moshe, M., *Langmuir*, 2003. **19**(3): p. 939-942.
36. Wei, Y., Hsueh, K.F., and Jang, G.-W., *Polymer*, 1994. **35**(16): p. 3572-3575, and references cited therein.
37. Delahay, P., *New instrumental methods in electrochemistry : theory, instrumentation, and applications to analytical and physical chemistry*. 1954, New York: Interscience. pp.9-10.
38. Harris, D.C., *Quantitative chemical analysis*. 5th ed. 1999, New York: W.H. Freeman. pp. 337-359, 471-499, 513.
39. Yu, L., Lee, J.I., Shin, K.W., Park, C.E., and Holze, R., *Journal of Applied Polymer Science*, 2003. **88**(6): p. 1550-1555.
40. Kissinger, P.T. and Heineman, W.R., *Laboratory techniques in electroanalytical chemistry*. 2nd , rev. and expanded ed. 1996, New York: Marcel Dekker Inc. pp.78-94, pp.249-250.
41. Mirmohseni, A. and Wallace, G.G., *Polymer*, 2003. **44**(12): p. 3523-3528.
42. Tallman, D.E. and Wallace, G.G., *Synthetic Metals*, 1997. **90**(1): p. 13-18, and references cited therein.
43. Skaarup, S., Bay, L., Vidanapathirana, K., Thybo, S., Tofte, P., and West, K., *Solid State Ionics*, 2003. **159**(1-2): p. 143-147, and references cited therein.
44. Chen, W.C., Wen, T.C., and Gopalan, A., *Synthetic Metals*, 2002. **128**(2): p. 179-189.
45. Do, J.-S. and Chang, W.-B., *Sensors and Actuators B: Chemical*, 2004. **101**(1-2): p. 97-106.
46. Tian, F.M. and Zhu, G.Y., *Analytica Chimica Acta*, 2002. **451**(2): p. 251-258.
47. Plambeck, J.A., *Electroanalytical chemistry : basic principles and applications*. 1982, New York: Wiley. pp.366-370.

48. Tatsuma, T., Ogawa, T., Sato, R., and Oyama, R., *Journal of Electroanalytical Chemistry*, 2001. **501**(1-2): p. 180-185.
49. Yabuki, S., Mizutani, F., and Hirata, Y., *Electroanalysis*, 2001. **13**(5): p. 380-383.
50. Singh, S., Chaubey, A., and Malhotra, B.D., *Analytica Chimica Acta*, 2004. **502**(2): p. 229-234.
51. Cho, W.J. and Huang, H.J., *Analytical Chemistry*, 1998. **70**(18): p. 3946-3951.
52. Open University. Introduction to Materials Course, T., *Electrons in solids*. 1973, Milton Keynes: Open University Press. pp.9-10.
53. Syed, A.A. and Dinesan, M.K., *Talanta*, 1991. **38**(8): p. 815-837.
54. Garbassi, F., *Polymer surfaces from physics to technology*. 1994, Chichester ; New York: Wiley. pp.164-165, pp.301-304.
55. Adamson, A.W., *Physical chemistry of surfaces*. 5th ed. 1990, New York: Wiley. pp.493-494.
56. Azioune, A., Siroti, F., Tanguy, J., Jouini, M., Chehimi, M.M., Miksa, B., and Slomkowski, S., *Electrochimica Acta*, 2005. **50**: p. 1661-1667.

3.1 Introduction

Polyaniline (PANI) has become the most extensively studied ICP over the past decade due to its reversible redox and pH switching properties, ease of synthesis and wide range of potential applications. It can be synthesised by either electrochemical or chemical oxidative polymerisation of aniline in acidic solution[1].

However, similar to other ICPs, its application has been limited due to the fact that it is infusible and only moderately soluble in common organic solvents; resulting in limitations in terms of lack of processibility[1-3]. Synthesis of nanoscale size conducting polymer particles can help improve the processibility of conducting polymers, which allows them to be more widely used. The nanometer sized conducting polymer components enable the preparation of useful composite materials[4]. For example, they can be used to produce highly transparent coatings which facilitate their use in transparent EMI shielding, antistatic coatings, display devices and electrochromics[4]. Moreover, the nanocomposite polymers can provide a much greater conductivity at lower ICP loadings because of the low percolation threshold obtained[5].

The preparation of PANI in colloidal form improves processibility in that colloidal dispersions may be applied in place of true solutions[3]. Such dispersions have many attractive features. For example, they can be applied as a coating over a surface to help static charge dissipation. The dispersion can be blended with latexes or solutions of commodity polymers to yield microstructured composites of conducting PANI particles dispersed in an insulating polymer matrix. These materials still maintain most of the electrical conductivity inherent to PANI[3]. Numerous methods can be used to prepare PANI

dispersions such as emulsion/inverse microemulsion polymerisation using surfactants[4,6-10] and synthesis of colloidal PANI using steric stabilisers[2,3,11-15].

Emulsion polymerisation (see Chapter 1, section 1.2.1) using surfactants has proved effective in producing ICP nanodispersions[4,6-10]. Kim *et al*[6] synthesised and characterised polyaniline nanoparticles prepared in sodium dodecylsulfate (SDS) solutions using hydrochloric acid as the dopant. This produced PANI dispersions consisting of 10-20 nm sized nanoparticles with a conductivity of 4-10 S/cm. It has been found that coalescence and coagulation were prevented by electrostatic repulsive interaction between anionic SDS micelles.

Han *et al*[4] used surfactant to produce conducting polymer dispersions of nanometer size by chemical oxidative polymerisation of aniline in a micelle solution of dodecyl benzenesulphonic acid (DBSA). The conductive nanoparticles obtained were 20-30 nm in diameter with conductivity as high as 24 S/cm. In the polymerisation process, DBSA played the role of surfactant and dopant. This work showed the use of surfactants to be superior to other kinds of dispersants (e.g. poly(styrene sulphonic acid) (PSS), poly(vinyl alcohol) (PVA), poly(vinyl pyrrolidone) and poly(ethylene oxide) (PEO), etc.) with respect to electrical conductivity[4]. In this work, large quantities of *nano*PANI-DBSA dispersions were synthesised using a modified micellar method initially developed by Han *et al*[4].

In the development of biosensors, the sensor detection limit can be lowered by fabrication of ultrathin and coherent layers of the conducting polymers[1]. Ink-jet printing is an option to achieve the ultrathin film. One feature important for a polymer dispersion to be ink-jet printed is its particle size. For successful printing to occur the polymer dispersion must contain a high concentration of small and well dispersed particles. Typical particle

size of the pigment based ink-jet ink was about 100-400 nm[16]. This is due to the small nozzle size of most ink-jet printer heads (30-60 μm in diameter)[17].

Previously, polyaniline nanofibres were synthesised by a rapid mixing (RM) method of Huang *et al*[18]. The fibres were inherently formed in the presence of HCl as the dopant. In this method, the oxidant was a limiting agent. Nanofibres were formed and the restriction of oxidant prevented secondary growth within the polymer chains. Therefore, the nanofibre chain lengths were small. This concept was applied to the PANI-DBSA nanoparticles. The oxidant was limited at the ratio of oxidant:monomer = 1:4 according to the nanofibre rapid mixing method. The inherent morphology of PANI-DBSA was spherical as the polymer was formed in the DBSA micelle. The PANI-DBSA-RM was anticipated to be the spherical nanoparticles in concentrated solution.

The aim of this chapter is to produce dispersible and/or ink-jet printable PANI nanoparticles in aqueous media using surfactant. Three PANI nanodispersions were prepared: PANI-DBSA via emulsion polymerisation (*nano*PANI-DBSA); supernatant of *nano*PANI-DBSA using centrifugation (*s*PANI-DBSA); and PANI-DBSA via a rapid mixing technique (PANI-DBSA-RM), and will be detailed in the following sections.

The open circuit potential (OCP) was monitored throughout the polymerisation as described previously by Wei *et al*[19] and Yu *et al*[7]. The polymers were characterised using UV-visible spectroscopy, Raman spectroscopy, cyclic voltammetry (CV), conductivity measurement, transmission electron microscopy (TEM) and dynamic light scattering (DLS). These processable polymers are exploited for biosensing in Chapters 7 and 9.

3.2 Experimental

3.2.1 Chemicals

Aniline was purchased from Aldrich and distilled before use. Ammonium peroxydisulfate (APS), sodium dodecylsulfate (SDS), hydrazine hydrate and sodium hydroxide (NaOH) were purchased from Aldrich and used as received. Dodecylbenzenesulphonic acid (DBSA) was purchased from Tokyo Kasei Kogyo Co., Ltd. Hydrochloric acid (HCl) was purchased from Asia Pacific Specialty Chemicals Limited. All solutions were prepared using Milli-Q water.

3.2.2 Equipment/Instrumentation

A two-electrode cell comprising a platinum mesh auxiliary and Ag/AgCl reference electrode (3.0 M NaCl) connected to a Hewlett Packard 34401A multimeter was used to monitor the OCP throughout the polymerisation (see Chapter 2, section 2.3.1). The synthesis was performed in a Julabo controlled temperature bath with a peristaltic pump (Minipuls 2, Gilson) used to control the rate of oxidant addition. The reaction mixture was dialysed using a 12,000 molecular weight cut-off cellulose membrane (Sigma). A Beckman (J2-MC, rotor JA10) or Eppendorf centrifuge (5702) was used to separate the polymer from solution. A three-electrode cell comprising a working electrode, Ag/AgCl reference electrode and Pt wire auxiliary electrode connected to E-Corder 401 with EDAQ Potentiostat was used for all electrochemical experiments. Particle size was determined using a DLS (Nano-ZS Zetasizer, Malvern Instruments) with 7^{o} angled back scattered light configuration (see Chapter 2, section 2.2.3) and TEM (H7000, Hitachi) at 100 KeV. UV-visible spectra were measured using a Shimadzu UV-1601 spectrophotometer. Raman spectra were obtained using a 632.8 nm laser (HR800, Jobin Yvon Horiba). Conductivity

measurements were performed on pressed pellets of the dried nanodispersion using the four-point probe method. A pH/Conductivity meter (Model 20, Denver) was used to measure the pH of all solutions. All potentials stated are vs. an Ag/AgCl (3.0 M NaCl) reference electrode.

3.2.3 Methods

3.2.3.1 Polymerisation and purification

To prepare the *nano*PANI-DBSA, a beaker containing 100 ml water was placed in a water bath at 20°C and the water was stirred well. DBSA was added into the beaker to a concentration of 1.3 M and stirred until completely dissolved. Aniline monomer was added to the DBSA micellar solution to a concentration of 1.3 M and stirred for 1 h. A 1.3 M solution of APS was separately prepared in 100 ml water. Upon mixing both solutions the final concentrations of aniline, APS and DBSA were 0.62 M. Polymerisation was performed by the addition of the APS solution into the micellar solution at a rate of 0.5 ml/min and continued stirring for 3.5 h. The open circuit potential (OCP) was measured throughout the course of polymerisation. Following synthesis the polymer was placed in a 12,000 Mw cut-off dialysis bag and dialysed against 0.05 M SDS solution for 42 h with the SDS solution being changed every 18 h. The dispersion was centrifuged at 10,000 rpm for 15 min and washed using 100 ml of Milli-Q water for 3 cycles.

The PANI-DBSA-RM nanodispersion was synthesised by preparing a DBSA solution at a concentration of 0.25 M in 20 ml water. 0.32 M of aniline and 0.08 M of APS were separately dissolved in 10 ml of 0.25 M DBSA. The aniline was added to the DBSA micellar solution and stirred for two min before the addition of the APS solution which was then stirred for 2.5 h. After polymerisation, 20 ml of 0.05 M SDS was added into the

reaction mixture to assist in the centrifugation as this solution was very viscous. The solution was centrifuged at 4400 rpm for 30 min. The supernatant was decanted and put in a dialysis bag and dialysed against 0.05 M SDS for 42 h with the SDS solution being changed every 18 h.

3.2.3.2 Characterisation of PANI nanoparticles and dispersions

The dedoping, oxidation and reduction behaviour of the polymer dispersions were characterised using UV-visible spectroscopy. The polymer dispersions were dedoped, oxidised and reduced using NaOH, APS and hydrazine hydrate, respectively. The polymer was dried in an oven at 40˚C until constant weight and pressed into pellets before measuring the conductivity by the four point probe technique. The particle size of the concentrated dispersions was measured using the DLS method. Low concentration dispersions were investigated to determine particle size and morphology using TEM. The polymer nanoparticles were characterised by Raman spectroscopy utilising a 632.8 nm laser wavelength. Mass of product from the syntheses was determined from solid content of the nanoparticles obtained based on total volume of the reaction media.

3.2.3.3 Stability test of *nano*PANI-DBSA

The stock solution of *nano*PANI-DBSA dispersion in water (5.25 % w/w) was kept in a closed container at room temperature. It was diluted in water to 0.03% w/v for UV-visible measurements, and to 1.31% w/v for cyclic voltammetry (CV). For colloidal stability, the *nano*PANI-DBSA dispersion was diluted to 0.06% w/v in water, in 0.01 M and in 0.001 M DBSA and left standing at room temperature. Photographs of the dispersions were taken and the supernatant was carefully removed to measure the particle size distribution at various time intervals.

3.3 Results and Discussion

3.3.1 *nano*PANI-DBSA

3.3.1.1 Polymerisation

According to the method developed by Kim *et al*[6], sodium dodecylsulfate (SDS) was used to synthesis PANI in the presence of HCl. Upon addition of APS the reaction proceeded as expected with the solution colour changing from white to yellow, then blue through turquoise and eventually becoming emeraldine green as also reported by Stejskal *et al*[20] and Haba *et al*[21]. However, the polymer obtained after centrifugation could not be redispersed in water. Hence the procedure developed by Han *et al*[4] where the DBSA acts as both surfactant and dopant was investigated.

Polymerisation of PANI-DBSA on a large scale using the ratio of aniline to APS used by Han *et al*[4] (1:0.5), was initially investigated. The polymerisation process was monitored using UV-visible spectroscopy. After 16 h, the solution still remained yellow indicating the formation of the reduced leucoemeraldine form of PANI. The aniline:APS ratio was subsequently increased to 1:1 and the polymerisation proceeded as described below.

Upon addition of the aniline to DBSA, the solution turned a milky white colour with an eventual increase in viscosity, indicating the formation of aniline.DBSA complex. This complex forms when the deprotonated negatively charged DBSA and positively charged aniline interact[21]. Upon addition of APS the solution colour changed from white to yellow, to blue, to turquoise for very short period and finally to emeraldine green. The colour changes are attributed to the different redox states of PANI (see Chapter 1, section 1.1.1).

The blue colour indicates the formation of pernigraniline salt (PS) PANI[20], which appeared for a short period of time before turning to dark green PANI-DBSA indicating the formation of PANI emeraldine salt (ES). This colour changing was also observed by Stejskal *et al*[20] and Haba *et al*[21]. The pH of the DBSA solution was 1.35 which then increased to 3.40 after addition of aniline, and decreased to less than 1 on completion of the APS addition.

The method used for purification also influenced the stability of the resultant polymer dispersion. When methanol was used to precipitate the polymer from solution, the polymer could not be redispersed back into water, possibly due to removal of the stabilising agent (DBSA) causing the polymer to aggregate. Therefore, water was used in all further washing procedures and the polymer was precipitated using centrifugation.

3.3.1.1.1 In-situ open circuit potential (OCP) measurement

The OCP of the reaction media was measured between a platinum electrode and a Ag/AgCl (3.0 M NaCl) reference electrode. The OCP depends on the concentration of electroactive species at the surface of electrodes[19] and is based on the Nernst equation[22] (see Chapter 2, section 2.3.1).

The OCP profile obtained during synthesis of the *nano*PANI-DBSA is shown in Figure 3.1. The OCP observed for the solution containing aniline/DBSA was about 0.4 V and increased sharply to 0.67 V upon addition of APS (t = 0). At the early stages of APS addition, the high viscosity of the solution resulted in a heterogeneous reaction media and hence instability in the potential measurements. However, the solution became less viscous with time and the potential readings became more consistent. A constant OCP indicates the polymerisation process has reached equilibrium. After completion of the APS addition, the

OCP dropped from about 0.59 V and then remained nearly constant at 0.47 V, and it was taken as equilibrium at this point. Therefore the reaction was stopped at 210 min. The maximum OCP and the potential observed at equilibrium were similar to those reported for the synthesis of PANI using SDS as a surfactant (about 0.65 V and 0.4 V vs. SCE, respectively)[7].

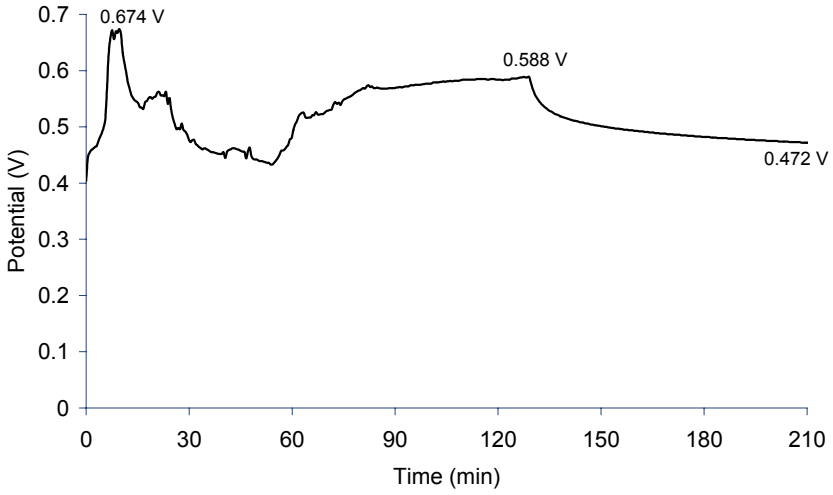

Figure 3.1 The OCP monitored during polymerisation of PANI-DBSA particles. APS is added at time = 0. The potentials are vs. Ag/AgCl (3.0 M NaCl). Concentrations of aniline, APS and DBSA were equal at 0.62 M based on total volume of the reaction media.

3.3.1.1.2 UV-visible spectroscopy during polymerisation

During the polymerisation process aliquots of nanoPANI-DBSA dispersions were taken every 30 min and UV-visible spectra recorded (Figure 3.2). 30 min after the addition of the oxidant, a deep blue colour was observed and the UV-visible spectrum indicated a protonated pernigraniline (PS) form of PANI (see Chapter 1, section 1.1.1) with a characteristic peak appearing at about 754 nm[20,21]. According to the discussion by Haba *et al*[21], the peak at 754 nm (Figure 3.2, curve 30 min) represents protonation of imine nitrogens. The absence of a peak at 360 nm indicated that the PANI chains formed at this

stage did not contain benzenoid units bound to the amine nitrogens which would indicate the presence of the emeraldine and/or leucoemeraldine oxidation states. Hence at this stage the predominant oxidation state is pernigraniline and not emeraldine and/or leucoemeraldine[21]. Beyond this 30 min reaction time, pernigraniline was converted to emeraldine as the reaction media quickly turned green and absorption bands appeared at 360 and 430 nm[20,21]. The presence of the π-π* and π-polaron peaks at 360 nm and 430 nm, respectively and the formation of a flat or distorted single peak indicated a high level of doping[4]. The absorption intensity remained constant after 160 min, indicating the concentration of ES PANI-DBSA produced remained constant.

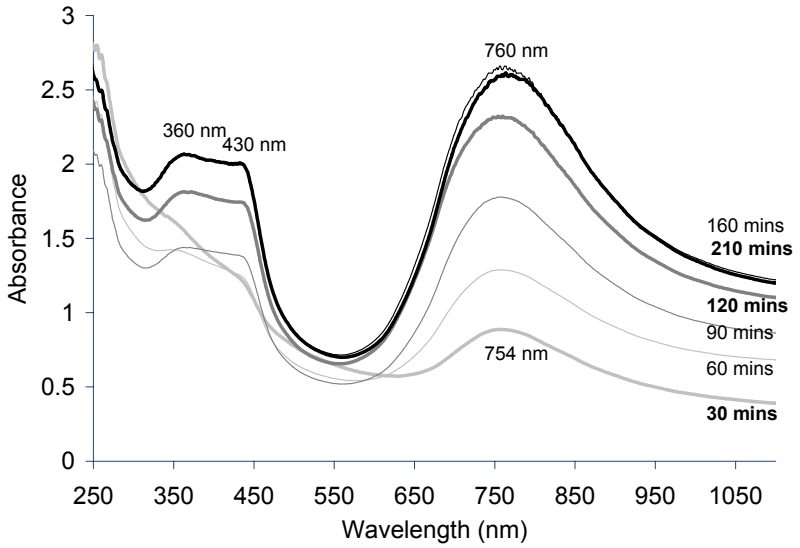

Figure 3.2 UV-visible spectra taken during polymerisation to obtain PANI-DBSA nanoparticles at concentration of aliquot 1.7 g/L. Concentrations of Aniline, APS and DBSA were equal at 0.62 M. The time points represent the time from addition of APS.

3.3.1.1.3 Particle size measurement during polymerisation by DLS

Particle size analysis of the solution containing *nano*PANI-DBSA was performed at various time intervals during polymerisation using the DLS method. The first measurement

was performed 30 min after the addition of APS to the aniline.DBSA complex. Table 3.1 presents the results.

Table 3.1 Particle size by % Number during polymerisation of PANI-DBSA nanoparticles (concentration of aliquots 1.7 g/L).

Time (min)	**% Number below 100 nm**	**% Number 100 – 300 nm**	**% Number 300 – 500 nm**	**% Number 500 – 1000 nm**	**% Number above 1000 nm**
30	0	67	31	0	3
60	0	65	35	0	1
90	0	4	57	36	3
120	0	2	60	34	3
160	0	0	66	28	6
210	0	13	61	23	3

The % Number represents the number of each particle size range assuming the combine amount is 100% (see Chapter 2, section 2.2.3 for further detail)

As the polymer forms (30 min after addition of APS) the DLS data in Table 3.1 showed 67% of the particles to be between 100-300 nm and 31% to be between 300-500 nm. However, transmission electron microscopy (section 3.3.1.2.1) showed particle sizes of the *nano*PANI-DBSA to be only 10 ± 2 nm. Therefore, the particle size ranges observed by DLS in Table 3.1 are attributed to the aggregation of the individual particles during synthesis. After 60 min reaction, the particle size was similar to that at 30 min (Table 3.1), indicating that as more polymer formed no further aggregation occurred. At 90 min, further aggregation of smaller particles occurred as indicated by the decrease of the 100-300 nm range percentage (from 65% to 4%) and the increase of the 300-500 nm range (from 35% to 57%), as well as the formation of larger aggregates in the 500-1000 nm range (36%).

The aggregation process continued further at 120 and 160 min as shown by the increase in larger particles in the ranges above 100-300 nm. At 210 min, the particle size range appeared to broaden from 100-1000 nm with the majority in the 300-500 nm range (61%). Although the size slightly decreased after 210 min, no significant change occurred suggesting that the size of the aggregation had reached equilibrium in solution. Haba *et al*[23] have reported that the aggregation process is a dynamic one whereby some aggregates increase in size whilst simultaneously other aggregates break down and this process occurs continuously[8,23].

It should be noted that at all stages during the polymerisation studied here only a small percentage (1-6%) of large aggregates (over than 1000 nm) were present.

3.3.1.2 Characterisation of nanoparticles and dispersions

3.3.1.2.1 Transmission electron microscopy (TEM), mass of product and conductivity

Upon completion of polymerisation, the product dispersions were purified as outlined in the experiment section (3.2.3.1). The particle size of purified *nano*PANI-DBSA was investigated using TEM, as shown in Figure 3.3. The image shows the PANI-DBSA nanoparticles to be spherical with an average diameter of 10 ± 2 nm. The spherical shape of these nanoparticles is the same as that reported for other PANI nanodispersions synthesised in the presence of surfactants[4,6,8,9], but the size is smaller. It should be pointed out that the particle size observed using TEM is smaller than the particle size observed using DLS (section 3.3.1.1.3). This is due to the very dilute sample required for TEM analysis in order to visualise the segregated particle under the microscope, whereas aggregates can be formed in the higher concentration polymer dispersions used in the DLS method.

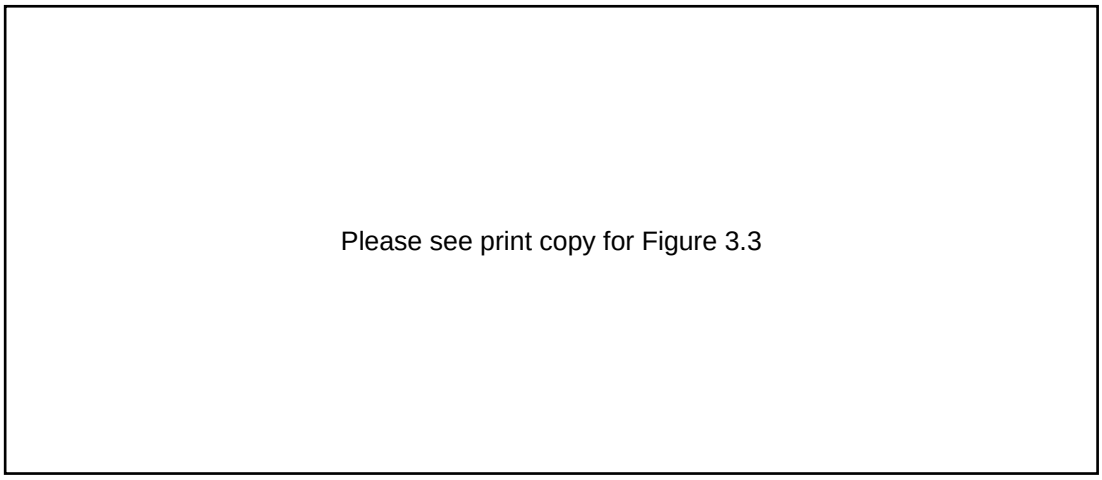

Figure 3.3 Transmission electron micrograph of *nano*PANI-DBSA dispersion at 200 k times magnification at 75 keV on copper/rhodium grids (ProSciTech Australia).

Conductivity measurements (as detailed in Chapter 2, section 2.4) on three pressed pellets showed the conductivity to be 34 ± 7 S/cm at room temperature. This is slightly higher than that reported by Han *et al*[4] which was 24 S/cm with a particle size of 20 nm. The higher conductivity found from our PANI may result from their smaller particle size-as it has been proposed that the electronic and optical properties of nanostructures are unique because the majority of atoms are at the surface rather than buried in the bulk of the material[24,25]. The characterisation data are summarised in Table 3.2.

Table 3.2 Characterisation data for *nano*PANI-DBSA nanoparticles.

Samples	Mass of product (g of dried polymer/L)	Particle size by TEM (nm)	Conductivity (S/cm)
nanoPANI-DBSA	118	10±2	34±7
PANI-DBSA	-	20*	24*

* data obtained from Han *et al*[4].

3.3.1.2.2 pH and redox switching

The *nano*PANI-DBSA was redispersed in water at a concentration of 0.26 g/L. Their UV-visible spectra (Figure 3.4 a) were characteristic of the conducting ES form of PANI. A π-π* band appeared at about 350 nm, a π-polaron band at 430 nm, and a localised polaron band at 808 nm. The spectrum indicated a "compact coil" conformation for the polymer backbone, as a free-carrier tail in the near IR region was absent[26]. This structure causes the polarons of each tetrameric unit in PANI to be electronically isolated from each other due to the twist defects between aromatic rings. Therefore, the polaron band is more localised[26]. For the purified polymer (Figure 3.4 a), the 808 nm polaron band is red shift by 48 nm compared to the corresponding band before purification (see Figure 3.2, 210 min curve) suggesting a long conjugation length for the PANI chain[27]. In addition, π-π* band at about 350 nm was diminished compared to the unpurified material (Figure 3.2 at 210 min) and the relative intensity of the 430 nm to 350 nm bands was higher, indicating a higher degree of doping. This shows that the degree of doping can be improved by the removal of undesirable components such as excess DBSA, APS and unreacted aniline[6].

When the PANI-DBSA nanodispersion was treated with 0.1 M NaOH, the protonated ES was converted to the blue emeraldine base (EB). As seen in Figure 3.4 b, the alkaline treatment caused the original π-π* band at about 350 nm to shift to 330 nm and the two polaron bands to be replaced by a band at 590 nm, which is in accordance with the peak positions assigned to the EB from of PANI[2,20,28-31]. The 590 nm peak is attributed to an excitonic transition (charge transfer band) between the benzenoid and quinoid rings of the PANI[29]. However, the shoulder observed around 700 nm indicates that the PANI-DBSA nanoparticles are difficult to fully deprotonate. This is probably due to the bulky DBS^- ion which cannot be removed easily, as also found by Lindfors and Ivaska[31].

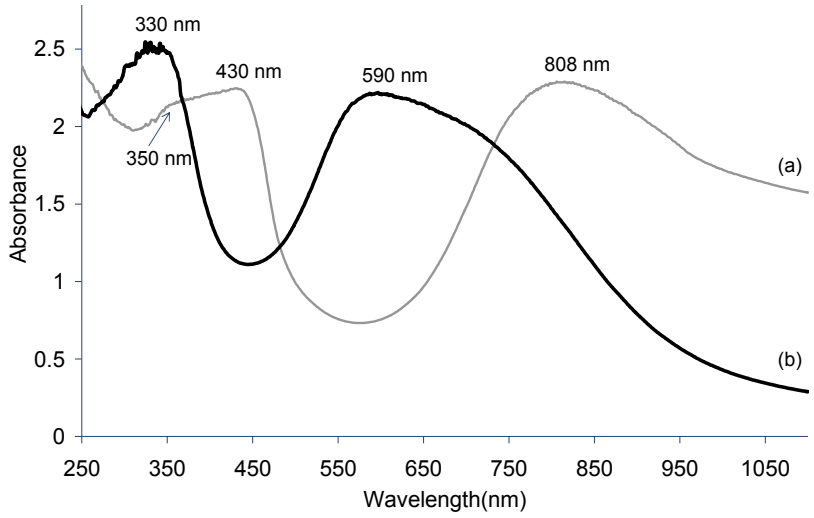

Figure 3.4 UV-visible spectra of: (a) purified *nano*PANI-DBSA (0.26 g/L) in the ES form, and (b) after dedoping to the EB form using 0.1 M NaOH.

The reduction behaviour for the *nano*PANI-DBSA in 4 M hydrazine (pH ~ 11) was investigated (Figure 3.5). Reduction to the fully reduced leucoemeraldine base (LB) form occurred, as evidenced by the decrease in the intensity of the 808 and 430 nm ES bands and the appearance of a strong π-π* band at 340 nm. These spectral changes were nearly complete after 20 min and complete after 12 h. The weak band at about 1050 nm is due to the presence of the reducing species, hydrazine.

The oxidation of the *nano*PANI-DBSA ES form to the pernigraniline salt (PS) form was achieved by addition of 0.07 M APS. The oxidation occurred instantly, with the solution changing from emeraldine green to blue. Upon oxidation, the characteristic absorption band of PS appeared at 695 nm[20], while the peaks for the original ES disappeared (Figure 3.6).

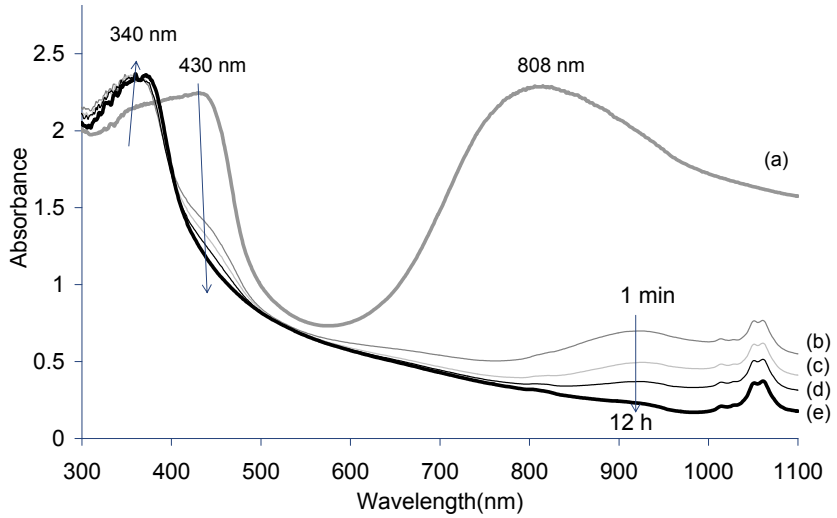

Figure 3.5 UV-visible spectra of: (a) *nano*PANI-DBSA (0.26 g/L) in the ES form, and reaction mixture after (b) 1, (c) 5, (d) 20 min, and (e) 12 h after addition of hydrazine.

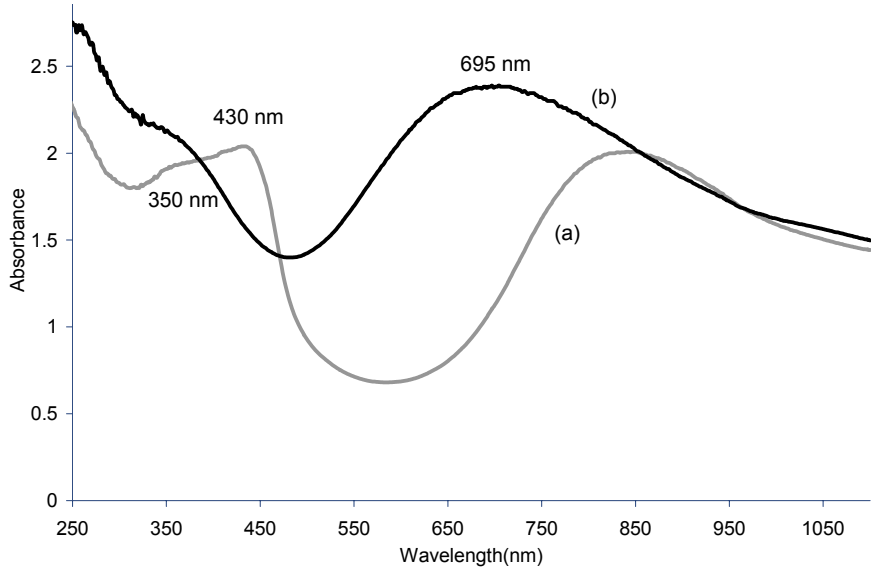

Figure 3.6 UV-visible spectra of: (a) *nano*PANI-DBSA (0.26 g/L) in the ES form, and (b) after oxidation to the PS form using 0.07 M APS.

3.3.1.2.3 Raman Spectroscopy

The ES *nano*PANI-DBSA was dried and its Raman spectrum obtained (Figure 3.7). The Raman spectrum was typical for ES PANI-DBSA and similar to that previously reported[32,33] for ES PANI-camphorsulphonic acid (HCSA) (Table 3.3). The C-C deformation band of the benzenoid ring appears at 1621 cm^{-1} and the C=N stretching of the quinoid ring at 1490 cm^{-1}. The 1320 cm^{-1}, 1343 cm^{-1} and 1257 cm^{-1} bands correspond to C-$N^{+\bullet}$ stretching modes in the polaronic units[34-36]. The benzenoid C-H bending deformation band is observed at 1169 cm^{-1} while the bands at 813 and 873 cm^{-1} are attributed to quinoid and benzenoid ring deformation, respectively. Band assignments are shown in Table 3.3, with the inclusion of bands for ES PANI-camphorsulphonic acid (HCSA) for comparison.

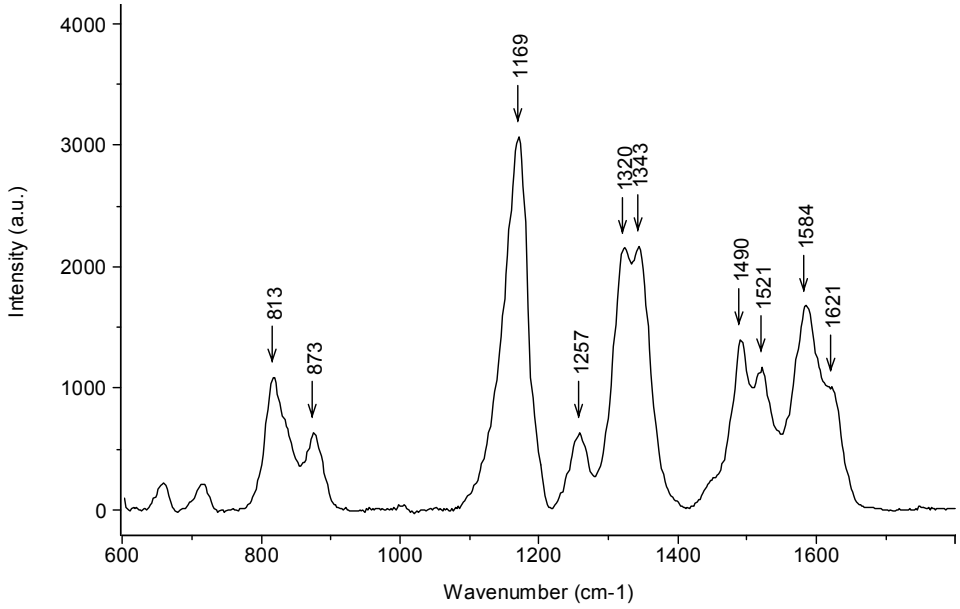

Figure 3.7 Raman spectrum of dried PANI-DBSA (ES form) nanoparticles observed using 632.8 nm excitation line.

Table 3.3 Assignments of the Raman bands for PANI using 632.8 nm excitation line.

Assignments	**PANI-CSA (cm^{-1})[32,33,37]**	***nano*PANI-DBSA (cm^{-1})**
C-H out of plane bending (Q)	811	813
C-H in-plane bending (B)	874	873
C-H in-plane bending (B)	1170	1169
$C\text{-}N^{+\bullet}$ stretching (B)	1255	1257
$C\text{-}N^{+\bullet}$ delocalised polaronic charge carriers	1318	1320
$C\text{-}N^{+\bullet}$ delocalised polaronic charge carriers	1341	1343
C=N streteching (Q)	1488	1490
N-H bending	1520	1521
C=C stretching (Q)	1584	1584
C-C stretching (B)	1622	1621

The benzenoid, quinoid units are denoted by B and Q, respectively

3.3.1.2.4 Cyclic voltammetry (CV)

Cyclic voltammetry was performed on the purified ES *nano*PANI-DBSA dispersion using a glassy carbon electrode as the working electrode (Figure 3.8). The CV is typical for PANI-ES[1], with the main peaks A and B corresponding to the transformation of LB to ES and ES to PS, respectively. On the reverse scan, peaks B′ and A′ correspond to the conversion of PS to ES and ES to LB, respectively. The presence of the peaks C/C′ is associated with the formation of *p*-benzoquinone and hydroquinone[38] as side products upon excursion to the high potentials necessary to observe the transition from ES to PS couple[39].

The current responses in Figure 3.8 a increased on subsequent scans, indicating that the nanoparticles aggregated/assembled on to the glassy carbon electrode surface. This process is hereafter called the electrodeposition process of the nanoparticles on the electrodes. The electrodeposited films were then scanned in 1 M HCl and CVs obtained (Figure 3.8 b). The PANI redox transformations were observed similar to the electrodeposition CV (Figure 3.8 a) described above.

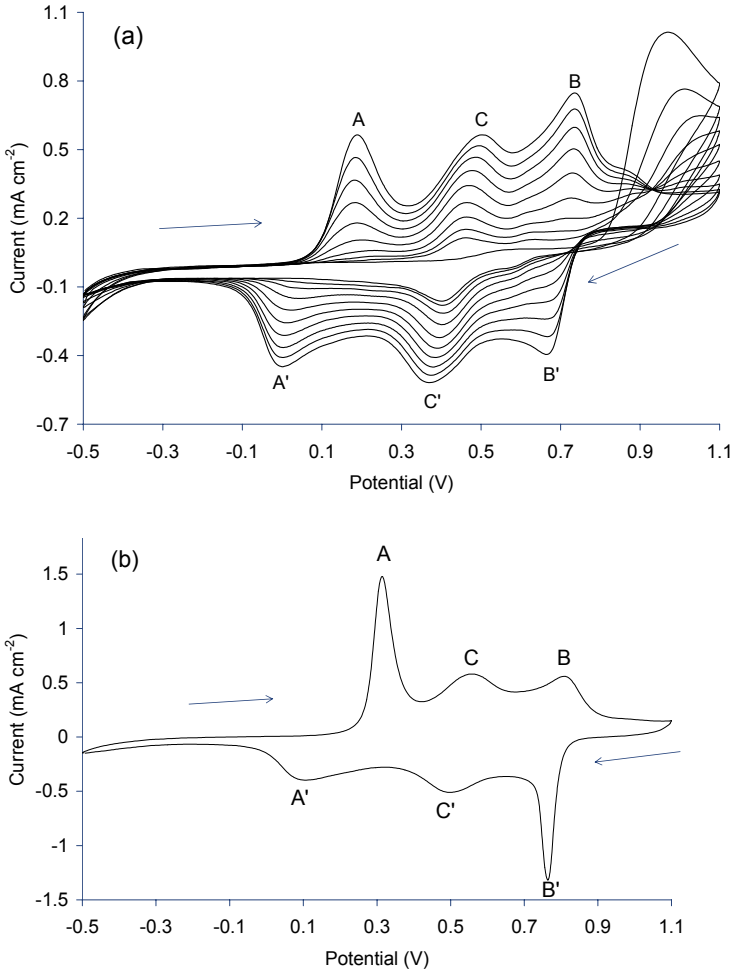

Figure 3.8 Cyclic voltammograms of: (a) electrodeposition of the *nano*PANI-DBSA (5.54 % w/w) using glassy carbon as the working electrode, and (b) the *nano*PANI-DBSA electrodeposited film from 10 electrodeposition cycles in 1 M HCl at a scan rate of 100 mV s^{-1} (arrows show the direction of the scan). $E_{initial}$ is -0.5 V and the potentials are vs. Ag/AgCl (3.0 M NaCl).

3.3.1.2.5 Stability test

The *nano*PANI-DBSA dispersion was prepared for stability tests as outlined in the experimental section (3.2.3.3). The UV-visible spectrum of the dispersion was found to be stable for up to 8 months, as evidenced in its similarity to the 1 week spectrum (Figure 3.9).

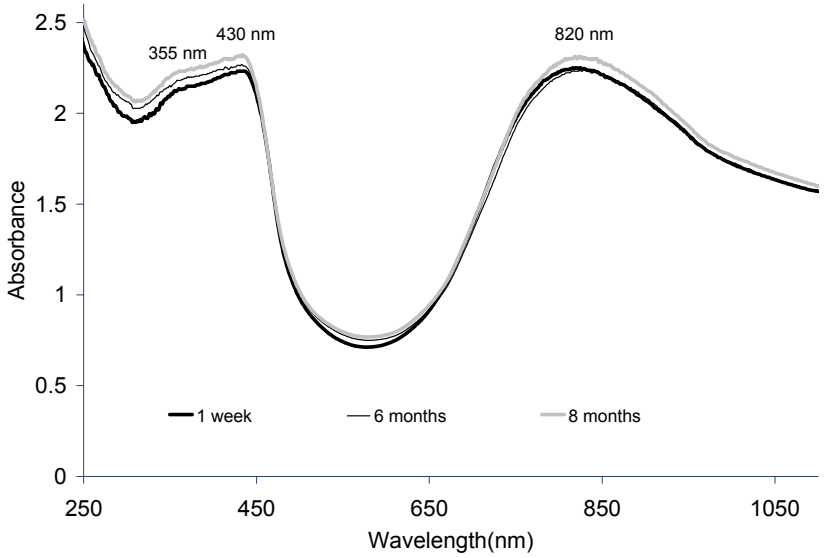

Figure 3.9 UV-visible spectra of *nano*PANI-DBSA (0.03% w/v) after storage at room temperature.

The electroactivity of the *nano*PANI-DBSA dispersion started to decrease after storage for 6 months and significantly decreased after 8 months (Figure 3.10). Besides the decrease in current magnitude, the redox couple B/B′ (indicating the transition between ES and PS) was greatly diminished after 8 months. The redox couple at around 0.5 V was also now more pronounced than the other two characteristic peaks indicating a higher content of degradation products[38], and responses were shifted to more positive potentials. The increase in the current magnitude with increasing number of potential cycles was also lower than for the fresh sample (result not shown). This indicated the deposition of the polymer onto the electrode decreased significantly with aging.

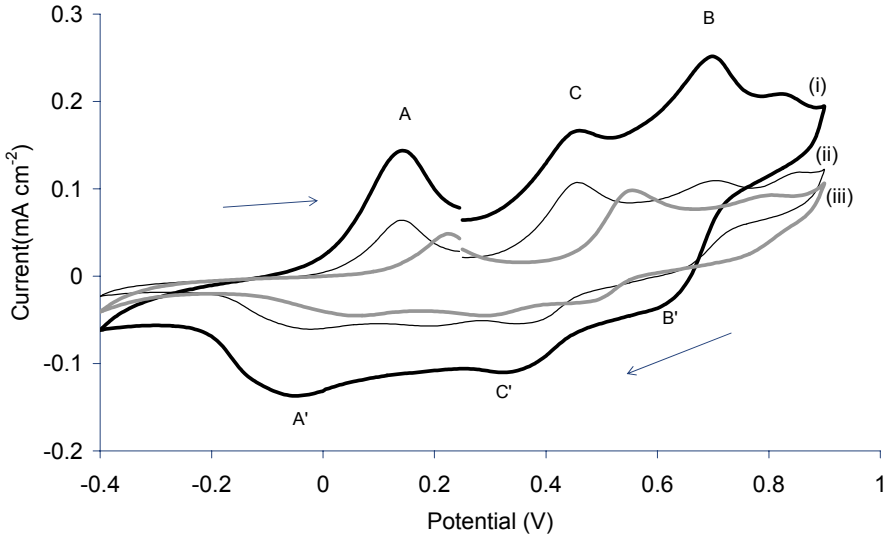

Figure 3.10 Cyclic voltammogram (5th scan) of *nano*PANI-DBSA dispersions (1.31% w/v) after: (i) 1 week, (ii) 6 months, and (iii) 8 months. The scan was performed using a GC working electrode at a scan rate of 100 mV/s, with the arrows show the direction of the scan. $E_{initial}$ is 0.25 V and all potentials are vs. Ag/AgCl (3.0 M NaCl).

The *nano*PANI-DBSA nanoparticles were found to be stable in solution for up to 13 months (Figure 3.11), after which time the particles appeared to settle out and form a precipitate on the bottom of the flask. However, there appeared to be some more stable particles still in solution as the polymer solution retained some PANI emeraldine colour beyond 13 months.

For the *nano*PANI-DBSA nanoparticles stored in water for 2 days after synthesis, the particle size distribution was bimodal with peaks at 92 and 185 nm [Figure 3.11 A (i)]. After 13 months, the dispersed particles aggregated and slowly precipitated out of solution. However, some aggregated particles were still suspended in solution with the particle size distribution shown to be 58, 262 and 417 nm (Figure 3.11 B (i)). The last two peaks obviously indicate the aggregation of the polymer with time.

The particle size distribution of the *nano*PANI-DBSA stored in aqueous 0.001 M DBSA for 2 days after synthesis [Figure 3.11 A (ii)] also showed bimodal distribution at 165 and 262 nm, with the 165 nm size dominating. After 13 months, the particle size variation was observed to be 104, 262, 417 nm, with the 104 size dominant [Figure 3.11 B (ii)]. The latter two peaks indicated that larger particles were formed from aggregation during this long storage time. Similar aggregation processes occurred in 0.01 M DBSA solution [Figures 3.11 A (iii) and 3.11 B (iii)].

Two days after synthesis, the particle size distribution of the *nano*PANI-DBSA stored in water [Figure 3.11 A (i)] showed a higher number of large particles than in 0.001 M DBSA [Figure 3.11 A (ii)] and 0.01 M DBSA [Figure 3.11 A (iii)]. With higher concentration of surfactant, higher numbers of small particles were observed. Moreover, the size distribution after 13 months showed more small particles in the higher concentration of surfactant solutions, indicating that the surfactant stabilised the nanoparticles and prevented them from aggregation.

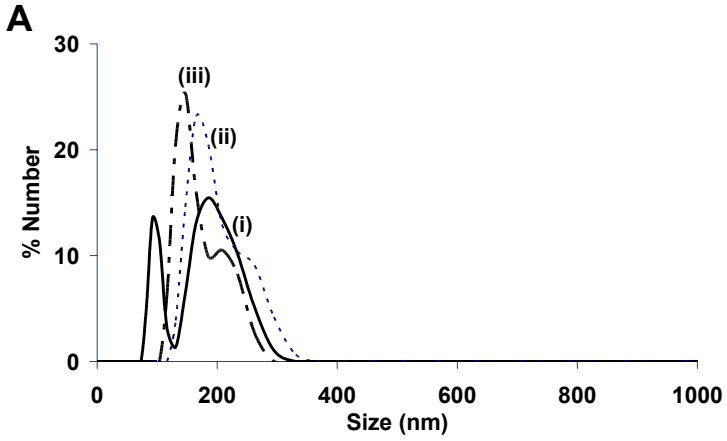

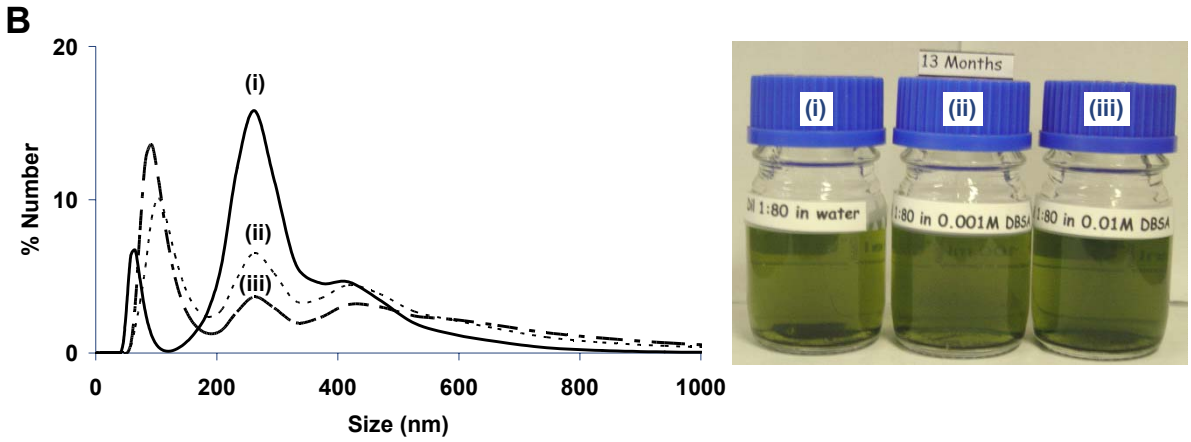

Figure 3.11 Photographs and particle size distribution of colloidal stability of *nano*PANI-DBSA dispersion (0.06% w/v) in: (i) water, (ii) 0.001 M DBSA, and (iii) 0.01 M DBSA after being stored for 2 days (A) and 13 months (B). Less than 1% of the particles are larger than 1000 nm (result not shown).

3.3.1.3 Further processing and characterisation

For ink-jet printing, small particle size in a concentrated solution is desirable. The particle size of the *nano*PANI/DBSA dispersions at concentrations of the order of 5 % w/w was too large for ink-jet printing. Therefore, the *nano*PANI-DBSA was further processed to obtain small particle sizes.

From the purification process of the *nano*PANI/DBSA, after centrifugation two separate components resulted, namely the precipitate and the supernatant. It was observed that the supernatant always contained small polymer particles which were unable to be removed at a centrifugation rate of 4000 rpm. Therefore, this process was used to separate small particles from large particles and prepare a supernatant of *nano*PANI-DBSA (*s*PANI-DBSA) solution for ink-jet printing.

3.3.1.3.1 Preparation method for the sPANI/DBSA

The *nano*PANI-DBSA nanoparticles (26.5 % w/w) were diluted to 5.3 % w/w in water. The solution was centrifuged at 4400 rpm for 30 min. The supernatant was diluted 1:1 with water and centrifuged again. The supernatant was then characterised using UV-visible spectroscopy, CV and DLS particle size analysis.

3.3.1.3.2 UV-visible spectroscopy

UV-visible spectrum of the *s*PANI-DBSA (Figure 3.12) shows the same features as those observed for the *nano*PANI-DBSA, indicating the same electronic properties.

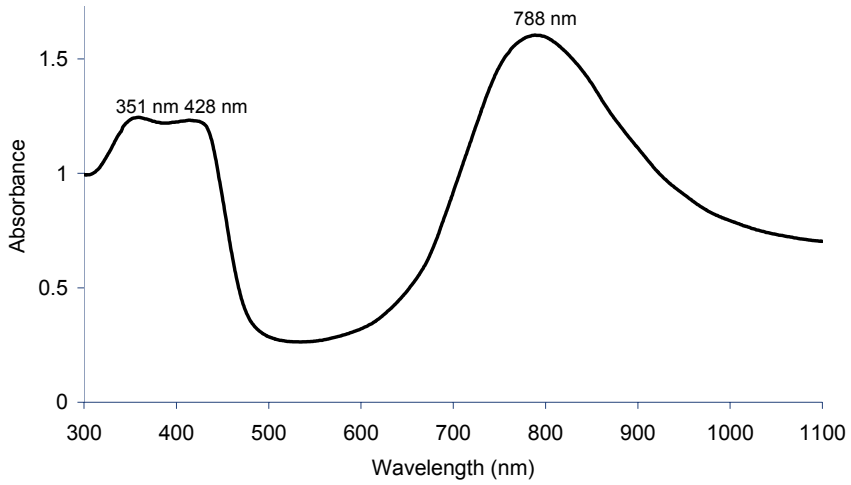

Figure 3.12 UV-visible absorption spectrum of *s*PANI-DBSA (0.09 g/L) in the ES form.

3.3.1.3.3 Cyclic Voltammetry (CV)

In order to check the electroactivity of the *s*PANI-DBSA, electrodeposition onto glassy carbon electrode was carried out using CV (Chapter 2, section 2.3.2). The current magnitudes increased as the number of cycles increased indicating successful electrodeposition (Figure 3.13 a). The voltammogram was similar to that observed for electrodeposition of the *nano*PANI-DBSA dispersions, albeit with lower currents due to the lower concentration of the nanoparticles in the dispersion (0.5 % w/w) used to achieve

electrodeposition. The electrodeposited film was then scanned in 0.1 M HCl. The resulting CVs showed two redox couples (A/A′ and B/B′ in Figure 3.13 b) indicating the expected redox transitions of PANI as mentioned in section 3.3.1.2.4 for the CV of *nano*PANI-DBSA. In Figure 3.13 b, the middle peak (C) associated with the formation of side products[38] was possibly merged with peak B associated with the transformation of the ES PANI to PS PANI.

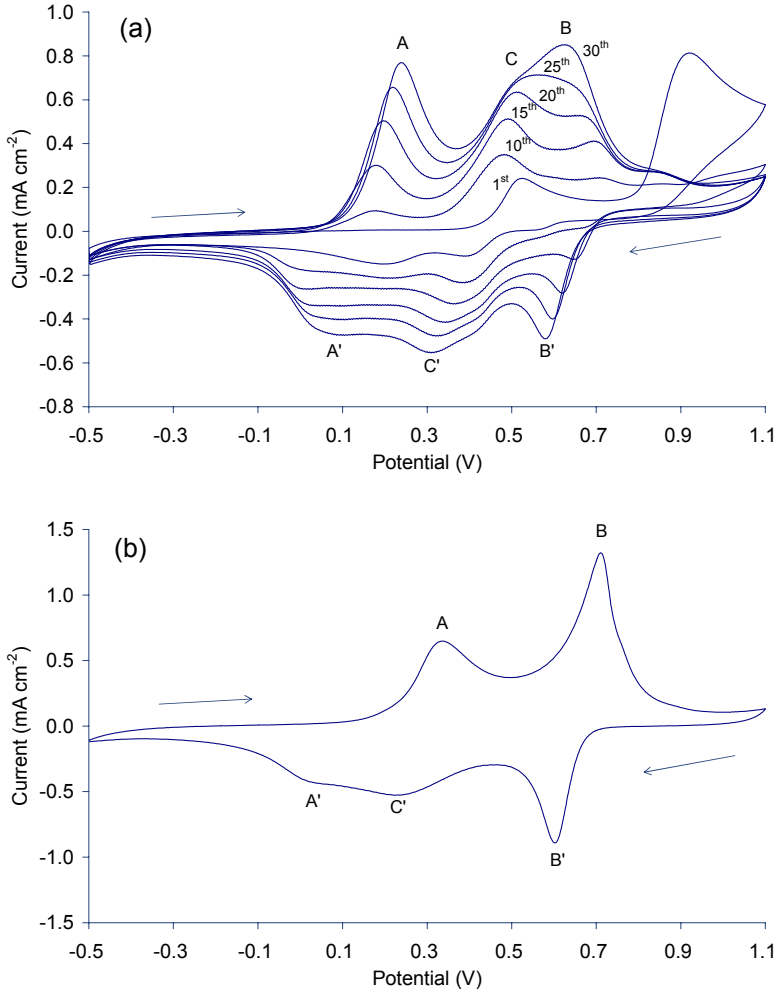

Figure 3.13 Cyclic voltammograms: (a) during electrodeposition of the *s*PANI-DBSA (0.5% w/w) using glassy carbon as the working electrode, with number of cycles marked on the curve, and (b) the *s*PANI-DBSA electrodeposited film from 30 electrodeposition cycles in 0.1 M HCl at a scan rate of 100 mV s^{-1} (arrows show the direction of the scan). $E_{initial}$ is -0.5 V and the potentials are vs. Ag/AgCl (3.0 M NaCl).

3.3.1.3.4 Particle size, morphology and conductivity

The particle size of the *s*PANI-DBSA (0.5 % w/w) dispersion determined by DLS is shown below both by % Volume (Figure 3.14 a) and % Number (Figure 3.14 b) distribution. The % Number indicates the number of particles in the particular size, and a few large particles in solution are insignificant with respect to the number of smaller particles. The difference between these two particle size presentations was explained in greater detail in Chapter 2, section 2.2.3. Since the *s*PANI-DBSA dispersion is a candidate for ink-jet printing, the % Volume distribution is taken into account as only a few large particles can block the print head.

In Figure 3.14, the particle size distribution of the *s*PANI-DBSA by % Volume shows a broad bimodal distribution of sizes in the dispersion with a significant amount of large particles around 2300 nm, whereas the % Number plot shows more than 99% of the particles to be smaller than 1000 nm. This result indicates that while larger particles are present in the *s*PANI-DBSA solution, they constitute only a very small number compared to particles with particles of sizes less than 1000 nm.

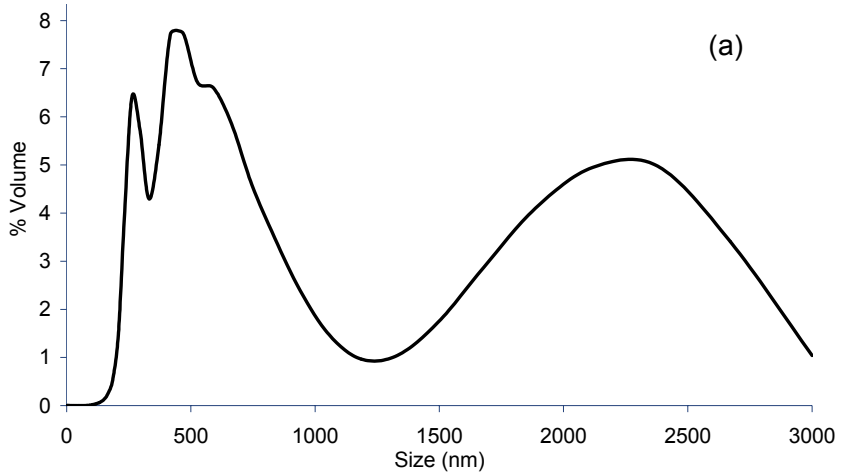

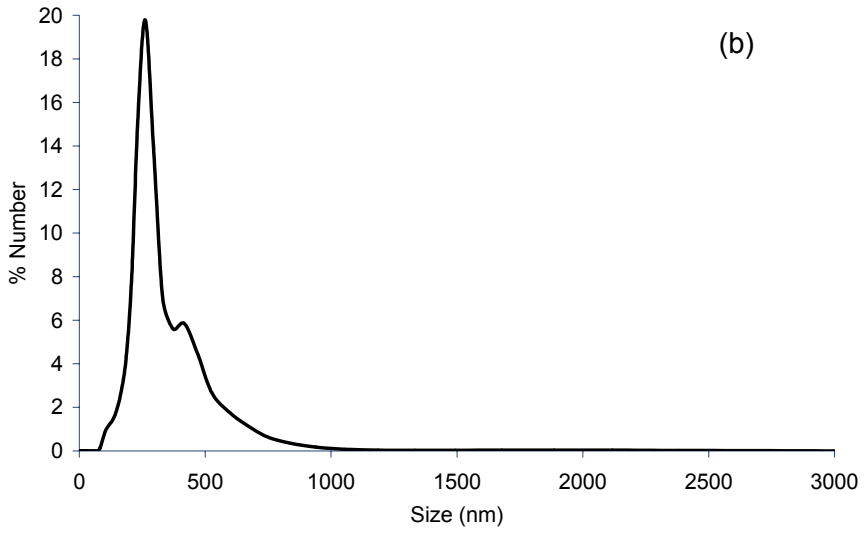

Figure 3.14 Size distribution of *s*PANI-DBSA indicated by: (a) % Volume, and (b) % Number.

A TEM of the *s*PANI-DBSA (Figure 3.15) showed most particles to be smaller than 100 nm, with some large aggregation present. The patchy grey area indicates the dried surfactant. The printability of this dispersion will be discussed in Chapter 9.

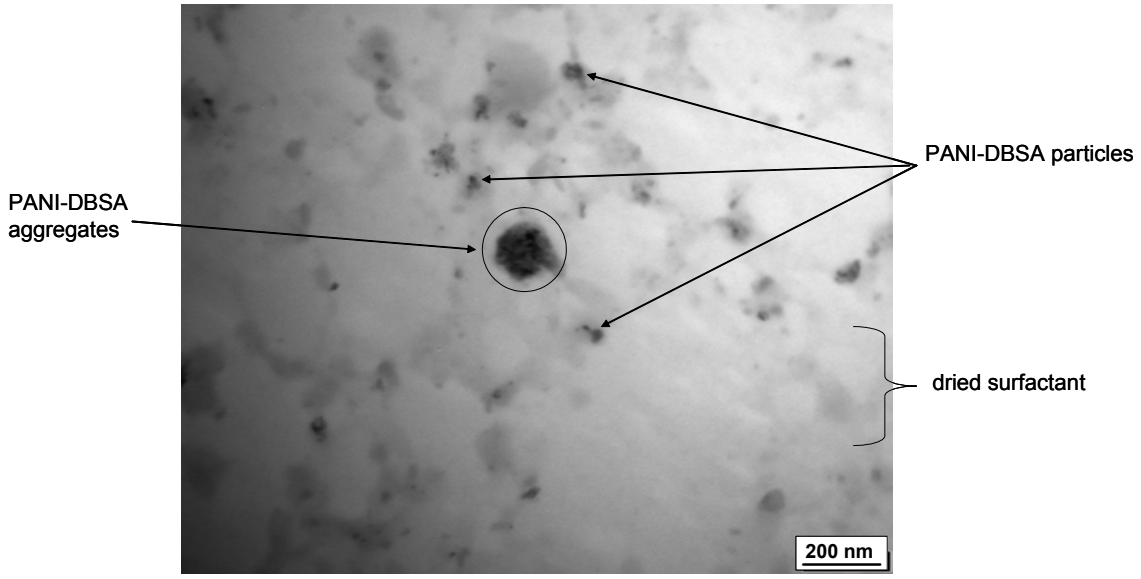

Figure 3.15 Transmission electron micrograph of *s*PANI-DBSA dispersion. Image was obtained at 100 keV at a magnification of 200k.

Conductivity of *s*PANI-DBSA measured on dried pressed pellets was found to be 0.42±0.03 S/cm which was lower than the *nano*PANI-DBSA. This indicated that the preparation process used to obtain the *s*PANI-DBSA altered electrical property of the *nano*PANI-DBSA.

3.3.2 PANI-DBSA-RM

3.3.2.1 Polymerisation

PANI-DBSA-RM was synthesised using the rapid mixing method developed by Huang *et al*[18]. Upon addition of aniline to a micellar solution of DBSA, an increase in solution viscosity and colour change similar to the synthesis of the *nano*PANI-DBSA in section 3.3.1.1 were observed. However, the rate of colour change was slower as the oxidant concentration was 4 times less than that of the monomer. The colour change from white to yellow to blue was observed about 10 min after the addition of APS. Moreover, the turquoise colour stayed longer than in the synthesis of the *nano*PANI-DBSA. The solution was very viscous upon completion of the polymerisation, therefore 0.05 M SDS solution (20 ml) was added to assist in the centrifuge process. After centrifugation, a precipitate of agglomerated polymer formed at the bottom of the centrifuge tube. The supernatant solution contained the nanoparticles, and was further characterised in the following section.

The OCP profile recorded during the synthesis of the PANI-DBSA-RM is shown in Figure 3.16. The potential of aniline/DBSA micellar solution was about 0.5 V and dropped sharply due to the single step addition of APS solution. The potential immediately increased to about 0.65 V within 5 min and then slightly decreased to about 0.62 V. The

colour of the reaction mixture at this stage was white. After 10 min, the colour had changed from white to pale blue and then turquoise, which is attributed to the redox and electronic transition of different forms of PANI as presented by Stejskal *et al*[20], and coincided with the increase of the OCP from about 0.62 to 0.65 V. The potential reached the plateau at 0.65 V before starting to decrease at about 35 min, which coincided with a colour changed from turquoise to emeraldine green. This is attributed to the conversion from the highly oxidised PS species to the ES form[20]. The nearly constant OCP (0.41 V) obtained after 120 min indicated that the polymerisation reached equilibrium. The maximum potential (0.65 V) and the potential at equilibrium (0.41 V) were slightly different from those obtained for the synthesis of the *nano*PANI-DBSA (Figure 3.1), which may possibly be due to the different concentration of reactants and also the ratio of aniline:APS used.

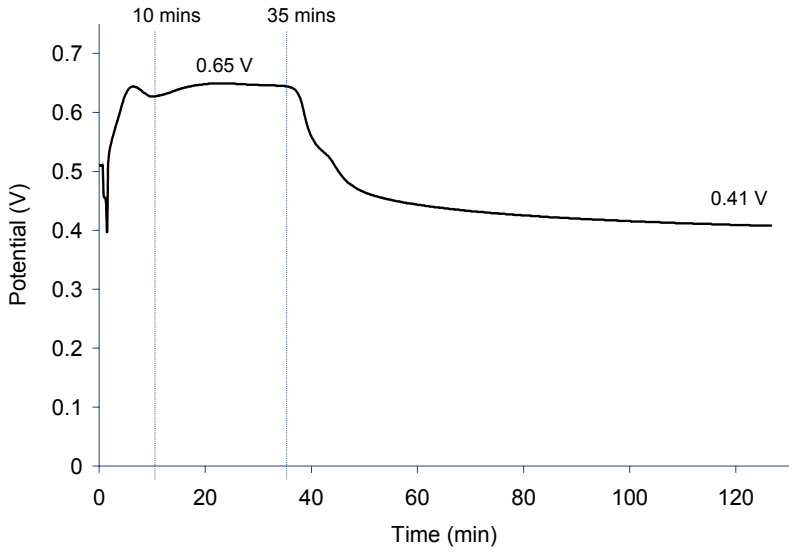

Figure 3.16 The OCP in-situ during polymerisation of PANI-DBSA-RM dispersions. The potentials are vs. Ag/AgCl (3.0 M NaCl). APS solution was added at t = 0.

3.3.2.2 Characterisations of PANI-DBSA-RM nanodispersions

3.3.2.2.1 UV-visible spectroscopy and redox switching

The PANI-DBSA-RM nanodispersions were purified as outlined in section 3.2.3.1 and diluted to 2.13 g/L in water. Their UV-visible spectra obtained (Figure 3.17 a) showed similar features to that observed for *nano*PANI-DBSA (Figure 3.4 a). However, the intensity of the π*-polaron band at about 415 nm was slightly lower than the π-π* band at 342 nm for PANI-DBSA-RM, indicating lower doping state[6] than the *nano*PANI-DBSA. This is possibly due to the lower oxidant concentration used in the former case.

The PANI-DBSA-RM nanodispersions were dedoped with 0.1 M NaOH (Figure 3.17 b). The dedoping process from ES to EB form was similar to that observed for *nano*PANI-DBSA in section 3.3.1.2.2 (Figure 3.4). However, the characteristic EB exciton band was now at 565 nm (25 nm lower than for *nano*PANI-DBSA), and no shoulder peak at around 700 nm was observed. This indicates an easier dedoping process which is possibly due to the smaller particle size.

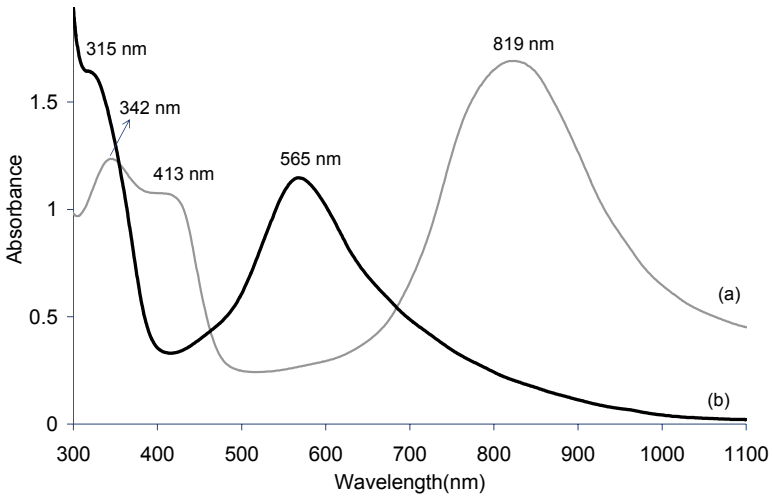

Figure 3.17 UV-visible spectra of: (a) PANI-DBSA-RM nanodispersion (2.13 g/L) in the ES form, and (b) after dedoping to the EB form using 0.1 M NaOH.

The reduction process of the PANI-DBSA-RM in 4 M hydrazine (pH ~ 10) was similar to the previous reduction of the *nano*PANI-DBSA (Figure 3.5), with the reduction to the fully reduced leucoemeraldine base (LB) form seen to be complete after 12 h (Figure 3.18).

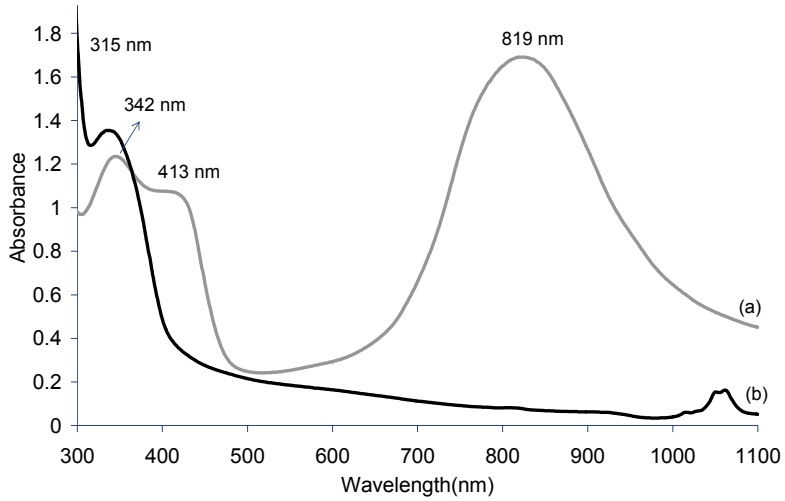

Figure 3.18 UV-visible absorption spectra of: (a) PANI-DBSA-RM (2.13 g/L) in the ES form, and (b) the LB form produced 12 h after addition of hydrazine.

The oxidation of PANI-DBSA-RM ES form to PS form was performed by addition of 0.07 M APS. The oxidation occurred instantly with the solution containing PANI-DBSA-RM changed from the green of the ES form to blue/purple. The corresponding UV-visible spectrum (Figure 3.19) shows a broad band centred at about 620 nm and is consistent with a mixture of PS (λ_{max} 690 nm) and perniganiline base (PB) (λ_{max} 540 nm)[20].

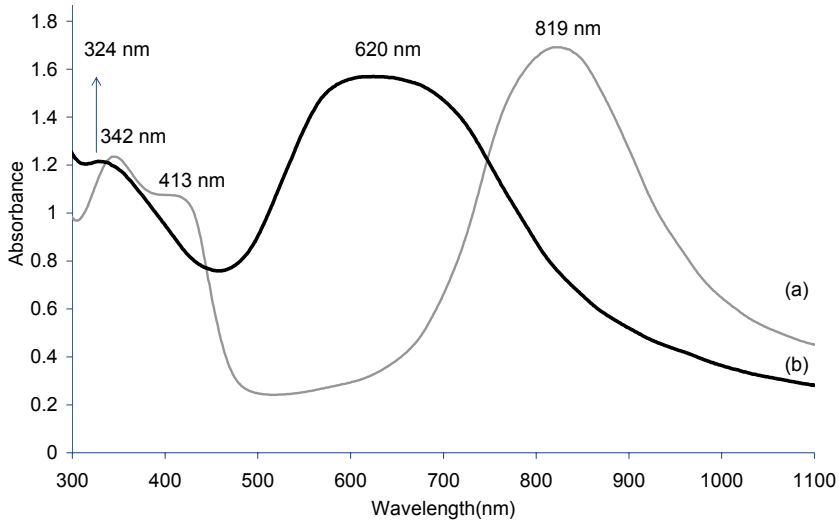

Figure 3.19 UV-visible absorption spectra of: (a) PANI-DBSA-RM in the ES form and (b) 2 min after oxidation to the PS form using 0.07 M APS.

3.3.2.2.2 Raman spectroscopy

Raman spectrum of the dried film of the ES PANI-DBSA-RM was obtained (Figure 3.20). The spectrum was typical for PANI emeraldine salts and have some band assignments similar to that summarised in Table 3.3, but with some features different from the Raman spectrum of the *nano*PANI-DBSA (Figure 3.7). The C-H out of plane bending of the benzenoid rings appeared at 811 cm^{-1} and C-H in plane bending of quinoid rings at 867 cm^{-1}. A C-H deformation band for quinoid rings appeared at 1164 cm^{-1}, instead of the band at 1169 cm^{-1} assigned to benzenoid segments in the Raman spectra of the *nano*PANI-DBSA (Figure 3.7). The band at 1229 cm^{-1} was attributed to the C-N stretching of the benzenediamine units. The absence of the 1584 cm^{-1} band (associated with C=C of quinoid rings) and the presence of the 1597 cm^{-1} band (associated with C-C benzenoid units) indicates less concentration of quinoid units in PANI-DBSA-RM nanoparticles than in *nano*PANI-DBSA. The characteristic band of the radical cation appeared in one peak centred at 1336 cm^{-1}. The appearance of the peaks at 1376 cm^{-1} and 1643 cm^{-1} was

attributed to the formation of a cross-linked polymer. The bands at 1475 cm^{-1} and 1504 cm^{-1} were assigned to the C=N stretching of the quinoid diimine units and N-H deformation, respectively[37]. These observations indicate that the PANI-DBSA-RM nanoparticles have a different structure from the *nano*PANI-DBSA.

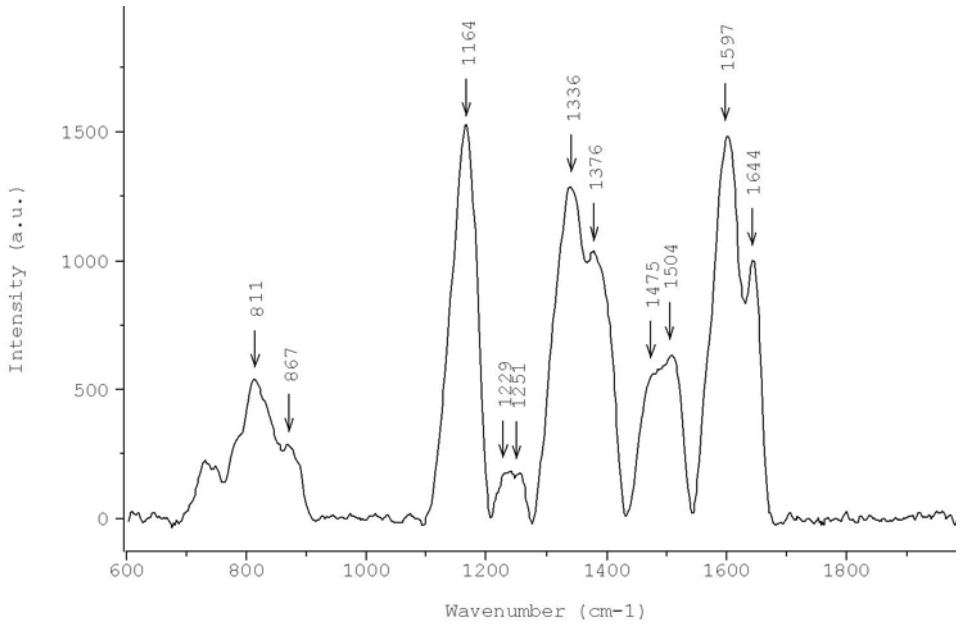

Figure 3.20 Raman spectrum of PANI-DBSA-RM (ES form) cast film observed using 632.8 nm excitation line.

3.3.2.2.3 Cyclic Voltammetry (CV)

Electrodeposition of the PANI-DBSA-RM nanodispersions showed increasing current magnitude as the number of cycles increased, as seen in Figure 3.21 a. The CV of electrodeposited film in 1 M HCl is shown in Figure 3.21 b, with a typical transformation of LB to ES (A/A′) and ES to PS (B/B′) similar to the CV of *nano*PANI-DBSA in section 3.3.1.2.4. The middle redox couple (C/C′) is associated with the formation of *p*-benzoquinone and hydroquinone[38] as side products upon excursion to the high positive potentials necessary to observe the B/B′ couple[39].

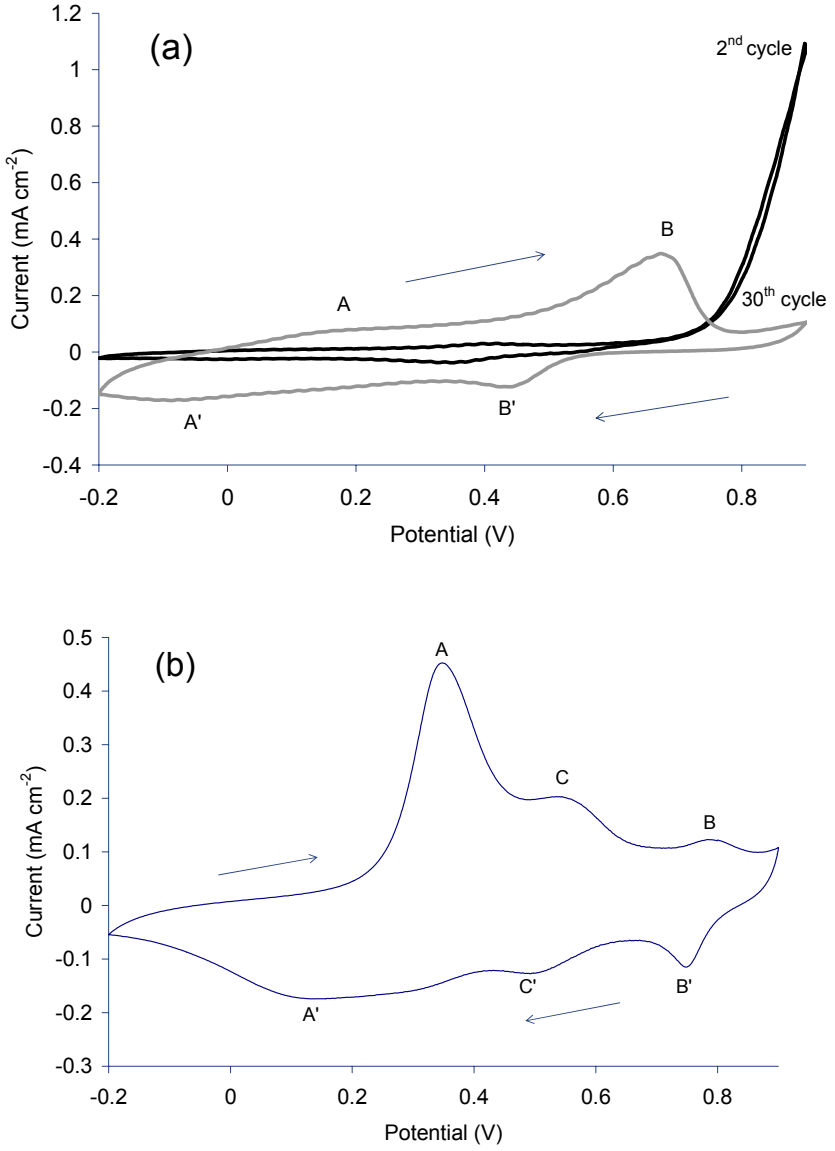

Figure 3.21 Cyclic voltammograms: (a) during electrodeposition PANI-DBSA-RM (4.26% w/w) onto glassy carbon electrode for 30 cycles at 100 mV/s, and (b) of the electrodeposited film in 1 M HCl. E_{intial} = -0.2 V and arrows indicate direction of potential scan. All potentials are vs. Ag/AgCl (3.0 M NaCl).

3.3.2.2.4 Conductivity, particle size and morphology

Conductivity of the evaporative cast films of the PANI-DBSA-RM were measured, using the four point probe technique as detailed in Chapter 2, section 2.4, and found to be 40 ± 8 mS/cm.

Particle size distribution of the PANI-DBSA-RM (4.26% w/w) determined using DLS (Figure 3.22) showed a narrow size distribution centred at about 50 nm, indicating small and uniform particle size which agrees with a TEM image (Figure 3.23). Moreover, the % Number is the same as % Volume, indicating that the dispersion consists of aggregates of PANI-DBSA-RM only between 30-57 nm.

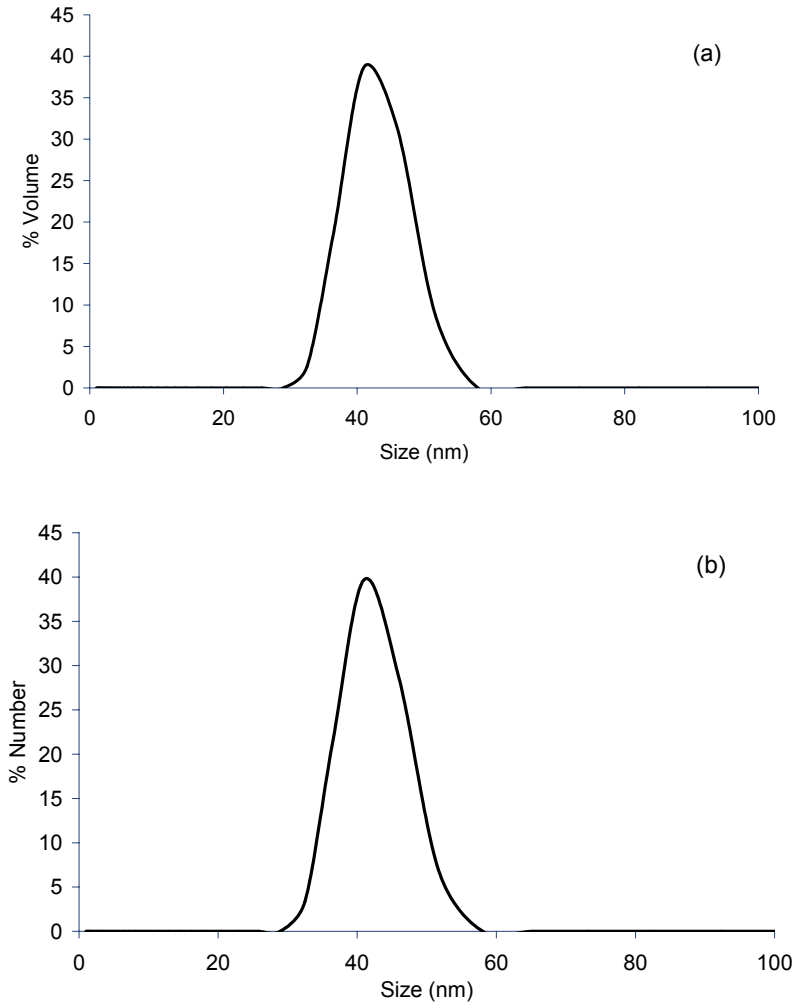

Figure 3.22 Size distribution of supernatant PANI-DBSA-RM (4.26 % w/w) indicated by: (a) % Volume, and (b) % Number.

TEM (Figure 3.23) shows the PANI-DBSA-RM nanoparticle islands surrounded by a white sheet of surfactant, with particle size similar to that observed by DLS in

concentrated solution (Figure 3.22). This suggests that the efficiency of this rapid mixing method produces monodispersed nanoparticles. The polymer morphology was different from Huang *et al*[18], who used HCl as the dopant and PANI nanofibre was produced. In the present work, the polymer was formed in DBSA micelles; hence spherical particles were obtained.

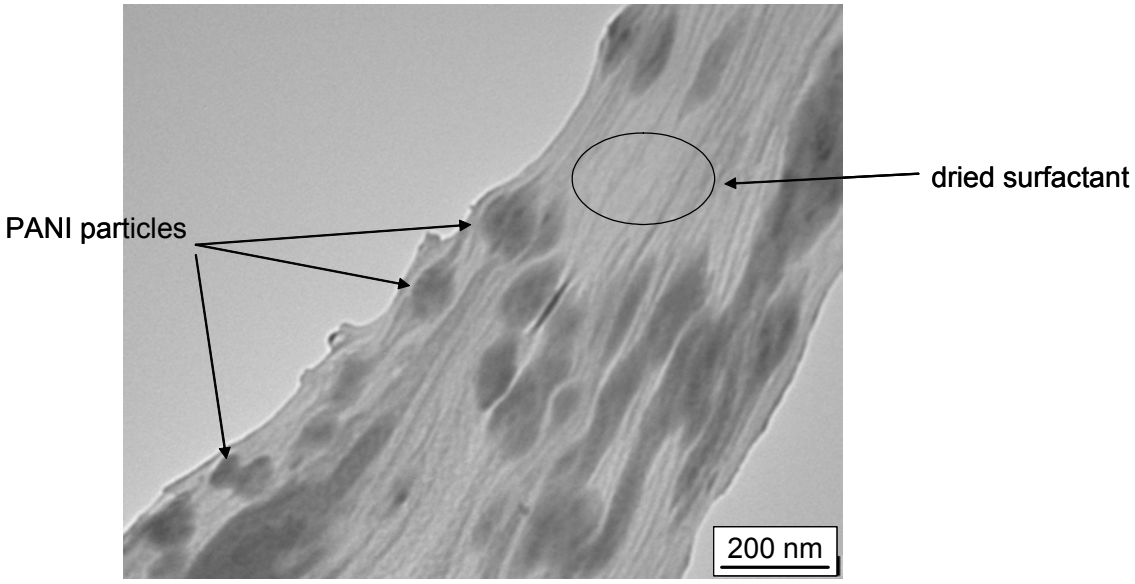

Figure 3.23 Transmission electron micrograph of PANI-DBSA-RM nanodispersions at 100 keV.

3.4 Conclusions

PANI nanodispersions have been synthesised using various methods. *nano*PANI-DBSA dispersions have been successfully synthesised in large scale using emulsion polymerisation method, indicating potential for mass production. Highly conductive and stable PANI nanoparticles were obtained, with the UV-visible spectra showing PANI to be in a "compact coil" formation and to be slightly resistive to deprotonation. The electrical conductivity of these nanoparticles is 34 ± 7 S/cm, with the spherical particles having a size of 10 ± 2 nm. The concentration of PANI-DBSA nanoparticles is 118 g/L based on total volume of the reaction medium. The dispersions are stable for up to 12 months and their electronic property remained constant for 8 months while their electrochemical property was stable for up to 6 months before beginning to deteriorate. The *nano*PANI-DBSA dispersions show excellent electrodeposition properties, indicating that it may have potential for use as a mediator in biosensor applications (see Chapter 7).

By separating the precipitate of the agglomerated polymer from the supernatant, a further form (*s*PANI-DBSA) can be prepared from the supernatant. The *s*PANI-DBSA (0.5% w/w) has various and inconsistent particle sizes, with some particles larger than 1000 nm. During electrodeposition from this dispersion, lower charging current are observed compared to *nano*PANI-DBSA, due to the lower concentration of the polymer in the solution used for electrodeposition. This *s*PANI-DBSA material was later used for ink-jet printing (see Chapter 9).

PANI-DBSA-RM nanodispersions have also synthesised for ink-jet printing (see Chapter 9). The particle size of PANI-DBSA-RM (4.26% w/w) is uniform around 50 nm. This material also shows good electroactivity and electrodeposition properties which are

amenable for biosensor application. The electrical conductivity of the PANI-DBSA-RM nanoparticles is 40±8 mS/cm. The particle size determined by DLS is similar to that observed by TEM, indicating the segregation of the particles in concentrated solution by the stabilising nature of the surfactant. A spherical morphology is observed for the nanoparticles, as the polymer was formed in DBSA micelles. This rapid mixing method was found to be an effective method to produce monodispersed PANI nanoparticles. Optimisation of this method to achieve higher conductivity nanoparticles will be further investigated.

3.5 References

1. Wallace, G.G., Spinks, G.M., Kane-Maguire, L.A.P., and Teasdale, P.R., *Conductive electroactive polymers : intelligent materials systems*. 2nd ed. 2002, Boca Raton, FL: CRC Press. , and references cited therein.
2. Gangopadhyay, R., De, A., and Ghosh, G., *Synthetic Metals*, 2001. **123**(1): p. 21-31.
3. Somani, P.R., *Materials Chemistry and Physics*, 2002. **77**(1): p. 81-85.
4. Han, M.G., Cho, S.K., Oh, S.G., and Im, S.S., *Synthetic Metals*, 2002. **126**(1): p. 53-60.
5. Mandal, B.M., *Bulletin of Materials Science*, 1998. **21**(2): p. 161-165.
6. Kim, B.J., Oh, S.G., Han, M.G., and Im, S.S., *Synthetic Metals*, 2001. **122**(2): p. 297-304.
7. Yu, L., Lee, J.I., Shin, K.W., Park, C.E., and Holze, R., *Journal of Applied Polymer Science*, 2003. **88**(6): p. 1550-1555.
8. Xia, H.S. and Wang, Q., *Journal of Nanoparticle Research*, 2001. **3**(5-6): p. 401-411.
9. Kim, D., Choi, J., Kim, J.Y., Han, Y.K., and Sohn, D., *Macromolecules*, 2002. **35**(13): p. 5314-5316.
10. Madathil, R., Parkesh, R., Ponrathnam, S., and Largo, M.C.J., *Macromolecules*, 2004. **37**(6): p. 2002-2003.
11. Ghosh, P., Siddhanta, S.K., Haque, S.R., and Chakrabarti, A., *Synthetic Metals*, 2001. **123**(1): p. 83-89.
12. Stejskal, J. and Sapurina, I., *Journal of Colloid and Interface Science*, 2004. **274**(2): p. 489-495.
13. Dorey, S., Vasilev, C., Vidal, L., Labbe, C., and Gospodinova, N., *Polymer*, 2005. **46**(4): p. 1309-1315.
14. Armes, S.P. and Aldissi, M., *Journal of the Chemical Society, Chemical Communications*, 1989(2): p. 88-89.
15. Armes, S.P., Aldissi, M., Agnew, S., and Gottesfeld, S., *Langmuir*, 1990. **6**(12): p. 1745-1749.
16. Magdassi, S. and Ben Moshe, M., *Langmuir*, 2003. **19**(3): p. 939-942.
17. Le, H.P., *Journal of Imaging Science and Technology*, 1998. **42**(1): p. 49-62.
18. Huang, J.X. and Kaner, R.B., *Angewandte Chemie-International Edition*, 2004. **43**(43): p. 5817-5821.
19. Wei, Y., Hsueh, K.F., and Jang, G.-W., *Polymer*, 1994. **35**(16): p. 3572-3575, and references cited therein.
20. Stejskal, J., Kratochvil, P., and Jenkins, A.D., *Collection of Czechoslovak Chemical Communications*, 1995. **60**: p. 1747-1755.
21. Haba, Y., Segal, E., Narkis, M., Titelman, G.I., and Siegmann, A., *Synthetic Metals*, 1999. **106**(1): p. 59-66.
22. Delahay, P., *New instrumental methods in electrochemistry : theory, instrumentation, and applications to analytical and physical chemistry*. 1954, New York: Interscience. pp.9-10.
23. Haba, Y., Segal, E., Narkis, M., Titelman, G.I., and Siegmann, A., *Synthetic Metals*, 2000. **110**(3): p. 189-193.
24. Mulvaney, P., *Langmuir*, 1996. **12**(3): p. 788-800.

25. Shipway, A.N., Katz, E., and Willner, I., *Chemphyschem*, 2000. **1**(1): p. 18-52.
26. Xia, Y., Wiesinger, J.M., MacDiarmid, A.G., and Epstein, A.J., *Chemistry of Materials*, 1995. **7**(3): p. 443-445.
27. Norris, I.D., Kane-Maguire, L.A.P., and Wallace, G.G., *Macromolecules*, 2000. **33**(9): p. 3237-3243.
28. Blinova, N.V., Sapurina, I., Klimovic, J., and Stejskal, J., *Polymer Degradation and Stability*, 2005. **88**(3): p. 428-434.
29. Pilla, V., Balogh, D.T., Faria, R.M., and Catunda, T., *Review of Scientific Instruments*, 2003. **74**(1): p. 866-868.
30. Albuquerque, J.E., Mattoso, L.H.C., Balogh, D.T., Faria, R.M., Masters, J.G., and MacDiarmid, A.G., *Synthetic Metals*, 2000. **113**(1-2): p. 19-22.
31. Lindfors, T. and Ivaska, A., *Journal of Electroanalytical Chemistry*, 2002. **531**(1): p. 43-52.
32. Cochet, M., Louarn, G., Quillard, S., Buisson, J.P., and Lefrant, S., *Journal of Raman Spectroscopy*, 2000. **31**(12): p. 1041-1049.
33. Cochet, M., Buisson, J.P., Wery, J., Jonusauskas, G., Faulques, E., and Lefrant, S., *Synthetic Metals*, 2001. **119**(1-3): p. 389-390.
34. Lindfors, T. and Ivaska, A., *Journal of Electroanalytical Chemistry*, 2005. **580**(2): p. 320-329.
35. Boyer, M., Quillard, S., Louarn, G., Lefrant, S., Rebourt, E., and Monkman, A.P., *Synthetic Metals*, 1997. **84**: p. 787-788.
36. Zhang, J.X., Liu, C., and Shi, G.Q., *Journal of Applied Polymer Science*, 2005. **96**(3): p. 732-739.
37. da Silva, J.E.P., de Faria, D.L.A., de Torresi, S.I.C., and Temperini, M.L.A., *Macromolecules*, 2000. **33**(8): p. 3077-3083.
38. Chen, W.C., Wen, T.C., and Gopalan, A., *Synthetic Metals*, 2002. **128**(2): p. 179-189.
39. Mirmohseni, A. and Wallace, G.G., *Polymer*, 2003. **44**(12): p. 3523-3528.

4.1 Introduction

The anionic dopant incorporated into a conducting polymer during synthesis has a profound effect on its processability and conductivity[1] (see Chapter 1, section 1.1). The use of appropriate dopants results in the formation of stable processable conducting dispersions. For example, Han *et al*[2] and Haba *et al*[3] used dodecylbenzenesulphonic acid (DBSA) as the dopant in the synthesis of polyaniline (PANI) to render solubility and stable dispersions. The stability of these PANI-DBSA dispersions can be attributed to the presence of excess DBSA molecules, which form strong hydrogen bonding with the PANI-DBSA particles and stabilise the particles[3]. Henderson *et al*[4] introduced a new method for stabilizing conducting polymer nanoparticles using short chain alcohol ethoxylate surfactants.

Functional molecules can be incorporated into a polymer to improve its properties and enhance selectivity[5]. There are many studies showing dye molecules incorporated into conducting polymers during synthesis. Yoshino *et al*[6] have studied the characteristics of a conducting polymer doped with photochromic dyes and found that photoluminescence and photoconductivity in the conducting polymer dramatically altered. Feng *et al*[7] examined the electrical and optical properties of soluble conducting polymer/dye composites and found that the composites helped improve the efficiency of the charge separation and transfer.

In this chapter the possibility of incorporating functional dye molecules as molecular dopants during the synthesis of PANI nanoparticles is investigated. A dye (carbolan blue-CB) with a structure similar to the surfactants used was chosen (Figure 4.1). It was envisaged that the alkyl chain and sulfonate group of the dye may interact with the polymer in a similar way to the surfactant, i.e. sulfonate ion doping and hydrophobic

interactions. PANI nanoparticles with and without dye incorporated were synthesised and characterised.

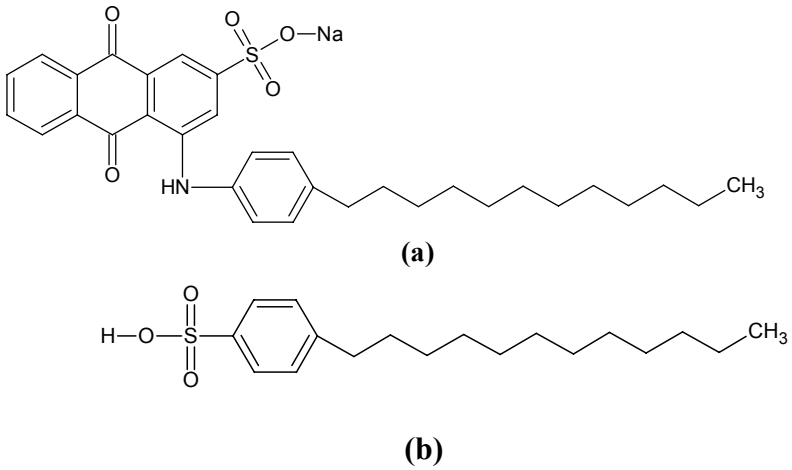

Figure 4.1 Chemical structures of: (a) Carbolan Blue dye, and (b) DBSA

4.2 Experimental

4.2.1 Chemicals

Aniline was purchased from Aldrich and distilled under vacuum and stored at -10 ºC. Ammonium peroxydisulfate (APS), sodium dodecylsulfate (SDS), hydrazine hydrate and sodium hydroxide were purchased from Aldrich and used as received. Dodecylbenzenesulphonic acid (DBSA) was purchased from Tokyo Kasei Kogyo Co., Ltd. Hydrochloric acid was purchased from Asia Pacific Specialty Chemicals Limited. Carbolan Blue (CB), supplied by CSIRO Textile and Fibre Technology Australia, was recrystallised from acetone. All solutions were prepared using Milli-Q water.

4.2.2 Equipment/Instrumentation

A two-electrode cell comprising a Pt mesh auxiliary and a Ag/AgCl reference electrode (3.0 M NaCl) connected to a Hewlett Packard 34401A multimeter was used to monitor the open circuit potential (OCP) throughout the polymerisation (see Chapter 2,

section 2.3.1). The synthesis was carried out in a Julabo controlled temperature bath and a peristaltic pump (Minipuls 2, Gilson) was used to control the rate of oxidant addition. The polymer was dialysed using a 12,000 Mw cut-off cellulose membrane (Sigma). An Eppendorf centrifuge (5702) was used to separate the polymer from solutions. A three-electrode cell comprising of a glassy carbon working electrode, Ag/AgCl reference electrode and a Pt wire auxiliary electrode connected to E-Corder 401 with EDAQ potentiostat was used for all electrochemical experiments. Particle size was determined using TEM (H7000, Hitachi) at 100 KeV. UV-visible spectra were measured using a Shimadzu UV-1601 spectrophotometer. Raman spectra were obtained using 632.8 nm laser excitation (HR800, Jobin Yvon Horiba). Conductivity measurements were performed on pressed pellets of the dried nanodispersion using the four-point probe method. All potentials stated are vs. Ag/AgCl (3.0 M NaCl) reference electrode.

4.2.3 Methods

4.2.3.1 Dye purification

The dye was purified by boiling 1.0 g of CB dye in 1.0 L acetone. The hot CB dye/acetone solution was filtered using No.1 Whatman filter paper to remove the solid impurities. The purified CB dye was recrystallised from the CB dye/acetone filtrate.

4.2.3.2 Polymerisation and purification

The synthesis procedure outlined in Chapter 3, section 3.2.3.1 was used to form PANI-DBSA and PANI-DBSA-CB nanodispersions. The reaction cell was placed in a water bath at 20˚C. The reference and Pt electrodes were connected to the multimeter interfaced to a computer and placed in the reaction cell. The water was stirred and DBSA

was gradually added. After stirring for 15 min, the CB dye was added gradually and the solution was stirred for an additional 30 min. The aniline monomer was then added drop wise to the DBSA/CB solution and stirred for a further 30 min. An aqueous solution of the APS oxidant was then added to the aniline/DBSA/CB solution at a controlled rate using a micro-peristaltic pump. The solution was stirred throughout the course of polymerisation. To prepare the PANI-DBSA dispersion the above procedure was repeated, however with the CB dye omitted. Synthesis conditions are summarised in Table 6.1.

Upon completion of the polymerisation process, the dispersions were placed into dialysis tubing (12000 Mw cut-off) and dialysed against 800 ml of 0.1 M SDS solution for 18 h, at which time the solution was changed and dialysis continued for a further 24 h. After dialysis, the dispersion was removed from the tube and centrifuged at 4400 rpm for 40 min after which the supernatant liquid was removed. The polymer was washed using a solution of 0.2 M SDS and centrifuged at 4400 rpm for 30 min. This process was repeated three times.

4.2.3.3 Characterisation of nanoparticles and dispersions

The dedoping, oxidation and reduction behaviour of the polymer dispersions were characterised using UV-visible spectroscopy. The polymer dispersions were dedoped, oxidised and reduced using NaOH, APS and hydrazine hydrate, respectively. The particle size of the dispersions was measured by transmission electron microscopy (TEM). The polymer films were cast and characterised using Raman spectroscopy. Mass of product from the synthesis was determined from solid content of the nanoparticles obtained based on total volume of the reaction. The polymer was dried in an oven at 40 ºC to constant

weight and pressed into pellets before measuring the conductivity by four point probe technique.

4.3 Results and Discussion

4.3.1 Polymerisation

The critical micelle concentration (CMC) of the CB dye was determined by measuring the conductivity of CB dye solutions of varying concentration. The concentration at which the conductivity increases sharply was taken to be the CMC. The conductivity increased sharply at a concentration of CB dye 1.8 mM, which is similar to the CMC of DBSA (2.0 mM). The latter has been used previously (Chapter 3) to produce PANI nanodispersions.

Attempts were made to prepare PANI nanodispersions from a solution containing CB dye and aniline with the addition of HCl to achieve the required pH (pH = 1). A green product formed, indicating that PANI was produced. However, the product precipitated out of solution immediately. This indicates that CB dye on its own was not a good enough dispersant for PANI, and that DBSA is needed to produce a stable dispersion. It was therefore decided to use DBSA as a micelle stabilising component with the synthesis conditions shown in Table 4.1.

Table 4.1 Synthesis conditions used to prepare PANI nanoparticles.

Polymer	DBSA [M]	Aniline [M]	APS [M]	Synthesis time (min)	CB dye [M]
PANI-DBSA	0.25	0.25	0.25	270	0
PANI-DBSA.CB	0.25	0.25	0.25	270	0.02

The polymerisation process of PANI-DBSA occurred as described in Chapter 3, section 3.3.1.1 for the synthesis of *nano*PANI-DBSA. Upon addition of aniline to the aqueous DBSA solution, the mixture turned milky white and the viscosity of the solution increased, indicating the formation of the aniline.DBSA complex. This complex was formed when the deprotonated negatively charged DBSA anion and positively charged anilinium ion interacted. The polymerisation solution colour sequentially turned to blue, turquoise and emeraldine green upon addition of the oxidant, indicating the formation of emeraldine salt (ES) PANI[8].

For PANI-DBSA-CB synthesis, aniline and DBSA were in stoichiometric excess compared to CB to ensure formation of the aniline.DBSA complex in the presence of the CB dye. When aniline was added to the DBSA.CB solution it was not possible to observe any milky white appearance, due to the intense blue colour of the CB dye. However, viscosity did increase considerably as described above for the PANI-DBSA synthesis in the absence of the CB dye. The polymerisation solution turned to a blue-green colour upon addition of the oxidant indicating the formation of ES PANI.

The open circuit potential (OCP) of the polymer solution was monitored during polymerisation (Figure 4.2). The OCP of the reaction media was measured between a Pt electrode and a Ag/AgCl (3.0 M NaCl) reference electrode. The OCP depends on the concentration of electroactive species at the surface of electrodes and is based on the Nernst equation[9,10] (see more detail in Chapter 2, section 2.3.1).

The OCP of the aniline.DBSA solution prior to addition of the oxidant was 0.4 V and immediately increased to about 0.7 V upon addition of the oxidant. The potential reached the plateau and then decreased (Figure 4.2 a). After about 30 min the polymerisation solution had changed in appearance from white to pale blue. This colour

change was possibly associated with the formation of pernigraniline salt (PS) oligomers of aniline, since it has been reported that the polymerisation of ES PANI proceeds via the initial formation of fully oxidised (PS), which then oxidises aniline and is in turn reduced to the ES form[11]. As polymerisation continued, the solution changed in appearance from blue to the typical emeraldine green colour of ES PANI. This occurred after about 55 min and the OCP began to decrease.

In Figure 4.2 a, the initial OCP of the aniline-DBSA solution containing CB dye was 0.35 V, which is slightly lower than that of aniline-DBSA (0.4 V) (Figure 4.2 b). Upon addition of the oxidant, the potential increased as in the case for PANI-DBSA. However, the potential did not plateau. After approximately 35 min the potential started to decrease; as opposed to 55 min for PANI-DBSA synthesis, indicating that the polymerisation process is facilitated in the presence of CB dye. The polymerisation solution containing the PANI-DBSA-CB reached a steady OCP of about 0.4 V after approximately 120 min of reaction, while the PANI-DBSA dispersion required approximately 200 min to reach equilibrium. The use of micelles has previously been reported to reduce reaction times[12] and this appears to be further facilitated by the presence of CB dye. The maximum potential reached during formation of PANI-DBSA-CB was 0.6 V, compared to 0.68 V during formation of PANI-DBSA, suggesting that the dye mediates the polymerisation process.

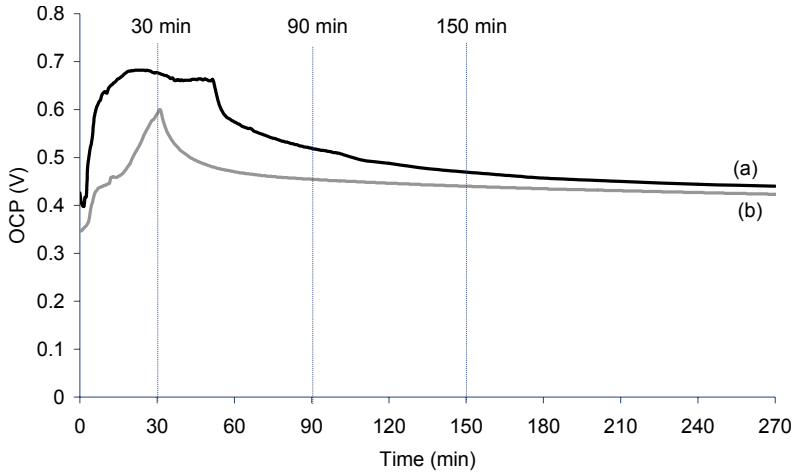

Figure 4.2 Open circuit potential of PANI dispersion during polymerisation of: (a) PANI-DBSA, and (b) PANI-DBSA-CB.

During the polymerisation process aliquots were taken every 30 min and UV-visible spectra obtained (Figure 4.3). Similar trends in the UV-visible spectra of polymerisation solutions during PANI synthesis to those observed in this study have been reported previously[8,13]. After 30 min of synthesis (Figure 4.3 a) three distinct peaks at 356 nm, 430 nm and 715 nm were observed. The first two peaks correspond to π-π^* and π-polaron bands, respectively. The absorption band at 715 nm lies between the characteristic peak of PS PANI (690nm) and the polaron band of ES PANI (about 800 nm), suggesting the presence of PANI nanoparticles in both the PS and ES oxidation states[8]. The intensity of each peak increased as the polymerisation process progressed. As the polymerisation process continued the absorption band at 715 nm shifted to 765 nm, indicating that the ES PANI dominated; while the ratio of absorption intensity of the 430 nm to 356 nm bands was higher, indicating a higher degree of doping[14]. There was no evidence of peak shift or any significant increase in intensity between 150 min and 260 min synthesis time (Figure 4.3 b and 4.3 c), suggesting the polymerisation was almost completed after 150 min.

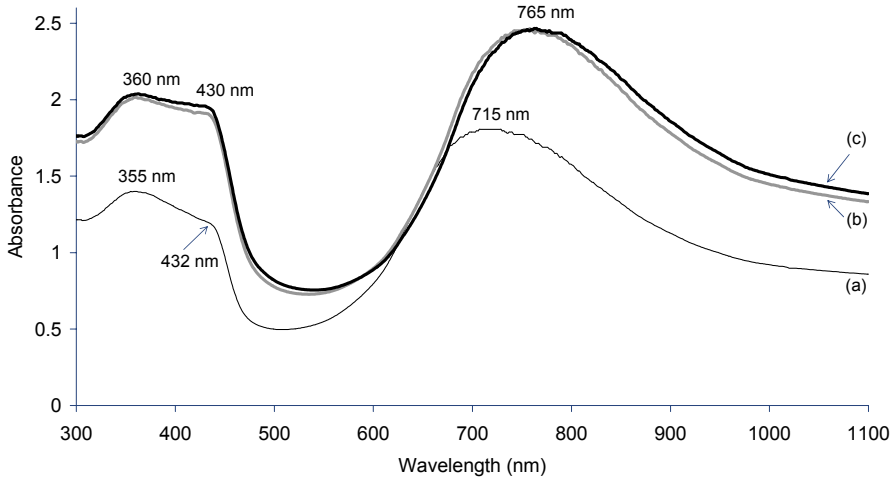

Figure 4.3 UV-visible absorption spectra taken during polymerisation to obtain PANI-DBSA nanoparticles: (a) 30 min, (b) 150 min, and (c) 260 min post addition of APS oxidant.

Aliquots of the polymerisation solution were also taken during the synthesis of the PANI-DBSA-CB and UV-visible spectra obtained (Figure 4.4). Similar spectral changes to those observed above for PANI-DBSA (Figure 4.3) were observed for PANI-DBSA-CB (Figure 4.4). However, due to the blue colour of CB dye being present, the solution colour change could not be observed easily. The absorption peaks for PANI-DBSA-CB were all red shifted with respect to PANI-DBSA (see section 4.3.2.2 for discussion). The fact that the UV-visible spectra for the PANI-DBSA-CB dispersion showed similar features to the PANI-DBSA dispersion suggests that the presence of the CB dye does not hinder the formation of PANI.

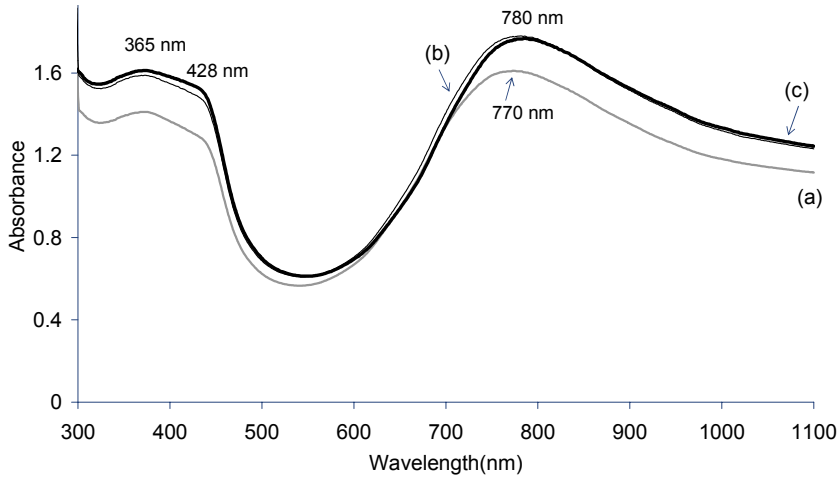

Figure 4.4 UV-visible absorption spectra taken during polymerisation to obtain PANI-DBSA-CB nanoparticles: (a) 30 min, (b) 150 min, and (c) 260 min post addition of APS oxidant.

4.3.2 Characterisations of nanoparticles and dispersions

Upon completion of polymerisation, the product dispersions were purified as outlined in the experimental section (4.2.3.2) and characterised using various techniques as described below.

4.3.2.1 Transmission electron microscopy (TEM), conductivity and mass of product

Transmission electron micrographs of the PANI-DBSA and PANI-DBSA-CB nanoparticles were obtained (Figure 4.5 a and 4.5 b, respectively). The average (n = 100) size of the spherical PANI-DBSA particles was 35 ± 9 nm, while for PANI-DBSA-CB the average (n = 150) size of the spherical particles was 60 ± 16 nm. In both PANI-DBSA and PANI-DBSA-CB the distribution of particles sizes was not Gaussian, with the largest particles observed being approximately 250 nm and 280 nm, respectively. It is possible that these large particles are in fact aggregates of the smaller particles that coagulated together during the drying of the polymer films for particle size measurements using TEM. The

presence of the CB dye resulted in an increase in the average particle size, possibly due to its incorporation into the PANI-DBSA micelle structure during synthesis.

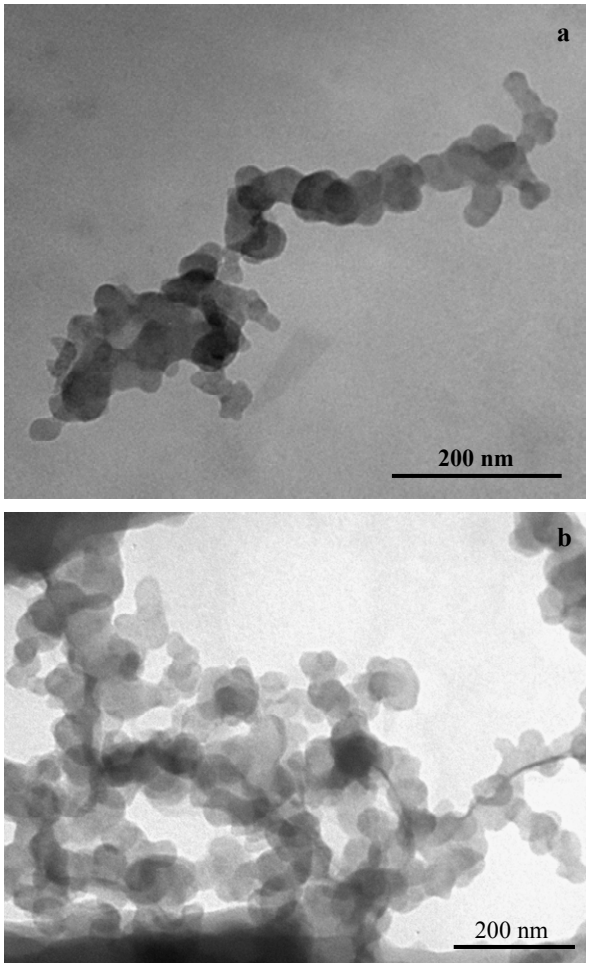

Figure 4.5 Transmission electron micrographs of: (a) PANI-DBSA, and (b) PANI-DBSA-CB nanodispersions. Images were obtained at 100 keV at a magnification of 200 k.

Conductivity of the PANI-DBSA-CB nanoparticles was in the same order of magnitude as the PANI-DBSA nanoparticles. The conductivity of the PANI-DBSA nanoparticles was lower than the *nano*PANI-DBSA produced in Chapter 3, which is possibly due to the different synthesis conditions. Characterisation data are summarised in Table 4.2.

Table 4.2 Characterisation data for PANI-DBSA-CB nanoparticles.

Sample	Mass of product (g of dried polymer/L)	Particle size by TEM (nm)	Conductivity (S/cm)
PANI-DBSA	50	35 ± 9	0.45 ± 0.11
PANI-DBSA-CB	61	60 ± 16	0.74 ± 0.19

4.3.2.2 pH switching

In the UV-visible absorption spectrum of the purified PANI-DBSA (Figure 4.6 b), the 810 nm polaron band is red shifted by 45 nm compared to the corresponding band before purification (see Figure 4.3) suggesting a longer conjugation length for the PANI chain in the former case[15]. Similarly, the high wavelength polaron band is red shift by 70 nm in the case of PANI-DBSA-CB after purification. The UV-visible absorption spectra showed PANI to be in the conducting ES form for both dispersions (Figure 4.6). PANI-DBSA-CB (Figure 4.6 a) showed a polaron band at 850 nm and π*- polaron and π-π* bands at 430 nm and 360 nm, respectively. These bands all exhibited red-shifts with respect to the PANI-DBSA dispersions (Figure 4.6 b). This red shift may be attributed to the presence of the CB dye in the PANI-DBSA-CB dispersion.

Upon base treatment of the ES PANI nanodispersions with 0.05 M NaOH, both were dedoped as evidenced by the rapid disappearance of polaron bands and shifting of the original π-π* band to lower wavelengths. In addition, strong bands appeared at 572 nm for PANI-DBSA and at 620 nm for PANI-DBSA-CB which may be assigned to the exciton band of the emeraldine base (EB) form in each case[16]. The exciton band of the PANI-DBSA-CB dispersion appeared at longer wavelengths (620 nm) and was very broad compared to that of PANI-DBSA, probably due to the presence of the CB dye. The UV-

visible spectra of the CB dye (Figure 4.6 c) showed that upon base treatment an absorption band appears at 700 nm for the deprotonated dye. It is likely that this band causes the exciton band of the EB form of PANI-DBSA-CB to appear broader.

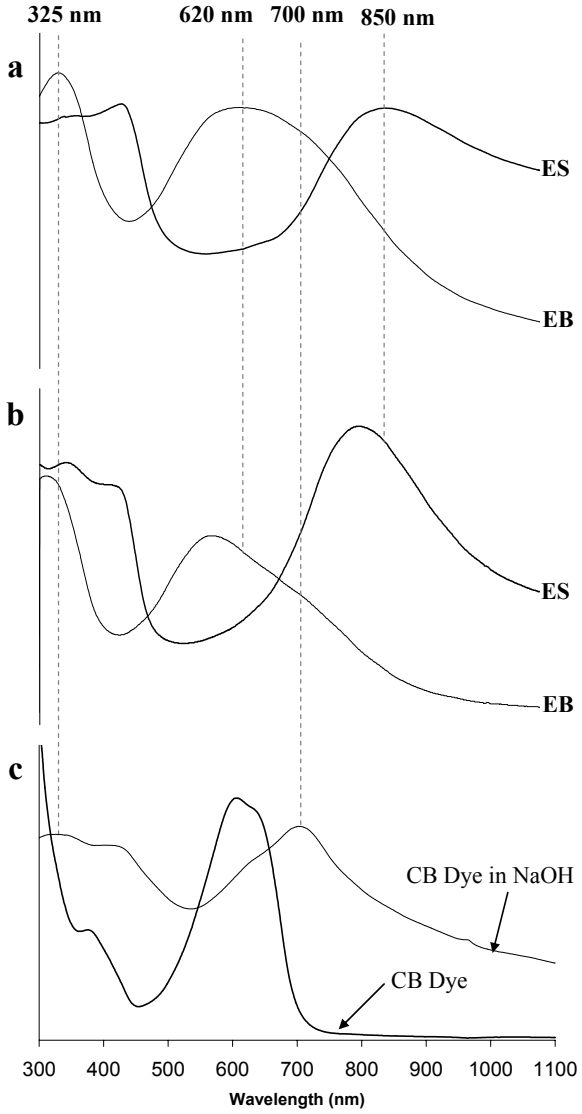

Figure 4.6 UV-visible spectra of: (a) PANI-DBSA-CB (0.14 g/L) in the ES and EB form, (b) PANI-DBSA (0.29 g/L) in the ES and EB form, and (c) Carbolan Blue dye (0.01%) before and after treating with 0.05 M NaOH.

4.3.2.3 Redox switching

UV-visible spectra of the PANI-DBSA-CB and PANI-DBSA nanodispersions following oxidation for 10 min with 0.07 M APS are shown in Figure 4.7 a and 4.7 b, respectively. A band at 615 nm appeared after oxidation of PANI-DBSA-CB (Figure 4.7 a), which is at a shorter wavelength than that observed upon oxidation of PANI-DBSA (650 nm) (Figure 4.6 b). These absorption bands observed upon oxidation of the PANI-DBSA and PANI-DBSA-CB dispersion are consistent with a mixture of PS (λ_{max} 690 nm) and perniganiline base (PB) (λ_{max} 540 nm)[17]. The absorption peak at 615 nm observed after oxidation of PANI-DBSA-CB coincides with the absorbance maximum of CB dye after treatment with APS (Figure 4.7 c). There were no observed changes to the absorption spectrum of CB before or after treated with APS.

Reduction of PANI-DBSA-CB was performed using 4.0 M hydrazine, with the effect on their UV-visible spectra shown in Figure 4.8. The polaron and π-polaron peaks disappeared and the π-π* peak intensities increased. The λ_{max} observed at 330-350 nm are consistent with reduction of both types of nanodispersions to the leucomeraldine base (LB) form. A weak peak at 620 nm also appeared after reduction of PANI-DBSA-CB (Figure 4.8 a). This additional peak was attributed to the presence of the CB dye since this peak is also present in the CB dye spectrum (Figure 4.8 c).

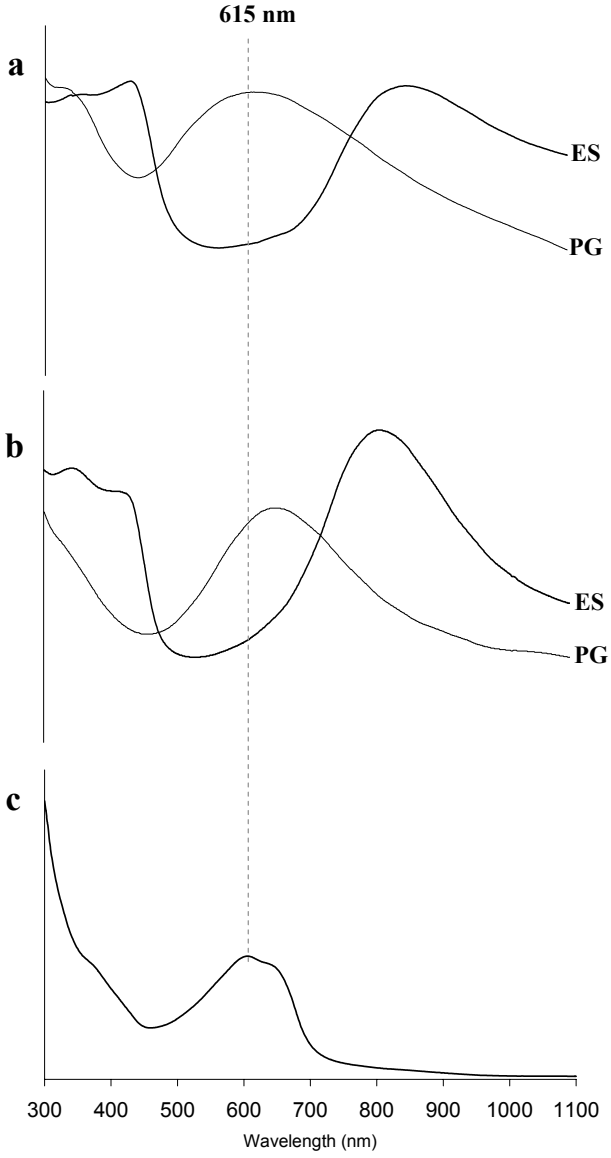

Figure 4.7 UV-visible spectra of: (a) PANI-DBSA-CB (0.14 g/L) in the ES and perniganiline (PG) form, (b) PANI-DBSA (0.29 g/L) in the ES and PG form, and (c) Carbolan Blue dye after treatment with 0.07 M APS.

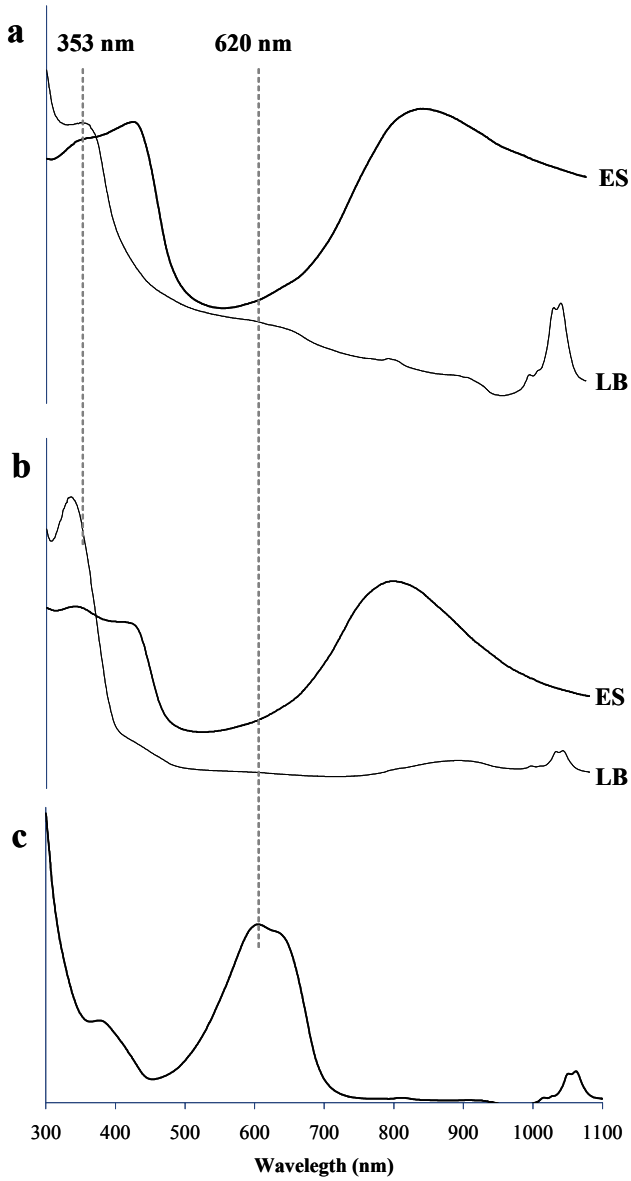

Figure 4.8 UV-visible spectra of: (a) PANI-DBSA-CB (0.14 g/L) in the ES and LB form, (b) PANI-DBSA (0.29 g/L) in the ES and LB form, and (c) Carbolan Blue dye after treatment with 4.0 M hydrazine.

Photographs of the reduced polymer nanodispersions (Figure 4.9) indicated that upon reduction of the PANI-DBSA-CB nanodispersion, the blue colour of the CB dye becomes more apparent. This was likely due to the pale yellow of the LB form, which allowed the blue colour of the CB dye to dominate.

To determine whether the CB dye was incorporated into the PANI dispersion, the LB dispersions of both PANI-DBSA and PANI-DBSA-CB were centrifuged at 4400 rpm for 30 min (Figure 4.9 a′ and 4.9 b′). Both solutions separated to produce a clear supernatant and a solid at the bottom of the centrifuge tube indicating that the CB dye was incorporated into PANI as it was 'spun down' with the polymer. When a solution containing only the CB dye was centrifuged no such separation was observed confirming incorporation of CB dye into the PANI nanoparticles.

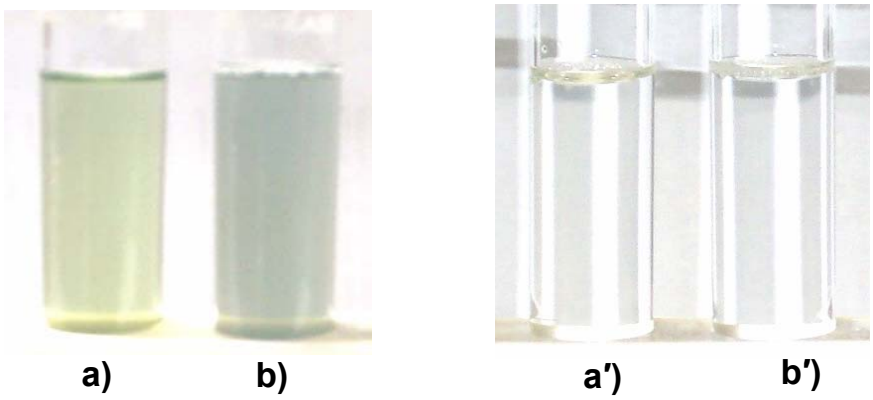

Figure 4.9 Photographs of: (a) reduced PANI-DBSA, and (b) reduced PANI-DBSA-CB prior to centrifuging at 4400 rpm for 30 min. Images (a′) and (b′) represent the same samples after centrifugation.

4.3.2.4 Raman Spectroscopy

Raman spectra of dried powders of PANI-DBSA and PANI-DBSA-CB nanoparticles as well as CB dye were obtained (Figure 4.10). In the spectrum of the PANI-DBSA (Figure 4.10 a), the C=C stretching of the quinoid units appeared at 1589 cm^{-1}, which is characteristic of semiquinone rings. The band at 1520 cm^{-1} is associated with the C-C stretching of the phenyl units, whist the C=N stretching of the quinoid ring was quite strong at 1490 cm^{-1}. The 1324 cm^{-1} and 1344 cm^{-1} bands correspond to $C–N^{\bullet+}$ stretching modes of delocalised polaronic charge carriers. The broad band at 1255 cm^{-1} can be

assigned to the C–N stretching mode of the polaronic units. Aromatic C–H bending deformation was observed at 1170 cm^{-1}, while the broad bands at 812 and 872 cm^{-1} are attributed to quinoid and benzenoid ring deformation, respectively. The band positions and assignments for PANI are summarised in Table 4.3.

The Raman spectrum of PANI-DBSA-CB (Figure 4.10 b) showed combined spectral features from both the PANI-DBSA and CB dye (Figure 4.10 c). The stretching modes of delocalised polaronic charge carriers (1324 cm^{-1} and 1344 cm^{-1}) were observed to combine into one peak centered at 1327 cm^{-1}, indicating a reduction in polaronic charge carriers possibly due to distortion of the PANI conjugated backbone by the CB dye. The band at 1635 cm^{-1} for PANI-DBSA-CB is attributed to the presence of the CB dye, which shows a band at 1644 cm^{-1}. Additional evidence for the incorporation of the CB dye into PANI-DBSA is provided by the bands at 926 cm^{-1}, 1030 cm^{-1} and 1412 cm^{-1} for PANI-DBSA-CB, which are attributed to the CB dye as these bands are present in the spectrum of the CB dye at 925 cm^{-1}, 1038 cm^{-1} and 1412 cm^{-1} (Figure 4.10 c) and are not observed in the spectrum of PANI-DBSA (Figure 4.10 a).

Table 4.3 Assignments of the Raman bands using 632.8 nm excitation line.

Assignments	**PANI-HCSA (cm^{-1})[18-20]**	**PANI-DBSA (cm^{-1})**	**PANI-DBSA-CB (cm^{-1})**
C-H out of plane bending (Q)	811	812	816
C-H in-plane bending (B)	874	872	874
C-H in-plane bending (Q)	1164	-	1164
C-H in-plane bending (B)	1170	1170	-
$C\text{-}N^{+\bullet}$ stretching (B)	1255	1255	1267
$C\text{-}N^{+\bullet}$ delocalised polaronic charge carriers	1318	1324	1327
$C\text{-}N^{+\bullet}$ delocalised polaronic charge carriers	1341	1344	
C-C stretching + C-H bending	1488	1490	1490
N-H bending	1520	1520	1523
C=C stretching (Q)	1584	1589	1590
C-C stretching (B)	1622	about 1620	1635

The benzenoid, quinoid units are denoted by B and Q, respectively.

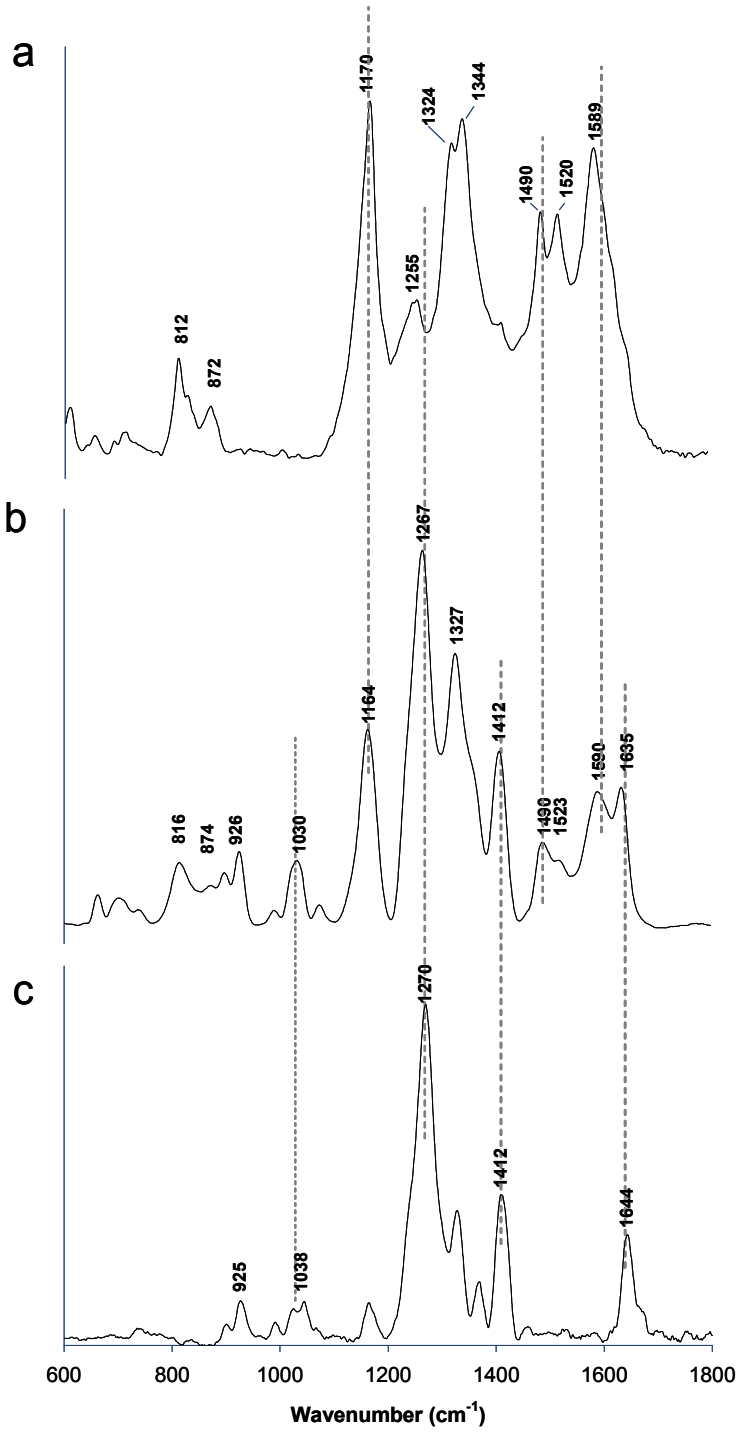

Figure 4.10 Raman spectra of: (a) PANI-DBSA in ES, (b) PANI-DBSA.CB in ES form, and (c) CB dye. Spectra recorded using 632.8 nm excitation.

The Raman spectral region between 1584 cm^{-1} and 1622 cm^{-1} corresponds to C=C and C-C in-plane stretching, respectively[21], corresponding to the aromatic backbone of PANI. To investigate the extent of interaction between the incorporated dye and PANI-DBSA, Raman spectra were recorded for PANI-DBSA, PANI-DBSA-CB and CB dye in this region using a 950 lines/inch grating with a sensitivity of 0.6 cm^{-1} (Figure 4.11). Considering Figure 4.11 (ii), the C=C stretching of the quinoid unit for ES PANI-DBSA-CB was shifted by 7.5 cm^{-1} to a higher wavenumber compared to ES PANI-DBSA (Figure 4.11 (iii)). The shift was towards the prominent CB dye peak at 1644.6 cm^{-1} (Figure 4.11 (i)), indicating a significant interaction between the PANI backbone and the CB dye.

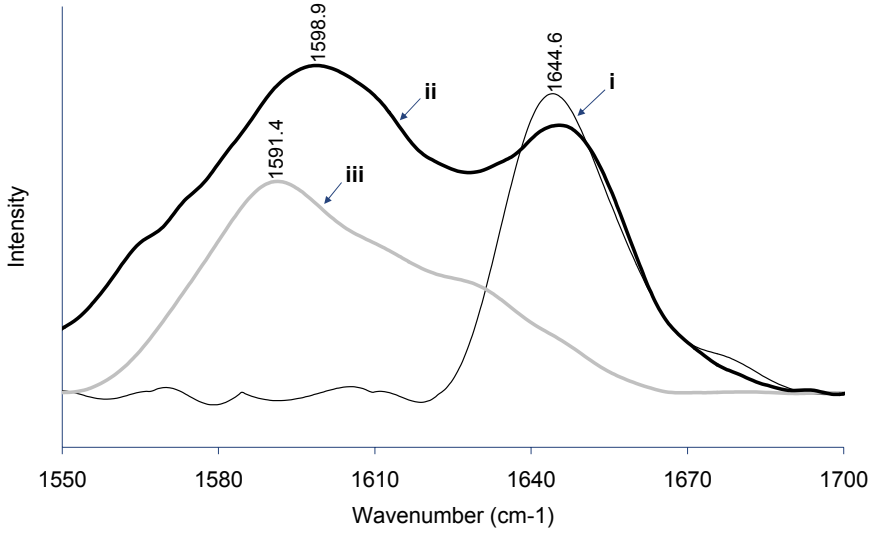

Figure 4.11 Raman spectra of PANI dispersions in the ES form: (i) CB dye, (ii) PANI-DBSA-CB, and (iii) PANI-DBSA. Spectra recorded using 632.8 nm excitation.

4.3.2.5 Cyclic Voltammetry (CV)

Cyclic voltammetry was performed on the as-synthesised PANI-DBSA (ES) and PANI-DBSA-CB (ES) nanodispersions using a glassy carbon electrode as the working electrode. The cyclic voltammogram of PANI-DBSA (Figure 4.12 a) is typical for ES

PANI[5], with the main peaks A and B corresponding to the transformation of LB to ES and ES to PS, respectively. On the reverse scan, peaks B′ and A′ correspond to the conversion of PS to ES and ES to LB, respectively. The presence of small middle peaks C/C′ is associated with the formation of *p*-benzoquinone and hydroquinone[22] as side products upon excursion to the potentials necessary to observe the B/B′ couple[23].

The current magnitude of the PANI-DBSA nanodispersion (Figure 4.12 a) was lower than for the *nano*PANI-DBSA in Chapter 3 (Figure 3.8 b) which is probably due to lower concentration of the PANI-DBSA in the dispersion; hence lower mass of polymer deposited on the electrode. A different potential scan rate was also used.

The CV of PANI-DBSA-CB (Figure 4.12 b) showed similar features to the CV of PANI-DBSA, which indicates that the presence of CB dye does not hinder the electroactivity of the PANI-DBSA nanodispersion.

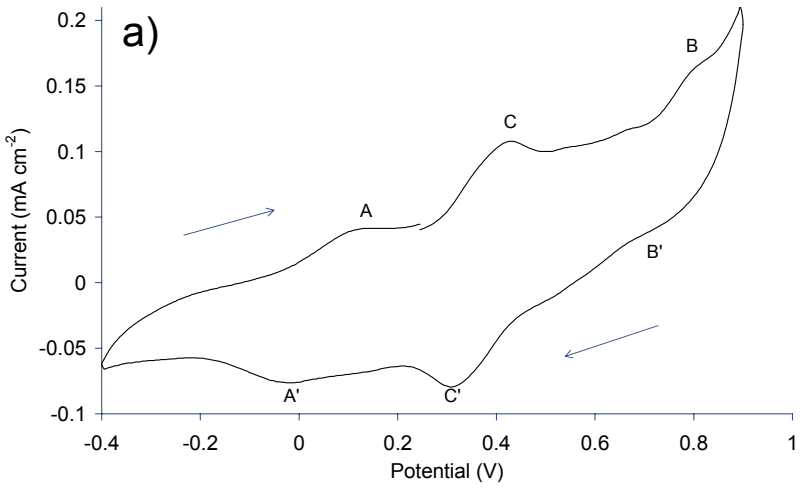

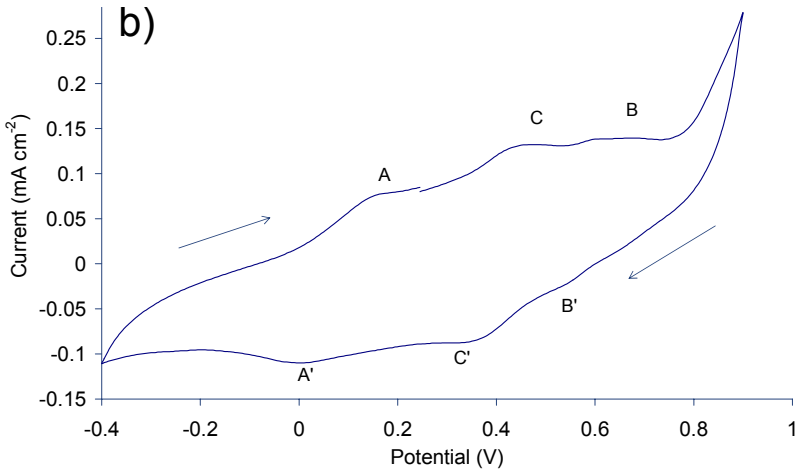

Figure 4.12 Cyclic voltammograms of: (a) PANI-DBSA-CB dispersions (1.40 % w/v) and b) PANI-DBSA dispersions (1.31% w/v). The scan was performed on a GC electrode with a scan rate of 50 mV/s (arrows show the direction of the scan). $E_{initial}$ is 0.25 V and all potentials are vs. Ag/AgCl (3.0 M NaCl).

4.3.2.6 Stability test

The electronic property of the PANI-DBSA-CB dispersion was stable for up to 8 months, as evidenced from the similarity of the UV-visible spectrum obtained in 1 week (Figure 4.13). However, the electroactivity of the dispersion started to decrease after storage for 6 months and significantly changed after 8 months (Figure 4.14). Besides the decrease in current magnitude, the redox couple B/B′ (indicating the transition between ES and PS) has almost disappeared after 8 months. The redox couple at around 0.5 V was more pronounced than the other two characteristic peaks, indicating higher content of degradation products[22].

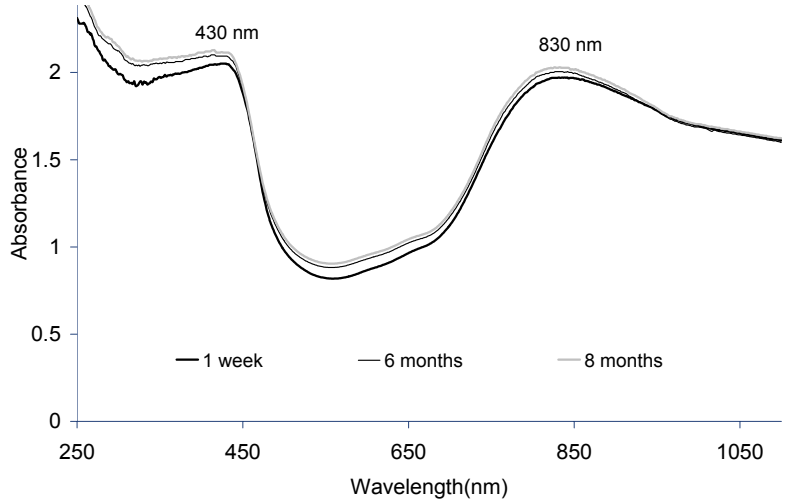

Figure 4.13 UV-visible spectra of PANI-DBSA-CB (0.03% w/v) after storage at room temperature.

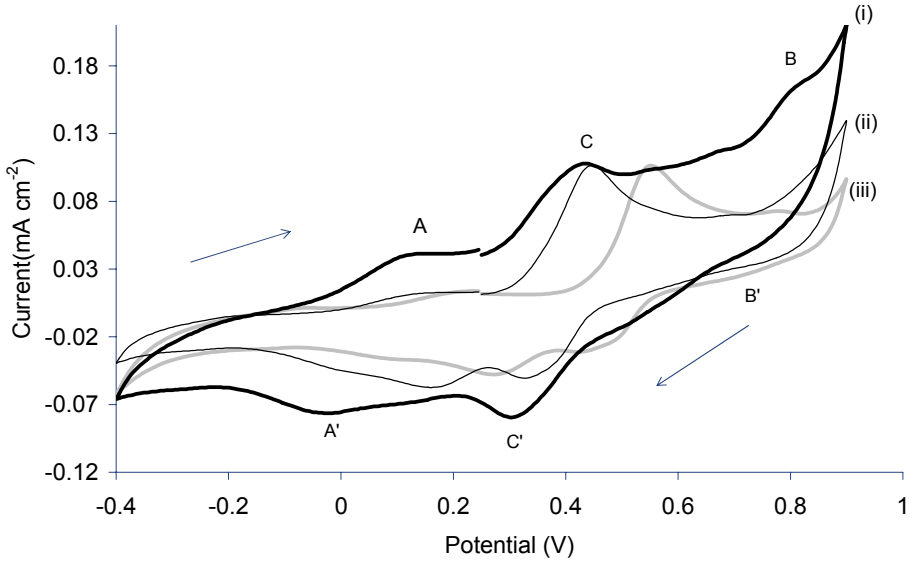

Figure 4.14 Cyclic voltammogram (5th scan) of PANI-DBSA-CB dispersions (1.4% w/v) after: (i) 1 week, (ii) 6 months, and (iii) 8 months. The scan was performed on a glassy carbon working electrode with a scan rate of 100 mV/s, (arrows show the direction of the scan). $E_{initial}$ is 0.25 V and all potentials are vs. Ag/AgCl (3.0 M NaCl).

4.4 Conclusions

The successful incorporation of the CB dye into PANI is achieved using emulsion polymerisation. The presence of the CB dye in PANI nanoparticles does not hinder their dedoping and redox switching behaviour. UV-visible spectra of the PANI-DBSA-CB nanodispersions show some different features from those observed for the PANI-DBSA nanodispersions, indicating the presence of the dye in PANI. The blue colour that appears for the reduced PANI-DBSA-CB nanodispersions also indicates the incorporation of the CB dye into PANI. When the reduced PANI-DBSA-CB is centrifuged a clear supernatant solution is observed, indicating that the CB dye is incorporated into PANI nanoparticles, i.e. it is spun down with the polymer.

Raman spectra show a shift of the C=C stretching of quinoid units of PANI-DBSA-CB nanoparticles towards the peak of the CB dye. This also suggests a significant interaction between the PANI backbone and the CB dye. As confirmed by TEM, the PANI-DBSA-CB nanoparticles still retain a spherical shape. However, the incorporation of the CB dye results in an increase in the average particle size. The electronic property of the PANI-DBSA-CB nanoparticles is stable for up to 8 months as observed using UV-visible spectroscopy while electrochemical property is stable for up to 6 months as observed by CV.

The PANI-DBSA-CB nanoparticles can be a good candidate for electrochromic devices since the LB form shows a blue colour which is different from the pale yellow of LB PANI-DBSA. It is possible to vary the colour of the LB PANI by incorporating different dyes into PANI. Also it may be possible to incorporate other functional groups into PANI using this procedure.

4.5 References

1. Dahman, S.J., *Polymer Engineering and Science*, 1999. **39**(11): p. 2181-2188.
2. Han, M.G., Cho, S.K., Oh, S.G., and Im, S.S., *Synthetic Metals*, 2002. **126**(1): p. 53-60.
3. Haba, Y., Segal, E., Narkis, M., Titelman, G.I., and Siegmann, A., *Synthetic Metals*, 2000. **110**(3): p. 189-193.
4. Henderson, A.M.J., Saunders, J.M., Mrkic, J., Kent, P., Gore, J., and Saunders, B.R., *Journal of Materials Chemistry*: p. 3037-3042.
5. Wallace, G.G., Spinks, G.M., Kane-Maguire, L.A.P., and Teasdale, P.R., *Conductive electroactive polymers : intelligent materials systems*. 2nd ed. 2002, Boca Raton, FL: CRC Press. , and references cited therein.
6. Yoshino, K., Tada, K., Yoshimoto, K., Yoshida, M., Kawai, T., Zakhidov, A., Hamaguchi, M., and Araki, H., *Synthetic Metals*, 1996. **78**(3): p. 301-312.
7. Feng, W., Fujii, A., Lee, S., Wu, H.C., and Yoshino, K., *Synthetic Metals*, 2001: p. 1595-1596.
8. Haba, Y., Segal, E., Narkis, M., Titelman, G.I., and Siegmann, A., *Synthetic Metals*, 1999. **106**(1): p. 59-66.
9. Wei, Y., Hsueh, K.F., and Jang, G.-W., *Polymer*, 1994. **35**(16): p. 3572-3575, and references cited therein.
10. Delahay, P., *New instrumental methods in electrochemistry : theory, instrumentation, and applications to analytical and physical chemistry*. 1954, New York: Interscience. pp.9-10.
11. MacDiarmid, A.G., Manohar, S.K., Masters, J.G., Sun, Y., Weiss, H., and Epstein, A.J., *Synthetic Metals*, 1991. **41**(1-2): p. 621-626.
12. Yu, L., Lee, J.I., Shin, K.W., Park, C.E., and Holze, R., *Journal of Applied Polymer Science*, 2003. **88**(6): p. 1550-1555.
13. Stejskal, J., Kratochvil, P., and Radhakrishnan, N., *Synthetic Metals*, 1993. **61**(3): p. 225-231.
14. Kim, B.J., Oh, S.G., Han, M.G., and Im, S.S., *Synthetic Metals*, 2001. **122**(2): p. 297-304.
15. Norris, I.D., Kane-Maguire, L.A.P., and Wallace, G.G., *Macromolecules*, 2000. **33**(9): p. 3237-3243.
16. Abd-Elwahed, A. and Holze, R., *Synthetic Metals*, 2002. **131**(1-3): p. 61-70.
17. Stejskal, J., Kratochvil, P., and Jenkins, A.D., *COLLECTION OF CZECHOSLOVAK CHEMICAL COMMUNICATIONS*, 1995. **60**: p. 1747-1755.
18. da Silva, J.E.P., de Faria, D.L.A., de Torresi, S.I.C., and Temperini, M.L.A., *Macromolecules*, 2000. **33**(8): p. 3077-3083.
19. Cochet, M., Louarn, G., Quillard, S., Buisson, J.P., and Lefrant, S., *Journal of Raman Spectroscopy*, 2000. **31**(12): p. 1041-1049.
20. Cochet, M., Buisson, J.P., Wery, J., Jonusauskas, G., Faulques, E., and Lefrant, S., *Synthetic Metals*, 2001. **119**(1-3): p. 389-390.
21. Zhang, J.X., Liu, C., and Shi, G.Q., *Journal of Applied Polymer Science*, 2005. **96**(3): p. 732-739.
22. Chen, W.C., Wen, T.C., and Gopalan, A., *Synthetic Metals*, 2002. **128**(2): p. 179-189.

23. Mirmohseni, A. and Wallace, G.G., *Polymer*, 2003. **44**(12): p. 3523-3528.

5.1 Introduction

The exploitation of PPy in commercial applications has been limited due to it being insoluble and infusible[1]. For this reason much effort has been spent improving the processability of this polymer by developing new polymer dispersions using surfactant[2,3] and steric stabiliser[4-16]. A result of these polymerisation routes is the polymer dispersions containing PPy nanoparticles which are more processable. Poly (vinyl alcohol) (PVA) has proved an effective steric stabiliser in previous studies[6-11]; hence it was used to produce PPy nanodispersions in this work.

Indeed it is the properties of these conducting polymer nanodomains embedded in a nonconducting dispersant that ultimately determine the optical, electronic and physical properties of such nanocomposites[17]. It has been shown that as the nanoparticle size decreases, conductivity increases due to an increase in the degree of doping and crystallinity[18].

Surfactants play an important role in the synthesis of ICP nanodispersions. In Chapter 3 and 4, polyaniline (PANI) nanodispersions were successfully synthesised using emulsion polymerisation. The surfactant functions as the stabiliser preventing the agglomeration of the polymer. The resultant polymer has nanometre dimensions as observed by TEM. However, the surfactant was not desirable in the ink-jet printing application which is the potential application interested for this project. Although it helps wetting the substrate surface and the larger coverage area could be obtained, too high surfactant concentration may cause the failure of the polymer adherence to the substrate and too low surface tension. Therefore surfactant was minimised in this work.

In the course of this work we have investigated various synthesis conditions to produce conducting PPy nanodispersions, which can be used in the concentrated form in ink jet printing applications (see Chapter 9). The polymer concentration needs to be high whereas the particle size must be small in order to ensure a uniform continuous print. The goal of this work is to achieve the PPy nanodispersions with particle size at least in the same order of magnitude to the typical particle size of conventional pigments in ink-jet inks (100-400 nm)[19]. PPy was synthesised using chemical oxidation with PVA as the steric stabiliser. Sodium dodecyl sulfate (SDS) was also used as the dopant and surfactant. The effects of temperature, PVA and SDS concentration were also studied. The dispersions were characterised by UV-visible spectroscopy, cyclic voltammetry (CV), Raman spectroscopy, transmission electron microscopy (TEM), dynamic light scattering (DLS) and conductivity measurement. For the ease of comparison between batch to batch, the particle size in this chapter was reported from % Number distribution which indicate the percentage of the particular size of the polymer in solution (see more detail in Chapter 2, section 2.2.3).

5.2 Experimental

5.2.1 Chemicals

Pyrrole (Merck) was distilled prior to use and stored at –12^{o}C when not in use. The oxidant ferric chloride ($FeCl_3$), sodium dodecylsulfate (SDS) and polyvinyl alcohol (PVA Mw 31k-50k) were obtained from Sigma-Aldrich and used as received.

5.2.2 Equipment/Instrumentation

The UV-visible spectrum of the PPy-DS-PVA nanodispersion was recorded using a Shimadzu UV-1601 UV-visible spectrophotometer. Raman spectra were obtained using an HR800, Jobin Yvon Horiba with a laser wavelength = 632.8 nm. Transmission electron microscopy (TEM) was carried out using a Hitachi H7000 TEM at 100 KeV. Particle size was determined using dynamic light scattering (Malvern Nano-ZS Zetasizer) on concentrated dispersions using back scattered light (8^o angle). An Eppendorf centrifuge (5702) was used to separate the polymer from solution.

Conductivity measurements were performed on cast films or pressed pellets of the dried nanodispersion using the four-point probe method. Cyclic voltammetry (CV) was carried out in a three-electrode cell using a glassy carbon working electrode with a platinum mesh and Ag/AgCl (3.0 M NaCl) as auxiliary and reference electrodes, respectively.

A two-electrode cell comprising a platinum mesh auxiliary and an Ag/AgCl reference electrode (3.0 M NaCl) connected to a Hewlett Packard 34401A multimeter was used to monitor the open circuit potential (OCP) throughout the polymerisation (see Chapter 2, section 2.3.1).

Residual pyrrole was determined using reverse phase HPLC with a Waters Bondapak C_{18} column and a Linear™ UVIS 200 UV detector (λ_{max} = 258 nm).

5.2.3 Methods

5.2.3.1 Polymerisation and purification

The oxidant ($FeCl_3$) to monomer (Py) molar ratio was kept constant at 1:1 and polymerisation was carried out in a thermostated bath. Varying quantities of SDS were added to 100 ml of water in a round-bottomed flask. Various concentrations of PVA were

then added and mixed under mechanical stirring for 30 min. Pyrrole monomer was added to the 100 ml PVA/SDS solution and stirred for 1 h followed by the addition of $FeCl_3$ solution at a constant rate of 1 ml/min. The OCP was recorded during synthesis using a two electrode set up and a Hewlett Packard multi meter. The polymerisation was allowed to proceed until a constant OCP was achieved.

Purification of the polymerised dispersion was achieved by dialysing against Milli-Q water using a 12,000 Mw cut-off dialysis membrane (Sigma) for 48 h with the SDS solution being changed every 18 h. After dialysis, the dispersion was centrifuged at 4,400 rpm for 10 min. The supernatant was discarded and approximately 100 ml of Milli-Q water was added to the remaining solid. The water/solid mixture was shaken to redisperse the solid, followed by centrifuging at 4,400 rpm for 10 min. This was repeated 3 times to remove excess SDS and PVA.

5.2.3.2 Characterisation of PPy nanodispersions

The polymer dispersions were characterised using UV-visible and Raman spectroscopy. The polymer was dried in an oven at 40˚C until constant weight and pressed into pellets before measuring the conductivity by the four point probe technique. The particle size of the concentrated dispersions was measured using the DLS method. Low concentration dispersions were investigated to determine particle size and morphology using TEM. Mass of product from the syntheses was determined from solid content of the nanoparticles obtained based on total volume of the reaction media.

5.2.3.3 Stability test of PPy-DS-PVA nanodispersions

The PPy-DS-PVA dispersions were left standing at room temperature for 15 months with aliquots of the supernatant carefully removed for the particle size analysis using DLS.

5.3 Results and Discussion

5.3.1 PPy-DS polymerisation

The reaction condition used is summarised in Table 5.1. The solution containing monomer and SDS was colourless. Upon addition of the oxidant, the solution instantly changed to black indicating the PPy formation[4]. Residual monomer evaluation using HPLC showed a conversion efficiency of 86.8%. Considering the molar ratio of one-electron oxidant $FeCl_3$ to Py = 2.3:1 usually employed for oxidation of Py[20,21], the conversion efficiency should reach only about 44% in this work as the molar ratio of $FeCl_3$:Py = 1:1 was used. The increase in polymerisation efficiency was possibly due to the oxygen was acting as an additional oxidant as the polymerisation was performed in an open system.

Table 5.1 Dispersion polymerisation conditions used for the synthesis of PPy-DS. Concentrations are stated as final concentrations in the reaction vessel.

Sample	Pyrrole (M)	SDS (M)	$FeCl_3$ (M)	Temp (ºC)	Time (min)
PPy-DS	0.05	0.05	0.05	25.0	150

The OCP is based on the Nernst equation which relates the concentration of electroactive species at the electrode surface as outlined in Chapter 2, section 2.3.1. In this study, the OCP was monitored during polymerisation (Figure 5.1) with the reaction reaches a steady OCP of about 0.25 V after approximately 90 min of reaction. At this point, it is

assumed that the concentration of reactants and products at the electrode surface have reached equilibrium. The maximum OCP monitored was 0.45 V which is similar to the potential observed for electrochemical oxidation of Py monomer in the presence of SDS[22].

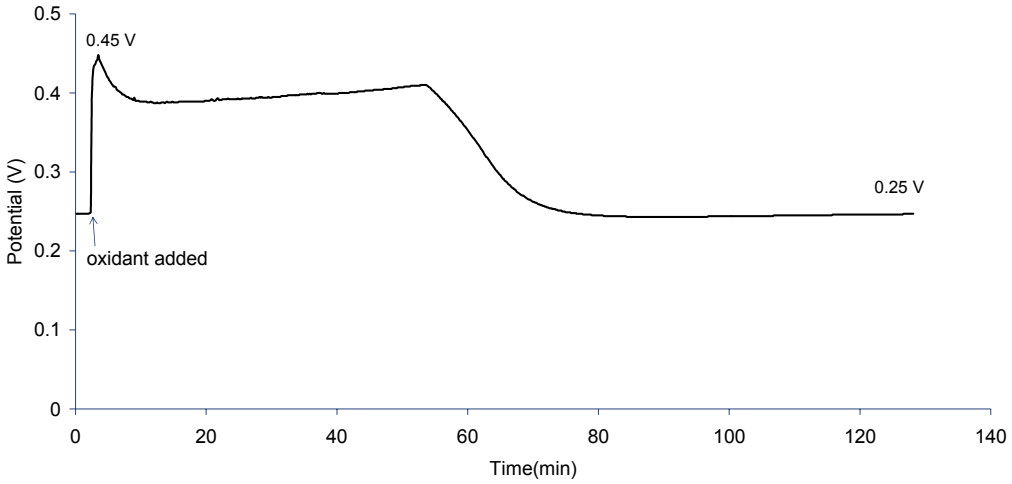

Figure 5.1 The OCP profile during synthesis of PPy-DS (0.05M) at 25°C. The potentials are vs. Ag/AgCl (3.0 M NaCl).

5.3.2 PPy-DS Characterisation

5.3.2.1 UV-visible spectroscopy

On completion of the polymerisation the PPy-DS dispersions were purified as outlined in the experimental section (5.2.3). The polymer was redispersed in water and UV-visible spectrum obtained (Figure 5.2). The absorbance maximum at 450 nm is assigned as the π-π* transition while the absorbance at wavelengths greater than 600 nm is assigned to the localised polaron band indicating oxidised PPy[23].

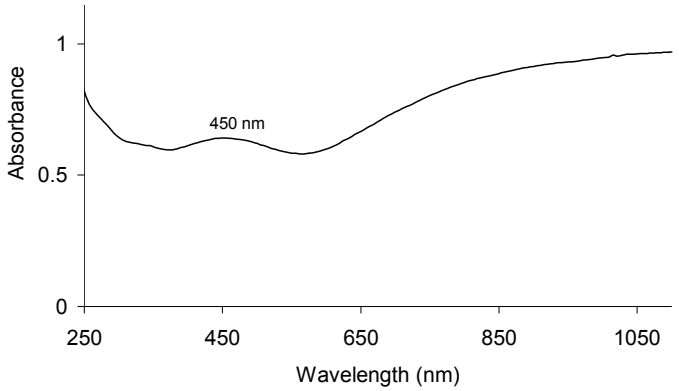

Figure 5.2 UV-visible spectrum obtained for PPy-DS dispersion (0.23g/L) in the conducting form.

5.3.2.2 Raman spectroscopy

Raman spectrum of dried PPy-DS nanoparticles (Figure 5.3) showed vibration frequencies typical of PPy when compared to the previous results (Table 5.2).

Liu and Hwang[24] have studied Raman spectrum of oxidised PPy and assigned the two peaks at about 1054 and 1086 cm^{-1} to the C-H in plane deformation of oxidised PPy. This agrees with the Raman of PPy-DS as shown in Figure 5.3 and also the C=C stretching band appeared at 1594 cm^{-1} indicating that the polymer was in the oxidised form[25]. The bands at 934 and 962 cm^{-1} are related to ring deformation associated with dication and radical cation, respectively[26]. Bands are summarised in Table 5.2.

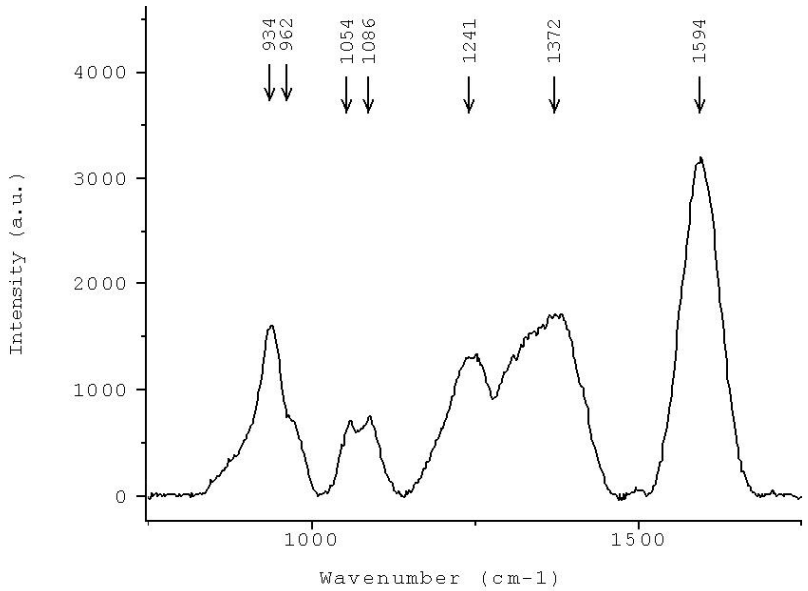

Figure 5.3 Raman spectrum obtained for dried powder PPy-DS using 632.8 nm excitation line.

Table 5.2 Assignments of the Raman bands of PPy using 632.8 nm laser beam.

Assignments	**PPy film**[24-26] (cm^{-1})	**PPy-DS** (cm^{-1})
Ring deformation associated with dication	934	934
Ring deformation associated with radical cation	968	962
Symmetrical C-H in plane bending associated with radical cation	1050	1054
Symmetrical C-H in plane bending associated with dication	1080	1086
Anti-symmetrical C-H in plane bending	1255	1241
Ring stretching	1320, 1372	1372
C=C stretching of the neutral species	about1570	-
C=C stretching of the oxidised species	about1602	1594

5.3.2.3 Cyclic Voltammetry (CV)

The PPy-DS dispersion was cast as a film onto a glassy carbon electrode. The electrochemistry of the cast film was investigated using CV. The CV (Figure 5.4) exhibited a redox couple associated with the two oxidation states of PPy. The broad oxidation peak started from -0.3 V and the reduction peak appeared at -0.62 V similar to results reported previously for PPy/DBSA films[27].

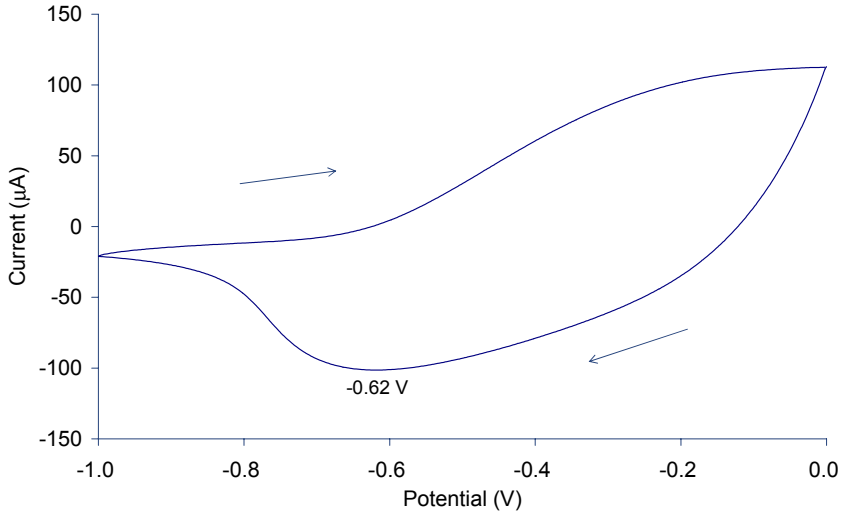

Figure 5.4 Cyclic voltammogram of cast film of PPy-DS dispersion on a GC electrode in 0.05 M SDS with a scan rate of 100 mV/s (arrows show the direction of the scan). $E_{initial}$ is 0.0 V and the potentials are vs. Ag/AgCl (3.0 M NaCl).

5.3.2.4 Mass of product, conductivity, particle size and morphology

The conductivity of PPy-DS nanoparticles was obtained from dried and pressed pellets and found to be 114.8 mS/cm. Mass of the polymer was determined from the solid content of the PPy-DS nanoparticles obtained based on the total volume of the reaction mixture and found to be 9.1 g/L. The particle size observed using the DLS method was over 3000 nm and the particles were not stable as they precipitated out of the solution overnight. Upon TEM investigation (Figure 5.5) the dispersion appears to contain small particles at 65±15 nm suggesting that the particle size determined by DLS is in fact aggregates of these smaller particles. In order to eliminate aggregation in the concentrated nanodispersion, PVA was added during synthesis as outlined in the following section.

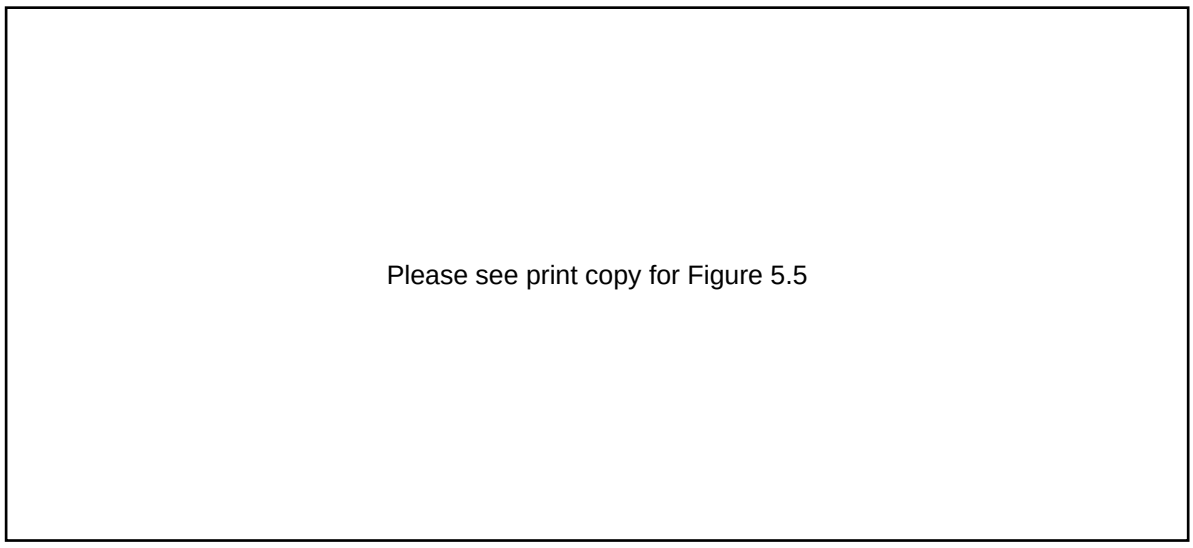

Figure 5.5 Transmission electron microscopic picture of PPy-DS, synthesised from 0.05M Py:0.05M SDS at 25ºC. Image obtained using 100 keV on copper/rhodium grids (ProSciTech Australia).

5.3.3 PPy-DS polymerisation in the presence of PVA

5.3.3.1 Effect of PVA concentration on nanoparticle formation

The reaction conditions outlined in Table 5.3 were employed here with the addition of PVA (Mw 31-50k) during the polymerisation. The PVA concentrations investigated were 0.3%, 0.6% and 1.2% w/v, while the Py, SDS and $FeCl_3$ concentrations were all kept constant at 0.05 M. The PVA was added 15 min after the addition of SDS. Oxidative polymerisation was initiated 60 min after adding Py into the PVA/SDS solution. The monomer content was determined using reverse phase HPLC with the percent conversion of monomer to polymer shown in Table 5.3. The percent conversion increased when synthesised in the presence of PVA. This is possibly due to the fact that the monomer was less aggregated and better dispersed in the presence of PVA thus the oxidation process between the oxidant and the monomer occurs to a greater extent. At 1.2% (w/v) PVA, the

polymer cannot be spun down by centrifugation (12,000 rpm for 30 min) indicating that the steric stabilisation effect of PVA results in a very stable dispersion.

Table 5.3 Emulsion polymerisation conditions for the synthesis of PPy-DS-PVA at various PVA concentrations (data set for each condition = 1). Concentrations are stated as final concentrations in the reaction media.

Code	PVA (% w/v)	Pyrrole (M)	SDS (M)	Temp (ºC)	Conversion (%)
5a	0	0.05	0.05	25	86.80
5b	0.3	0.05	0.05	25	94.00
5c	0.6	0.05	0.05	25	98.73
5d	1.2	0.05	0.05	25	90.38

The OCP measurement (Figure 5.6) suggests that PVA does not affect the chemical oxidation process to any great extent. The maximum potential generated (0.44 V) and the equilibrium potential (0.28 V) were similar to those obtained when PVA was not present (Figure 5.1). However, with PVA present the synthesis reached equilibrium at about 120 min after oxidant addition whilst without PVA, synthesis equilibrium was reached at about 90 min (Figure 5.1). This is presumably due to the effect of the PVA which lower the rate of polymerisation.

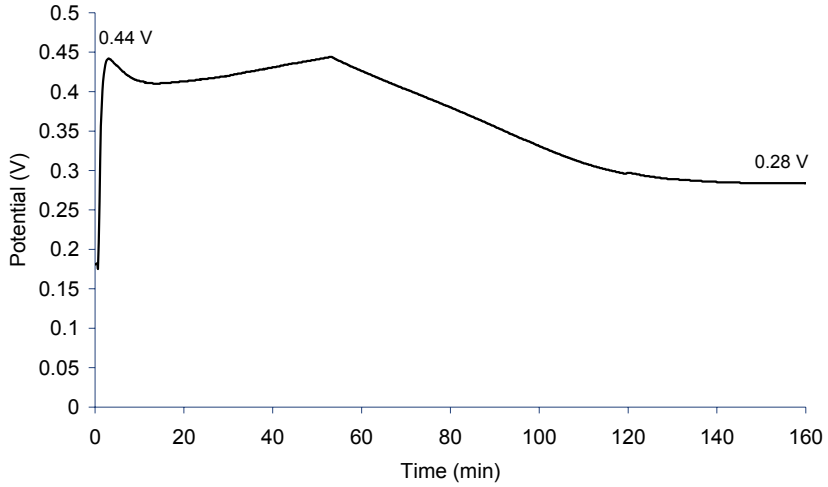

Figure 5.6 The OCP profile obtained during synthesis of PPy-DS-PVA (0.05M:0.05M:1.2% w/v) at 25ºC. The potentials are vs. Ag/AgCl (3.0 M NaCl).

Upon completion of the purification process as outlined in the experimental section (5.2.3), the particle size analysis was obtained using DLS method (see Chapter 2, section 2.2.3). The size of the particles synthesised without PVA or with PVA lower than 1.2 % (w/v) was much larger than 3 μm. At 1.2% (w/v) PVA, the size decreased dramatically to lower than 1000 nm suggesting stabilising effect of PVA. Therefore 1.2% (w/v) PVA will be used for all further experiments. The effect of synthesis temperature and SDS concentration on the particle size were then investigated.

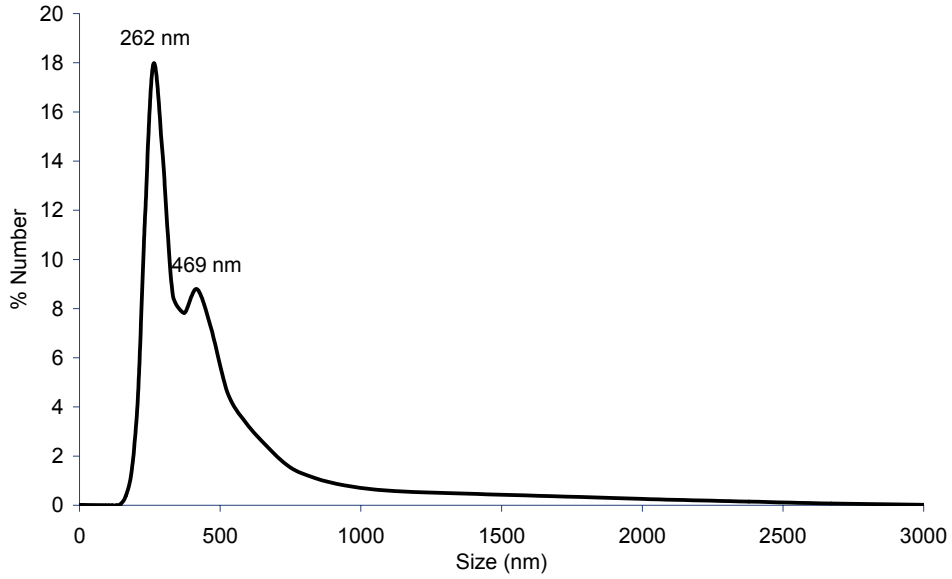

Figure 5.7 The particle size distribution of the polymer synthesised from 0.05M Py, 0.05M SDS and 1.2% PVA (w/v).

5.3.3.2 Effect of polymerisation temperature on nanoparticle formation

Using 1.2% (w/v) PVA, 0.05 M SDS and 0.05 M Py, the temperature during polymerisation was varied to 10, 25 and 40ºC. The OCP profiles during synthesis were observed (Figure 5.8). According to the Nernst equation, the higher temperature would result in the lower OCP where the concentrations of starting materials are the same. This agrees with the OCP of the Py/PVA/SDS solution before the oxidant addition which are 0.182, 0.181 and 0.113 V for the polymerisation temperature of 10, 25 and 40ºC, respectively.

At 10ºC, a black product was observed 10 min after oxidant addition whereas the product was observed in less than one min after oxidant addition when synthesised at 25ºC or 40ºC. From the OCP profile (Figure 5.8), the reaction mixture reached equilibrium quicker at higher temperatures indicating a higher rate of polymerisation. The OCP reached

equilibrium at about 50, 140 and 170 min when the polymer was synthesised at 40, 25 and 10ºC, respectively.

At 40ºC, the potential reached a plateau at about 0.52 V and remained at that potential for nearly 2 h hence the polymerisation was ended. However, the particles were not stable in solution as they precipitated within an hour. The supernatant was yellow whereas it was colourless when the synthesis was carried out at 10 or 25ºC. This indicated that polymerisation at 40ºC had different reaction kinetic compare with those at 10ºC and 25ºC as shown in OCP profile (Figure 5.8 c).

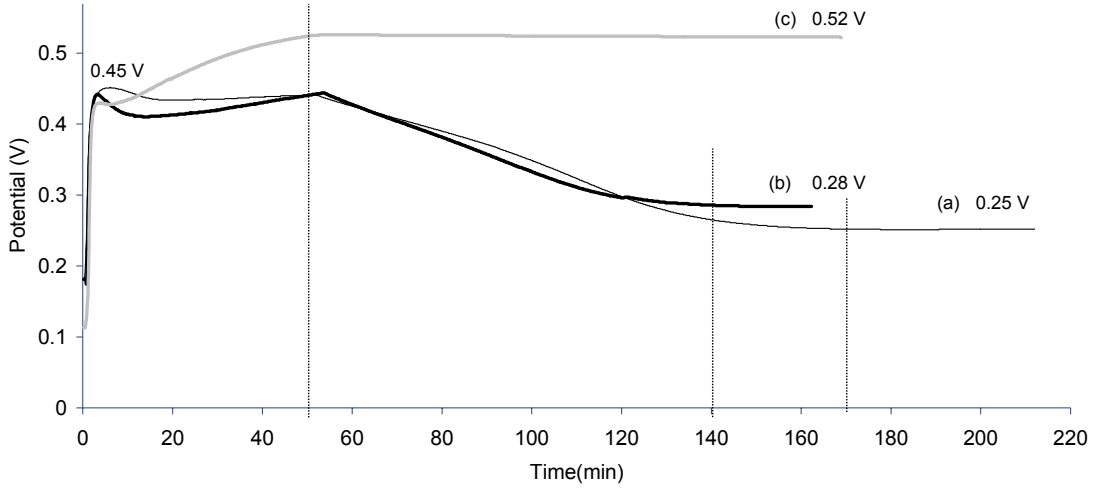

Figure 5.8 The OCP during synthesis of PPy-DS-PVA (0.05M:0.05M:1.2% w/v) synthesised at: (a) 10ºC, (b) 25ºC, and (c) 40ºC. The potentials are vs. Ag/AgCl (3.0 M NaCl).

The particle size distributions were determined (Figure 5.9). With polymerisation at 40ºC, the polymer was not well dispersed in the solution hence it was impossible to get reliable particle size data. The particle size of the polymer synthesised at 10ºC was slightly larger than the product obtained at 25ºC and it took a longer time to complete the polymerisation. Therefore, the 25ºC polymerisation temperature was the optimum temperature and was used for all further synthesis.

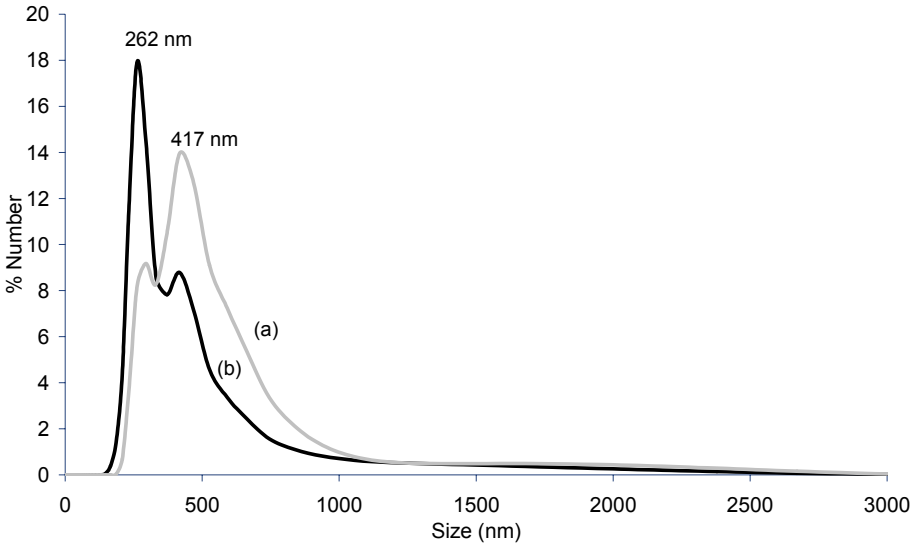

Figure 5.9 The particle size distribution of the polymer synthesised from 0.05 M Py, 0.05M SDS and 1.2% PVA (w/v) at (a) 10ºC, and (b) 25ºC.

5.3.3.3 Effect of SDS concentration on nanoparticle formation

As mentioned in the introduction (section 5.1), the presence of surfactant in a solution is not desirable in printing systems. In an attempted synthesis at lower surfactant concentrations, polymerisation was performed with varying ratio of Py:SDS. While maintaining the concentration of Py at 0.05 M, the molar ratios of Py:SDS was varied from 1:1 to 1:0.5, 1:0.25 and 1:0.125. Assuming partly doped PPys with one positively charge for every 4 to 6 monomer units, less SDS content was not preferable as more Cl^- dopant could incorporate into PPy molecules. The Cl^- dopant has been shown to adversely affect the electroactivity and conductivity of poly-N-methylpyrrole (PNMP) films as reported by Vidanapathirana *et al*[28]. The OCP profiles were similar to those presented above.

The under size plot indicates the percentage of particles on the Y-axis that is smaller than the particle size indicated on the X-axis. Figure 5.10 is the under size plot (by % Number) of the PPy-DS-PVA nanoparticles synthesised from various molar ratio of

Py:SDS. The curve for the polymer synthesised from molar ratio of Py:SDS = 1:0.125 shows that about 90 % of the particles are smaller than 400 nm whereas it was about 65-75 % for the polymers synthesised from different molar ratios. Therefore, the ratio of Py:SDS = 1:0.125 was used for all further syntheses because it contributed to the smallest particle size.

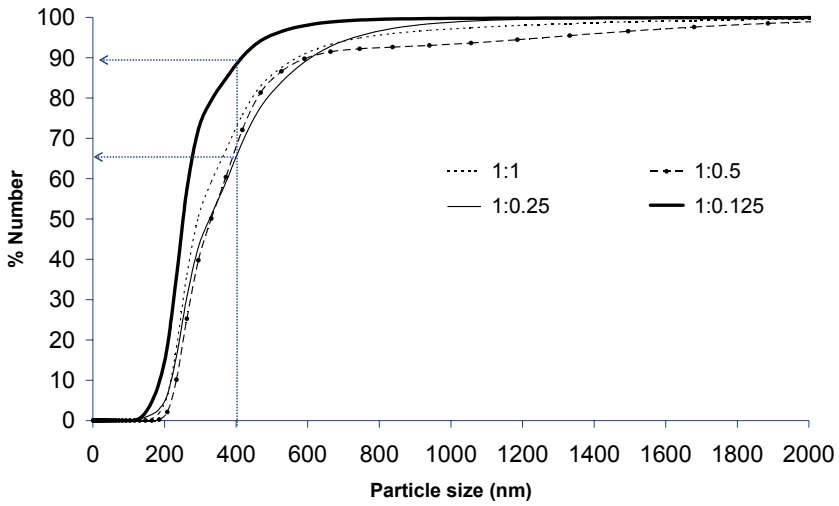

Figure 5.10 The under size plot (by % number) of the polymer synthesised at 1.2 % (w/v) PVA with various molar ratio of Py:SDS.

It is proposed in this study that the smaller particle size at lower concentration of SDS is related to the micellar formation. Typically, micelles tend to be approximately spherical at the concentration above the critical micelle concentration (CMC); at higher concentrations (approximately higher than 40% w/v) and under appropriate conditions these spherical micelles may adopt a cylindrical, ellipsoidal, or lamellar form[29,30] (see more detail in Chapter 1, section 1.2.1). Although the concentration of SDS used in our systems was much lower than 40% w/v the presence of PVA possibly promoted the change in the micellar structure to non-spherical forms and contributed to the increase in the particle size observed (Figure 5.10).

5.3.3.4 Effect of monomer concentration on nanoparticle formation

For ink-jet printing, the polymer concentration needs to be high to ensure a uniform continuous print. In an attempt to achieve this, the monomer concentration was increased. While the molar ratio of monomer to SDS was kept at 1:0.125, PVA concentration was reduced as much as possible using the synthesis conditions shown in Table 5.4.

Table 5.4 Emulsion polymerisation conditions for the synthesis of PPy-DS-PVA at various monomer concentrations. Concentrations are stated as final concentrations in the reaction media.

Code	Pyrrole (M)	SDS (M)	PVA (% w/v)	$FeCl_3$ (M)	Temp (ºC)
5e	0.05	0.00625	1.2	0.05	25
5f	0.10	0.01250	1.2	0.10	25
5g	0.20	0.02500	1.2	0.20	25
5h	0.40	0.05000	2.4	0.40	25

The increase in monomer concentration had no effect on the OCP profile during synthesis (e.g. Figure 5.11). The maximum potential generated (0.44 V) and the equilibrium potential (0.27 V) of PPy-DS-PVA dispersions (0.4 M Py-0.05 M SDS-2.4% (w/v) PVA) were similar to those obtained for PPy-DS in Figure 5.1 which were 0.45 and 0.25 V, respectively.

Figure 5.12 shows the under size plots (by % Number) of the PPy-DS-PVA synthesised from various concentrations of the Py and PVA whilst the ratio of Py:SDS was maintained constant at 1:0.125. Sample 5e and 5f (Figure 5.12 a and 5.12 b, respectively) synthesised from 0.05 M and 0.1 M Py, respectively contained about 90-96% of particles that are smaller than 400 nm. When the concentration of Py was increased to 0.2 M, the particle size increased dramatically as only 54% of the particles were smaller than 400 nm.

Therefore, for sample 5h synthesised from 0.4 M Py, the PVA concentration was increased to maintain small particle size. Approximately 74% of the particle size obtained from sample 5h synthesised from 0.4 M Py, 0.05 M SDS and 2.4 % PVA was smaller than 400 nm at high concentration (3.6 % w/w). This means that the high concentration of nanodispersions was obtained using this synthesis condition. Therefore, this synthesis condition was used to produce the PPy-DS-PVA for ink-jet printing in Chapter 9.

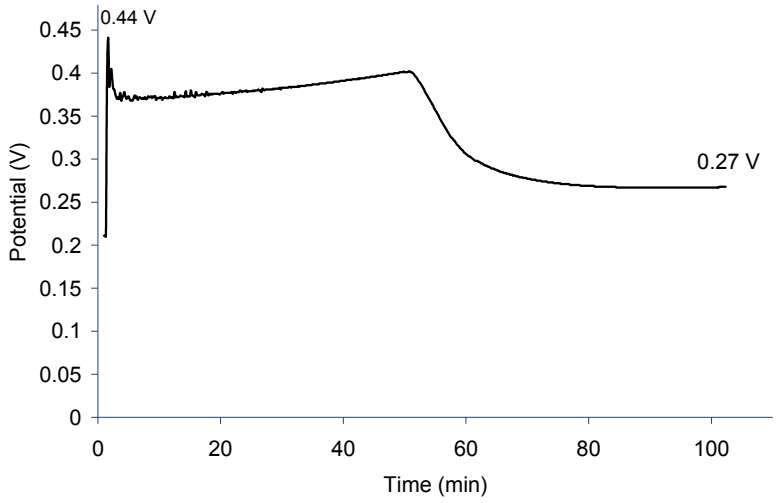

Figure 5.11 The OCP profile during synthesis of PPy-DS-PVA (0.4 M-0.05M-2.4% w/v) at 25ºC. The potentials are vs. Ag/AgCl (3.0 M NaCl).

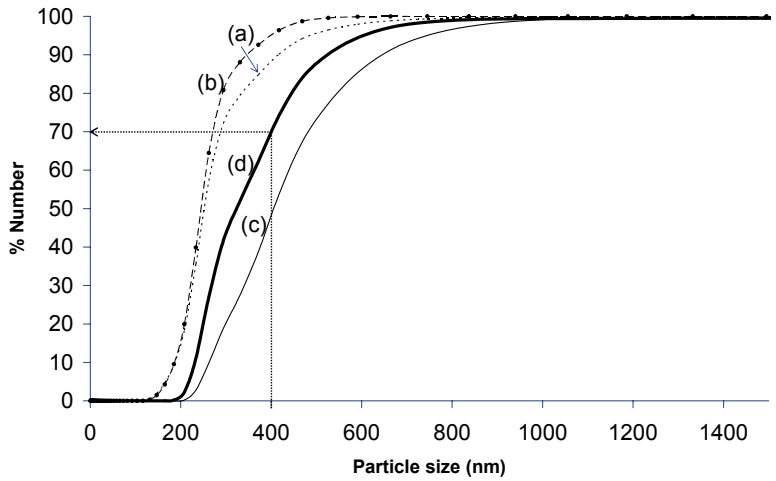

Figure 5.12 The under size plot of the PPy-DS-PVA synthesised from ratio of Py:SDS = 1:0.125 at various monomer concentrations sample: (a) 5e, (b) 5f, (c) 5g, and (d) 5h. Synthesis conditions are shown in Table 5.4.

5.3.4 Characterisation of PPy-DS-PVA nanodispersions

5.3.4.1 UV-visible spectroscopy

UV-visible spectra obtained for the polymer dispersion synthesised in the presence of PVA show the same characteristic absorption band of PPy (Figure 5.13 a-d). The samples 5e, 5f, 5g and 5h have shown the bipolaron band slightly red-shifted from 465 nm to 478 nm as the monomer concentration increased from 0.05 M to 0.4 M. This shift was more significant for the PPy-DS nanoparticles for which the polaron band appeared at 450 nm (Figure 5.2). This red-shift can be attributed to the higher conjugation length obtained in the PPy-DS-PVA nanoparticles compared to the PPy-DS nanoparticles[14,31].

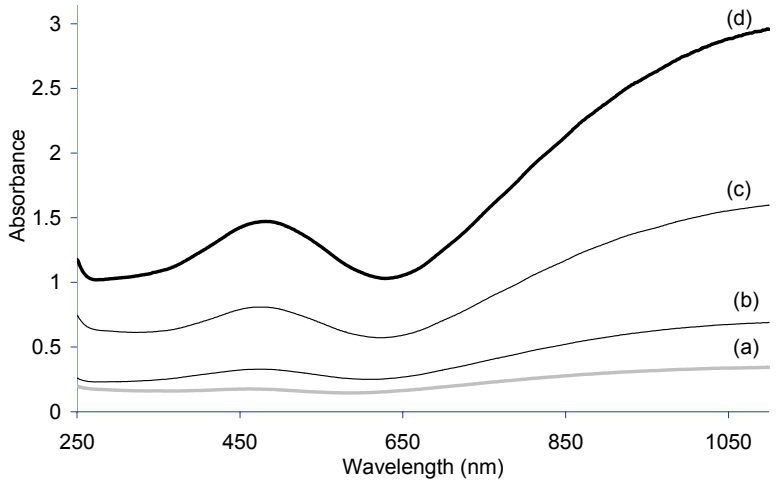

Figure 5.13 UV-visible spectra of PPy-DS-PVA dispersions in the same dilution factor (1:200) after purification of sample: (a) 5e, (b) 5f, (c) 5g, and (d) 5h

5.3.4.2 Raman spectroscopy

Raman spectrum was obtained using a dried PPy-DS-PVA film cast from the 5h dispersion obtained using the synthesis conditions detailed in section 5.3.3.4. Although

most of the bands obtained for this film (Figure 5.14 a) were similar to those reported above for PPy-DS (Figure 5.14 b) but some different features were observed. For the PPy-DS-PVA (Figure 5.14 a), the combined peaks at about 1056 and 1089 cm^{-1} indicated an increase in the neutral form of PPy[24] and the double peaks at 1321 and 1373 attributed to the ring stretching mode of PPy[32]. The peak of C=C stretching appeared at 1594 cm^{-1} for PPy-DS (Figure 5.14 b) nanoparticles whereas it appeared at 1573 cm^{-1} for PPy-DS-PVA (Figure 5.14 a) which indicated the neutral species PPy in the latter case as reported by Han *et al*[25] and Chen *et al*[32]. Moreover, the intensity ratio of the band at about 966 cm^{-1} (associated to radical cation) to the band at about 929 cm^{-1} (associated to dication) was increased significantly for PPy-DS-PVA with respect to the ratio of these two bands for PPy-DS indicating higher content of radical cation in the former case. These results indicate that the PPy-DS-PVA has a lower doping level than the PPy-DS nanoparticles[32].

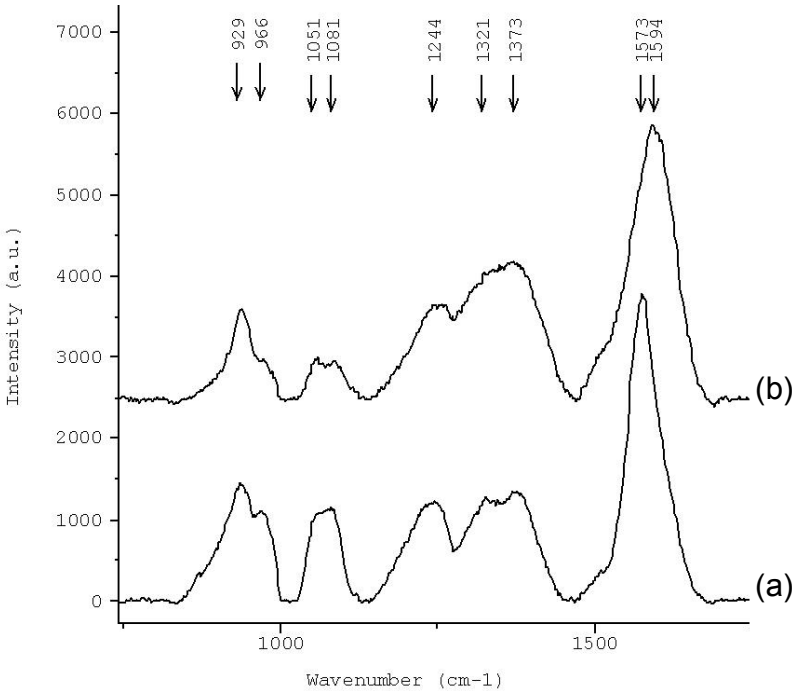

Figure 5.14 Raman spectra of: (a) PPy-DS-PVA film synthesised from 0.4 M Py, 0.05 M SDS and 2.4 % (w/v) PVA, and (b) PPy-DS nanoparticles synthesised from 0.05 M Py, 0.05 M SDS. The spectra were observed using 632.8 excitation line.

5.3.4.3 Cyclic Voltammetry (CV)

PPy-DS-PVA could not be cast as an insoluble film and hence CVs were obtained from dispersions in water. The concentrated dispersion of sample 5d was places in a three-electrode cell using a glassy carbon as the working electrode and CVs obtained (Figure 5.15). The CVs showed a broad oxidation peak at about -0.42 V and a reduction peak at -0.64 V with a very low current magnitude. This is probably due to the insulating nature of PVA which may hinder the electron transfer process.

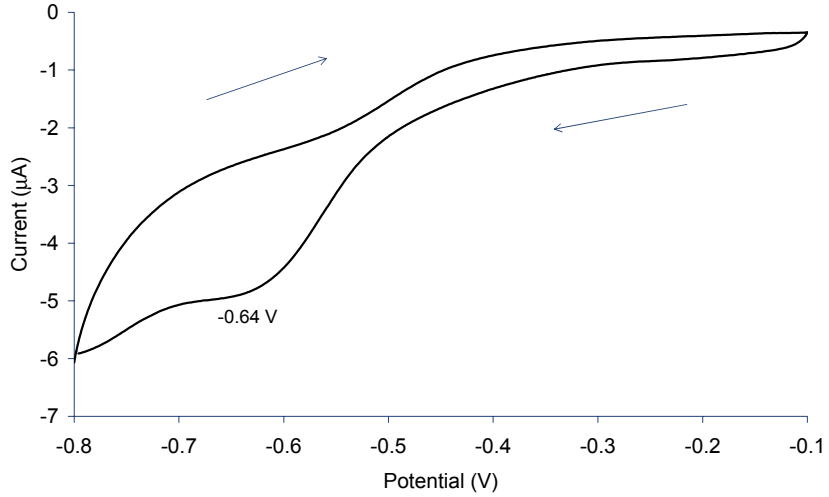

Figure 5.15 Cyclic voltammogram of the PPy-DS-PVA dispersion (5d), synthesised from 0.05M Py, 0.05 M SDS and 1.2% (w/v) PVA, using glassy carbon working electrode with a scan rate of 100 mV s^{-1}. The potentials are vs. Ag/AgCl (3.0 M NaCl). Arrows show the direction of the scan.

5.3.4.3 Mass of product, conductivity, particle size and morphology

Mass of product of the 5h dispersion, synthesised from 0.4 M Py, 0.05 M SDS and 2.4 % (w/v) PVA, was measured and found to be 35.8 g/L. Conductivity measurement was performed, using the four-point probe method, on the dried polymer film and it was found to be 40.1 mS/cm which was lower than the PPy-DS nanoparticles (114.8 mS/cm). Assuming partly doped PPy, one anion is needed for every 4 Py units. For PPy-DS nanoparticles, the ratio of Py:DS was 1:1 which means the dopants were adequate for PPy doping. In the case of PPy-DS-PVA, only one DS^- ion was available for every 8 Py units as the ratio of Py:SDS was 1:0.125. Therefore, the DS^- ion was doped to every 4 Py units with the Cl^- ion from the oxidant ($FeCl_3$) was doped to the other 4 Py units. The dopant Cl^- ion has been found to decrease the conductivity of PNMP films as reported by Vidanapathirana *et al*[28]. Therefore, the conductivity of PPy-DS-PVA nanoparticles was lower than the PPy-DS nanoparticles. Moreover, the PVA surrounding the polymer could have contributed to the low conductivity observed for PPy-DS-PVA nanoparticles[33,34].

The particle size distribution of sample 5h was determined using DLS and more than 99% of the particles were smaller than 1000 nm (Figure 5.16 a).

The morphological picture of the PPy-DS-PVA nanoparticles (sample 5h) taken by TEM is presented in Figure 5.17 and shows the segregation of the spherical particles in the size of 52±5 nm. This is due to the stabilising effect of the PVA. However, the particle size obtained from concentrated solution using DLS (Figure 5.16 a) was larger indicating that some aggregation occurred at higher concentrations. This dispersion was very stable and it could not be centrifuged out at 12000 rpm for 30 min.

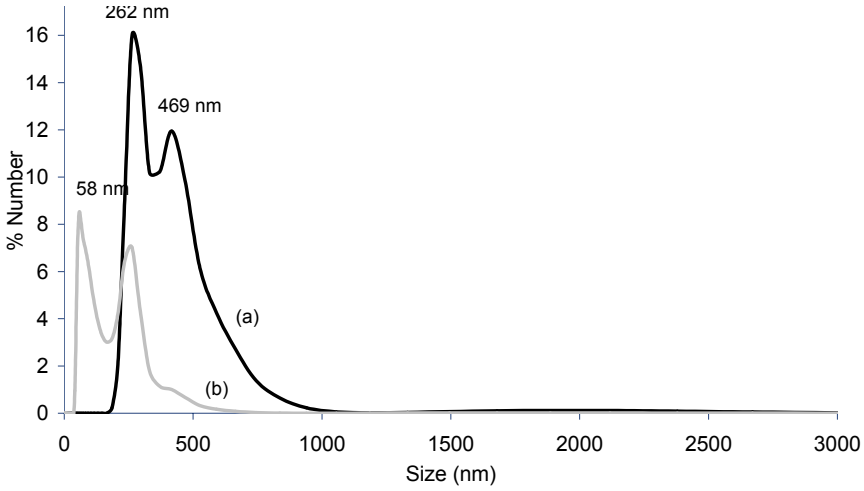

Figure 5.16 The particle size distribution of the PPy-DS-PVA dispersion (5h) synthesised from 0.4 M Py, 0.05M SDS and 2.4% PVA (w/v): (a) fresh dispersions, and (b) 15 months dispersions.

The stability of this dispersion was investigated as outlined in the experimental section (5.2.4). The particle size in dispersions after 15 months standing at room temperature was compared to the fresh sample as shown in Figure 5.16. The particle size of 15 months (Figure 5.16 b) stored sample was smaller than the fresh sample. Two major peaks appeared at 262 nm and 469 nm for the fresh sample (Figure 5.16 a) whereas additional peak at 58 nm is shown and dominated for the 15 months stored sample. The dominant peak coincided with the particle size of the individual particle observed using TEM in Figure 5.17. This peak was not observed in the fresh sample and also the peak at 469 nm was lower in the 15 months stored sample. This is presumably due to the larger particles aggregating and precipitating out of the solution with time and the smaller particles dominated and segregated in the solution. The black colour of the 15 months stored sample indicated high concentration of the PPy-DS-PVA remained in the solution and hence it was not possible to visualise the precipitate from photographs.

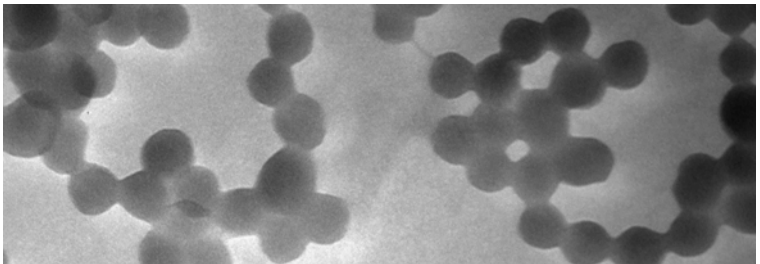

Figure 5.17 Transmission electron microscopic picture at 100 KeV of PPy-DS-PVA nanoparticles synthesised from 0.4M Py:0.05M SDS:2.4% (w/v) PVA at 25ºC.

5.4 Conclusions

This chapter has demonstrated that PPy nanodispersions can be successfully synthesised. Although PPy-DS nanoparticles have higher conductivity and better electroactivity compared to PPy-DS-PVA nanoparticle, their particle sizes are large and the particles aggregate at high concentration. Moreover, the dispersion is not stable as it precipitated out of the solution overnight. The use of steric stabiliser (PVA) in the synthesis provides stable nanodispersions with the size decreasing with increasing PVA content. The polymerisation temperature has affected on the polymerisation rate, OCP and the particle size. The optimum synthesis temperature is 25ºC and the optimum ratio of PPy to SDS is 1:0.125. High loading of PPy with small particle sizes and stable nanodispersions is obtained using 0.4 M Py, 2.4% (w/v) PVA and 0.05 M SDS. The nanodispersions have reasonable conductivity of 40.1 mS/cm and particle size less than 1000 nm in the concentrated solution (3.6 % w/w) as observed using DLS. Transmission electron microscopic picture shows that the size of the segregated spherical nanoparticles is 52±5 nm indicating the stabilising efficiency of PVA. The small particles remained in the solution for up to 15 months whereas the large particles precipitated out of the solution as investigated using DLS.

In summary, the concentrated PPy nanodispersions with 74% of the particles smaller than 400 nm were successfully synthesised for ink-jet printing. The print quality of these nanodispersions will be discussed in Chapter 9.

5.5 References

1. Lee, Y.H., Lee, J.Y., and Lee, D.S., *Synthetic Metals*, 2000. **114**(3): p. 347-353.
2. Song, M.K., Kim, Y.T., Kim, B.S., Kim, J., Char, K., and Rhee, H.W., *Synthetic Metals*, 2004. **141**(3): p. 315-319.
3. Omastova, M., Trchova, M., Kovarova, J., and Stejskal, J., *Synthetic Metals*, 2003. **138**(3): p. 447-455.
4. Armes, S.P., Miller, J.F., and Vincent, B., *Journal of Colloid and Interface Science*, 1987. **118**(2): p. 410-416.
5. Cairns, D.B., Armes, S.P., and Bremer, L.G.B., *Langmuir*, 1999. **15**(23): p. 8052-8058.
6. Eisazadeh, H., Gilmore, K.J., Hodgson, A.J., Spinks, G., and Wallace, G.G., *Colloids Surfaces A: Physicochemical Engineering Aspects*, 1995. **103**: p. 281-288.
7. Aboutanos, V., Barisci, J.N., Innis, P.C., and Wallace, G.G., *Colloids and Surfaces a-Physicochemical and Engineering Aspects*, 1998. **137**(1-3): p. 295-300.
8. Sahmetlioglu, E., Yuruk, H., Toppare, L., Cianga, I., and Yagci, Y., *Polymer International*, 2004. **53**(12): p. 2138-2144.
9. Mirmohseni, A. and Wallace, G.G., *Polymer*, 2003. **44**(12): p. 3523-3528.
10. Lin, C.W., Hwang, B.J., and Lee, C.R., *Journal of Applied Polymer Science*, 1999. **73**(11): p. 2079-2087.
11. Bhat, N.V., Gadre, A.P., and Bambole, V.A., *Journal of Applied Polymer Science*, 2001. **80**(13): p. 2511-2517.
12. Riede, A., Helmstedt, M., Riede, V., and Stejskal, J., *Langmuir*, 1998. **14**(23): p. 6767-6771.
13. Stejskal, J. and Sapurina, I., *Journal of Colloid and Interface Science*, 2004. **274**(2): p. 489-495.
14. Lee, E.S., Park, J.H., Wallace, G.G., and Bae, Y.H., *Polymer International*, 2004. **53**(4): p. 400-405.
15. Chattopadhyay, D., Chakraborty, M., and Mandal, B.M., *Polymer International*, 2001. **50**(5): p. 538-544.
16. Maeda, S. and Armes, S.P., *Journal of Materials Chemistry*, 1994. **4**(6): p. 935-942.
17. Mulvaney, P., *Langmuir*, 1996. **12**(3): p. 788-800.
18. Shipway, A.N., Katz, E., and Willne, I., *Chem. Phys. Chem*, 2000. **1**: p. 18-52.
19. Magdassi, S. and Ben Moshe, M., *Langmuir*, 2003. **19**(3): p. 939-942.
20. Armes, S.P., *Synthetic Metals*, 1987. **20**(3): p. 365-371.
21. Wallace, G.G., Spinks, G.M., Kane-Maguire, L.A.P., and Teasdale, P.R., *Conductive electroactive polymers : intelligent materials systems*. 2nd ed. 2002, Boca Raton, FL: CRC Press. , and references cited therein.
22. John, R., John, M.J., Wallace, G.G., and Zhao, H., *Use of Surfactants in the Oxidative Synthesis of Conductive, Electroactive Polymers*, in *Electrochemistry in Colloids and Dispersions*, R.A. Mackay and J. Texter, Editors. 1992, VCH Publishers, Inc.: New York.
23. Nabid, M.R. and Entezami, A.A., *Journal of Applied Polymer Science*, 2004. **94**(1): p. 254-258, and references cited therein.
24. Liu, Y.-C. and Hwang, B.-J., *Synthetic Metals*, 2000. **113**(1-2): p. 203-207.

25. Han, G.Y., Shi, G.Q., Qu, L.T., Yuan, J.Y., Chen, F.E., and Wu, P.Y., *Polymer International*, 2004. **53**(10): p. 1554-1560.
26. Dauginet-Da Pra, L. and Demoustier-Champagne, S., *Polymer*, 2005. **46**(5): p. 1583-1594.
27. Skaarup, S., Bay, L., Vidanapathirana, K., Thybo, S., Tofte, P., and West, K., *Solid State Ionics*, 2003. **159**(1-2): p. 143-147, and references cited therein.
28. Vidanapathirana, K.P., Careem, M.A., Skaarup, S., and West, K., *Solid State Ionics*, 1999. **123**(1-4): p. 287-292.
29. Shaw, D.J., *Introduction to Colloid and Surface Chemistry*. 1991, Oxford: Butterworth-Heinemann Ltd. 87-88.
30. Everett, D.H., *Basic Principles of Colloid Science*. 1988, London: Royal Society of Chemistry. 153-155.
31. Visy, C., Krivan, E., and Peintler, G., *Journal of Electroanalytical Chemistry*, 1999. **462**(1): p. 1-11.
32. Chen, F., Shi, G.Q., Fu, M.X., Qu, L.T., and Hong, X.Y., *Synthetic Metals*, 2003. **132**(2): p. 125-132.
33. Saunders, B.R., Saunders, J.M., Mrkic, J., and Dunlop, E.H., *Pccp Physical Chemistry Chemical Physics*, 1999. **1**(7): p. 1563-1568.
34. Wallace, G.G., Spinks, G.M., Kane-Maguire, L.A.P., and Teasdale, P.R., *Conductive electroactive polymers : intelligent materials systems*. 2nd ed. 2002, Boca Raton, FL: CRC Press. p. 51-119, and references cited therein.

6.1 Introduction

Polythiophenes (PThs) are highly stable from both an electrochemical and environmental point of view. A range of functional groups can be covalently attached to PThs using readily accessable chemistries[1-13] which can be used to tune chemical, biological[4], optical[2,9,10] and electrical properties[3,5,10,12]. Application of PThs have been limited due to poor processability being insoluble and infusible[14-16]. In this chapter, we seek to improve the processability of PThs by synthesising nanodispersions in aqueous media which could lead to an easily and environmental friendly processing. PThs are generally stable in their reduced form which is a non-conducting form. However, synthesis of PThs in nanometre size is still useful as unique electrical and electrochemical properties could be expected and lead to improved performances in various applications (see Chapter 1, section 1.2).

Numerous studies have used surfactants to aid the solubilisation of thiophene monomer in water for subsequent electropolymerisation[17-25]. Sodium dodecylsulfate (SDS) is most useful in that it assists in solubilising the monomer, lowers the oxidation potential, accelerates the rate of polymerisation and improves adhesion to the electrode substrate[17,19,26]. Choi *et al*[27] prepared poly (3,4-ethylenedioxythiophene) (PEDOT) nanoparticles using oxidative polymerisation in dodecylbenzene sulphonic acid (DBSA) micellar solutions. The particle size of the polymer obtained ranged from 35 to 100 nm as determined by field emission scanning electron microscopy (FE-SEM). These nanoparticles were difficult to disperse in water, however promptly dispersed by mechanical stirring in alcoholic solvents[27]. Lei *et al*[28] used 2-naphthalenesulfonic acid sodium salt as an emulsifier and dopant for the oxidative synthesis of PEDOT. The polymer obtained

aggregated and showed rod-like and layer-like morphology[28].

Preliminary work showed that the polymer obtained from the chemical synthesis of polybithiophene in a mixture of acetonitrile/SDS micellar solution could not be dispersed in water. Therefore DBSA was considered for use to produce the PTh nanodispersions since it was successfully used to synthesise aqueous nanodispersions of polyaniline (PANI) in Chapter 3. Brustolin *et al*[29] showed that the use of a small amount of organic solvent to help the solubility of the monomer in water. Chloroform is a very good solvent for both DBSA and thiophene monomers and was therefore used to solubilise terthiophene (TTh) monomer in aqueous micellar solutions in this work.

An alternative approach to obtaining stable aqueous nanodispersions involves the use of ionic liquids (ILs). ILs are also called molten salts because they are in liquid form at room temperature[30]. They have a wide electrochemical potential window range and good thermal stability[30-32]. They are non-volatile and non-flammable thus can be used to replace more toxic molecular solvents[31,32]. ILs have been used in the synthesis of inherently conducting polymers (ICPs) since they can be the source of dopants as well as the solvent[32]. They have been reported to enhance lifetimes of electrochemical mechanical actuators made from ICPs[31], and improve the photovoltaic performance of poly(3-thiophenylacetic acid)-sensitised metal oxide photoelectrochemical cells[33]. Polythiophene, polybithiophene and polyterthiophene (PTTh) has been successfully synthesised, electrochemically, in 1-ethyl-3-methylimidazolium bis(trifluoromethane-sulfonyl)amide (emiTFSA) (Figure 6.1). The polymer films were found to have good electrochemical activity and redox reversibility[32].

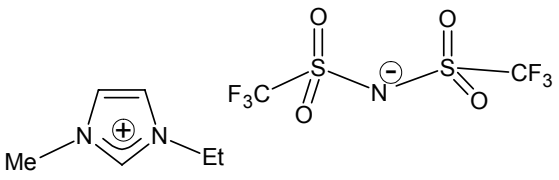

Figure 6.1 Structure of emiTFSA.

Gold (III) chloride ($AuCl_3$) was used to oxidise poly (3-hexylthiophene)[34] and PEDOT[35] films to yield materials of high electronic conductivity. It is also soluble in the chosen IL; hence it was used as the oxidant in the chemical synthesis of PTTh in IL.

It has been reported that TTh can be polymerised at a lower oxidation potentials than thiophene and bithiophene due to its longer conjugation length[36-38]. Moreover, PTTh films from electrochemical synthesis were found to be more stable than polybithiophene and PTh grown under similar conditions[37]. Therefore PTTh was chosen in this study.

In this chapter two approaches were used, namely synthesis in the presence of DBSA and synthesis in IL. The open circuit potential (OCP) was monitored during polymerisation. The polymers obtained were characterised using various techniques, such as particle size measurement by dynamic light scattering method (DLS) and transmission electron microscopy (TEM), UV-visible spectroscopy, Raman spectroscopy and cyclic voltammetry (CV). For the ease of comparison from batch to batch, the particle sizes in this chapter were reported from the % Number distribution which indicate the percentage of the polymer in the particular size (see Chapter 2, section 2.2.3 for more details).

6.2 Experimental

6.2.1 Chemicals

2,2':5',2"-Terthiophene, gold (III) chloride ($AuCl_3$), sodium dodecyl sulfate (SDS), ammonium peroxydisulfate (APS), and lithium perchlorate ($LiClO_4$) were purchased from Sigma-Aldrich. Ethyl alcohol was purchased from Asia Pacific Specialty Chemicals Ltd.

Dodecylbenzene sulphonic acid (DBSA) was purchased from TCI, Japan. Chloroform and acetonitrile were purchased from Ajax Finechem. Ferric chloride ($FeCl_3$) was purchased from BDH. Tetrabutylammonium perchlorate (TBAP) was purchased from Fluka. EmiTFSA synthesised by Dr.Jenny Pringle at Monash University, Victoria, Australia and was degassed by purging nitrogen through for 15 min before used. All solutions were prepared using Milli-Q water.

6.2.2 Equipment/Instrumentation

A two-electrode cell comprising of a Pt mesh auxiliary electrode and an Ag/AgCl reference electrode (3.0 M NaCl) and connected to a Hewlett Packard 34401A multimeter was used to monitor the OCP throughout chemical polymerisation of PTTh-DBSA. Chemical syntheses were performed in a Julabo controlled temperature bath using a peristaltic pump (Minipuls 2, Gilson) to control the rate of oxidant addition. A 5702 Eppendorf centrifuge was used to purify polymers. A three-electrode cell comprising of a glassy carbon or ITO-coated glass working electrode, an Ag/AgCl (3.0 M NaCl) (in aqueous solution) or an Ag/Ag^+ (in organic solution) reference electrode and a Pt wire auxiliary electrode connected to an EDAQ E-Corder 401 with EDAQ Potentiostat was used for all electrochemical experiments. Particle size was determined using dynamic light scattering (Nano-ZS Zetasizer, Malvern Instruments) with 8^o angled back scattered light configuration. Transmission electron microscopy (TEM) was carried out using a Hitachi H7000 at 100 KeV. UV-visible Spectrophotometer (Shimadzu, UV-1601) was used to investigate absorption spectra. Raman spectra were recorded using a 632.8 nm laser (Jobin Yvon Horiba, HR800). ITO-coated glass with surface conductivity of $\leq 10\ \Omega\ sq^{-1}$ from Delta Technologies Ltd, USA, was used as the electrode substrate. A UV-ozone cleaner

(Jelight Company, Inc., Model No.42-220,) was used for pretreatment of the ITO-coated glass.

6.2.3 Methods

6.2.3.1 Electrochemical synthesis of PTTh-DBSA

The monomer dispersion was prepared by adding 0.0498 g TTh into 20 ml of aqueous 0.1 M $LiClO_4$. This solution was stirred and 1.3 ml DBSA was added into the solution followed by 1 ml $CHCl_3$. Final concentrations of TTh and DBSA were 0.01 M and 0.2 M, respectively. Electrochemical polymerisation was performed using CV between -0.2 V and 1.0 V at a scan rate of 50 mV/s for 30 cycles.

6.2.3.2 Chemical synthesis of PTTh-DBSA nanoparticles

Aqueous solutions of DBSA were prepared at various concentrations at 20°C with thorough stirring. After the DBSA was completely dissolved, the TTh monomer was added to the DBSA micellar solution. After the monomer was dispersed throughout the DBSA solution, chloroform was added and the solution stirred for a further 2 min. Various concentrations of APS were separately dissolved in the same volume of water and polymerisation was initiated by adding the APS solution to the TTh-containing solution at a rate of 1 ml/min. The solution was stirred overnight with the potential measured throughout the course of the polymerisation. Following synthesis the polymer was placed in a 12,000 Mw cut off dialysis bag and dialysed against 0.05 M SDS solution for 42 h with the SDS solution being changed ever 18 h. The product mixture was then centrifuged at 4400 rpm for 15 min and the precipitate washed three times using 20 ml of 0.05M SDS solution.

6.2.3.3 Chemical synthesis of PTTh nanoparticles in IL

TTh monomer 0.0621 g was weighed and dissolved in 5 ml of emiTFSA and the solution was heated to about 40 ºC with continuous stirring in order to completely dissolve the monomer. The solution was then cooled down to room temperature. Solutions of $AuCl_3$ with various concentrations were added to the TTh-containing solution and the mixture was stirred overnight. The reaction mixture was centrifuged (4400 rpm, 30 min) and the precipitate washed three times with 5 ml ethanol.

6.2.3.4 Characterisation of PTTh nanoparticles

The polymer dispersions were characterised using UV-visible spectroscopy. The particle size of the concentrated dispersions was measured using the DLS method. Low

concentration dispersions were investigated to determine particle size and morphology using TEM. The polymer nanoparticles were characterised by Raman spectroscopy. Mass of product from the syntheses was determined from solid content of the nanoparticles obtained based on total volume of the reaction media.

6.3 Results and Discussion

6.3.1 PTTh-DBSA

6.3.1.1 Electrochemical synthesis of PTTh-DBSA

Zhang *et al*[37] and Chen *et al*[7] have previously reported that TTh can be electrochemically polymerised at an oxidation potential of about 0.7-0.8 V in an organic solvents. In order to study the oxidation potential of the PTTh/DBSA system, electrochemical synthesis of PTTh-DBSA was conducted. Its oxidation potential, UV-visible spectrum, Raman spectrum and CVs were observed and used as reference for the PTTh-DBSA obtained from chemical synthesis in section 6.3.1.2. Cyclic voltammograms obtained during synthesis of PTTh/DBSA films are shown in Figure 6.2. The increase in current magnitude from the 1st cycle to the 30th cycle (Figure 6.2) and green/brown colour observed on the ITO-coated glass indicated the formation of an electroactive PTTh film on the electrode surface[39]. The first scan showed an oxidation peak at about 0.80 V which is attributed to the oxidation of TTh.

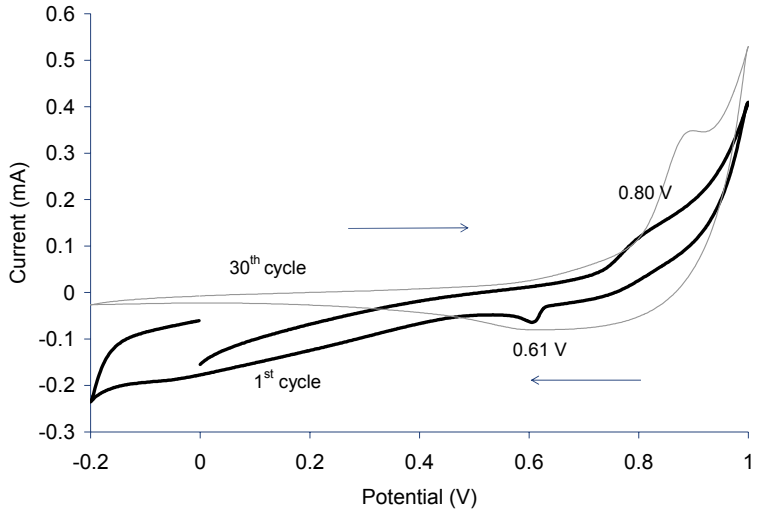

Figure 6.2 Cyclic voltammograms (1st and 30th scan) during synthesis of PTTh-DBSA from a solution containing TTh:DBSA= 0.01:0.2 M in 0.1M $LiClO_4$. Working electrode was ITO-coated glass. Number of scan cycles was 30, at 50 mV/s scan rate (arrows show the direction of the scan). $E_{initial}$ is 0.0 V and the potentials are vs. Ag/AgCl (3.0 M NaCl).

The CV obtained after polymerisation in aqueous-based electrolyte (Figure 6.3) also showed anodic and cathodic peaks at 0.85 V and 0.58 V, respectively. The CV obtained in acetonitrile-based electrolyte (Figure 6.4) showed much more well defined redox couples at 0.27 V/0.18 V and 0.92 V/0.72 V which were similar to those reported by Saraac *et al*[38] and Parakka *et al*[40]. The current intensity decreased for the first to second scan for CV in both aqueous and organic electrolytes but became more stable in the later scans. This may have been due to the dissolving of some oligomers or short chain polymers with only long polymer chains remaining on the electrode surface, as explained by Sarac *et al*[38,41].

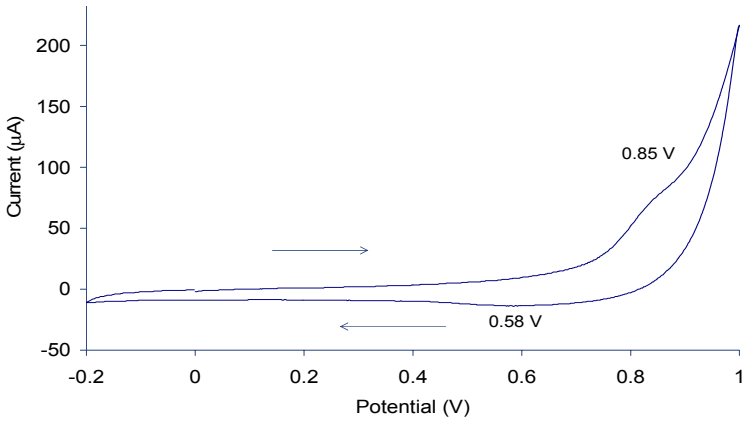

Figure 6.3 Cyclic voltammograms of electrochemically synthesised PTTh-DBSA film in 0.1M $LiClO_4/H_2O$ at 50 mV/s scan rate (arrows show the direction of the scan). $E_{initial}$ is 0.0 V and the potentials are vs. Ag/AgCl (3.0 M NaCl).

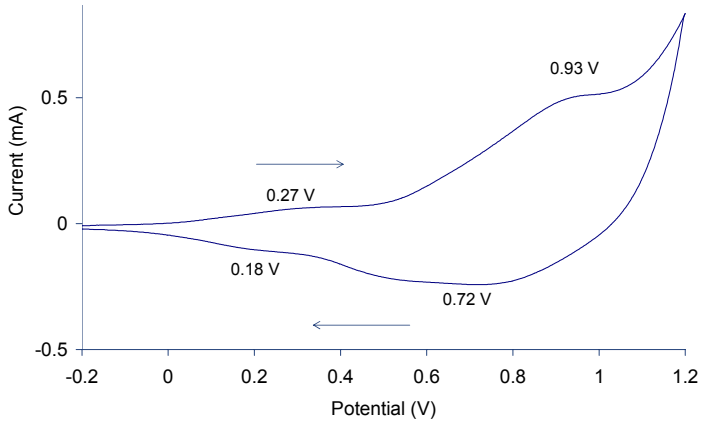

Figure 6.4 Cyclic voltammograms of electrochemically synthesised PTTh-DBSA film in 0.1M TBAP/ACN at 50 mV/s scan rate (arrows show the direction of the scan). $E_{initial}$ is 0.0 V and the potentials are vs. Ag/Ag^+.

The UV-visible spectrum of an as-grown by CV PTTh-DBSA film is shown in Figure 6.5. The wavelength at maximum absorption (λ_{max}) of this film appeared at 400 nm and is assigned to π-π^* transitions[7,37] which is in agreement with that reported by Zhang *et al*[37]. The second feature at wavelengths higher than 850 nm is associated with the polaron band and indicates the polymer is unexpectedly in the oxidised conducting form[7] which is

more preferable in various applications than the reduced non-conducting form.

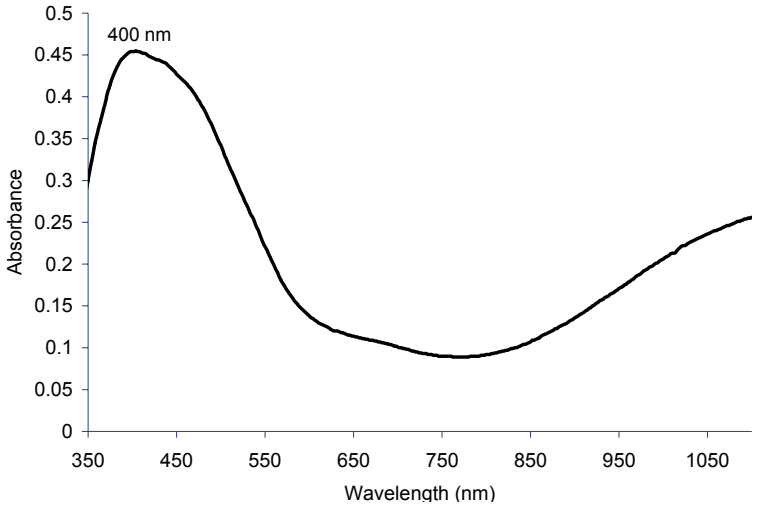

Figure 6.5 UV-visible spectra obtained for electrodeposited PTTh-DBSA films (30 cycles) from a solution containing TTh:DBSA= 0.01:0.2 M in 0.1M $LiClO_4$. ITO-coated glass was used as the working electrode and cycled from -0.2 to +1 V at 50 mV/s scan rate.

The Raman spectrum of an electrochemically synthesised PTTh-DBSA film is shown in Figure 6.6 with peak assignments summarised in Table 6.1. Bazzaoui *et al*[42] have described that the ν_1 band is assigned to the symmetric stretching of the aromatic C=C bond ring. This feature shifts toward higher frequencies when conjugation length of the oligomer precursor is increased. The position shifts to 1505 cm^{-1} after synthesised from α-terthiophene which has a higher conjugation length. This corresponds with the band at 1505 cm^{-1} in this spectrum. The Q_1 and Q_2 peaks at about 1420 and 1400 cm^{-1} associated with the quinoid species (radical cations and dications, respectively)[43] of the polymer are possibly overlapped in this case and shown as a weak band at 1406 cm^{-1} in Figure 6.6 indicating that the PTTh-DBSA was partially oxidised. This is supported by the peaks of ν_6, ν_7 and D kink bands[42] at around 650-740 cm^{-1}, which are known to be stronger in the oxidised form of the polymer than for the reduced form[42-45]. These results indicate that the electrodeposited

PTTh-DBSA was in between reduced and oxidised forms.

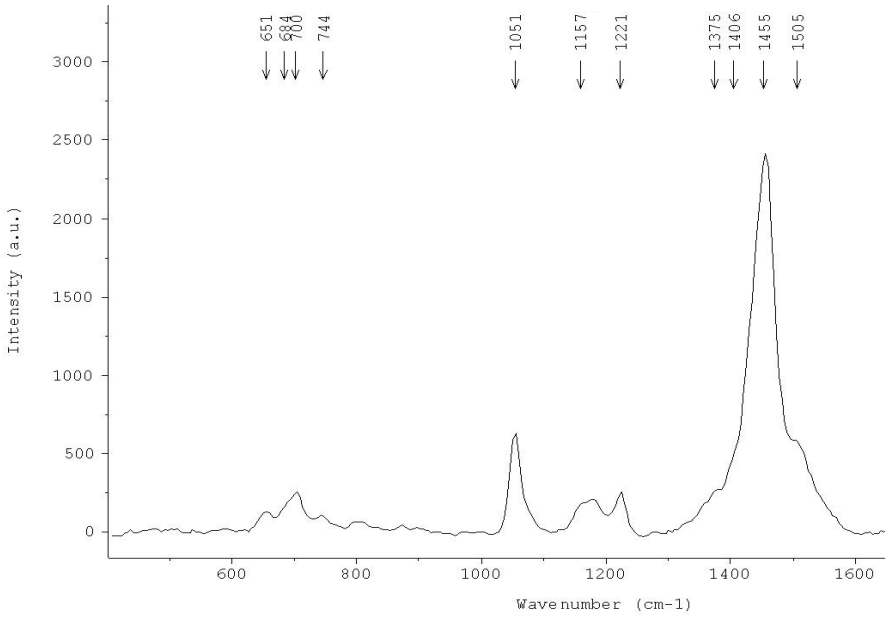

Figure 6.6 Raman spectrum of electrochemically synthesised PTTh-DBSA film observed using a 632.8 nm excitation line.

Table 6.1 Band assignments of oxidised and reduced polythiophene (PTh) films[42,43] and of an electrodeposited PTTh-DBSA film.

Assignments	**Notes**	**PTh[42,43] (cm^{-1})**		**PTTh-DBSA (cm^{-1})**
		reduced	**oxidised**	
Ring deformation C-S-C	ν_7	702	698	700
Ring deformation C-S-C	ν_6	731	742	744
C_β-H bending	ν_5	1045	1056	1051
Kink mode	D_3	1149	1159	1157
C_α-C_α, stretching	ν_4	1219	1217	1221
C_β-C_β, ring stretching	ν_3	1370	1360	1375

Quinoid (dications)	Q_2	-	1400	1406
C_α=C_β ring stretching	ν_2	1455	1454	1455
C_α=C_β ring stretching (anti)	ν_1	1502	1502	1505

6.3.1.2 Chemical synthesis of PTTh-DBSA nanoparticles

The aim of this part of the investigation was to optimise the chemical synthesis conditions to obtain stable nanodispersions. Effects of the oxidant and surfactant concentrations to the formation of PTTh nanoparticles and their properties were investigated.

6.3.1.2.1 Effect of oxidant concentration

When $FeCl_3$ was used as the oxidant for the synthesis of PTTh-DBSA, no polymerisation occurred. Ammonium peroxydisulphate (which has higher oxidation potential than $FeCl_3$; 1.94 V and 0.77 V vs SHE, respectively[36]) was successfully used to polymerise the TTh monomer at room temperature. Attempts to synthesise PTTh-DBSA without using chloroform in the aqueous reaction media were unsuccessful. Without chloroform the monomer was not completely dissolved and the polymerisation was therefore inhibited. As a result, all further polymerisations were performed using APS and small amounts of chloroform. The synthesis conditions are shown in Table 6.2.

Table 6.2 Conditions for synthesis of PTTh-DBSA nanoparticles in aqueous-based chloroform/DBSA system using various concentrations of APS. Concentrations are stated as final concentrations in the reaction media.

[APS]/M	[TTh]/M	[DBSA]/M	Total volume/ml	Volume Chloroform/ml

1.5	0.01	0.2	40	2
1.0	0.01	0.2	80	4
0.5	0.01	0.2	80	4
0.2	0.01	0.2	80	4

In this study, the OCP was monitored during polymerisation (Figure 6.7) and the reaction terminated when the potential reached equilibrium. The oxidation potential only reached 0.8 V in two instances - for the samples synthesised in the presence of 1.5 M and 1.0 M APS as shown in Figure 6.7 a and 6.7 b, respectively. When the APS concentration was lowered (Figure 6.7 c and 6.7 d) the maximum potential was less than 0.8 V, and partial polymerisation occurred as the reaction media changed from yellow to brown-yellow colour. While higher APS concentrations induced polymerisation it still required at least 10 h to form the polymer as observed by the appearance of brown/green colour of PTTh. Although the sample synthesised using APS concentration of 1.0 M APS reached an OCP of 0.8 V it took nearly six hours longer to reach the plateau compared to the sample synthesised with 1.5 M APS (Figure 6.7). These results indicated that, as has been expected, the APS concentrations affected the polymerisation process.

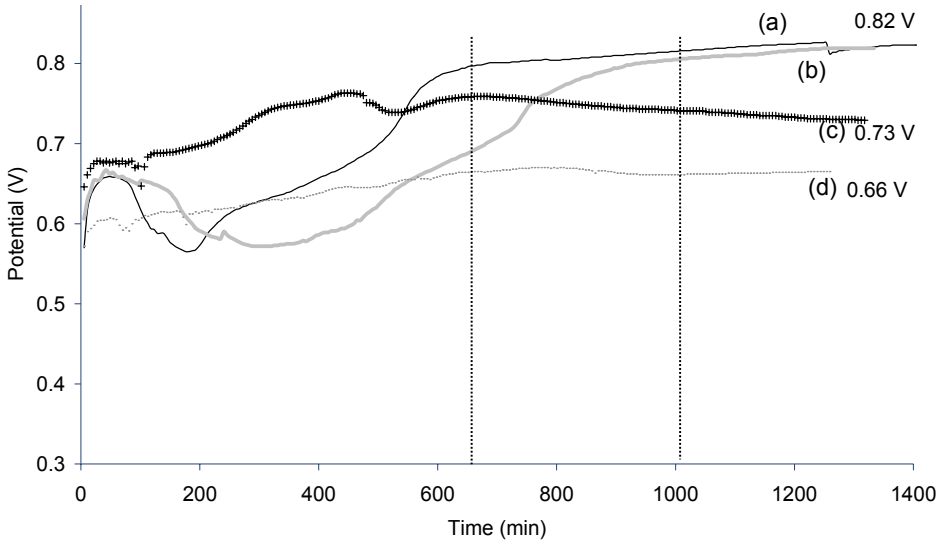

Figure 6.7 The OCP in-situ of PTTh polymerised at RT in various concentrations of APS: (a) 1.5 M APS, (b) 1.0 M APS, (c) 0.5 M APS, and (d) 0.2 M APS. Final potentials are indicated for each APS concentration. The potentials are vs. Ag/AgCl (3.0 M NaCl).

A dark brown/green product was obtained for the samples synthesised from 1.5 M and 1.0 M APS whereas the polymer was more brownish in colour when APS concentrations of 0.5 M and 0.2 M APS were used. This suggested that a lower doping level was achieved for PTTh-DBSA synthesised using low APS concentrations since PTTh is red in its reduced form and blue to black in its oxidised form[19,34]. All samples could be redispersed in water after centrifugation and washing.

UV-visible spectra (Figure 6.8) of most samples showed a single broad peak with λ_{max} in the range of 390 to 410 nm. These λ_{max} were assigned as π-π^* transition of the conjugated backbone. Polymerisation process results in a decrease in the π-π^* transition energy and an increase in the conjugation length of the polymer, hence a different peak position shown in the UV-visible spectrum[36,37]. The red-shift and blue-shift of the spectra obtained from PTTh growth at various oxidation potentials have also been investigated by Zhang *et al*[37] who concluded that the ring linkage and the chain length of the polymer were

greatly influenced by the applied oxidation potential. In this study, using 0.2 M APS during synthesis, the polymerisation reaction partially proceeded as the monomer absorption peak was still observed at 359 nm (Figure 6.8 d). The λ_{max} of the monomer solution in ethanol was measured and appeared at 354 nm (data not shown). The sample possibly contains only oligomers and short chain polymer as the maximum oxidation potential from the OCP profile (Figure 6.7 d) reached only 0.66 V for the PTTh-DBSA nanoparticles synthesised using 0.2 M APS. The oxidation potential increased to 0.73 V in the reaction media containing 0.5 M APS and the λ_{max} obtained at 411 nm (Figure 6.8 c) indicated a higher conjugation length. When the oxidant concentration was increased to 1.0 M or 1.5 M, the OCP increased to about 0.82 V and the λ_{max} appeared at 395 and 385 nm (Figure 6.8 b and a), respectively. These polymers possibly have shorter conjugation length, as also reported by Zhang *et al*[37] using infrared spectroscopy that the peak of irregularly α,β-linked thiophene rings appeared from the polymer synthesised at applied potential 0.85 V resulting in a decreased effective conjugated chain length. Polaronic band at about 990 nm normally indicates the polymer to be in the doped state. This band was only slightly observed in UV-visible spectra when 1.5 M and 1.0 M APS were used during synthesis (Figure 6.8 a and b). Therefore, all samples were most likely to be in neutral state. The doping level was investigated further in Raman study section below.

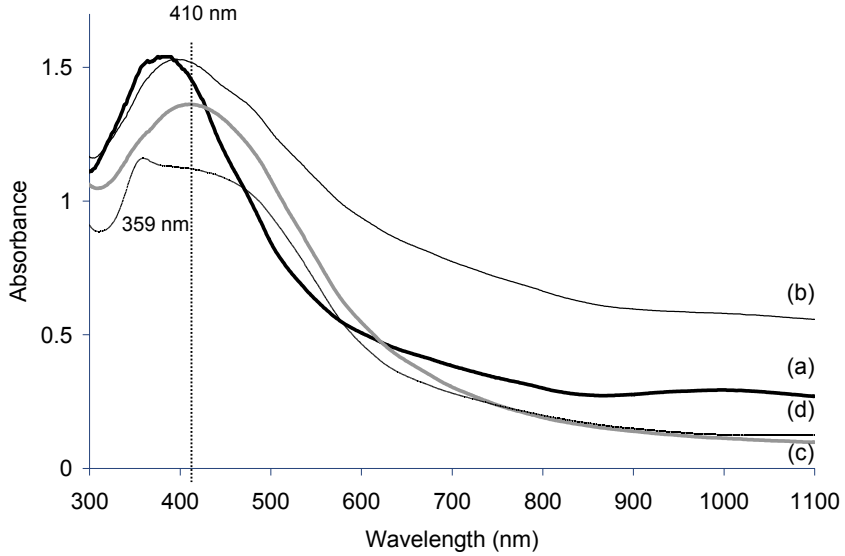

Figure 6.8 UV-vis absorption spectrum of PTTh-DBSA from various concentrations of APS used: (a) 1.5 M, (b) 1.0 M, (c) 0.5 M, and (d) 0.2M.

The OCP (Figure 6.7) showed that PTTh-DBSA synthesised with 1.0 M APS reached equilibrium at the same oxidation potential as when 1.5 M APS was used. UV-visible spectrum of PTTh-DBSA synthesised using 1.0 M APS showed λ_{max} at higher wavelengths indicating higher conjugation length compared to PTTh-DBSA synthesised using 1.5 M APS. Therefore, 1.0 M APS was used as oxidant for all further experiments.

The oxidation level of dried PTTh-DBSA nanoparticles synthesised using various concentrations of APS was investigated using Raman spectroscopy (Figure 6.9). The Q_1 (1420 cm^{-1}) and Q_2 (1400 cm^{-1}) peaks of quinoid species (see Table 6.1) were present only as shoulders. Also the ratio intensities of the ν_6 (736 cm^{-1}), ν_7 group (693 cm^{-1}) and D kink bands (about 650-740 cm^{-1}) to the intensity of the ν_2 peak at about 1455 cm^{-1} was lower than in the Raman spectra obtained for electrochemically synthesised PTTh-DBSA. These results are in good agreement with UV-visible spectra in Figure 6.8 as only a very weak

polaronic band appeared indicating that the chemically synthesised PTTh-DBSA nanoparticles was predominantly in the neutral state. The oxidation state among the PTTh-DBSA synthesised from various APS concentration was investigated as discussed below.

Synthesised with 1.0 M APS suggests that the peak at 1437 cm^{-1} may be caused by some overlap between Q_1 radical cations band (about 1420 cm^{-1}) and ν_2 (about 1455 cm^{-1}) peaks (Figure 6.9 a). The peak at 1517 cm^{-1} of ν_1 band is assigned to the symmetric stretching of the aromatic C=C bond ring which shifts to higher frequencies as the conjugation length is increased[42]. Moreover, the intensity ratio of the ν_6, ν_7 group and D kink bands to the intensity of the ν_2 peak was highest in this sample. The sample prepared with 0.2 M APS (Figure 6.9 c) showed the ν_1 band at a lower wavenumber (1501 cm^{-1}) indicating a shorter conjugation length. From these results, it appeared that the sample prepared with 1.0 M APS had a higher oxidation level compared to the polymer synthesised with 0.2 M and 0.5 M APS.

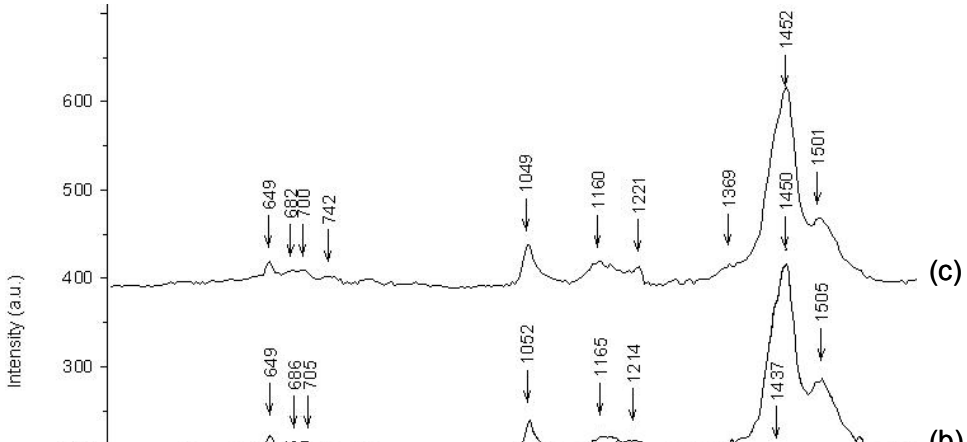

Figure 6.9 Raman spectra of dried PTTh-DBSA from various concentrations of APS used: (a) 1.0 M, (b) 0.5 M, and (c) 0.2 M. The spectra were observed using 632.8 nm excitation line.

Mass of product obtained after synthesis (g product/L reaction mixture) of these samples are shown in Table 6.3. DLS was used to determine particle size of the PTTh-DBSA synthesised using various concentrations of APS and particle size distribution of the sample synthesised with 1.0 M APS is shown in Figure 6.10. Although the sample synthesised using 0.5 M APS gave the maximum quantity of polymer the particle size was very large (over 3000 nm). The particle size of the sample synthesised using 0.2 M APS was also over 3000 nm.

Table 6.3 Mass of product of PTTh-DBSA synthesised from various concentrations of APS used.

[APS]/M	Mass of product (g/L)
1.0	2.40
0.5	3.47
0.2	1.88

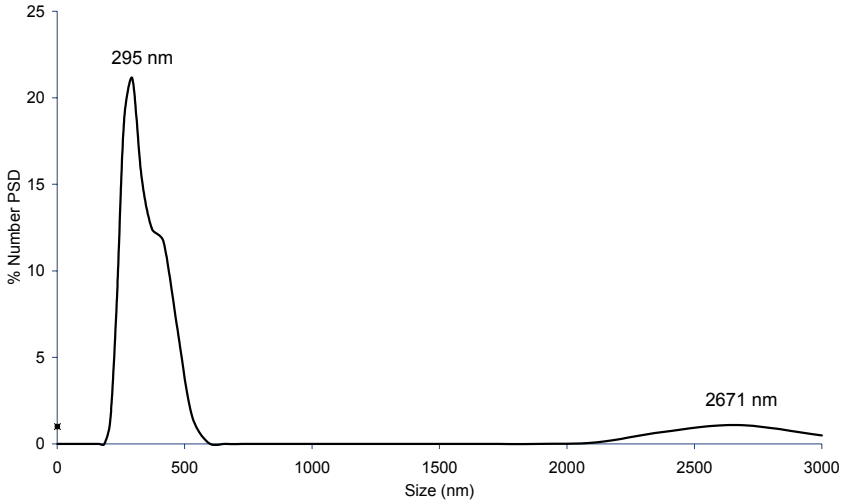

Figure 6.10 Particle distribution of chemically synthesised PTTh-DBSA from 1.0 M APS, 0.01 M TTh and 0.2 M DBSA.

The sample synthesised with 1.0 M APS appears to be the best as it contained the smallest particle size (Figure 6.10), and also had the highest oxidation level as indicated by UV-visible and Raman spectroscopy above. This confirmed that 1.0 M APS was the optimum oxidant concentration and was then used as oxidant to investigate the effect of surfactant concentration.

6.3.1.2.2 Effect of surfactant concentration

The effect of DBSA concentration on the polymerisation process was investigated. The concentration of TTh monomer was maintained at 0.01 M and, from the results of the previous section, the oxidant concentration was chosen to be 1.0 M. The concentration of DBSA was varied from 0.05 - 0.2 M. These samples were prepared using an overhead stirrer with higher speed than previously used; hence the system reached the equilibrium potential in a shorter period of time (Figure 6.11). The equilibrium OCP for all DBSA concentrations used was 0.80-0.82 V. It was found that the higher the DBSA concentration,

the longer it took to reach equilibrium (Figure 6.11). The OCP of the reaction media containing 0.2 M DBSA reached equilibrium after about 800 min, whereas the sample containing 0.05 M DBSA reached equilibrium at about 400 min. The slower polymerisation process is probably due to higher viscosity at higher DBSA concentration hindering the mobility of oxidant and monomer. Fall *et al*[18] also reported that monomer becomes trapped inside micelles resulting in slower rate of polymerisation.

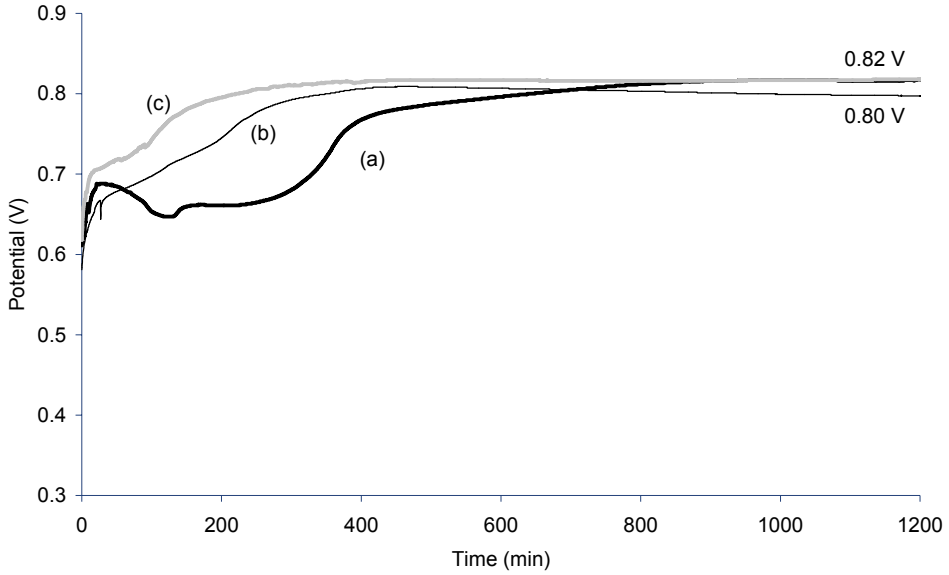

Figure 6.11 The OCP in-situ of PTTh polymerised at RT in various concentrations of DBSA: (a) 0.2 M, (b) 0.1 M, and (c) 0.05 M. The potentials are vs. Ag/AgCl (3.0 M NaCl).

UV-visible spectra (Figure 6.12) obtained for PTTh-DBSA dispersions synthesised using various concentrations of DBSA were similar to those observed when the oxidant concentration was varied (Figure 6.8). The UV-visible spectrum of the reaction product obtained using 0.05 M DBSA (Figure 6.12 c) showed λ_{max} at 408 nm and a peak at 352 nm. Since the TTh monomer has a λ_{max} of 354 nm, the UV-visible spectrum indicated incomplete polymerisation for this sample. The value for λ_{max} was found to be highest for the sample prepared using 0.1 M DBSA (408 nm) indicating a longer conjugation length in

the polymer backbone. However, a weak shoulder peak appeared at about 359 nm and no polaron band was observed for this sample (Figure 6.12 b). These observations suggest an incomplete polymerisation process in these two samples whereas the sample grown with 0.2 M DBSA showed the λ_{max} at 395 nm without the monomer peak at about 354 nm (Figure 6.12 a) which indicates more complete polymerisation.

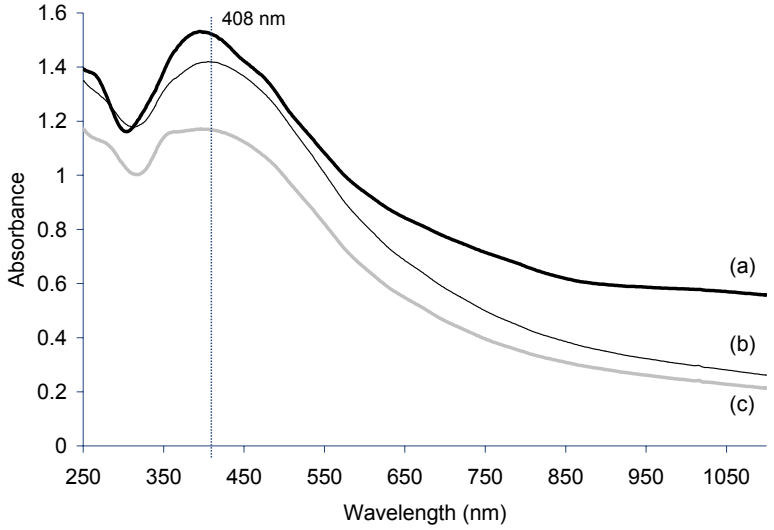

Figure 6.12 UV-vis absorption spectra of PTTh-DBSA from various concentrations of DBSA used: (a) 0.2 M, (b) 0.1 M, and (c) 0.05 M.

Raman spectra of dried PTTh-DBSA nanoparticles synthesised using various concentrations of DBSA were studied and found to have similar features as the spectra shown in Figure 6.9. The band of Q_1 at about 1420 cm^{-1} and ν_2 at about 1455 cm^{-1} were overlapped and shown at about 1437-1445 cm^{-1} in the PTTh-DBSA nanoparticles synthesised using various concentrations of DBSA (Figure 6.13). The ratio of signal intensities for the ν_6, ν_7 group and D kink bands (about 650-740 cm^{-1}) to the intensity of the ν_2 peak at about 1455 cm^{-1} was highest in this sample. Therefore, the polymer synthesised from 0.2 M DBSA seems to have the highest doping level of those investigated.

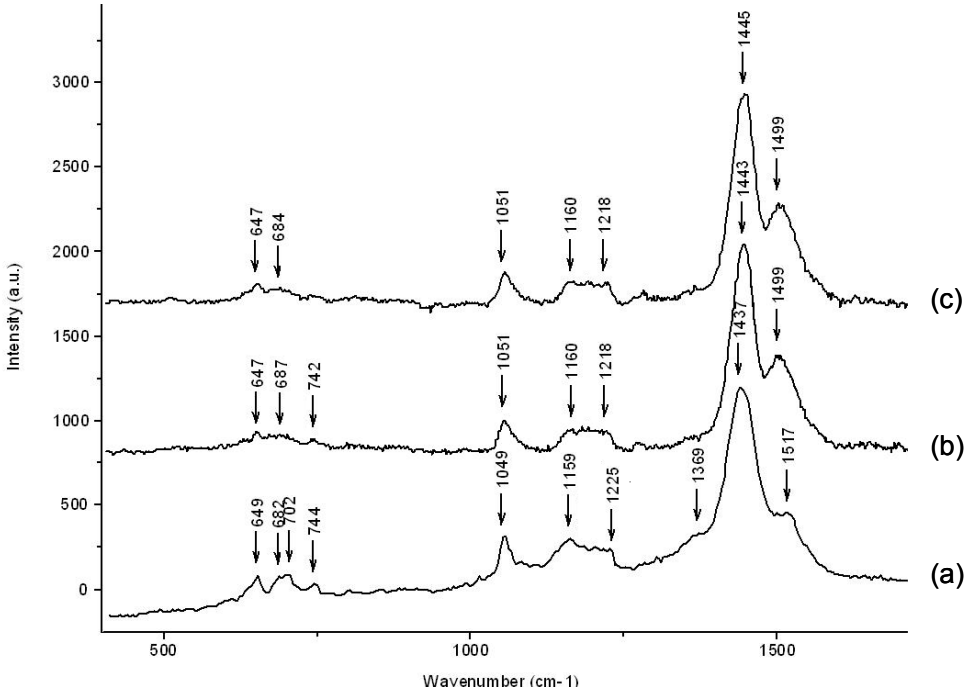

Figure 6.13 Raman spectra of dried PTTh-DBSA from various concentrations of DBSA used: (a) 0.20 M, (b) 0.10 M, and (c) 0.05 M. The spectra were observed using 632.8 nm excitation line.

The mass of product obtained are shown in Table 6.4. The particle size distribution of PTTh-DBSA nanoparticles synthesised from 0.10 M DBSA is shown in Figure 6.14. The PTTh-DBSA synthesised from 0.05 M DBSA showed very large particle sizes (over 3000 nm) possibly due to insufficient surfactant concentration to stabilise the polymer particle, hence they aggregated. The PTTh synthesised using 0.10 M DBSA provided the maximum quantity of polymer obtained from polymerisation and the particle size was in the same range as that produced using 0.20 M DBSA (Figure 6.10) but it showed a lower doping level as indicated by the UV-visible and Raman spectra described earlier.

Table 6.4 Mass of product of PTTh-DBSA from various concentrations of DBSA used during synthesis.

[DBSA]/M	Mass of product (g/L)
0.20	3.53
0.10	3.00
0.05	3.07

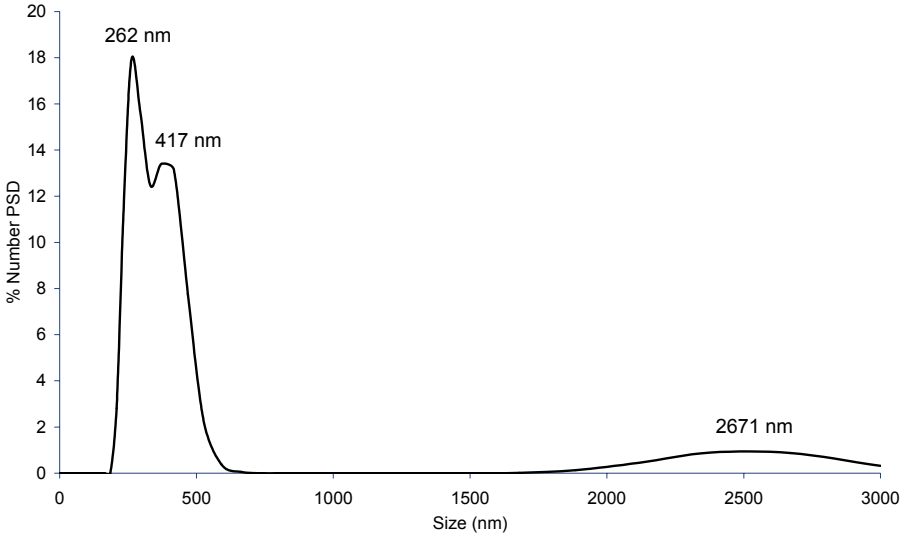

Figure 6.14 Particle size distribution of chemically synthesised PTTh-DBSA from 0.1 M DBSA, 0.01 M TTh and 1.0 M APS.

From the results of UV-visible, Raman, particle size and mass of product, it was concluded that decrease in the APS and DBSA concentration did not result in any improved properties but contributed to larger particle size. Therefore, further investigation was undertaken on PTTh-DBSA synthesised with 1.0 M APS and 0.2 M DBSA.

6.3.1.2.3 Electroactivity study

Cyclic voltammetry was used to investigate the electrochemical properties of the PTTh-DBSA synthesised using 1.0 M APS and 0.2 M DBSA. Attempts to monitor the electroactivity of a polymer dispersion in aqueous 0.1M $LiClO_4$ electrolyte was not successful, therefore the polymer was cast as a film onto a glassy carbon electrode and CVs obtained (Figure 6.15). Only the first cycle is shown as the current dropped very quickly on the later scans. The loss of current magnitude may be due to the particles not well adhered to the electrode surface[39]. The CV obtained was featureless, however showed very weak and broad reduction peak at about 0.53 V.

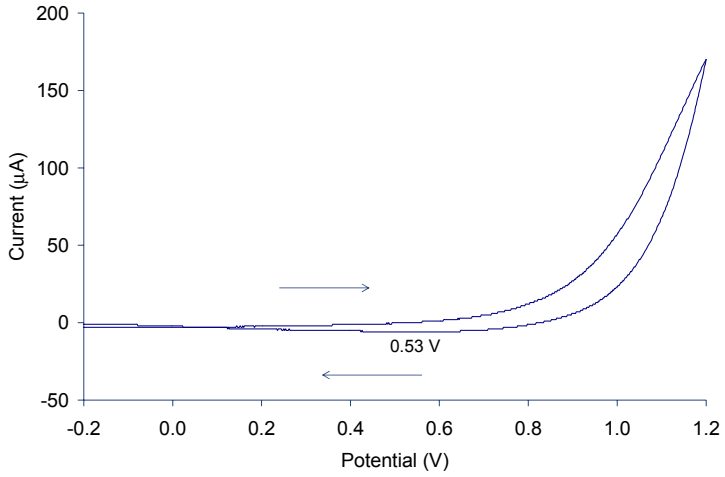

Figure 6.15 Cyclic voltammograms of chemically synthesised PTTh-DBSA cast onto ITO-coated glass, at scan rate of 50 mV/s in 0.1M $LiClO_4$/water (arrows show the direction of the scan). $E_{initial}$ is 0.0 V and the potentials are vs. Ag/AgCl (3.0 M NaCl).

The PTTh-DBSA cast film was also scanned in a solution containing 0.1M tetrabutyl ammonium perchlorate (TBAP) in acetonitrile (Figure 6.16). The CV was stable only for a couple of cycles with the current decaying rapidly indicating instability of the film once again. The CV was similar to those obtained when scanned in aqueous-based electrolyte. It was featureless and showed only reduction peak at about 0.42 V.

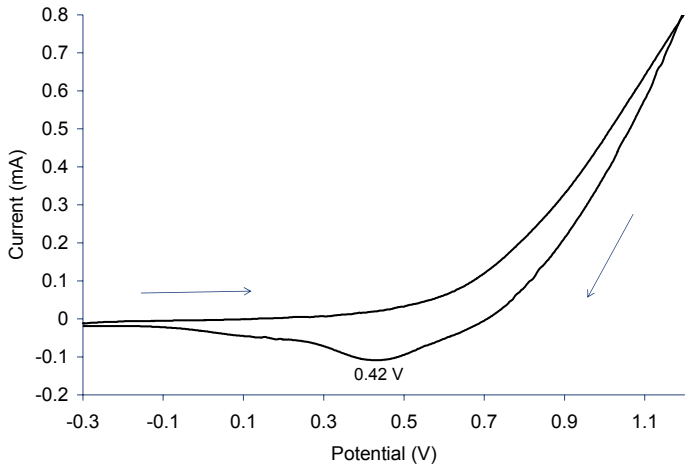

Figure 6.16 Cyclic voltammograms of chemically synthesised PTTh-DBSA cast onto glassy carbon electrode at scan rate of 50 mV/s in 0.1M TBAP/acetonitrile (arrows show the direction of the scan). $E_{initial}$ is 0.0 V and the potentials are vs. Ag/Ag^{+}.

Using an alternative approach to obtain a better electrochemical signal for PTTh-DBSA nanoparticles, the polymer was dried and redissolved in chloroform. The PTTh-DBSA nanoparticles were only partially soluble in chloroform, however chloroform-soluble fraction was cast as a film onto a glassy carbon electrode and the CV obtained in an aqueous- or acetonitrile-based electrolyte solutions. The CV in aqueous solution was still featureless and similar to Figure 6.15, although a slight anodic peak was observed at about 1.0 V (not shown). Conversely, the CV in acetonitrile-based electrolyte showed, after the first scan, two stable redox couples at about 0.49 V/0.33 V and 0.92 V/0.78 V (Figure 6.17). This result agrees with previous observations that PTTh shows better electroactivity and reversibility in organic solvents[36]. The decrease of current after the first cycles is possibly caused by poor film adherence to the electrode[39].

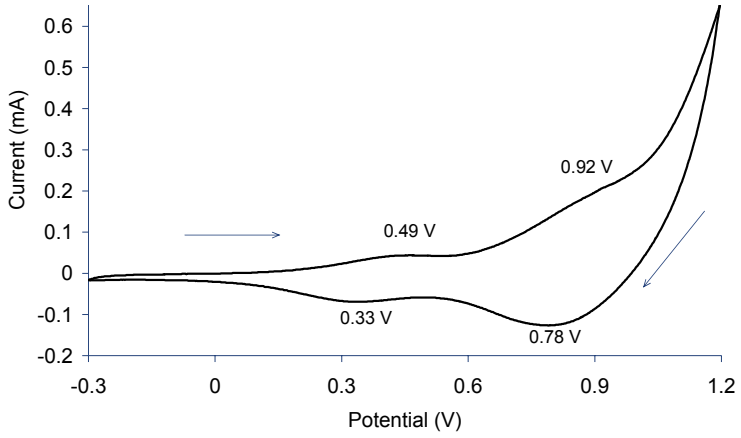

Figure 6.17 Cyclic voltammograms of film cast from chloroform soluble fraction of chemically synthesised PTTh-DBSA on ITO-coated glass, at scan rate 50 mV/s (arrows show the direction of the scan). 0.1M TBAP in acetonitrile was used as electrolyte. $E_{initial}$ is 0.0 V and the potentials are vs. Ag/Ag^{+}.

6.3.1.2.4 Colloidal stability

The PTTh-DBSA nanoparticles were diluted to a concentration of 5.6 mg/ml in water or 0.05 M SDS. These were left standing in glass vials at room temperature for 8 months. Most of the polymer precipitated after the first day, with small particles remaining in the solution for up to 8 months for both solutions (Figure 6.17). There was no influence of electrolyte concentrations as the sample in water and in SDS showed the same stability.

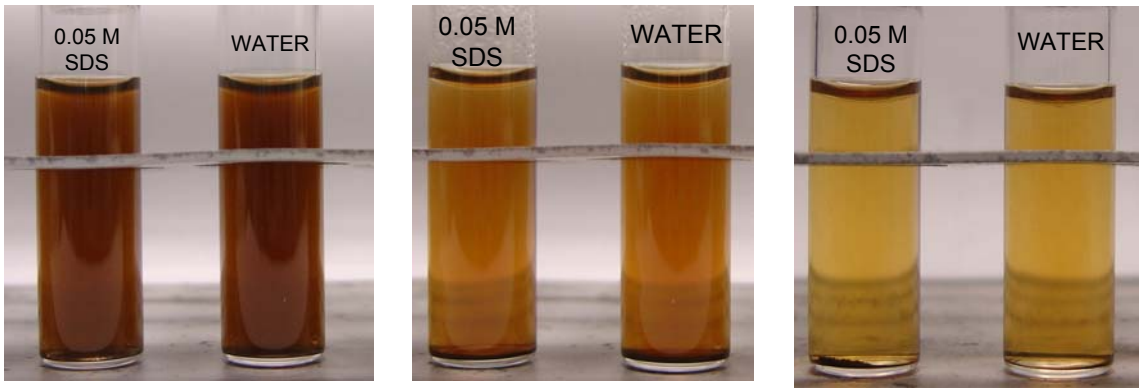

(a) (b) (c)

Figure 6.18 Photographs of chemically synthesised PANI-DBSA nanodispersion stability in 0.05 M SDS and water (5 mg/ml) (a) initial, (b) day 1 and (c) 8 months.

6.3.1.2.5 Size and morphology study using TEM

TEM obtained for the PTTh-DBSA nanoparticles showed mixed morphology ranging from spherical particles to irregular clusters as shown in Figure 6.19. The size of nanoparticles varied from about 30 to 200 nm.

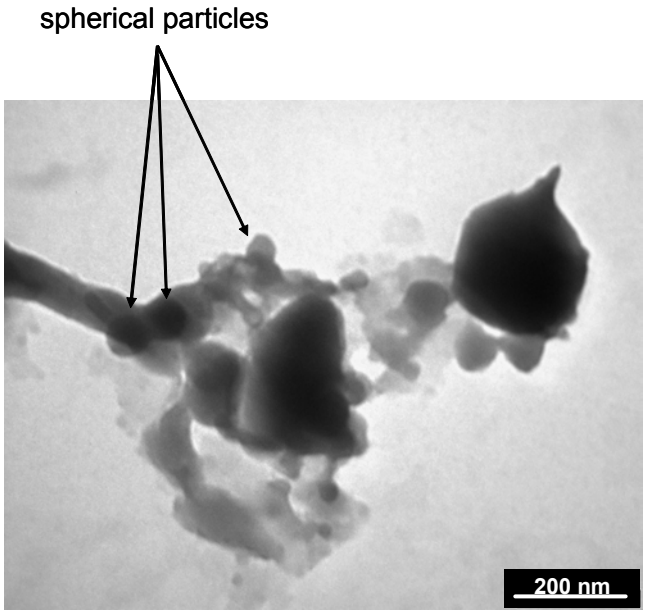

Figure 6.19 Transmission electron microscopic picture of chemically synthesised PTTh-DBSA at 100 KeV.

6.3.2 PTTh nanoparticles synthesised in IL

6.3.2.1 Chemical synthesis of PTTh nanoparticles in emiTFSA

6.3.2.1.1 Effect of oxidant concentration

Preliminary results showed that APS was partially dissolved in the IL emiTFSA whereas $AuCl_3$ was highly soluble at least up to 0.2 M. The TTh monomer was also partially soluble in emiTFSA at room temperature. However, gentle heating up to about 40 °C allowed 0.050 M TTh to be dissolved. The polymerisation started instantly upon

addition of the oxidant as indicated by a colour change from yellow to black and precipitate formation. The oxidation of the TTh monomer is coupled to the reduction of Au(III) to gold metal. It is therefore most likely that gold metal was incorporated during the synthesis.

In order to investigate the effect of oxidant concentration, the monomer concentration was maintained at 0.050 M and the oxidant was varied from 0.010 – 0.050 M.

Upon completion of polymerisation, the product dispersions were purified as outlined in the experiment section (6.2.3.3). The polymer was dispersed in water using 5 min sonication. UV-visible spectra of the PTTh nanodispersions prepared using various $AuCl_3$ oxidant concentrations are shown in Figure 6.20. The π-π* transition peak appears at about 370 nm for all samples. The polaronic wave starting from about 650 nm to 850 nm was more pronounced for the sample synthesised using the higher concentration of the oxidant. The peak at about 514 nm was possibly due to the surface plasmon absorbance of the gold nanoparticles as observed by Itoh *et al*[46]. This provided some evidence for the incorporation of gold metal into the PTTh nanoparticles.

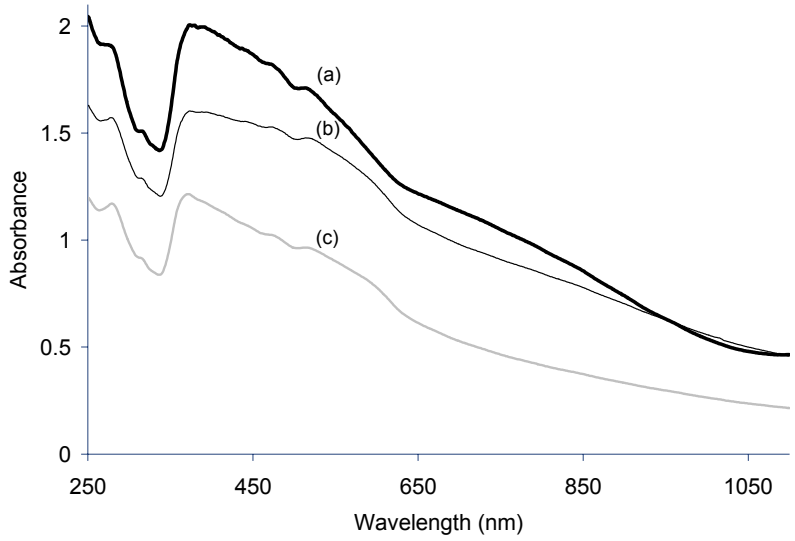

Figure 6.20 UV-visible spectra of PTTh nanoparticles synthesised in emiTFSA from: (a) 0.05 M, (b) 0.025 M, and (c) 0.01 M $AuCl_3$, dispersed in water.

The oxidation state of PTTh nanoparticles synthesised in emiTFSA was examined using Raman spectroscopy (Figure 6.21). The Raman bands obtained for the samples synthesised from various concentrations of $AuCl_3$ showed up in the same position (Figure 6.21) but were slightly different from the chemically synthesised PTTh-DBSA sample (Figure 6.9 and Figure 6.13). The peak of quinoid band Q_1 appeared to be slightly more pronounced at about 1425 cm^{-1} than that observed for PTTh-DBSA. This suggested PTTh nanoparticles synthesised in emiTFSA had a slightly higher doping level than the chemically synthesised PTTh-DBSA nanoparticles.

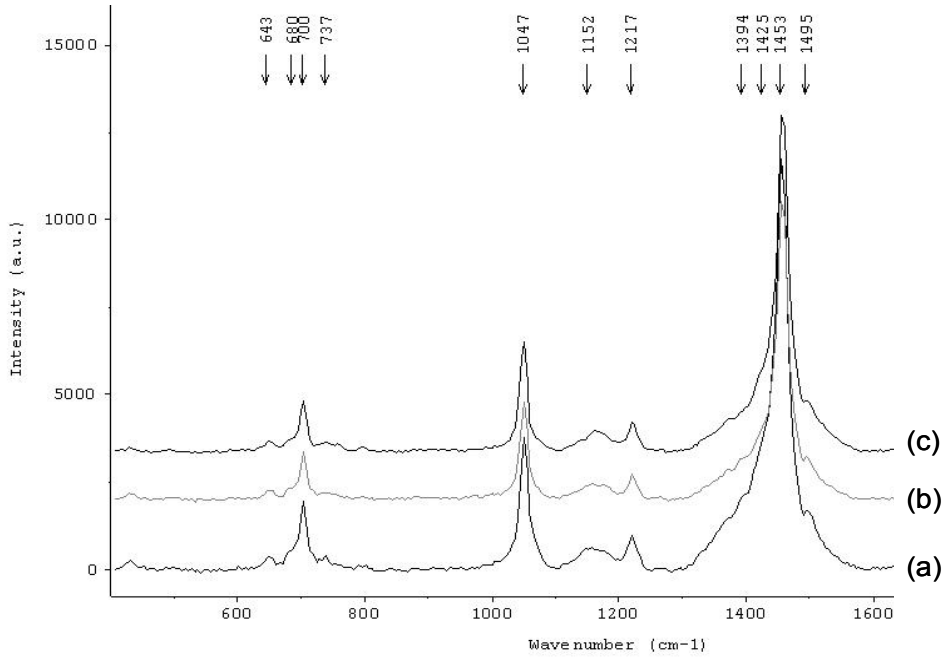

Figure 6.21 Raman spectra of PTTh nanoparticles synthesised in IL using: (a) 0.05 M, (b) 0.025 M, and (c) 0.01 M $AuCl_3$. The spectra were observed using 632.8 nm excitation line.

The PTTh nanoparticles synthesised in IL can be dispersed in water using a short period of sonication and the particle size distribution obtained is shown in Figure 6.22.

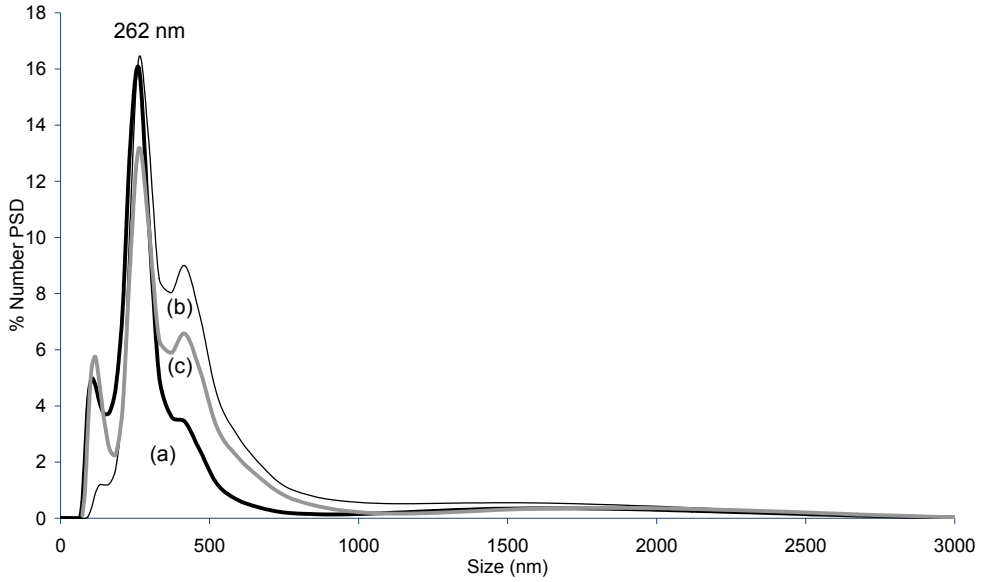

Figure 6.22 Particle size distribution of PTTh nanoparticles synthesised in IL using: (a) 0.05 M, (b) 0.025 M, and (c) 0.01 M $AuCl_3$.

The particle size of all samples was in the same range with the highest population at 262 nm. The particle size of PTTh nanoparticles synthesised in emiTFSA were smaller than for the PTTh-DBSA nanoparticles as it showed some smaller particles about 116 nm, and also lower percentage of the particles in the large size range at about 2671 nm compared to the particle size distribution of PTTh-DBSA (Figure 6.10).

6.3.2.1.2 Effect of solvent

The effect of varying the polymerisation solvent was investigated by synthesis of PTTh in ethanol. The concentrations of monomer and oxidant were maintained constant at 0.05 M. UV-visible spectra, CVs and Raman spectra were obtained for the resultant polymers.

The UV-visible spectrum obtained for PTTh nanoparticles synthesised in ethanol

(Figure 6.23 b) showed λ_{max} at 392 nm, which is red-shifted 22 nm from the PTTh nanoparticle synthesised in emiTFSA (Figure 6.23 a) indicating a higher conjugation length. The free carrier tail was also slightly more pronounced than the sample synthesised in emiTFSA indicating more conductive PTTh synthesised in ethanol compared to those synthesised in emiTFSA.

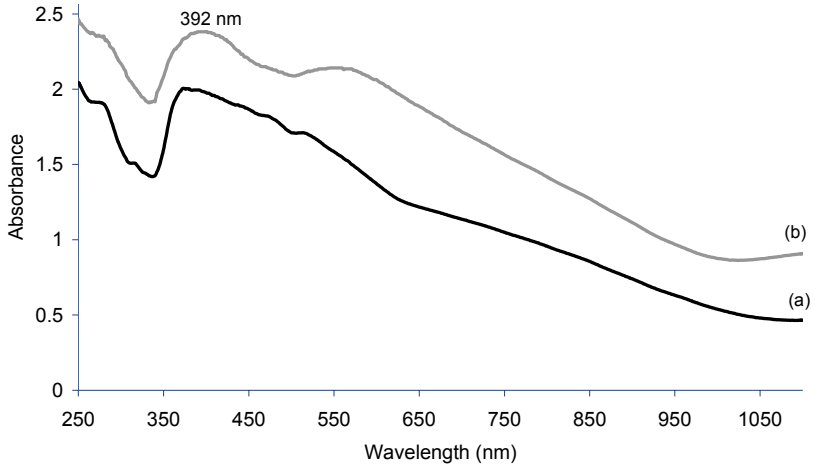

Figure 6.23 UV-vis absorption spectra obtained for PTTh/gold nanoparticles synthesised in: (a) emiTFSA , and (b) ethanol, dispersed in water.

The Raman spectra of PTTh synthesised in ethanol and in emiTFSA showed slight difference in terms of doping state as bands appeared at similar wavenumbers (Figure 6.24). The peak of quinoid band Q_1 for PTTh nanoparticles synthesised in emiTFSA (Figure 6.24 a) appeared to be slightly more pronounced at about 1425 cm^{-1} than that observed for the PTTh synthesised in ethanol (Figure 6.24 b). Also the intensity ratio of the ν_7 peak at about 702 cm^{-1} to the ν_2 peak at about 1452 cm^{-1} was slightly higher for the sample synthesised in emiTFSA indicating a slightly higher doping level in this sample.

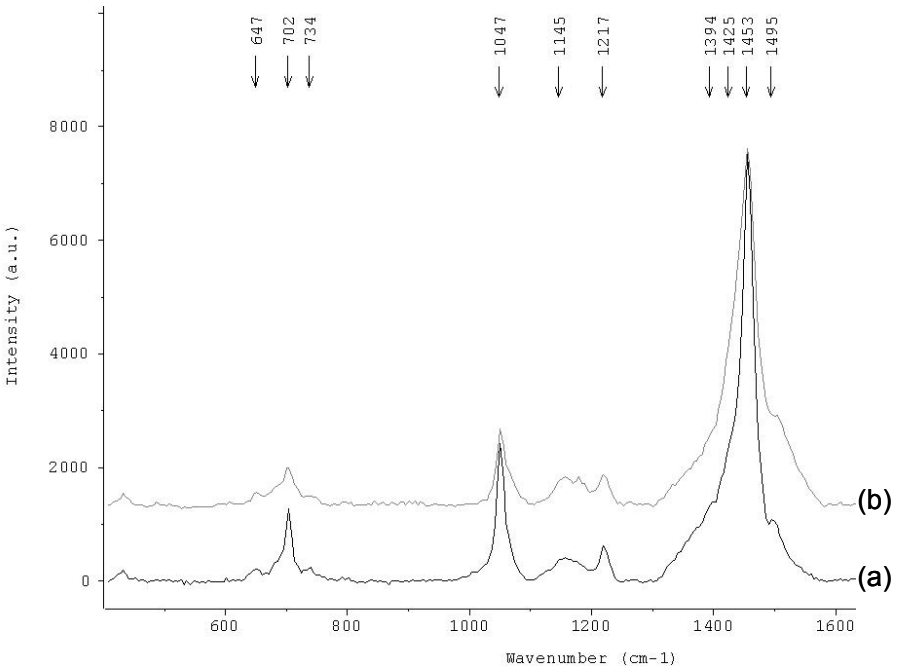

Figure 6.24 Raman spectra of PTTh nanoparticles synthesised in: (a) emiTFSA, and (b) ethanol. The spectra were observed using a 632.8 nm excitation line.

6.3.2.1.3 Electroactivity study

PTTh nanoparticles synthesised in emiTFSA were cast as films onto glassy carbon electrodes and characterised using CV. These films were scanned in aqueous-based and acetonitrile-based electrolyte solutions as shown in Figure 6.25 and 6.26, respectively. The oxidation and reduction peaks are summarised in Table 6.5. The CVs were more defined in acetonitrile as two reduction peaks were observed (Table 6.5). Also the CVs obtained for the PTTh nanoparticles synthesised in emiTFSA using a 0.025 M and 0.050 M $AuCl_3$ were well defined and two reduction peaks were observed whereas only one reduction peak appeared when 0.010 M $AuCl_3$ was used.

The CVs obtained from cast films of PTTh nanoparticles synthesised in emiTFSA performed in either aqueous-based (Figure 6.25) or acetonitrile-based (Figure 6.26) electrolyte were much more defined than the CVs obtained from cast films of PTTh-DBSA nanoparticles performing in the same electrolyte (Figure 6.15 and 6.16). This indicated more effective charge transfer in PTTh nanoparticles synthesised in emiTFSA than PTTh-DBSA nanoparticles which is possibly due to the incorporation of gold in the polymer matrix.

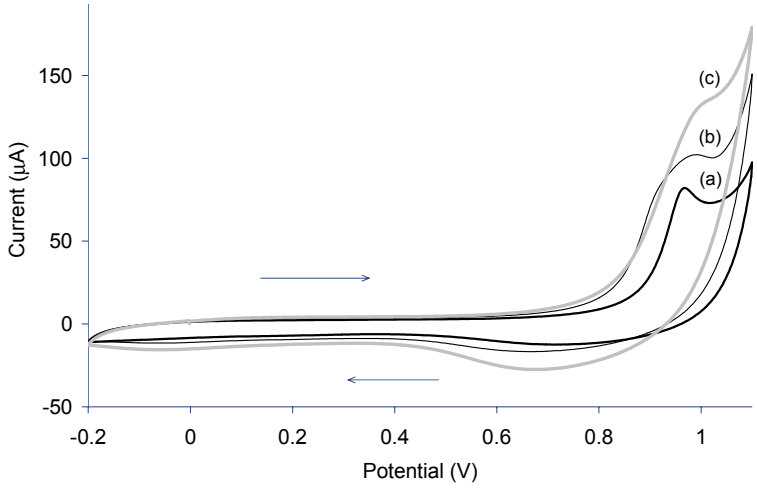

Figure 6.25 Cyclic voltammograms in 0.1 M $LiClO_4$/water of cast films of PTTh nanoparticles synthesised in emiTFSA from: (a) 0.05 M, (b) 0.025 M, and (c) 0.01 M $AuCl_3$ at scan rate100 mV/s (arrows show the direction of the scan). $E_{initial}$ is 0.0 V and the potentials are vs. Ag/AgCl (3.0 M NaCl).

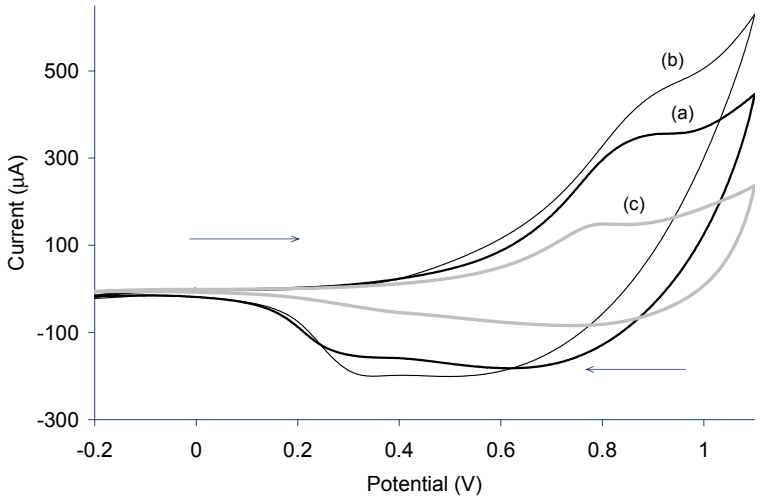

Figure 6.26 Cyclic voltammograms in 0.1 M TBAP/ACN of drop cast films of PTTh nanoparticles synthesised in emiTFSA from: (a) 0.05 M, (b) 0.025 M, and (c) 0.01 M $AuCl_3$ at scan rate100 mV/s (arrows show the direction of the scan). $E_{initial}$ is 0.0 V and the potentials are vs. Ag/Ag^+.

Table 6.5 Summary of oxidation and reduction peaks from drop cast films of PTTh nanoparticles synthesised in emiTFSA , scanned in water and acetonitrile.

$[AuCl_3]$/M	cycled in water (Figure 6.25)		cycled in acetonitrile (Figure 6.26)		
	E_{ox2}/V	E_{red2}/V	E_{ox2}/V	E_{red1}/V	E_{red2}/V
0.010	1.00	0.66	0.81	0.36	-
0.025	0.99	0.66	0.92	0.32	0.50
0.050	0.98	0.68	0.90	0.33	0.61

The electroactivity of the polymer synthesised in ethanol was also investigated (Figure 6.27). The oxidation peak at 0.94 V was well defined and two reduction peaks were observed at 0.35 V and 0.57 V (Figure 6.27). This CV was similar to the CVs obtained with the PTTh nanoparticles synthesised in emiTFSA (Figure 6.26). The CVs obtained for PTTh nanoparticles synthesised in both emiTFSA and ethanol are similar to those reported by Zhang *et al*[37] who synthesised PTTh in boron-fluoride ethyl ether (BFEE).

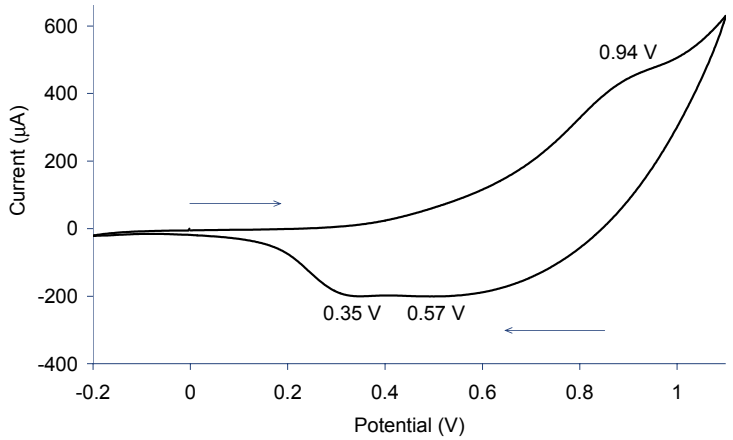

Figure 6.27 Cyclic voltammograms in 0.1 M TBAP/ACN of drop cast films PTTh nanoparticles synthesised in ethanol at scan rate100 mV/s (arrows show the direction of the scan). $E_{initial}$ is 0.0 V and the potentials are vs. Ag/AgCl (3.0 M NaCl).

6.3.2.1.4 Colloidal stability

The PTTh nanoparticles synthesised in emiTFSA can be dispersed in water using 5 min sonication. The particles stayed in the solution for several hours, thus the colloidal stability was not as good as the chemically synthesised PTTh-DBSA nanoparticles.

The PTTh nanoparticles obtained from synthesis in ethanol were not well dispersed in aqueous solution. Approximately 10 min sonication was used to disperse the PTTh nanoparticles synthesis in ethanol and the precipitates were observed after the dispersion was left standing for 5-10 min suggesting poor colloidal stability.

6.3.2.1.5 Size and morphology study by TEM

TEMs of PTTh nanoparticles synthesised in emiTFSA are shown in Figure 6.28. The morphology of the PTTh nanoparticles synthesised in emiTFSA is spherical but the particle size varied from about 50 nm to a few hundred nanometres. This sample showed a much improved uniform particle size distribution compared to PTTh-DBSA.

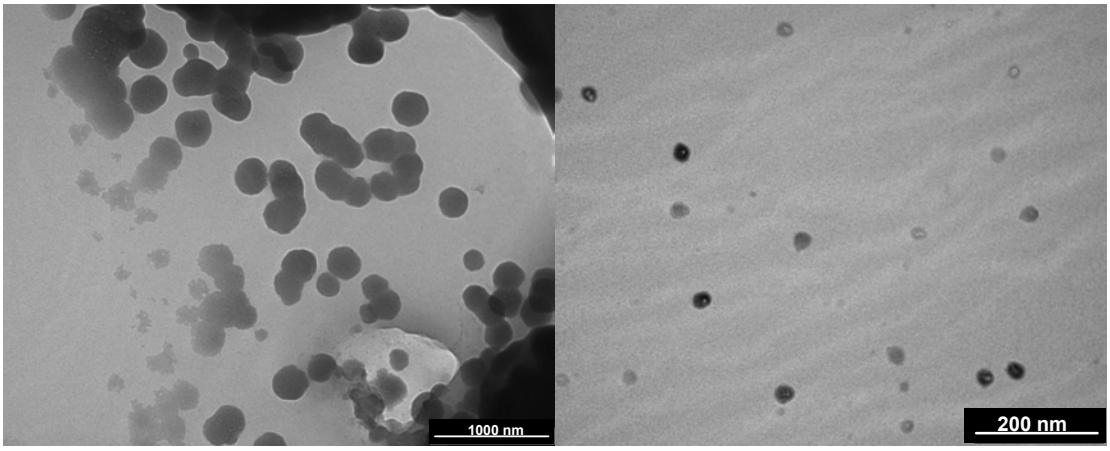

Figure 6.28 Transmission electron microscopic picture at 100 KeV of PTTh nanoparticles synthesised from 0.05M Th and 0.025 M $AuCl_3$ in emiTFSA.

6.4 Conclusions

This chapter demonstrates that PTTh nanoparticles synthesised in the presence of surfactant (DBSA) and in IL (emiTFSA) could be dispersed in water. For the chemical synthesis of PTTh-DBSA, the optimal concentration of the oxidant is 1.0 M and the surfactant concentration is 0.20 M when 0.01 M TTh is used. The particle size of PTTh-DBSA, as observed by TEM, varies from small spherical particles (about 30 nm) to irregular clusters. These nanoparticles can be readily dispersed in water without sonication. Although most of the particles precipitated out of the solution overnight some small particles were suspended in the solution for up to 8 months. The PTTh-DBSA nanodispersions show poor electroactivity. UV-visible and Raman spectra also indicate the formation of short chain polymers with lower doping level.

Although the PTTh nanoparticles synthesised in emiTFSA need sonication to be dispersed in water they show good electrochemistry and the particle sizes in the range of about 50 nm to a few hundred nanometres as observed by TEM. UV-visible and Raman spectra indicate relatively high doping levels in PTTh nanoparticles synthesised in emiTFSA or ethanol. The potential use of these nanoparticles in photovoltaic devices is being investigated in another study within our laboratory. The PTTh nanoparticles synthesised in ethanol cannot be dispersed in water. However, they show similar electrochemical properties as the polymer synthesised in emiTFSA.

6.5 References

1. Chan, H.S.O. and Ng, S.C., *Progress in Polymer Science*, 1998. **23**(7): p. 1167-1231.
2. Andreani, F., Angiolini, L., Caretta, D., and Salatelli, E., *Journal of Materials Chemistry*, 1998. **8**(5): p. 1109-1111.
3. Welzel, H.-P., Kossmehl, G., Boettcher, H., Engelmann, G., and Hunnius, W.-D., *Macromolecules*, 1997. **30**(24): p. 7419-7426.
4. Emge, A. and Bauerle, P., *Synthetic Metals*, 1999. **102**(1-3): p. 1370-1373.
5. Skabara, P.J., Serebryakov, I.M., Perepichka, I.F., Sariciftci, N.S., Neugebauer, H., and Cravino, A., *Macromolecules*, 2001. **34**(7): p. 2232-2241.
6. Collis, G.E., Burrell, A.K., and Officer, D.L., *Tetrahedron Letters*, 2001. **42**: p. 8733-8735.
7. Chen, J., Burrell, A.K., Collis, G.E., Officer, D.L., Swiegers, G.F., Too, C.O., and Wallace, G.G., *Electrochimica Acta*, 2002. **47**(17): p. 2715-2724.
8. Grant, D.K., Officer, D.L., and Burrell, A.K., *Synthetic Metals*, 2003. **135-136**: p. 103-104.
9. Nilsson, K.P.R., Olsson, J.D.M., Konradsson, P., and Inganas, O., *Macromolecules*, 2004. **37**(17): p. 6316-6321.
10. Ribeiro, A.S., Gazotti, J., Wilson A., dos Santos Filho, P.F., and De Paoli, M.-A., *Synthetic Metals*, 2004. **145**(1): p. 43-49.
11. Jeffries-EL, M., Sauve, G., and McCullough, R.D., *Advanced Materials*, 2004. **16**(12): p. 1017-1019.
12. Gambhir, S., Wagner, K., and Officer, D.L., *Synthetic Metals*, 2005. **154**: p. 117-120.
13. Cutler, C.A., Burrell, A.K., Collis, G.E., Dastoor, P.C., Officer, D.L., Too, C.O., and Wallace, G.G., *Synthetic Metals*, 2001. **123**: p. 225-237.
14. Ahn, S.H., Czae, M.Z., Kim, E.R., Lee, H., Han, S.H., Noh, J., and Hara, M., *Macromolecules*, 2001. **34**(8): p. 2522-2527.
15. Louwet, F., Groenendaal, L., Dhaen, J., Manca, J., Van Luppen, J., Verdonck, E., and Leenders, L., *Synthetic Metals*, 2003. **135**(1-3): p. 115-117.
16. Ballav, N. and Biswas, M., *Polymer International*, 2004. **53**(2): p. 198-203.
17. Bazzaoui, E.A., Aeiyach, S., and Lacaze, P.C., *Synthetic Metals*, 1996. **83**(2): p. 159-165.
18. Fall, M., Aaron, J.J., Sakmeche, N., Dieng, M.M., Jouini, M., Aeiyach, S., Lacroix, J.C., and Lacaze, P.C., *Synthetic Metals*, 1998. **93**(3): p. 175-179.
19. Sakmeche, N., Aeiyach, S., Aaron, J.J., Jouini, M., Lacroix, J.C., and Lacaze, P.C., *Langmuir*, 1999. **15**(7): p. 2566-2574.
20. van Stam, J., Imans, F., Viaene, L., De Schryver, F.C., and Evans, C.H., *Journal of Physical Chemistry B*, 1999. **103**(25): p. 5160-5166.
21. Haegel, F.H., Schlupen, J., Schultze, J.W., Winkels, S., and Stromberg, C., *Electrochimica Acta*, 2001. **46**(26-27): p. 3973-3984.
22. Fall, M., Assogba, L., Aaron, J.J., and Dieng, M.M., *Synthetic Metals*, 2001. **123**(3): p. 365-372.
23. Fall, M., Dieng, M.M., Aaron, J.J., Aeiyach, S., and Lacaze, P.C., *Synthetic Metals*, 2001. **118**(1-3): p. 149-155.

24. Lekpittaya, P., Yanumet, N., Grady, B.P., and O'Rear, E.A., *Journal of Applied Polymer Science*, 2004. **92**(4): p. 2629-2636.
25. Li, C. and Imae, T., *Macromolecules*, 2004. **37**(7): p. 2411-2416.
26. Sadki, S. and Chevrot, C., *Electrochimica Acta*, 2003. **48**(6): p. 733-739.
27. Choi, J.W., Han, M.G., Kim, S.Y., Oh, S.G., and Im, S.S., *Synthetic Metals*, 2004. **141**(3): p. 293-299.
28. Lei, Y., Oohata, H., Kuroda, S., Sasaki, S., and Yamamoto, T., *Synthetic Metals*, 2005. **149**(2-3): p. 211-217.
29. Brustolin, F., Goldoni, F., Meijer, E.W., and Sommerdijk, N., *Macromolecules*, 2002. **35**(3): p. 1054-1059.
30. Bonhote, P., Dias, A.-P., Papageorgiou, N., Kalyanasundaram, K., and Gratzel, M., *Inorganic chemistry*, 1996. **35**: p. 1168-1178.
31. Lu, W., Fadeev, A.G., Qi, B.H., Smela, E., Mattes, B.R., Ding, J., Spinks, G.M., Mazurkiewicz, J., Zhou, D.Z., Wallace, G.G., MacFarlane, D.R., Forsyth, S.A., and Forsyth, M., *Science*, 2002. **297**(5583): p. 983-987.
32. Pringle, J.M., Forsyth, M., MacFarlane, D.R., Wagner, K., Hall, S.B., and Officer, D.L., *Polymer*, 2005. **46**(7): p. 2047-2058.
33. Senadeera, G.K.R., Nakamura, K., Kitamura, T., Wada, Y., and Yanagida, S., *Applied Physics Letters*, 2003. **83**(26): p. 5470-5472.
34. Abdou, M.S.A. and Holdcroft, S., *Synthetic Metals*, 1993. **60**: p. 93-96.
35. Lee, M., Kim, B.W., Nam, J.D., Lee, Y., Son, Y., and Seo, S.J., *Molecular Crystals and Liquid Crystals*, 2003. **407**: p. 397-402.
36. Wallace, G.G., Spinks, G.M., Kane-Maguire, L.A.P., and Teasdale, P.R., *Conductive electroactive polymers : intelligent materials systems*. 2nd ed. 2002, Boca Raton, FL: CRC Press. , and references cited therein.
37. Zhang, D.H., Qin, J.G., and Xue, G., *Synthetic Metals*, 1999. **100**(3): p. 285-289.
38. Sarac, A.S., Evans, U., Serantoni, M., and Cunnane, V.J., *Carbon*, 2003. **41**(14): p. 2725-2730.
39. Brillas, E., Oliver, R., Estrany, F., Rodrigeuz, E., and Tejero, S., *Electrochimica Acta*, 2002. **47**(10): p. 1623-1631.
40. Parakka, J.P., Jeevarajan, J.A., Jeevarajan, A.S., Kispert, L.D., and Cava, M.P., *Advanced Materials*, 1996. **8**(1): p. 54-59.
41. Sarac, A.S., Evans, U., Serantoni, M., Clohessy, J., and Cunnane, V.J., *Surface & Coatings Technology*, 2004. **182**(1): p. 7-13.
42. Bazzaoui, E.A., Levi, G., Aeiyach, S., Aubard, J., Marsault, J.P., and Lacaze, P.C., *journal of physical chemistry*, 1995. **99**(17): p. 6628-6634.
43. Chen, F., Shi, G., Zhang, J., and Fu, M., *Thin Solid Films*, 2003. **424**(2): p. 283-290.
44. Casado, J., Katz, H.E., Hernandez, V., Lopez, J.T., and Navarrete, J.T., *Journal of Physical Chemistry B*, 2002. **106**(10): p. 2488-2496.
45. Fu, M., Shi, G., Chen, F., and Hong, X., *Physical Chemistry Chemical Physics*, 2002. **4**: p. 2685-2690.
46. Itoh, H., Naka, K., and Chujo, Y., *Journal of American Chemical Society*, 2004. **126**: p. 3026-3027.

7.1 Introduction

Polypyrroles, polythiophenes and polyanilines have all been utilised in the development of new biosensing technologies[1-12]. Polyanilines (PANI) have proven particularly useful in the development of biosensors[7-12]. Iwuoha *et al*[8] have described a biosensor format where PANI was electrochemically synthesised, in the presence of polyvinylsulphonate (PVS), onto the surface of a screen-printed carbon paste electrode. The enzyme horseradish peroxidase (HRP) was then incorporated onto the surface of the polymer by electrostatic interactions with the polymer backbone. An amperometric method has been used to examine the immobilised HRP[8], and this biosensor format has since been extended to develop rapid, single-step, separation-free immunosensors for real-time monitoring[9,10] and incorporating multi-calibrant measurements[11].

Polyanilines are synthesised readily from aqueous media and most commonly deposited on electrode surfaces by means of electropolymerisation of aniline[10]. However, processability issues arise from this method, as aniline is a carcinogen, and also must be distilled prior to use. In addition, acidic media are required for the formation of the most highly conductive form of aniline, which does not lend itself to entrapment of proteins for biosensing applications.

Protocols for the synthesis of PANI nanoparticles doped with dodecylbenzenesulphonic acid (DBSA) (*nano*PANI-DBSA) have been developed (Chapter 3). The synthesis of these nanoparticles helps to overcome the processability issues with PANI. Such nanoparticles are purified and readily dispersed in aqueous media. Little or no monomer should be present in these nanoparticle dispersions, thereby reducing carcinogenic properties. The pH of these dispersions could be adjusted to neutral hence

rendering the entrapment of biomolecular species. Nanodimensional conducting polymers have also been shown to exhibit unique properties such as greater conductivity and more rapid electrochemical switching speeds[13].

The work in this chapter illustrates that PANI nanoparticles (*nano*PANI-DBSA), as outlined in Chapter 3, section 3.3.1, can be successfully electrodeposited on the surface of glassy carbon electrodes to form nanostructured films suitable to act as mediators in biosensors. The electrodeposited polymer films were examined by scanning electron microscopy (SEM), atomic force microscopy (AFM), and profilometry. Biomolecules were then electrostatically adsorbed onto this surface for subsequent biosensing. The biosensor performance has been characterised by amperometric detection of hydrogen peroxide with immobilised HRP (see Chapter 1, section 1.3.1).

7.2 Experimental

7.2.1 Chemicals

Horseradish peroxidase (HRP) was purchased from Biozyme Laboratories or Sigma-Aldrich. Bovine serum albumin (BSA), 2,2'-azino-bis(3-ethylbenzthiazoline-6-sulphonic acid) (ABTS), and silver enhancer kit (SE-100) was purchased from Sigma-Aldrich. Colloidal gold-labelled HCGβ monoclonal antibody (MoAb) was purchased from Fitzgerald Industries International (USA). Hydrogen peroxide (H_2O_2) solution, 30% (v/v), was purchased from Merck. Anhydrous di-sodium hydrogen orthophosphate (Na_2HPO_4) was purchased from APS Finechem. Potassium di-hydrogen orthophosphate (KH_2PO_4) was purchased from BDH

Unless otherwise stated, all electrochemical measurements were carried out in a phosphate buffered saline (PBS) solution (0.1 M phosphate, 0.137 M NaCl and 2.7 mM

KCl, pH 6.4). Colorimetric assays were carried out in 10 mM phosphate buffer, (0.33 mM KH_2PO_4 and 0.66 mM Na_2HPO_4), pH 7.0. The ABTS buffer was 200 mM dihydrogen phosphate and 100 mM citric acid, and adjusted to pH 5.5 with concentrated NaOH. Polyaniline-dodecylbenzenesulphonic acid nanoparticles (*nano*PANI-DBSA) were synthesised as outlined in Chapter 3, section 3.3.1.

7.2.2 Equipment/Instrumentation

All electrochemical protocols were performed either on a BAS100/W electrochemical analyser with BAS100/W software, or a CH1000 potentiostat with CH1000 software, using either cyclic voltammetry or time-based amperometric modes. An Ag/AgCl (3.0 M NaCl) reference electrode and a platinum mesh auxiliary electrode were used for bulk electrochemical experiments. Scanning electron microscopy (SEM) was performed with a Hitachi S 3000N scanning electron microscope and an acceleration voltage of 20 kV was employed. Atomic force spectroscopy (AFM) was performed with a Dimension 3100 (Digital Instruments) in contact mode. Profilometer readings were taken with a Dektak V-220-Si Stylus Profilometer (Veeco Instruments Ltd., Cambridge, UK).

7.2.3 Methods

7.2.3.1 Preparation of *nano*PANI-DBSA modified electrodes

The *nano*PANI-DBSA (5.54 % w/w) was dispersed in distilled water and the modified electrodes were prepared by electrodeposition from this solution onto the surface of the glassy carbon working electrode using cyclic voltammetry (CV). The potential was cycled between –0.5 V and 1.1 V at 100 mV/s for the required number of cycles.

Following electrodeposition of the *nano*PANI-DBSA, the electrode was transferred to a 10 ml batch cell. To ensure the attainment of homogeneous reduced polymer film, the surface of the polymer was reduced in PBS (degassed for 10 min with nitrogen) at –0.5 V vs. Ag/AgCl (3.0 M NaCl) for 1500 s in potentiostatic mode. Protein (i.e. HRP or BSA) was prepared in PBS at the required concentration prior to use. Immediately after reduction was complete, PBS buffer was removed from the cell and quickly replaced with the protein solution, with no stirring or degassing. Oxidation was performed immediately at 0.7 V vs. Ag/AgCl for 1500 s. During this oxidation, the protein becomes electrostatically attached to the polymer surface. The protein solution was carefully recovered from the cell and re-stored at 2ºC for later use.

For real-time monitoring of protein interactions in a batch cell, the modified electrode after the immobilisation of protein was placed in PBS (10 ml) in a batch cell. Amperometric experiments were performed in the stirred buffer solution at a constant applied potential of –0.1 V vs. Ag/AgCl (3.0 M NaCl) and hydrogen peroxide (8 mM) was added once the current had reached steady state[9-11]. The H_2O_2 concentrations stated are based on the total volume of the amperometric cell. The sensor response was obtained by subtracting the catalytic signal from the background signal (see Chapter 2, section 2.3.3).

In order to optimise the mass of HRP on the electrode surface, a range of dilutions of HRP beginning at 10 mg/ml was prepared in PBS. These solutions were used for the immobilisation of HRP onto the surface of a series of electrodes. An amperometric test was performed where a solution of H_2O_2 (8 mM) in PBS was added to the stirred buffer solution.

7.2.3.2 Characterisations of the polymer modified electrodes

The electrodeposited *nano*PANI-DBSA film was cycled in 1 M HCl electrolyte at various scan rates. The potential was cycled between –0.5 V and 1.1 V for ten cycles. The anodic and cathodic peak heights of the second cycle were plotted as a function of scan rate.

Scanning electron microscopy was employed to study the morphology of protein on *nano*PANI-DBSA-modified electrodes. Colloidal gold-labelled HCGβ MoAb of varying concentrations was electrostatically deposited onto the surface of the polymer film according to section 7.3.2.1 and allowed to dry in air. Equal volumes (1 ml) of solutions A and B from the silver enhancer kit were mixed together, and dropped onto the surface of the electrode. After 6 min, the solution was removed, and potassium thiosulphate (0.2 M, 20 μL) was then dropped on the surface for 2 min in order to stop the silver reaction.

7.3.2.3 Colorimetric enzyme assay

Colorimetric assays were carried out according to Morrin *et al*[14]. Solutions of HRP in doubling dilutions beginning at 10 mg/ml were prepared in phosphate buffer, pH 7, for use as a set of calibration standards. A solution of ABTS (5.33 mg/ml) was prepared, containing H_2O_2 (0.3 mM). 20 μL of the HRP solutions were transferred to the wells of a microtitre plate with 180 μL of the ABTS/H_2O_2 solution. The plate was covered and left in the dark for 35 min followed by absorbance reading at 620 nm.

Colorimetric enzyme assays were performed on the surfaces of modified glassy carbon electrodes according to a similar protocol. In this instance, HRP-modified electrodes were placed in the well of the microtitre plate along with 20 μL phosphate buffer to replace the HRP solutions in the calibration standards.

7.3 Results and Discussion

7.3.1 Preparation of *nano*PANI-DBSA films onto glassy carbon electrodes

Aqueous dispersions of polyaniline nanoparticles (*nano*PANI-DBSA) (particle sizes of the order of 10 nm) were prepared as outlined in Chapter 3, section 3.3.1.

Cyclic voltammetry was used for electrodeposition of the *nano*PANI-DBSA emeraldine salt (ES) onto glassy carbon electrodes from the aqueous dispersion of the nanoparticles (Figure 7.1 a). The potential was swept from –0.5 V to 1.1 V vs. Ag/AgCl (3.0 M NaCl) at a scan rate of 100 mV/s, as PANI is redox active within this region at acidic pH. The CV is typical for PANI-ES[15,16] with the main peaks A (0.20 V) and B (0.74 V) corresponding to the transformation of leucoemeraldine base (LB) to ES and ES to pernigraniline salt (PS), respectively. On the reverse scan, peaks B′ (0.66 V) and A′ (0.08 V) correspond to the conversion of PS to ES and ES to LB, respectively. The presence of a redox peak around 0.50 V/0.36 V (C and C′) is associated with the formation of *p*-benzoquinone and hydroquinone as a side product upon cycling the potential to 0.90 V and beyond[17-19]. It was also found that the current responses increased on subsequent scans suggesting that the nanoparticles aggregated/assembled on the glassy carbon electrode surface created a higher surface area electrode.

Shifts in peak potentials began to occur after a number of cycles (Figure 7.1 a). This may be the result of increased resistance of the electrode, as the film deposited becomes thicker. The electrodeposited film (Figure 7.1 b) showed reasonably stable CVs corresponding to the transformation of different PANI forms similar to the electrodeposition CV (Figure 7.1 a) described above.

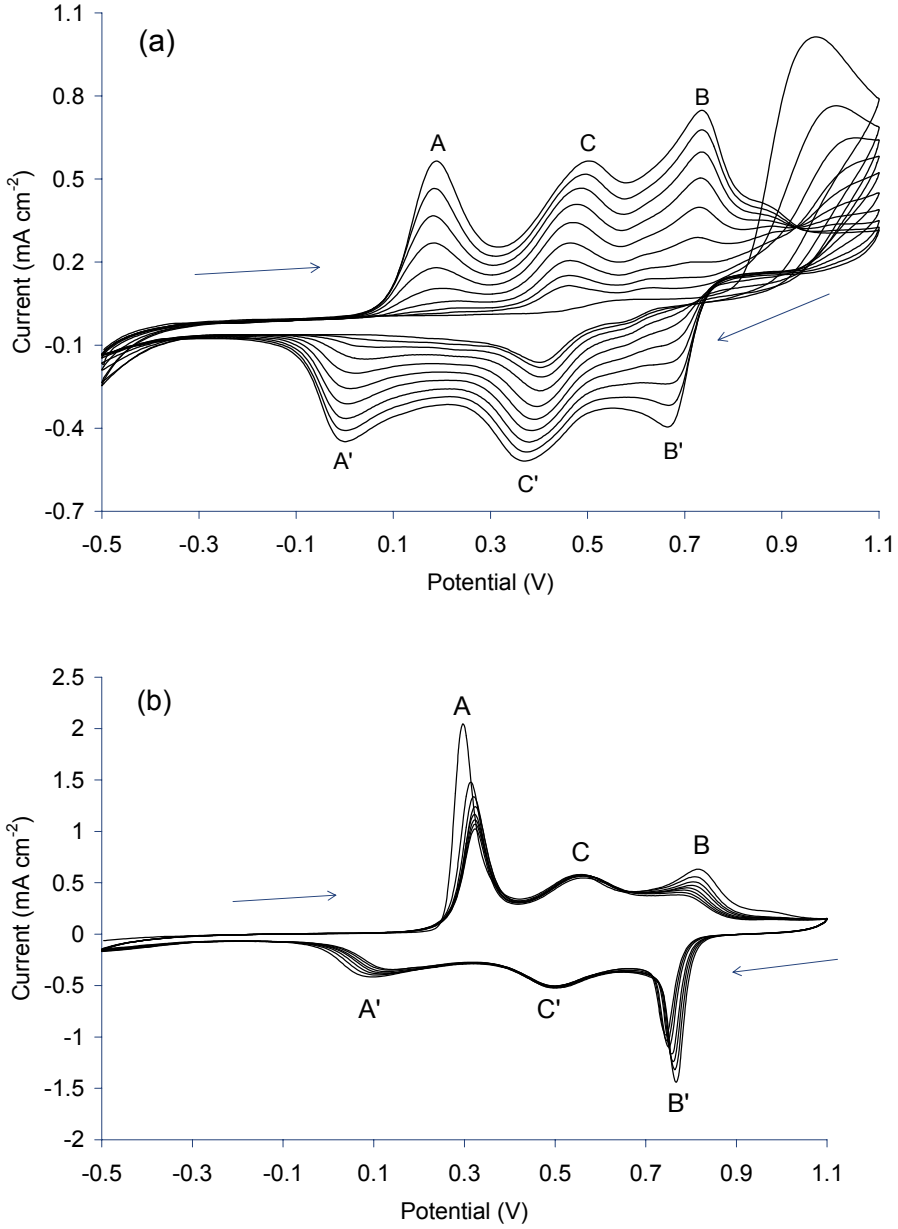

Figure 7.1 Cyclic voltammograms of: (a) electrodeposition of the *nano*PANI-DBSA (5.54 % w/w) film onto a glassy carbon electrode, and (b) the *nano*PANI-DBSA electrodeposited film from 10 electrodeposition cycles in 1 M HCl at a scan rate of 100 mV/s (arrows show the direction of the scan). $E_{initial}$ is -0.50 V and the potentials are vs. Ag/AgCl (3.0 M NaCl).

The deposition of PANI-DBSA from a solution containing the aniline monomer in the presence of DBSA was also performed. However, mixing aniline and DBSA in aqueous

media resulted in a white, highly viscous material, due to the formation of the insoluble crystalline anilinium-DBSA complex[20]. Although it was possible to deposit PANI-DBSA onto glassy carbon from this medium, the resulting films were patchy and inhomogeneous, and not suitable for further work.

Various concentrations of *nano*PANI-DBSA were used to obtain electrodeposits by cycling the potential ten times over the potential range of -0.5 to 1.1 V. The electrodeposited films were then subjected to cyclic voltammetry in 1 M HCl. The cathodic peak currents (B′) in Figure 7.1 b was the most defined and stable therefore it was chosen to plot against the *nano*PANI-DBSA concentration used to produce the film (Figure 7.2), and the optimal concentration of *nano*PANI-DBSA was determined.

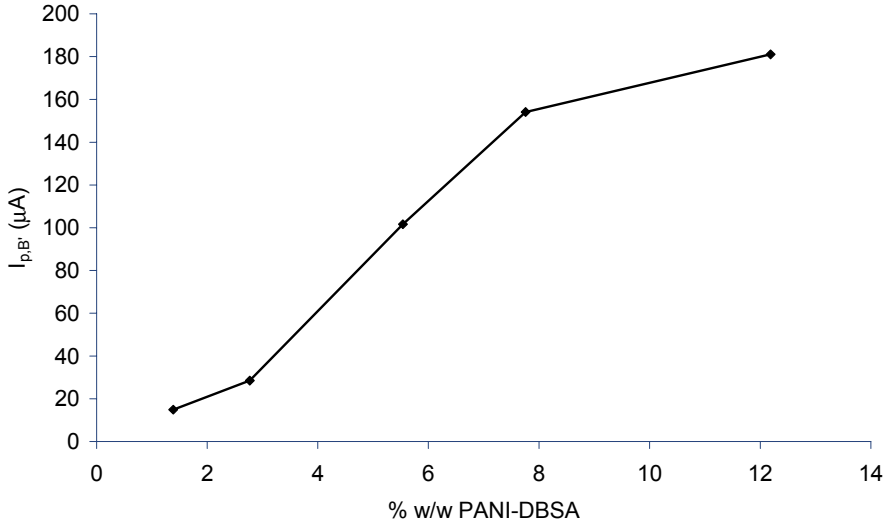

Figure 7.2 Dependence of cathodic peak current ($i_{p,B'}$) (2nd cycle) on concentration of *nano*PANI-DBSA used for electrodeposition on glassy carbon (10 electrodeposition cycles). The electrodeposited films were cycled from -0.5 to 1.1 V in 1 M HCl at a scan rate of 100 mV/s.

At concentrations of 2.77 % w/w or below, the peak heights were quite low, showing that there was not sufficient electrical connectivity for an effective communication

between the PANI particles. Increasing the concentration to 5.54 % w/w, a sharp increase was observed in peak current. This could be a critical concentration for the PANI-DBSA nanoparticles to interact; hence producing much larger currents. Increasing the concentration above values of 5.54 % w/w resulted in increases in current magnitude. However, beyond concentrations of 7.76 % w/w, the slope of the graph began to decrease, indicating that inhibition of charge transfer was occurring in films fabricated using greater than 7.76 % w/w *nano*PANI/DBSA. As a result, a concentration of 5.54 % w/w was used to produce electrodeposited films in all further work.

7.3.2 Characterisations of electrodeposited *nano*PANI-DBSA films

Scan rate studies on peaks B and B′ from CVs of electrodeposited film in HCl (Figure 7.1 b) showed each of the peak currents were directly proportional to scan rate, υ, consistent with that anticipated for an electrochemical reaction involving a surface confined species[21] (r^2 = 0.996 and 0.997, respectively) (Figure 7.3).

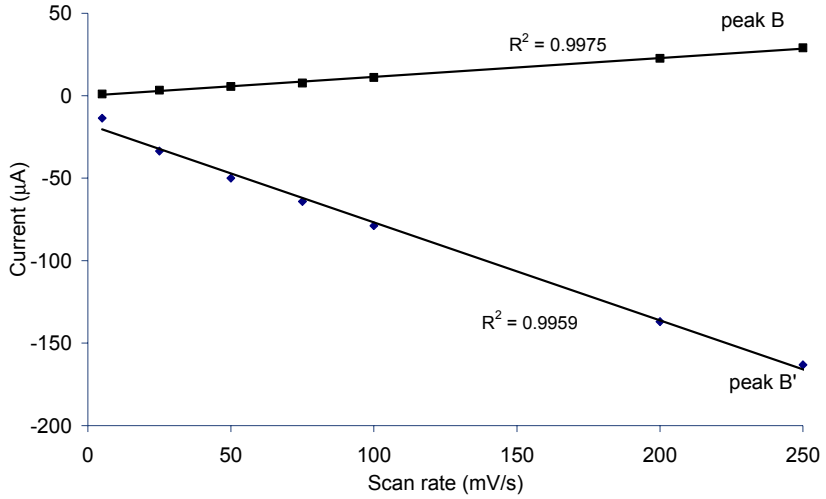

Figure 7.3 Peak heights of anodic peak B and cathodic peak B′ as a function of scan rate (υ) of electrodeposited *nano*PANI-DBSA film scanned in 1 M HCl.

Profilometry results indicate that the electrodeposited film (using 30 voltammetric cycles) from *nano*PANI-DBSA (5.54 % w/w) was approximately 350 nm thick. This was about 100-times less than the 35 μm found from PANI-PVS synthesis (using the optimum 10 voltammetric cycles)[10].

SEM studies also showed a significantly smoother electrodeposited film of *nano*PANI/DBSA compared to the electropolymerised film of PANI-PVS (Figure 7.4). Electropolymerised polyaniline films grown from acidic media, usually exhibit a sponge-like, branched, porous-structure[9-11] (Figure 7.4a). Since electrodeposition of nanoparticles involves deposition of preformed polymer, no nucleation or branching occurs and a more ordered deposit results (Figure 7.4b).

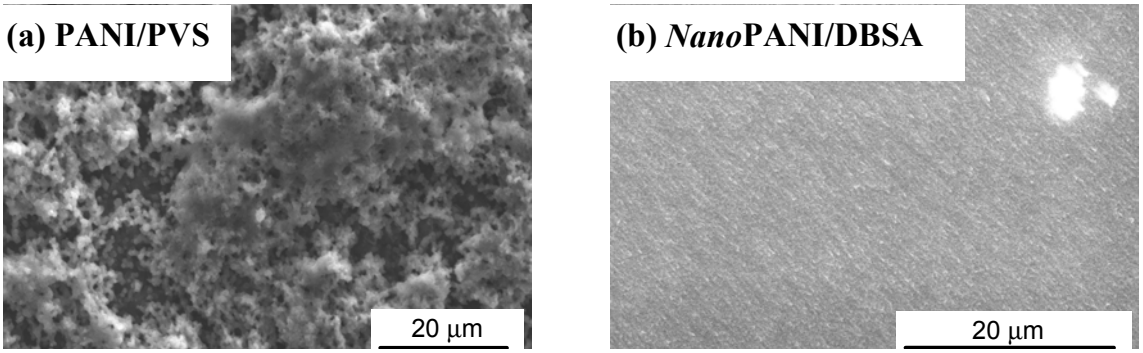

Figure 7.4 Typical scanning electron micrograph of: (a) PANI-PVS electropolymerised on a glassy carbon electrode surface (10 cycles) (1,500 X magnification), and (b) *nano*PANI/DBSA (5.54 % w/w) electrodeposited on a glassy carbon electrode surface (30 cycles) (2,500 X magnification).

Atomic force microscopy was also employed to characterise the surface morphology of the electrodeposited *nano*PANI-DBSA film. The root mean square (RMS) surface roughness for the electrodeposited films formed using various voltammetric cycles

was calculated. RMS average of height deviations were taken from the mean data plane using the formulation below:

$$\text{RMS} = \sqrt{\frac{\sum Z_i^2}{n}} \qquad (7.1)$$

where Z is the height (nm) and n is the number of data points taken.

The RMS roughness data from different scan areas show the roughness of the films increased up to 30 cycles and decreased at 40 cycles as shown in Figure 7.5.

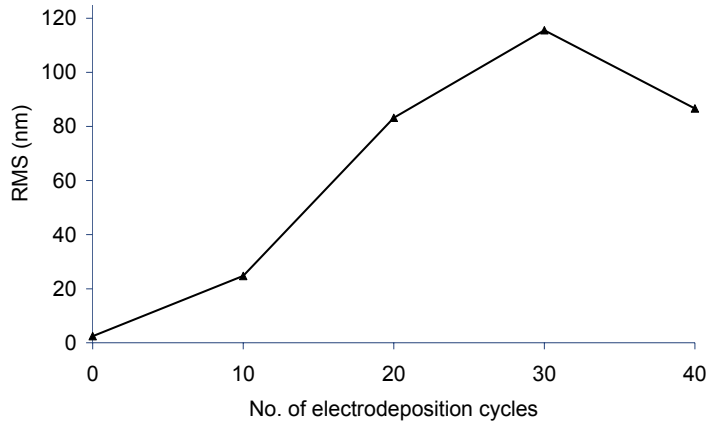

Figure 7.5 Root mean square (RMS) surface roughness of various electrodeposition cycles of *nano*PANI-DBSA film on a glassy carbon plate.

The AFM images show *nano*PANI-DBSA films with uniform roughness (Figure 7.6). The surface from 30 CV scans is characterised by a uniform array of PANI-DBSA nodules (Figure 7.6 d). The surface morphology agrees with the RMS surface roughness data as the number of cycles increased, the roughness of the films also increased up to 30 cycles. At 40 cycles the roughness decreased, possibly due to the merging of individual nodules to form a continuous film (Figure 7.6 e). The higher the roughness of the films the higher exposed area for biomolecules to interact on the surface. These results indicate the optimum electrodeposition cycles was 30 cycles as this resulted in formation of a uniform and highly ordered nanostructured films with the highest surface roughness.

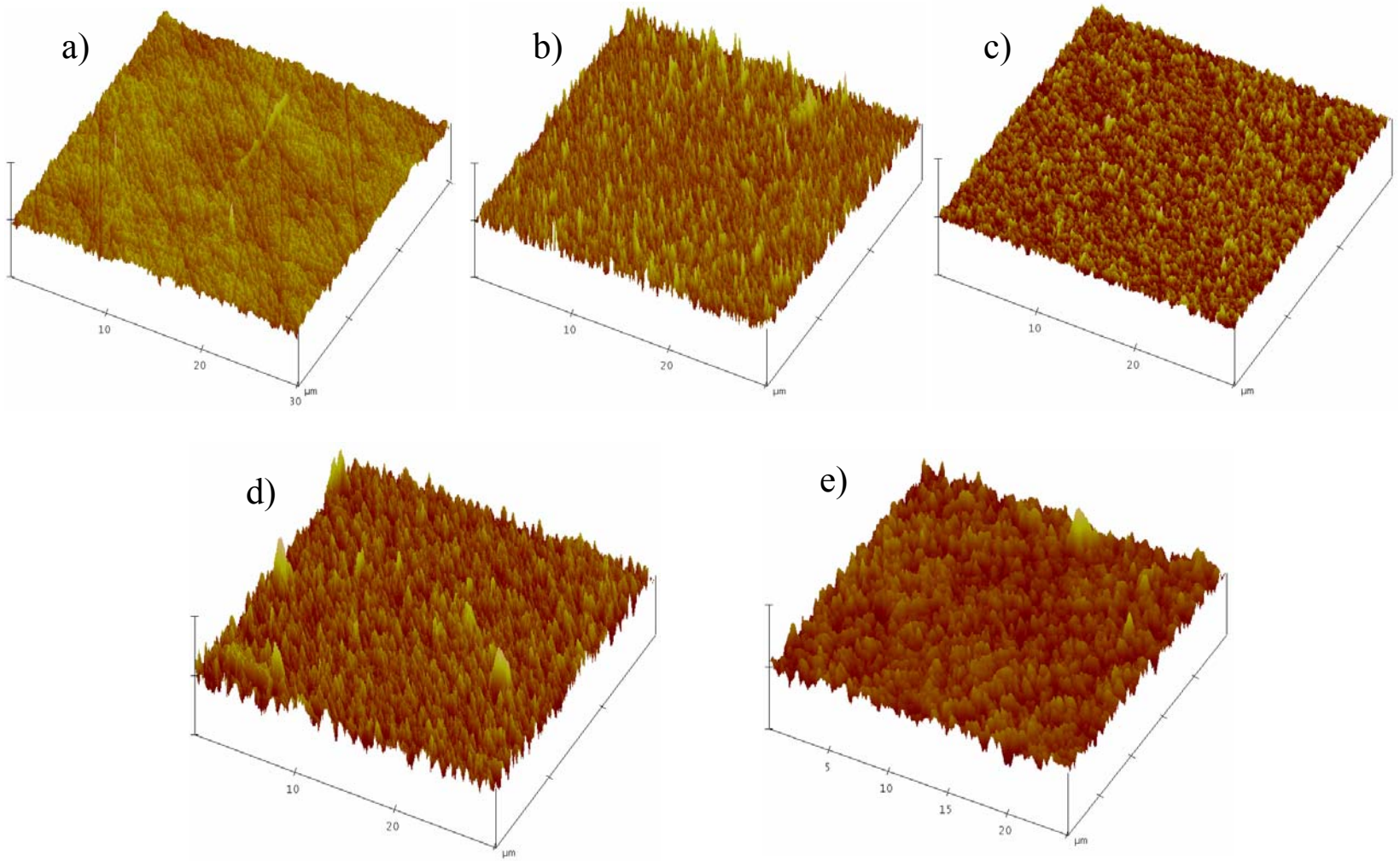

Figure 7.6 Atomic force microscopic 3-D image of PANI-DBSA (5.54 % w/w) electrodeposited on a glassy carbon plate: a) blank glassy carbon plate, b) 10, c) 20, d) 30, and e) 40 electrodeposition cycles.

7.3.3 Optimisation of the mass of HRP on the electrode surface

Preliminary work was performed on surfaces obtained by electrodeposition of 5.54 % w/w *nano*PANI-DBSA dispersions using 10 potential cycles over the range -0.5 V to 1.1 V. The enzyme HRP, 0.1 mg/ml, was electrostatically immobilised onto this polymer surface. The amperometric (applied potential = -0.1 V vs. Ag/AgCl) response obtained from addition of 8 mM H_2O_2 is shown in Figure 7.7. The applied potential of –0.1 V was chosen in order to directly compare the amperometric response of the *nano*PANI-DBSA sensor with a previously reported PANI-PVS biosensor[10]. The background current density (5.71 μA/cm^2) is much lower than previously obtained (42.44 μA/cm^2) using PANI-PVS polymers. Response time, the time from the addition of H_2O_2 to the maximum current response obtained, was observed. Upon addition of 8 mM H_2O_2 (at 500 s), the current increased sharply, with the response time of less than 1 s (0.62 ± 0.04 s) and it was much less than the 9.46 ± 4.12 s found for the PANI-PVS format.

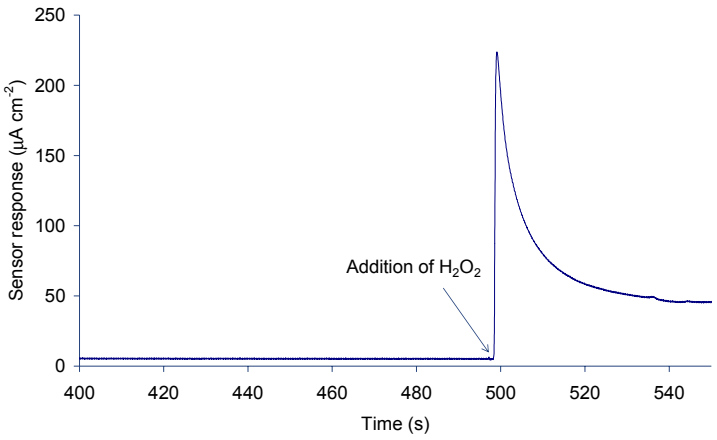

Figure 7.7 Amperometric response of electrodeposited *nano*PANI-DBSA sensor to 8 mM H_2O_2 after electrostatic immobilisation of 0.1 mg/ml HRP. Applied potential = -0.1 V vs. Ag/AgCl (3.0 M NaCl).

Amperometric methods and SEM techniques were used to characterise the immobilised protein. The amperometric response as a function of enzyme concentration

used during immobilisation was obtained (Figure 7.8). Optimal amperometric responses were achieved when HRP was immobilised using a concentration of 0.1 mg/ml. Above this concentration the responses decreased, possibly due to the formation of large insulating HRP multilayers which may have reduced the electron transfer kinetics in the PANI film. To ascertain that the response was due to catalytic activity of HRP, BSA was immobilised onto the electrode and an amperometric test performed. The sensor response from the immobilised 1 mg/ml BSA onto the electrode surface was 0.55 ± 0.36 μA/cm^2 which was negligible compared to the sensor response observed when 1 mg/ml HRP was used (62.94 ± 4.67 μA/cm^2).

The optimum catalytic signals for the PANI-PVS platform was obtained when HRP was immobilised using a concentration of 0.66 mg/ml[10]. In this work, the optimal catalytic signals were obtained using an enzyme immobilisation concentration approximately six times lower than required for the PANI-PVS system, showing that a much more efficient deposition of protein is achieved on the *nano*PANI-DBSA nanoparticulate surface.

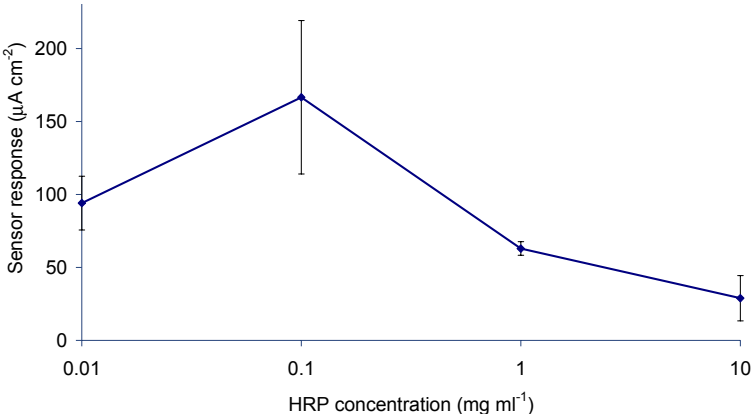

Figure 7.8 Dependence of the amperometric response obtained using electrodeposited *nano*PANI-DBSA sensor to 8 mM H_2O_2 on the concentration of HRP used for immobilisation. Applied potential = -0.1 V vs. Ag/AgCl (3.0 M NaCl).

Although AFM and SEM provide adequate surface information on the overall topography of polymer films, the resolution of individual protein or groups of proteins was not possible. Through the use of proteins conjugated to an electron-dense particle such as gold, it was possible to indirectly visualise the distribution of proteins. A colloidal gold-labelled HCGβ MoAb was used as a model for the visualisation of protein on the *nano*PANI-DBSA film. Figure 7.9 contains the SEM images of colloidal gold-labelled protein electrostatically immobilised to the surface of *nano*PANI-DBSA films (5.54 % w/w, 30 voltammetric cycles). All surfaces were enhanced with silver, in order to visualise the gold label. This enhancing process caused the reduction of silver ions from solution, resulting in the precipitation of metallic silver around the gold particles on the polymer surface. A trend of increasing surface coverage was observed as the concentration of protein used for immobilisation was increased. At a level of 0.001 mg/ml, low surface coverage was observed. This surface coverage increased gradually until 10 mg/ml, which had a very dense layer of protein covering the polymer layer. These images of protein-modified *nano*PANI-DBSA films showed that protein was uniformly distributed over the surface of the *nano*PANI-DBSA film and no clustering was evident. The particle size of the protein was smaller when higher concentrations were used for immobilisation. This was possibly due to the electrostatic charge repulsion between the protein molecules which prevents their expansion when they get closer.

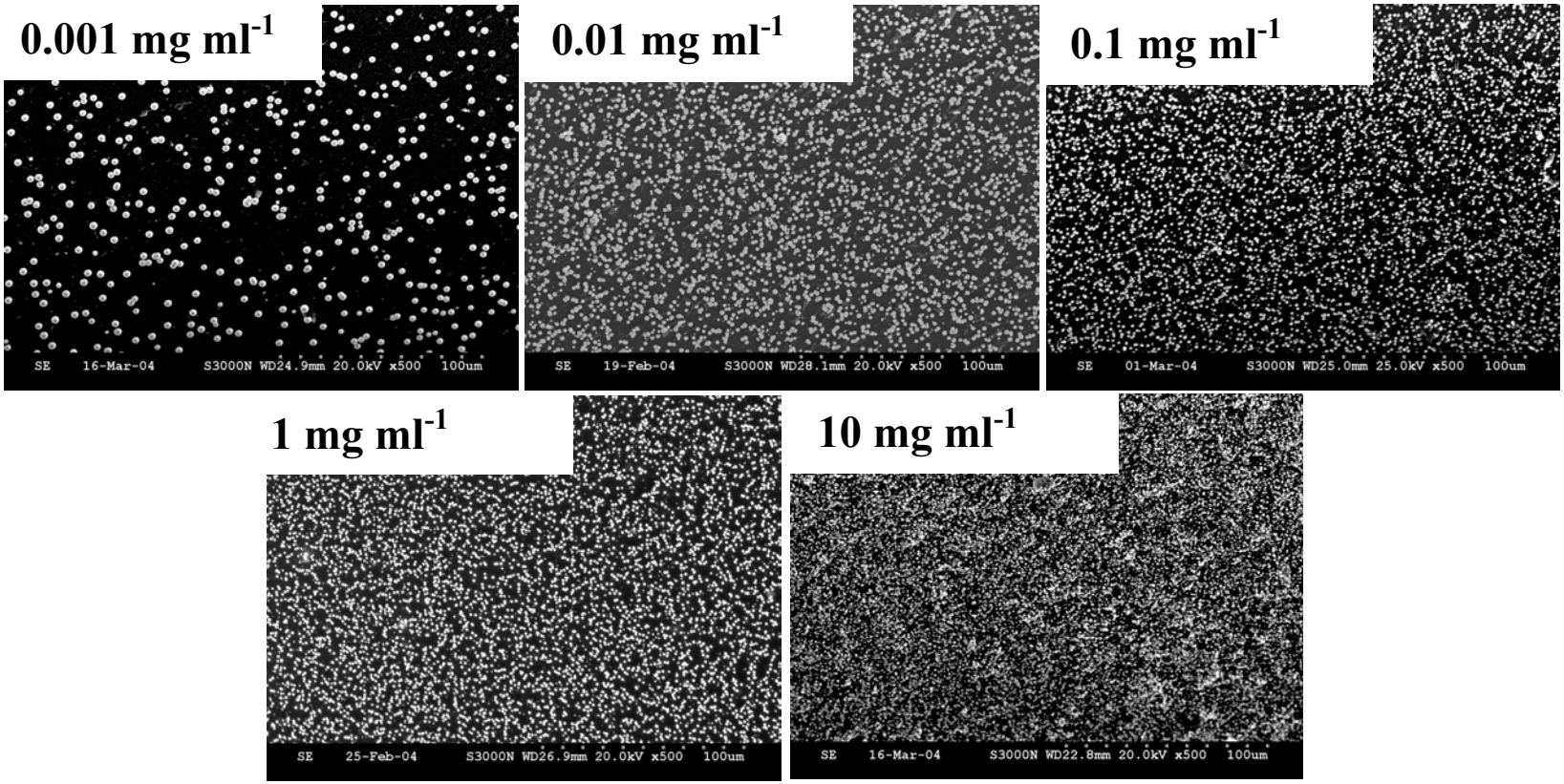

Figure 7.9 SEM images of *nano*PANI-DBSA films with varying concentrations of electrostatically immobilised HCG MAb-Colloidal Gold. The protein can be seen to be uniformly distributed over the surfaces, with the coverage increasing for increasing concentrations (500 X magnification). All surfaces were silver-enhanced in order to be able to visualise the protein gold label.

7.3.4 Optimisation of electrodeposition

The dependence of the sensor response on the number of cycles used for electrodeposition was investigated (Figure 7.10). Up to a limit of 30 cycles, the response increased and then above 30 cycles, the response decreased. This was possibly due to the thicker polymer film hindering the electron transfer properties between the electrode surface and the bulk solution.

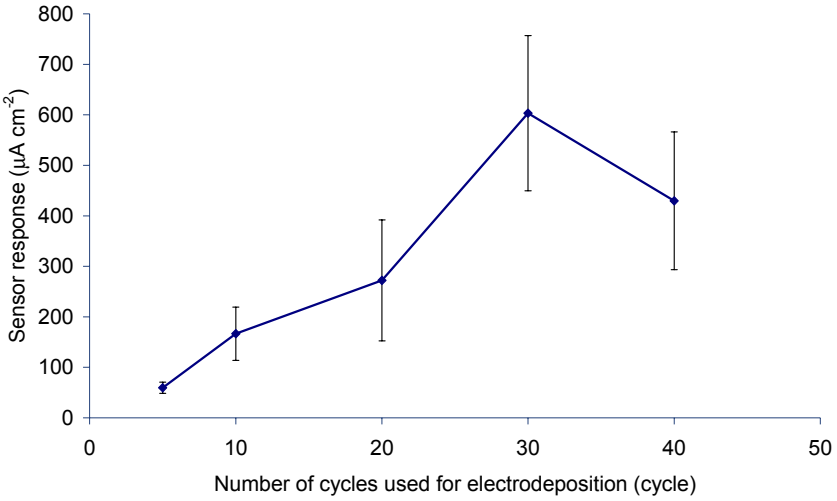

Figure 7.10 Relationship between amperometric response of HRP-modified *nano*PANI-DBSA to H_2O_2 (8 mM) and number of cycles used for electrodeposition of the *nano*PANI-DBSA film. HRP (0.1 mg/ml) was electrostatically immobilised on polymer films of varying thicknesses.

This result agrees with the film morphology study using AFM (section 7.3.3) which showed the optimum electrodeposition cycle was 30 and the uniform and highly ordered films could have contributed to the enhanced sensor performance. The highest sensor response was 603±154 μA/cm^2 and the signal-to-noise ratio was 61±3. In the previous study of PANI-PVS formats, the highest sensor response was 1004±198 μA/cm^2 and the signal-to-noise ratio was 17±4 under the optimum conditions (10 voltammetric electrodeposition cycles, 0.66 mg/ml HRP solution was used for immobilisation)[10].

7.3.5 Colorimetric enzyme assay

The absolute mass of enzyme immobilised at the solution concentration of 0.1 mg/ml was determined by a colorimetric enzyme assay[14], and was calculated to be 5.0×10^{11} molecules. Assuming an ideal flat two-dimensional *nano*PANI-DBSA surface with an area of 7.07×10^{-6} m^2, the theoretical number of molecules of HRP (radius: 26 Å) necessary to form a monolayer on the surface of these electrodes was estimated to be 3.33×10^{11} molecules[14]. This theoretical number of molecules of HRP required to form a monolayer at this surface can be compared to the number of molecules immobilised at optimum concentration (0.1 mg/ml). Therefore, it would appear that at this concentration, roughly a monolayer of protein is formed at the surface. In comparison to the PANI-PVS formats[10] previously developed, both optimum catalytic signals and monolayer formation for the *nano*PANI-DBSA platform occur when the concentration of protein for immobilisation is six-fold lower. This extra efficiency of the nanoparticulate system leads to a more economic biosensor in terms of protein reagents used.

7.4 Conclusions

This work illustrates deposition of a uniform, highly ordered, nanometric structured polyaniline film on a glassy carbon electrode from the *nano*PANI-DBSA dispersions. This uniform surface shows improved enzyme deposition characteristics and better signal-to-noise ratios than when polyaniline is electrochemically deposited from bulk monomer solutions. The *nano*PANI-DBSA film is more efficient in terms of protein immobilisation and requires a concentration of protein six-fold lower than the PANI-PVS layer for monolayer coverage. In addition, the signal-to-noise ratio of the *nano*PANI-DBSA biosensor (61±13) is approximately three times higher than the PANI-PVS biosensor (17±4) to H_2O_2 (8 mM) under optimum conditions (*nano*PANI-DBSA: 30 voltammetric electrodeposition cycles, HRP immobilised at 0.1 mg/ml; PANI-PVS: 10 voltammetric electropolymerisation cycles, HRP immobilised at 0.66 mg/ml). The response time for the optimised *nano*PANI-DBSA biosensor (0.62±0.04 s) is at least one order of magnitude lower than that of the PANI-PVS biosensor (9.46±4.12 s), under the optimum conditions stated above.

These data show that the *nano*PANI-DBSA is more powerful as a biosensor platform, due to its highly ordered nanostructure. This system provides modified electrode platforms with improved processability and functionality over previously described methods.

7.5 References

1. Khan, G.F. and Wernet, W., *Thin Solid Films*, 1997. **300**(1-2): p. 265-271.
2. Lu, W., Zhou, D.Z., and Wallace, G.G., *Analytical Communications*, 1998. **35**(8): p. 245-248.
3. Bender, S. and Sadik, O.A., *Environmental Science & Technology*, 1998. **32**(6): p. 788-797.
4. Gooding, J.J., Wasiowych, C., Barnett, D., Hibbert, D.B., Barisci, J.N., and Wallace, G.G., *Biosensors and Bioelectronics*, 2004. **20**(2): p. 260-268.
5. Campbell, T.E., Hodgson, A.J., and Wallace, G.G., *Electroanalysis*, 1999. **11**(4): p. 215-222.
6. Garner, B., Georgevich, A., Hodgson, A.J., Liu, L., and Wallace, G.G., *Journal of Biomedical Materials Research*, 1999. **44**(2): p. 121-129.
7. Tatsuma, T., Ogawa, T., Sato, R., and Oyama, R., *Journal of Electroanalytical Chemistry*, 2001. **501**(1-2): p. 180-185.
8. Iwuoha, E.I., de Villaverde, D.S., Garcia, N.P., Smyth, M.R., and Pingarron, J.M., *Biosensors & Bioelectronics*, 1997. **12**(8): p. 749-761, and references cited therein.
9. Killard, A.J., Zhang, S.Q., Zhao, H.J., John, R., Iwuoha, E.I., and Smyth, M.R., *Analytica Chimica Acta*, 1999. **400**: p. 109-119.
10. Killard, A.J., Micheli, L., Grennan, K., Franek, M., Kolar, V., Moscone, D., Palchetti, I., and Smyth, M.R., *Analytica Chimica Acta*, 2001. **427**(2): p. 173-180.
11. Grennan, K., Strachan, G., Porter, A.J., Killard, A.J., and Smyth, M.R., *Analytica Chimica Acta*, 2003. **500**(1-2): p. 287-298.
12. Fernandes, K.F., Lima, C.S., Pinho, H., and Collins, C.H., *Process Biochemistry*, 2003. **38**(9): p. 1379-1384, and references cited therein.
13. Wallace, G.G. and Innis, P.C., *Journal of Nanoscience and Nanotechnology*, 2002. **2**(5): p. 441-451, and reference cited therein.
14. Morrin, A., Guzman, A., Killard, A.J., Pingarron, J.M., and Smyth, M.R., *Biosensors & Bioelectronics*, 2003. **18**(5-6): p. 715-720.
15. Han, M.G., Cho, S.K., Oh, S.G., and Im, S.S., *Synthetic Metals*, 2002. **126**(1): p. 53-60.
16. Wallace, G.G., Spinks, G.M., Kane-Maguire, L.A.P., and Teasdale, P.R., *Conductive electroactive polymers : intelligent materials systems*. 2nd ed. 2002, Boca Raton, FL: CRC Press. p.137-139, 237, and references cited therein.
17. Chen, W.C., Wen, T.C., and Gopalan, A., *Synthetic Metals*, 2002. **128**(2): p. 179-189.
18. Mirmohseni, A. and Wallace, G.G., *Polymer*, 2003. **44**(12): p. 3523-3528.
19. Haba, Y., Segal, E., Narkis, M., Titelman, G.I., and Siegmann, A., *Synthetic Metals*, 1999. **106**(1): p. 59-66.
20. Yang, R., Ruan, C.M., Dai, W.L., Deng, J.Q., and Kong, J.L., *Electrochimica Acta*, 1999. **44**(10): p. 1585-1596.
21. Do, J.-S. and Chang, W.-B., *Sensors and Actuators B: Chemical*, 2004. **101**(1-2): p. 97-106.

8.1 Introduction

Poly(2-methoxyaniline-5-sulphonic acid) (PMAS) is a water-soluble self-doped polyaniline (PANI) which has been synthesised from the corresponding substituted monomer (see Chapter 1, section 1.1.2). Although it has lower conductivity and lower molecular weight than the parent PANI it is useful in applications such as sensors and biosensors as it is processable and redox active in neutral or high pH solution[1,2].

In polymer-modified amperometric biosensors, conducting polymers are usually fabricated on a conducting substrate. The biomolecules can be entrapped in the conducting polymer by electrochemical polymerisation of the conducting polymer in the presence of the biomolecules[3-9] or they can be subsequently immobilised on the polymeric films by the means of electrochemical deposition[10-12], evaporative casting[13] or dip-coating[14]. Tatsuma *et al*[15] demonstrated a one-step fabrication method that involved evaporative casting a mixture of PMAS and the biomolecules to fabricate an HRP based biosensor onto glassy carbon electrode. This method allows the amount of biomolecules to be controlled and minimises waste. Moreover, this method provides better accessibility of the polymer to the biomolecules, as the biomolecules are not just absorbed on the polymer surface but entrapped in the polymer matrix encouraging polymer and biomolecules interaction throughout the film[15].

The water solubility of PMAS is useful in that it can be solubilised in the same medium as used for biomolecules. However, the mixture of PMAS and biomolecules must be rendered insoluble on a suitable conductive substrate before it can be subjected to electrochemical measurements operated in aqueous medium[15]. Polycations such as poly(L-lysine) hydrochloride (PLL), poly(ethyleneimine) (PEI), and

poly(diallydimethylammonium chloride) (PDDA) are used to form insoluble complexes with the water soluble polymers[15-17]. In this work, according to Tatsuma *et al*[15], PLL was used to form a complex with the PMAS-HRP mixture. The complex is formed between the negatively charged sulphonate group in PMAS and the positively charged polycation. Structures are shown in Figure 8.1.

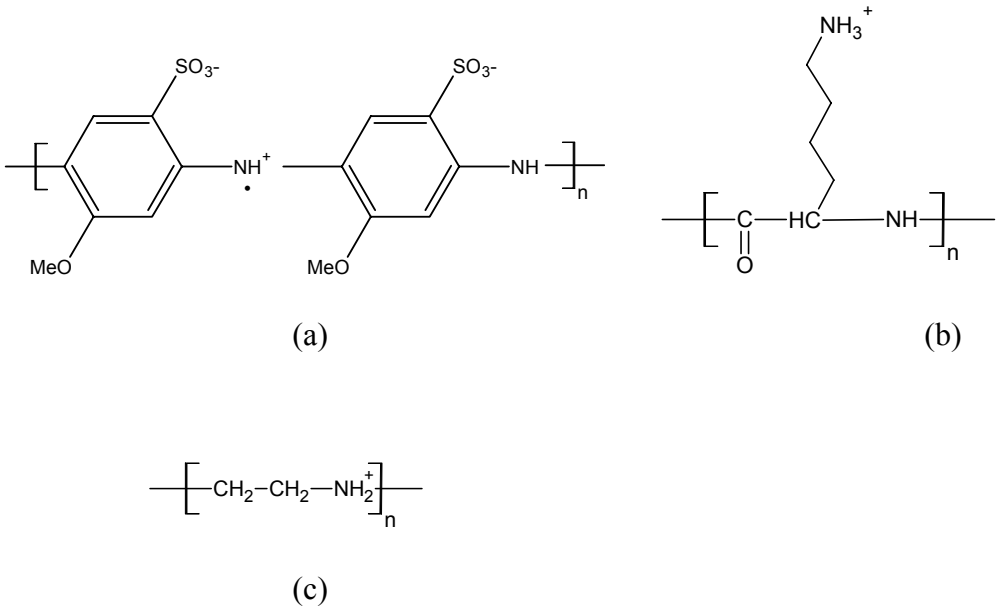

(a) (b)

(c)

Figure 8.1 Structures of (a) PMAS, (b) PLL and (c) PEI.

Using electrochemical fabrication methods (Chapter 7), PANI has been used as the mediator for HRP based biosensors. In this chapter, we use the polymer complex PMAS-PLL as the mediator for fabrication of a HRP-H_2O_2 biosensor. The sensor is fabricated by evaporative casting of a mixture of PMAS-HRP-PLL onto ITO-coated mylar. The effect of PMAS and PLL concentrations is studied using cyclic voltammetry (CV). The morphology and thickness of the polymer films are characterised using atomic force microscopy (AFM). Amperometric detection is employed to detect the response upon the addition of H_2O_2. Response of PMAS-HRP-PLL electrodes as a function of HRP concentration, H_2O_2

concentration, pH of buffer solution, applied potential and storage time are also investigated.

8.2 Experimental

8.2.1 Chemicals

PMAS was synthesised using a method developed previously in our laboratories by Dr. Syed Ashraf. ITO-coated polyester mylar (OC^{TM} 50, resistance 45 Ω/sq.) from CPFilms Inc. was used as the electrode substrate. Isopropyl alcohol and hydrogen peroxide (H_2O_2) were purchased from Asia Pacific Specialty Chemicals Limited (APS). Anhydrous di-sodium hydrogen orthophosphate (Na_2HPO_4) was purchased from APS Finechem. Potassium di-hydrogen orthophosphate (KH_2PO_4) from BDH, sodium chloride (NaCl) from Fluka, and hydrochloric acid (HCl) from Ajax Finechem were all used as received. Potassium chloride (KCl), poly-L-lysine hydrochloride (PLL), horseradish peroxidase (HRP), bovine serum albumin (BSA), L-ascorbic acid and polyethyleneimine (PEI) were purchased from Sigma.

Unless otherwise stated, all electrochemical measurements were carried out in phosphate buffered saline (PBS) (0.1 M phosphate, 0.137 M NaCl and 2.7 mM KCl, pH 6.4). PBS solutions of different pH were prepared by mixing 0.1M KH_2PO_4 buffer and 0.1M Na_2HPO_4 until the desired pH was obtained. All solutions were prepared using Milli-Q water.

8.2.2 Equipment/Instrumentation

A Denver Model 20 pH/Conductivity Meter was used. UV cleaner, Jelight Company Inc. Model No. 42-220, was used for pre-treatment of the ITO-coated mylar. All electrochemistry was performed in a three-electrode cell using a polymer modified working electrode with platinum mesh and Ag/AgCl (3.0 M NaCl) auxiliary and reference electrodes, respectively. A Bioanalytical Systems (BAS) CV-27 workstation, interfaced with ADInstruments/4e (ADI/4e) MacLab analogue/digital converter connected to a computer was used to record the cyclic voltammograms and amperometric responses. The cell was purged with nitrogen gas prior to amperometric experiments. All potentials stated are vs. Ag/AgCl (3.0 M NaCl) reference electrode. Atomic force microscopy (AFM) was performed with a Dimension 3100 (Digital Instruments) in contact mode.

8.2.3 Methods

8.2.3.1 Preparation of polymer modified electrodes

To clean the ITO-coated mylar (1 x 3 cm^2), it was sonicated in an anionic detergent solution for 5 min, washed with tap-water twice, washed with isopropyl alcohol twice and left to dry in the open air before cleaning in a UV ozone cleaner for 15 min. The pretreated mylar was masked by adhesive tape to give a constant exposure area (1 cm^2).

While keeping the mass ratio (w/w) of PMAS:PLL = 1:1, mixtures of PMAS-PLL at various PMAS concentrations were prepared. The mixtures (35 μL) were cast onto the pretreated ITO-coated mylar and the films allowed to dry overnight in a desiccator at 2 ºC. Cyclic voltammograms were obtained in 0.1 M HCl (-0.2 V to 1.1 V) for 10 cycles at 100 mV/s. The magnitude of the oxidation peak at about 0.65 V (third scan) was plotted against PMAS concentration. The optimal PMAS concentration was chosen and the PLL

concentration varied. In the same manner, the solutions containing various ratios of PMAS:PLL were cast and CVs recorded as above.

HRP or BSA was dissolved at various concentrations in the PMAS solution. This solution was further mixed with PLL based on the optimal ratio of PMAS:PLL. The mixture was cast onto UV treated ITO-coated mylar. The films were dried in a desiccator at 2ºC. The amperometric test was conducted the following day.

8.2.3.2 Characterisation of the polymer modified electrodes

The cast PMAS-PLL film was cycled in 0.1 M HCl electrolyte at various scan rates. The potential was cycled between -0.2 V and 1.1 V for the required number of cycles. The anodic and cathodic peak heights were plotted as a function of square root of scan rate.

The film thickness of the polymer modified electrode was measured using AFM. A small area of the polymer film was removed from the substrate surface by gently scratching. The scratch was made in the middle of the film to avoid the effect of the film tapering at the edge. Atomic force microscopy was run in contact mode over the scratched area. Cross section analysis was used to measure the different heights from the top of the polymer films to the substrate surface to determine the thickness of the films (see more detail in Chapter 2, section 2.2.2)

To perform real-time monitoring of protein interactions in a batch cell, the modified PMAS-HRP (or BSA)-PLL electrodes were used as the working electrode in a 10 ml three-electrode cell. Phosphate buffer saline solution (10 ml) was added into the cell and degassed prior the test. The cell was connected to an amperometric analyser. The solution was stirred while a constant potential was applied to the cell. After the constant current was obtained, the desired amount of H_2O_2 was added into the cell. The sensor response was

obtained by subtracting the catalytic signal from the background signal (see more detail in Chapter 2, section 2.3.3).

A hundred PMAS-HRP-PLL sensors were made at once and separated into two series to be kept in a closed container in air and in PBS solution (pH 6.4) at 2ºC. Amperometric tests were carried out using different sensors at various time intervals for six months to establish long term stability.

As well as the long term stability, the effect of an interference was also studied. The effect of 200 μM ascorbic acid, which is common compound present in biological samples[4,5], was investigated.

The error bars in all graphs represent the standard deviation calculated from the data set (n).

8.3 Results and Discussion

8.3.1 Complexation and fabrication methods

Initially, PMAS was cast onto electrodes and allowed to dry without the addition of a polycation. Due to PMAS being water-soluble, the film immediately began to dissolve once in contact with aqueous media. Addition of a polycation such as PLL into the PMAS solution prior to casting, resulted in the formation of a PMAS-PLL film that was insoluble. This insoluble film results from the electrostatic cross-linking of the sulphonate groups in PMAS to the positive NH_3^+ groups in the polycation PLL[15]. The mixing sequence of these two polymers was investigated. The first approach involved casting the PMAS solution, drying and subsequent casting with PLL. The second method involved casting the PLL solution onto the substrate, drying and subsequent casting with PMAS. The third approach

was to pre-mix the PMAS and PLL and cast this solution onto the substrate. For all approaches the PMAS:PLL w/w ratio was maintained at 1:0.50.

The films obtained from these three approaches are shown in Figure 8.2. Although the films from the first two methods (Figure 8.2 a and 8.2 b) appeared non-continuous, they were insoluble in water. The CVs of these films were similar to those obtained using the film from the third pre-mixing method (see Figure 8.3 a), albeit lower current intensities were observed (result not shown). The higher currents obtained from the pre-mixed films were possibly caused by a greater extent of PMAS adhering to the substrate, indicating more effective PMAS-PLL interaction in the pre-mixed films. The consistency of the films from the first two approaches could probably be improved if the second layer was cast onto the first layer from very small droplets using spray or ink-jet printing, as it could help improve the mixing efficiency of PMAS and PLL.

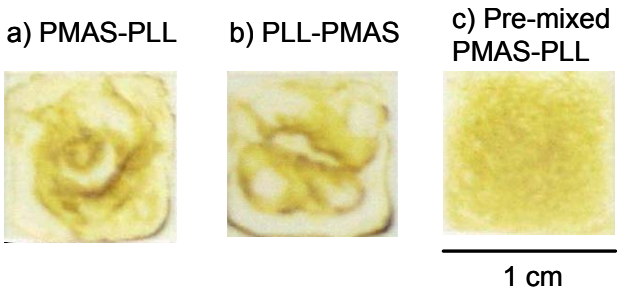

Figure 8.2 Photographs of films from sequential and pre-mixed casting of PMAS and PLL: (a) casting of PLL solution onto PMAS film, (b) casting of PMAS solution onto PLL film, and (c) pre-mixed and cast the mixture of PMAS-PLL. All films were allowed to dry at room temperature.

Pre-mixing of PMAS and PLL resulted in formation of large fibres in the solution and a film exhibiting a rough morphology. In order to improve the film morphology, other polycation (PEI) was used as the complexing agents. Polyethyleneimine (PEI) (Figure 8.1 c) was complexed with PMAS resulting in even larger fibres in solution than observed for

PMAS-PLL. The CV of the film cast from this solution (being partially soluble in water) showed much lower current intensity than the film cast from PMAS-PLL. These results suggest that PLL is the best polycation PMAS complexing and it therefore was used for all further experiments.

8.3.2 Optimisation of PMAS concentration

A cyclic voltammogram was recorded in 0.1M HCl after coating the ITO-coated mylar with PMAS-PLL (Figure 8.3 a). Two redox couples appearing at 0.2/0.0 V (A/A′) and 0.64/0.38 V (B/B′) are tentatively assigned to conversion of the leucoemeraldine form of PMAS to the emeraldine salt (ES) form (A/A′) and the ES to pernigraniline (B/B′), respectively (Figure 8.3 a). This CV is similar to that obtained for the film cast from an ethanol slurry of PMAS-poly(4-vinylpyridine) mixture and scanned in 0.1 M HCl, as reported by Tallman and Wallace[16].

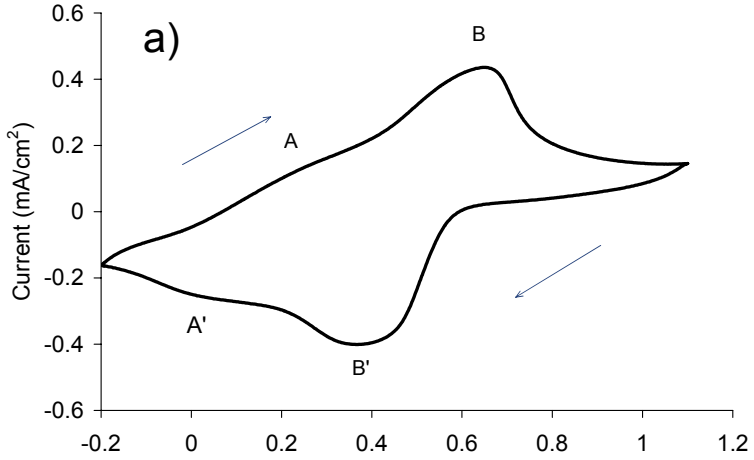

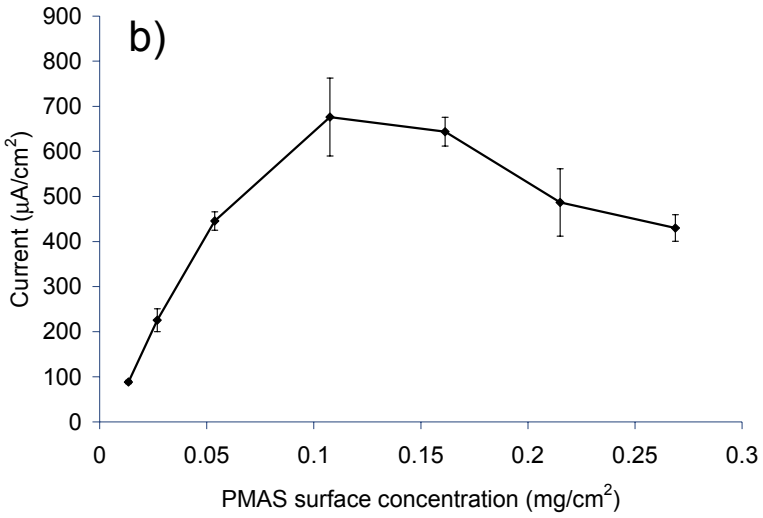

Figure 8.3 (a) Cyclic voltammogram of a cast film from PMAS-PLL (0.110 mg/cm^2), PMAS:PLL ratio = 1:1, on UV treated ITO-coated mylar in 0.1M HCl at scan rate 100 mV/s (arrows show the direction of the scan). $E_{initial}$ is – 0.5 V and the potentials are vs. Ag/AgCl (3.0 M NaCl). (b) Dependence of anodic peak current ($i_{p,B}$) on the surface concentration of PMAS-PLL (n=3).

While maintaining the ratio of PMAS:PLL at 1:1, the PMAS surface concentration used to cast onto the ITO-coated mylar surface was varied from 0.010 to 0.250 mg/cm^2. Using CV, the maximum oxidation current (peak B) was observed at a PMAS surface concentration of 0.110 mg/cm^2 (Figure 8.3 b). This implies that the concentration of PMAS was high enough to form an interconnected conducting film on the ITO surface. At PMAS surface concentrations greater than 0.110 mg/cm^2 the current decreased. This may be due to a thicker film forming, reducing the charge transfer between the PMAS and the ITO.

8.3.3 Optimisation of PLL concentration

Maintaining a concentration of 0.110 mg/cm^2 PMAS, the PLL concentration was varied and CVs of the cast films obtained (Figure 8.4). The higher the PLL content, the lower the current magnitude observed. Minimising the amount of PLL in the mixture to a

ratio of 1:0.25 PMAS/PLL gave the best electrochemistry, but resulted in dissolution of the cast film when scanned in 0.1 M HCl. A stable film was obtained when a ratio of PMAS:PLL = 1:0.50 or higher was used, and with a ratio of PMAS:PLL = 1:0.50 the films also exhibited well defined PMAS electrochemistry. Therefore this ratio was chosen for further experiments.

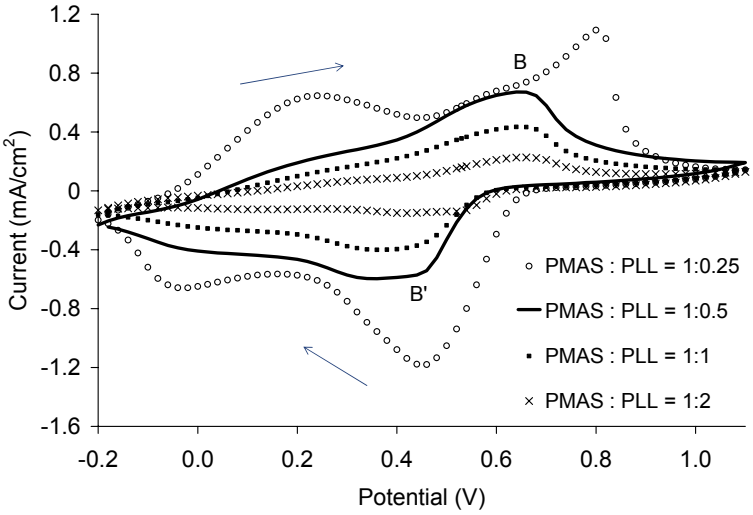

Figure 8.4 Cyclic voltammograms obtained in 0.1 M HCl at 100 mV/s scan rate for various ratios of PMAS:PLL on ITO-coated mylar. 0.110 mg/cm^2 PMAS concentration was used for all castings. Arrows show the direction of the scan. $E_{initial}$ is –0.5 V and the potentials are vs. Ag/AgCl (3.0 M NaCl).

The previous results show that the optimal film composition is 0.110 mg/cm^2 PMAS and 0.055 mg/cm^2 PLL surface concentrations. A film cast from this composition was further characterised using CV. Potential scan rate studies of peak B and B′ in Figure 8.4 showed each of the peak currents were directly proportional to the square root of scan rate rate, $\upsilon^{1/2}$, (R^2 = 0.996 and 0.997, respectively) as shown in Figure 8.5. This indicates that the redox process is a diffusion limited process [4].

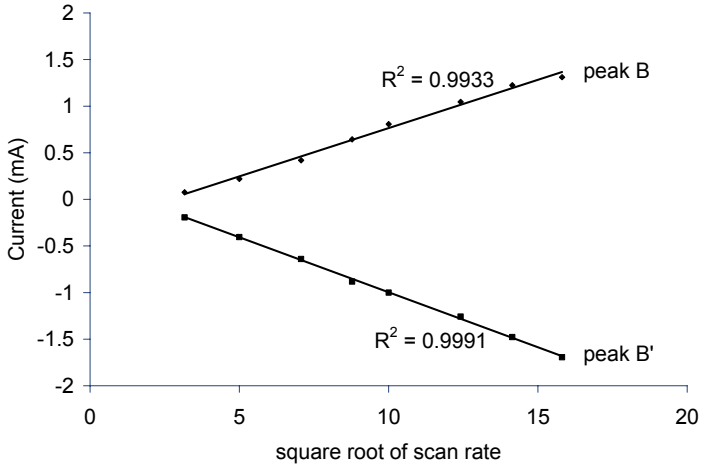

Figure 8.5 Peak heights of 2nd cycle anodic peak B ($i_{p,B}$) and cathodic peak B′($i_{P,B'}$) as a function of square root of scan rate of a PMAS:PLL = 1:0.50 cast film scanned in 0.1 M HCl.

Atomic force microscopy characterisation of the PMAS-PLL film (ratio 1:0.50) indicated the cast film to be very rough (Figure 8.6). This is presumably due to the fibrous nature of the preformed complex of PMAS and PLL. Root mean square (RMS) surface roughness of the film was measured (see Chapter 7, section 7.3.2) and found to be 216.2 nm.

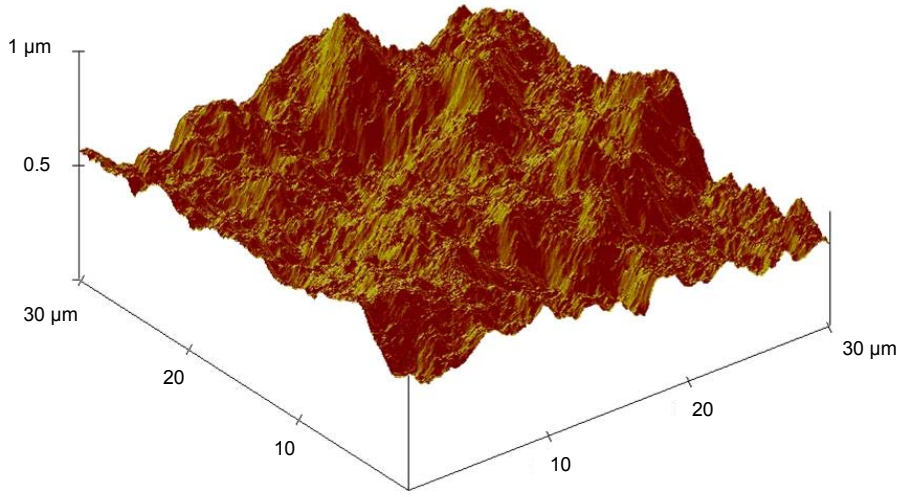

Figure 8.6 Atomic force microscopic image from 30 x 30 µm scan size of a PMAS:PLL = 1:0.50 film cast onto ITO-coated mylar.

8.3.4 Optimisation of the mass of HRP on the electrode surface

The sensor performance of the cast PMAS-PLL film was studied using the HRP-H_2O_2 system and the amperometric method (see experimental, section 8.2.3.2). The typical response from this format showed steady state sensor response after the addition of H_2O_2 (Figure 8.7).

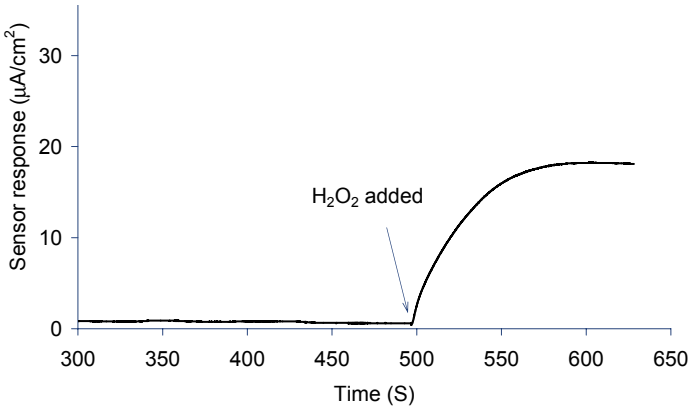

Figure 8.7 Typical sensor response for PMAS-HRP-PLL biosensors upon addition of 10 mM H_2O_2 with a constant potential of -0.1 V applied.

Initially the effect of the mass of HRP utilised in the polymer was studied. While maintaining the PMAS:PLL ratio at 1:0.50, the amount of HRP was varied in order to obtain the optimal sensor response. Various concentrations of HRP were pre-mixed with PMAS-PLL before casting onto the electrode. The catalytic response to H_2O_2 using various surface concentrations of immobilised HRP on the electrode was determined (Figure 8.8). To confirm that the current response was due to catalytic reduction of H_2O_2 by HRP, a blank PMAS-BSA-PLL polymer composite was also tested.

The response obtained from pre-mixed PMAS-HRP-PLL compared to PMAS-BSA-PLL confirmed the activity of HRP, as there was negligible catalytic response when BSA was used in place of HRP (Figure 8.8). The highest sensor response was obtained when a

HRP surface concentration of 0.14 mg/cm^2 was used (Figure 8.8). At concentrations greater than 0.14 mg/cm^2, the signal decreased which is attributed to the formation of HRP multilayers that may reduce the electron transfer kinetics due to large insulating layer formation.

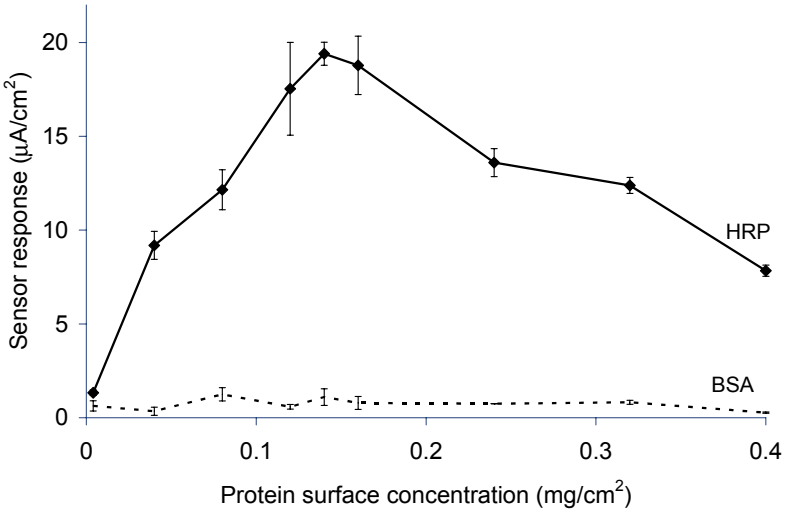

Figure 8.8 Dependence of catalytic response on [HRP] or [BSA] pre-mixed with PMAS-PLL mixture (n=3). Concentration of H_2O_2 used was 10 mM.

Atomic force microscopy was employed to measure the film thickness of the PMAS-PLL and PMAS-HRP-PLL cast films (Figure 8.9). The higher the HRP concentration, the greater the sensor response at least until 0.14 mg/cm^2. Also thicker films were obtained with increased HRP loading. The highest sensor response was found at a HRP concentration of 0.14 mg/cm^2, with the film thickness being 838 nm. The sensor response started to decrease beyond this point, which coincided with an increase in film thickness indicating the inhibition of the electron transfer in this thick film.

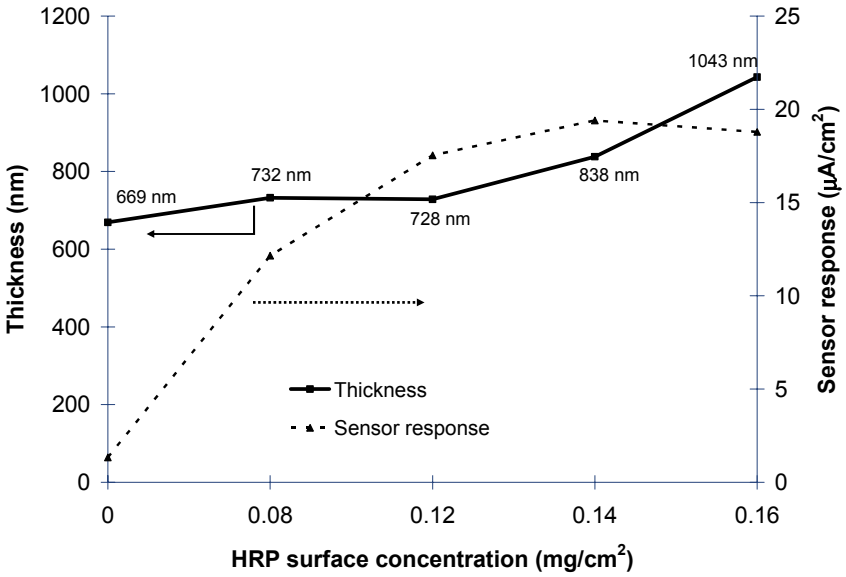

Figure 8.9 Dependence of film thickness and sensor response to immobilised HRP concentration in PMAS-HRP-PLL films.

8.3.5 Characterisations of the PMAS-HRP-PLL sensors

8.3.5.1 Sensor response to various applied potentials and buffer pH

A potential of -0.1 V vs. Ag/AgCl (3.0 M NaCl) was applied during the amperometric test, converting PMAS to its reduced form. The reduced leucoemeraldine base form of PMAS was needed as the electron transfer mediator to complete the electron transfer cycle as described by Iwuoha *et al*[18] (see Chapter 1, section 1.3.1-Figure 1.20). The applied potential was varied from -0.5 V to 0.0 V and the effect on the amperometric sensor response was determined upon addition of 10 mM H_2O_2 in PBS solution pH 6.4 (Figure 8.10).

Application of -0.5 V provided the highest response, but reproducibility was poor with the response from BSA also being high. This is possibly due to the effect of interference species which could be reduced at this high reduction potential. Although the

sensor response obtained at -0.1 V was lower than at -0.5 V, the ratio of response from HRP to BSA was higher. The ratio of sensor response from HRP to BSA was 22.3 and 4.0 at -0.1 V and –0.5 V applied potential, respectively. Moreover, the best reproducibility was obtained at an applied potential of –0.1 V. Hence this potential was used for all further experiments.

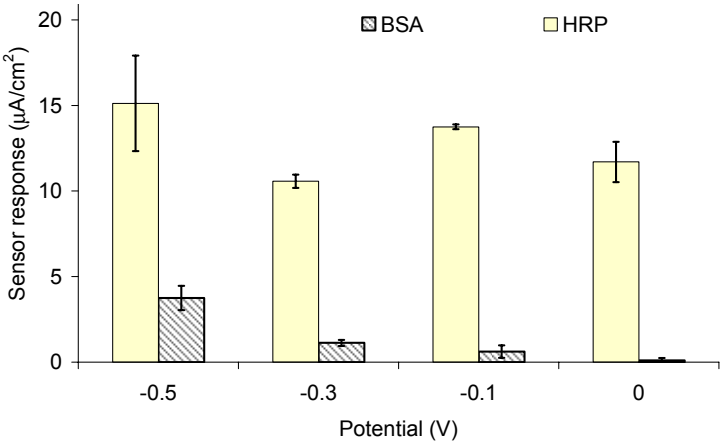

Figure 8.10 Responses of PMAS-HRP-PLL biosensors to 10 mM H_2O_2 at various applied potentials (n=3).

As the pH of the buffer can affect the electrochemistry of PMAS[15], the effect of the pH of the PBS solution was also studied. Calibration curves in the three different buffers (4.4, 6.4 and 8.4) were obtained (Figure 8.11). At an acidic pH of 4.4, the sensor response was highest at concentrations of H_2O_2 greater than 1 mM. The sensor response was higher at lower concentrations of H_2O_2 at pH 6.4. Therefore, the pH 6.4 buffer was chosen as it showed highest sensor response at the lowest concentration of HRP. No detectable sensor response was observed below 0.01 mM H_2O_2 in all buffers; therefore the minimum detectable concentration of this sensor was taken as 0.01 mM H_2O_2. The minimum detectable concentration was higher than the analogous PMAS-HRP-PLL sensors which were fabricated on ITO-coated glass reported by Tatsuma *et al*[15] (0.01 μM). This may be

attributed to the difference in conductivity of the electrode substrate and the source of PMAS, which could affect the electrochemistry of the sensors and consequently the biosensing performance.

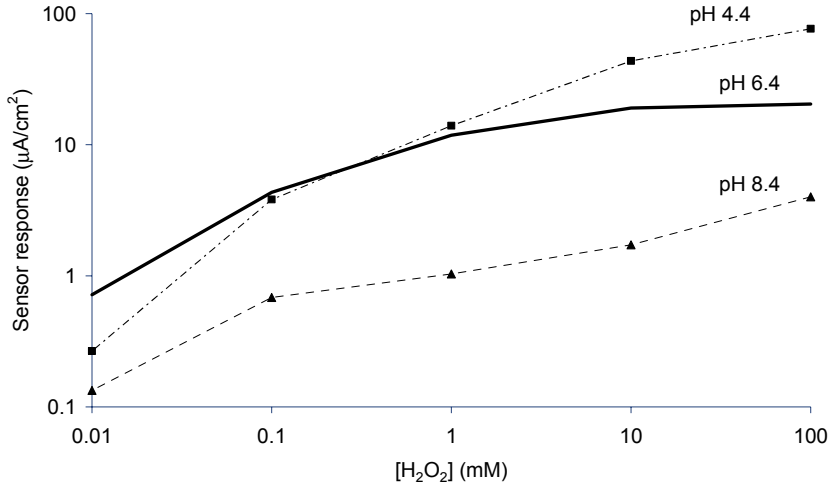

Figure 8.11 Cathodic current responses of PMAS-HRP-PLL biosensors to various concentrations of H_2O_2 in PBS pH 4.4, 6.4 and 8.4 (n=3). A constant potential of -0.1 V was applied.

8.3.5.2 Linearity and sensitivity

In pH 6.4 PBS, the response to various H_2O_2 concentrations from 0.01 to 5 mM was obtained (Figure 8.12).

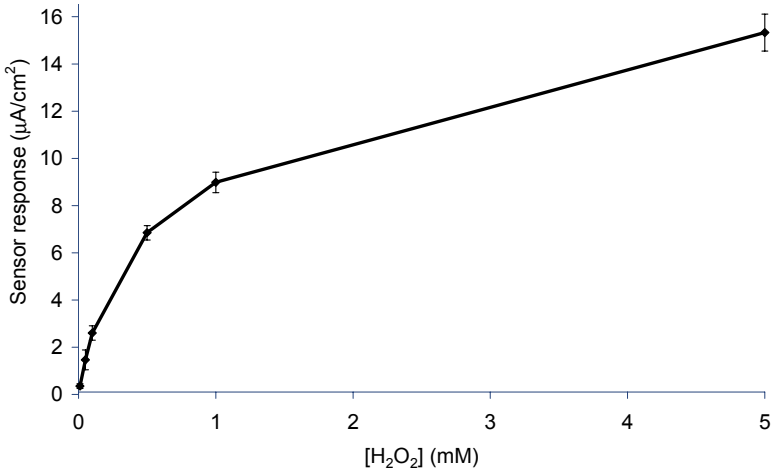

Figure 8.12 The responses of biosensors (immobilised 0.14 mg HRP /cm^2) to H_2O_2 in pH 6.4 PBS (n=3). A constant potential of -0.1 V was applied.

In Figure 8.13, linearity of the sensor response in pH 6.4 PBS solution was found in the range of 0.01 to 0.1 mM H_2O_2, with a sensitivity of 24.9 $\mu A/cm^2$ mM^{-1} and correlation coefficient 0.9966. This linear range is similar to the glucose sensors using PPy/ceramic carbon as the electrode material reported by Tian and Zhu[4] which have shown a linear response range from 0.08 to 1.3 mM.

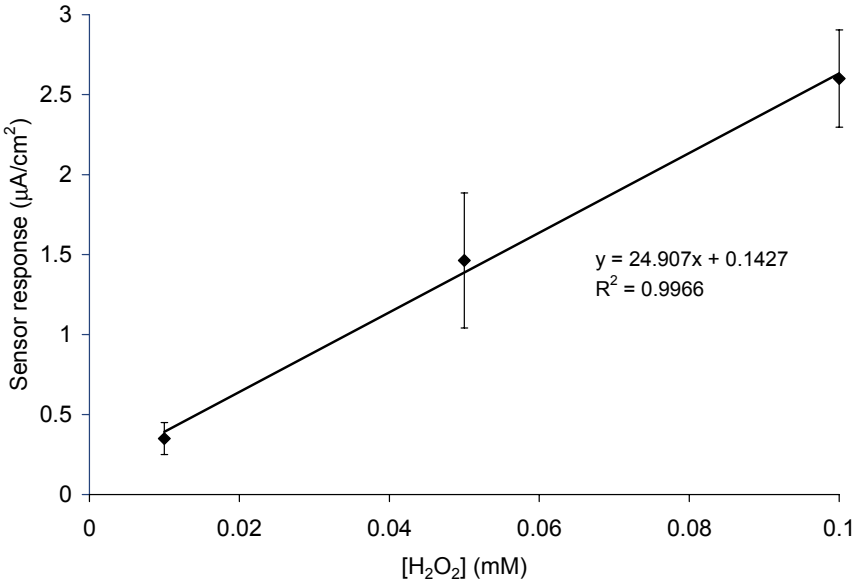

Figure 8.13 Linear range of the sensor in PBS pH 6.4 from 0.01 mM to 0.1 mM H_2O_2. A constant potential of -0.1 V was applied.

8.3.5.3 Interference test

The interference test was performed by using ascorbic acid as the model. The concentration of ascorbic acid used was 200 μM which is a normal physiological level presenting in biologic samples[5]. Amperometric test was performed in the absence and presence of ascorbic acid: the response after addition of 200 μM H_2O_2 was 4.43 ± 0.25 $\mu A/cm^2$ and 4.3 ± 0.25 $\mu A/cm^2$, respectively. This indicated that, at -0.1 V, there was negligible effect from the presence of ascorbic acid.

8.3.5.4 Long-term stability test

The results of amperometric stability tests on three sensors kept in air or in PBS pH 6.4 in a closed container for up to 180 days are shown in Figure 8.14. The sensors were very stable, as the response obtained after 6 months storage remained at 95% of that observed with freshly prepared sensors.

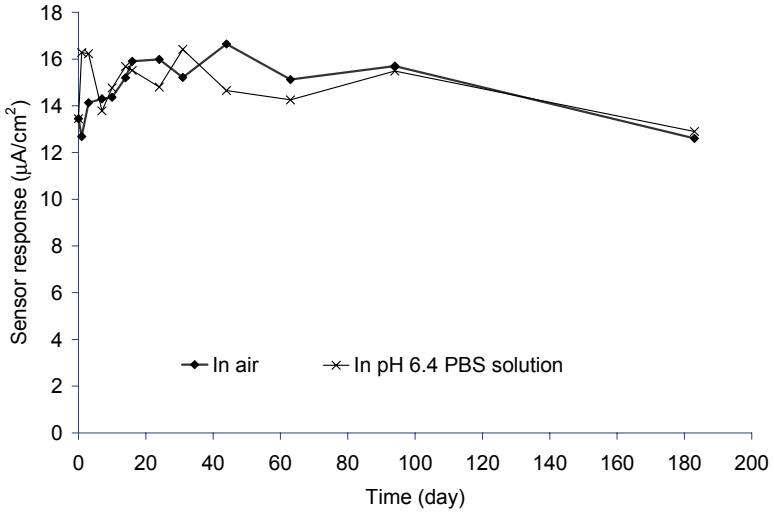

Figure 8.14 Stability of the sensor stored at 2 ºC in air and in pH 6.4 PBS solution.

8.4 Conclusions

The use of ITO-coated mylar as the base electrode for a H_2O_2 sensor is demonstrated using PMAS as the insoluble conducting polymer mediator by complexing with the polycation PLL. Investigation of the mixing sequence of PMAS and PLL on the substrate shows that the cast film from pre-mixing of PMAS and PLL has the best electrochemistry, film stability and morphology. The optimal PMAS to PLL ratio is 1:0.50, and the optimal surface concentrations of PMAS and PLL are 0.110 mg/cm^2 and 0.055 mg/cm^2, respectively. The HRP enzyme is easily pre-mixed with PMAS and then PLL before casting onto the ITO-coated mylar electrode. The higher the surface concentrations of HRP the thicker the film becomes, with greater sensor response until up to 0.14 mg/cm^2. At surface concentrations of HRP greater than 0.14 mg/cm^2, the thick film hinders the charge transfer process between the polymer film and the electrode surface resulting in a decreased sensor response.

The sensor has a minimum detectable concentration of 0.01 mM H_2O_2 with a linear range between 0.01 and 0.1 mM H_2O_2, and a sensitivity of 24.9 μA/cm^2 mM^{-1}. The sensor has high selectivity at a constant applied potential of -0.1 V, as no catalytic effect from the presence of the interference ascorbic acid is observed. It also exhibits very good long-term stability when stored in air and in pH 6.4 PBS at 2ºC.

In summary, this work demonstrates the ability to easily fabricate biosensors by evaporative casting conducting polymer nanoparticles onto conductive substrates. The sensors have good performance with long-term stability. The water solubility of PMAS is also amenable for ink-jet printing and its printability will be discussed further in Chapter 9.

8.5 References

1. Wallace, G.G., Spinks, G.M., Kane-Maguire, L.A.P., and Teasdale, P.R., *Conductive electroactive polymers : intelligent materials systems*. 2nd ed. 2002, Boca Raton, FL: CRC Press. , and references cited therein.
2. Mazeikiene, R., Niaura, G., and Malinauskas, A., *Synthetic Metals*, 2003. **139**(1): p. 89-94.
3. De Benedetto, G.E., Palmisano, F., and Zambonin, P.G., *Biosensors and Bioelectronics*, 1996. **11**(10): p. 1001-1008.
4. Tian, F.M. and Zhu, G.Y., *Analytica Chimica Acta*, 2002. **451**(2): p. 251-258.
5. Singh, S., Chaubey, A., and Malhotra, B.D., *Analytica Chimica Acta*, 2004. **502**(2): p. 229-234.
6. Gaspar, S., Habermuller, K., Csoregi, E., and Schuhmann, W., *Sensors and Actuators B-Chemical*, 2001. **72**(1): p. 63-68.
7. Thanachasai, S., Rokutanzono, S., Yoshida, S., and Watanabe, T., *Analytical Sciences*, 2002. **18**(7): p. 773-777.
8. Gao, M., Dai, L.M., and Wallace, G.G., *Electroanalysis*, 2003. **15**(13): p. 1089-1094.
9. Cen, L., Neoh, K.G., and Kang, E.T., *Langmuir*, 2002. **18**(22): p. 8633-8640.
10. Killard, A.J., Zhang, S.Q., Zhao, H.J., John, R., Iwuoha, E.I., and Smyth, M.R., *Analytica Chimica Acta*, 1999. **400**: p. 109-119.
11. Killard, A.J., Micheli, L., Grennan, K., Franek, M., Kolar, V., Moscone, D., Palchetti, I., and Smyth, M.R., *Analytica Chimica Acta*, 2001. **427**(2): p. 173-180.
12. Grennan, K., Strachan, G., Porter, A.J., Killard, A.J., and Smyth, M.R., *Analytica Chimica Acta*, 2003. **500**(1-2): p. 287-298.
13. Yang, R., Ruan, C.M., Dai, W.L., Deng, J.Q., and Kong, J.L., *Electrochimica Acta*, 1999. **44**(10): p. 1585-1596.
14. Caramori, S.S. and Fernandes, K.F., *Process Biochemistry*, 2004. **39**(7): p. 883-888.
15. Tatsuma, T., Ogawa, T., Sato, R., and Oyama, R., *Journal of Electroanalytical Chemistry*, 2001. **501**(1-2): p. 180-185.
16. Tallman, D.E. and Wallace, G.G., *Synthetic Metals*, 1997. **90**(1): p. 13-18, and references cited therein.
17. Yu, X., Sotzing, G.A., Papadimitrakopoulos, F., and Rusling, J.F., *Analytical Chemistry*, 2003. **75**(17): p. 4565-4571.
18. Iwuoha, E.I., de Villaverde, D.S., Garcia, N.P., Smyth, M.R., and Pingarron, J.M., *Biosensors & Bioelectronics*, 1997. **12**(8): p. 749-761, and references cited therein.

9.1 Introduction

In previous chapters, the use of conducting polymer nanoparticles as mediators in biosensor applications has been demonstrated. The polymer layer is usually electrodeposited (Chapter 7), or evaporative cast (Chapter 8) onto the conductive substrates. This chapter investigates the use of ink-jet printing of ICP nanodispersions to produce biosensors.

Ink-jet printing is a non-contact printing method and the high speed printing ability makes it amenable to mass production. Precise and accurate printing patterns can be controlled using conventional computer software[1]. Furthermore, different materials can be printed simultaneously via different nozzles[2], and only picolitre volumes are consumed per printed drop[3].

Epson produces a commercially available ink-jet printing machine. It is controllable through common computer programs such as Power Point™ which renders the desirable printing format. It has been used to print polyelectrolytes to pattern electronic circuits and print poly(3,4-ethylenedioxythiophene) (PEDOT) and PANI to fabricate RC filter circuits[4-6]. Due to the low cost and availability, an Epson C45 printer was used in this work. This model utilises a Micro Piezo print head which contains 48 black nozzles and 45 colour nozzles (15 nozzles for each colour) with a maximum resolution of 2880 x 720 dot-per-inch (DPI)[7]. There are however, some limitations with this type of printer, such as the substrate must be flexible in order to be able to feed through the printer, and the cartridge and print heads are usually plastic and not compatible with some organic solvents[8]. The nozzle diameter for the Epson printer is normally less than 30 μm which means printable

materials must be either completely soluble or be present as only small particles in dispersions.

The viscosity of the dispersions to be printed should be sufficiently low as the power generated by the piezo-electric membrane to force the ink ejecting out the nozzles is limited[8]. The suitable viscosity range for ink-jet printing is 1 - 30 mPa·s[8,9]. The surface tension of the ink should also be in between 20-70 dyne/cm as it must be high enough to be held in the nozzle without dripping and low enough to allow spreading over the substrate surface to form continuous films[10,11]. Conventional pigments in ink-jet inks contain particles in the size range of 100-400 nm[12] with a concentration high enough to achieve good printed colour.

When printing multiple materials, the tri-colour cartridge was used. This cartridge contains three colour chambers: magenta, yellow and cyan. By mixing these three colours, any other colour (other than white) can be achieved. This is known as the subtractive CYMK colour model[13]. Computer software however uses a different colour model, known as the Red Green Blue (RGB) colour model. These models are shown in Figure 9.1.

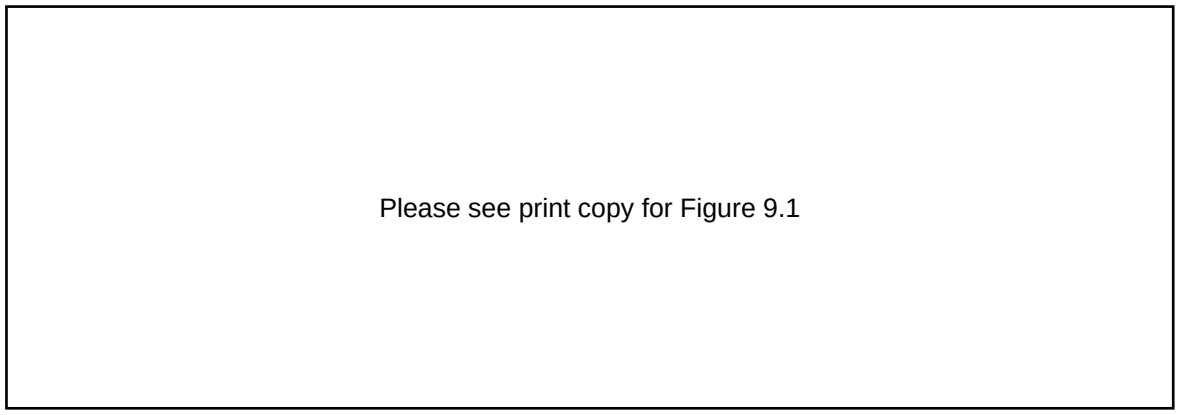

Figure 9.1 Colour model: (a) RGB model using in computer, and (b) CMYK model using in printer[13].

Considering these two models, in order to print material from the magenta chamber of the cartridge, for example, it is necessary to select magenta on the computer software by ensuring it contains 50 % blue and 50 % red only. Similarly, in order to print the red, the printer would use both the yellow (50 %) and magenta (50 %) inks to print.

The print head is an intricate part of the printer, and contains ink channels and the piezoelectric element. Ink is jetted from the cartridge through the printhead onto the substrate at a given frequency according to the settings of the piezoelement. A print head was cut open (Figure 9.2 and 9.3). On one side was the piezoelement which causes the ink to be jetted (Figure 9.2a). Underneath this element were the ink channels for the different colour print heads (Figure 9.2b).

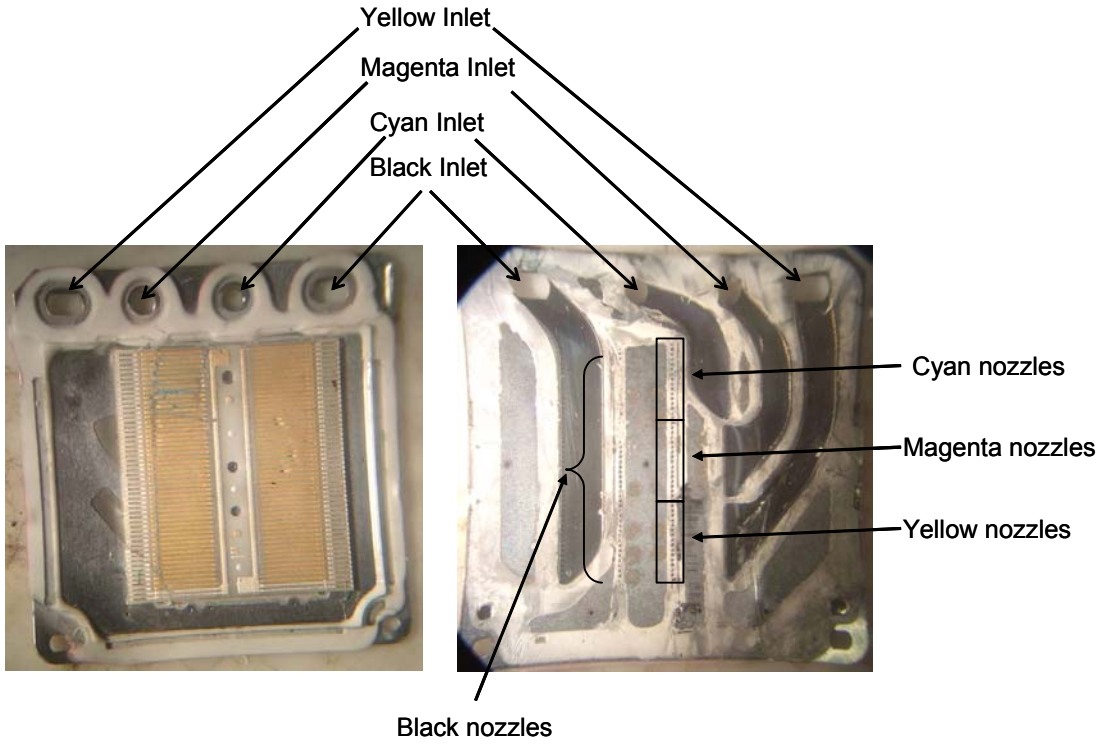

Figure 9.2 Inner working of Epson C45 print head: (a) piezoelectric elements, and (b) Black, Cyan, Magenta and Yellow channels.

The ink nozzles are completely separated from each other as shown in Figure 9.2b making it possible for several different solutions to print separately and simultaneously. The benefits from this approach will be outlined in the poly(2-methoxyaniline-5-sulphonic acid) (PMAS)-poly(L-lysine) hydrochloride (PLL) section (9.3.4.3).

Polymer nanoparticles generally tend to aggregate (see Chapter 3, 4 and 5) and this is not favourable for ink-jet printing as they can block the print head. In order to have a printable material, it must form dispersions with very small particle size. Numerous methods have been used to make polymers with controlled particle size using surfactant (Chapter 3, 6), steric stabiliser (Chapter 5) or centrifugation to isolate small particles. A total of four conducting polymer materials; namely PMAS, supernatant of *nano*PANI-DBSA (*s*PANI-DBSA), PANI-dodecylbenzene sulphonic acid-rapid mixing (PANI-DBSA-RM) and polypyrrole-dodecylsulfate-poly (vinyl alcohol) (PPy-DS-PVA) were investigated as potentially printable materials (see Table 9.1).

This chapter aims to demonstrate that ink-jet printing is a feasible, practical approach for printing polymer-modified biosensors (see Chapter 1, section 1.3). Conducting flexible plastic sheets were used as substrates. They were coated with gold, indium tin oxide (ITO) or conducting polymer. The electrochemical potential window of all these substrates was examined to determine their suitability for use as electrode platforms in electrochemical sensing. Also, their hydrophilic/hydrophobic property was indirectly investigated using contact angle measurements. All of the conducting polymer materials investigated here were characterised by measuring the viscosity of the dispersions containing them, the wetting ability of the polymer dispersions to the substrate surface using contact angle measurement and finally the printability and quality of the prints obtained. Each ink-jet printed ICP film was characterised electrochemically prior to its

evaluation as a suitable biosensor. The suitability of the film for use as a biosensor was investigated using a horseradish peroxidase (HRP) for amperometric detection of hydrogen peroxide (H_2O_2) (see Chapter 1 section 1.3.1).

9.2 Experimental

9.2.1 Chemicals

Phosphate buffer saline solution (PBS) (0.1 M phosphate, 0.137 M NaCl and 2.7 mM KCl, pH 6.4) was used as electrolyte for amperometric measurements. Horseradish peroxidase (HRP), poly-L-lysine hydrochloride (PLL) and sodium hydroxide (NaOH) were purchased from Sigma. Hydrogen peroxide (H_2O_2) and ethyl alcohol were purchased from Asia Pacific Specialty Chemicals Limited. Hydrochloric acid (HCl) was purchased from Ajax Finechem. All solutions were prepared using Milli-Q water. The conducting polymer materials used in this chapter are summarised in Table 9.1.

Table 9.1 The conducting polymer nanodispersions used for ink-jet printing.

Materials	Conductivity (mS/cm)	Concentration (% w/w)	Preparation method (Reference)
PMAS	11	0.5	Synthesised by Dr. Syed Ashraf, IPRI, University of Wollongong
*s*PANI-DBSA	421	0.5	Chapter 3 section 3.3.1.3
PANI-DBSA-RM	40	4.3	Chapter 3 section 3.3.2 (Huang and Kaner[14])
PPy-DS-PVA	40	3.6	Chapter 5 section 5.3.3

9.2.2 Substrate

ITO-coated polyester Mylar (OC^{TM} 50, resistance 45 Ω/sq.) from CPFilms Inc, Gold coated mylar from CPFilms Inc. and poly(3,4-ethylenedioxythiophene) (PEDOT) coated mylar from Agfa were used.

9.2.3 Equipment/Instrumentation

An Epson C45 printer was used to perform all printing. An Epson chip-resetter was purchased from 9to6[15]. Contact angle values were obtained using the contact angle instrument (CAM 100 version 1.50, KSV Instruments Ltd.). Viscosity measurements were performed using Ubbelohde viscometer No. 0B K659. An E-Corder 401 with EDAQ Potentiostat was used for all electrochemical experiments. A UV cleaner (Model No.42-220, Jelight Company, Inc.) was used for pretreatment of the ITO-coated mylar. Particle size was determined using dynamic light scattering (Nano-ZS Zetasizer, Malvern Instruments) with 8^{o} angled back scattered light. Atomic force microscope (Dimension 3100, Digital Instruments) was used to measure film thickness by cross-section analysis (see Chapter 2 section 2.2.2). A Multimeter (QM 1535, Digitech) was used to measure resistance across the polymer films. An optical microscope (eyepiece LMPlan FI 10X/0.25) was used to observed macroscopic morphology of the polymer films.

9.2.4 Methods

9.2.4.1 Viscosity measurements and pH adjustment of the ICPs nanoparticles

Viscosity measurements were performed using an Ubbelohde viscometer (Figure 9.3). The time the liquid required to travel the glass viscometer from mark D to mark F (efflux time) was recorded in seconds and multiplied by the viscometer constant to obtain

the kinematic viscosity. This value was used to calculate to absolute viscosity (μ) by multiplying by density of the liquid as shown in equation 9.1.

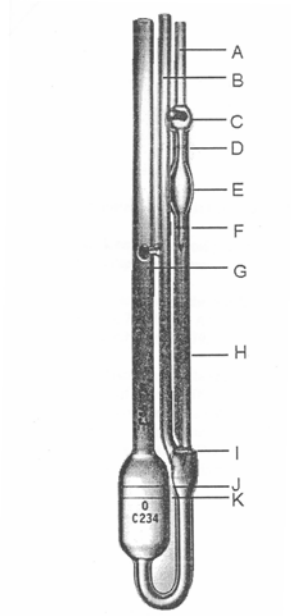

μ (mPa·s) = constant x efflux time (s) x density (g/ml) (9.1)

where constant for viscometer no. OB K659 = 0.004849 mm^2/s^2

Figure 9.3 The Ubbelohde viscometer.

As the neutral pH is a suitable condition for immobilisation of biomolecules, the ICP nanodispersions were pH adjusted by slowly adding 0.1 M NaOH solution. The adjustment was carried out in a vigorously stirred solution.

9.2.4.2 Printing method for Epson C45 printer

In order to refill the cartridge, the top cover was cut open, the internal sponge was removed and the cartridge was repeatedly washed using Milli-Q water. The material of interest was then poured into the cartridge, the chip was reset if necessary by pushing the chip-resetter to the cartridge electronic board until green light appear. The top of the cartridge was then resealed. Unless otherwise stated, the area of each sensor, 0.25 cm^2, was designed through Microsoft Power Point program as squares (0.5 x 0.5 cm). According to Chen *et al*[5]., more continuous films were obtained by annealing after every single print on the hotplate at 50 ^oC. In this work, the temperature of the hot plate was set at about 40 °C

so as not to denature the HRP. Hence, after each print, the substrate was placed on hotplate set at 40 °C for a 2-3 min or until the film dried.

9.2.4.3 Film preparation

Excess surfactant was washed off the ink-jet printed film using ethanol (0.25 ml of ethanol per single sensor) which was gently dropped on to the surface of the film. To ensure the removal of the surfactant, the film was placed vertically after the addition of the ethanol and left to dry before subsequent addition.

9.2.4.4 Real-time monitoring of enzyme/substrate interactions in a batch cell

Amperometry was conducted in a 10 ml cell containing PBS (pH 6.4) with continuously stirring. The cell was purged with nitrogen gas prior to amperometric experiments. All potentials stated are vs an Ag/AgCl (3.0 M NaCl) reference electrode. According to Killard *et al*[16,17] and Grennan *et al*[18] the potential applied was -0.1 V and 10 mM hydrogen peroxide was added when a steady background current was obtained.

The sensor response was calculated by subtracting the catalytic signal from background signal (see details of amperometric test in Chapter 2 section 2.3.3).

9.3 Results and Discussion

9.3.1 Instrumentation

Epson have imposed certain technologies in their printers (including the C45) so that they cannot be refilled with generic inks. The Epson C45 printer cartridges contain built-in chip technology to indicate the ink level. The printer will not print with an empty cartridge read by the chip on the cartridge. Once the chip is reset, the cartridge will read as

full and the printer will print. Therefore, in order to refill the cartridge, the chip resetter[15] was used.

The print heads eventually became blocked resulting in a low quality print or no print at all. The built in cleaning systems of the printer was used to clear the blockage but often the problem was still fatal therefore limiting the lifetime of each printer. In general, it was found that the printer could be cleaned a maximum of 40 times, or approximately 350 sensors were produced, before complete failure. When changing the ink, the ink was removed from the cartridges and Milli-Q water was placed in the cartridges followed by multiple printing. Isopropyl alcohol, a conventional print head cleaner, was found to be unsuitable here as it caused polymer to adhere to the print head and terminally block the nozzle. Milli-Q water was found to be an effective cleaner.

9.3.2 Substrate characterisation

9.3.2.1 Electrochemistry

The electrochemical potential window of all substrates was examined as it indicated the suitable range which electrochemistry of the polymer films could be performed without any interference from the substrates (Figure 9.4 to 9.6). 0.1 M HCl was the chosen electrolyte as it was used to investigate electrochemistry of the polymer-modified electrodes in this chapter (section 9.3.4.3, 9.3.4.4 and 9.3.4.5).

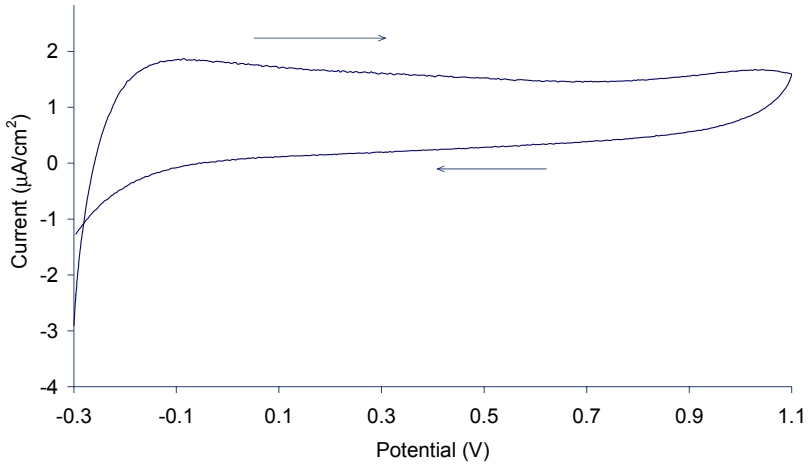

Figure 9.4 Cyclic voltammogram of non UV-treated ITO-coated mylar in 0.1M HCl at 100 mV/s scan rate. $E_{initial}$ is -0.3 V with the arrows indicating the direction of potential scan. All potentials are vs. Ag/AgCl (3.0 M NaCl).

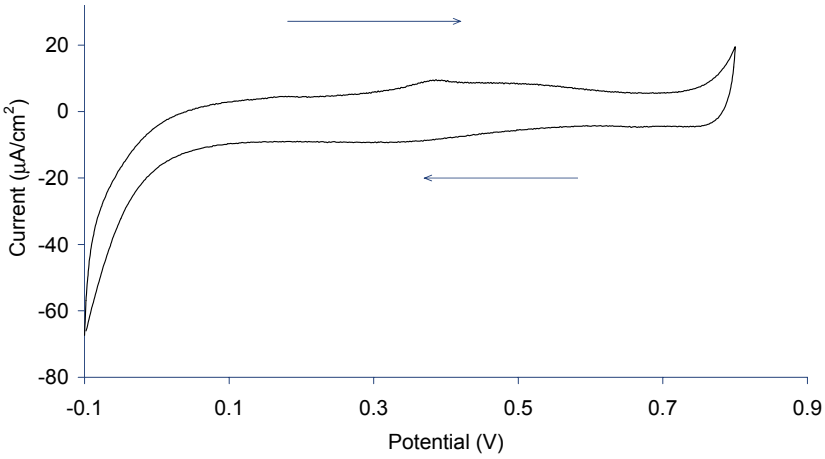

Figure 9.5 Cyclic voltammogram of non-UV treated gold coated mylar in 0.1M HCl at 100 mV/s scan rate. $E_{initial}$ is -0.1 V with the arrows indicating the direction of potential scan. All potentials are vs. Ag/AgCl (3.0 M NaCl).

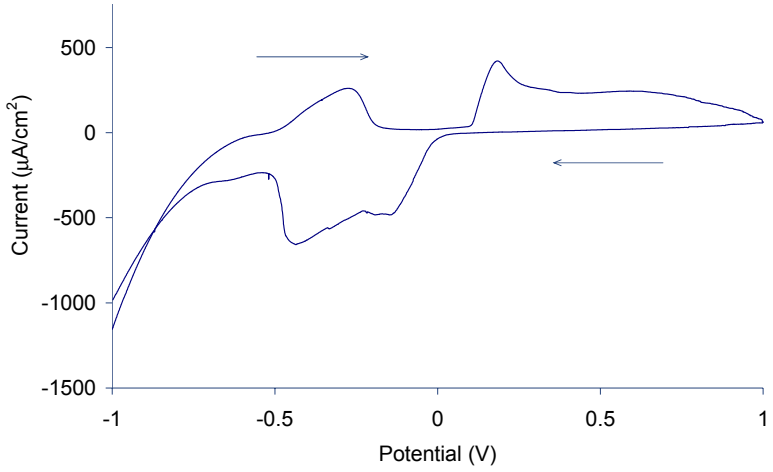

Figure 9.6 Cyclic voltammogram of non-UV treated PEDOT coated mylar in 0.1M HCl at 100 mV/s scan rate. $E_{initial}$ is -1.0 V with the arrows indicating the direction of potential scan. All potentials are vs. Ag/AgCl (3.0 M NaCl).

From CVs of all substrates, the ITO-coated mylar was shown to have the widest potential range with limits of -0.3 V to 1.0 V where there was no faradaic current observed. The on-set of dissolved oxygen reduction at $E_{1/2}$ ~-0.1 V[19] originally appeared in CV obtained using the ITO-coated mylar but this was eliminated by purging nitrogen gas through the electrolyte. However, oxidation/reduction responses were still evident for the gold and PEDOT coated mylar films even after purging with nitrogen. Hence they had a much narrower potential window than the ITO-coated mylar.

9.3.2.2 Hydrophilicity of substrates

The hydrophilic/hydrophobic nature of the substrate as indirectly determined by contact angle measurements (see Chapter 2 section 2.5) is important as this influences the spreading of ink drops[4]. A low contact angle for liquid on the substrate surface indicates a high hydrophilicity. Hence the ink can spread easily resulting in smooth homogeneous films. Contact angle measurements were carried out on the non UV-treated substrates using

water (1 µl). Similar contact angles were obtained for gold and ITO-coated mylar (Table 9.2). It was found that PEDOT coated mylar has the highest contact angle indicating the lowest hydrophilicity.

From an electrochemical perspective, ITO-coated mylar is the most desirable as the widest electrochemical window was observed. From these results and additionally in order to directly compare the sensor performance with PMAS-HRP-PLL biosensors as outlined in Chapter 8, this work was continued with ITO-coated mylar.

Table 9.2 Contact angle values of each of the substrates measured using 1 µL of Milli-Q water.

Substrates	**Contact Angle (°)**
PEDOT coated mylar	115±2
ITO-coated mylar	87±3
Gold coated mylar	72±3

9.3.3 Properties of ICP nanoparticles

9.3.3.1 Particle size in concentrated solution

A critical property of the ICP nanodispersions for printing is the particle size in concentrated solution. From a printing perspective, the typical pigment particle size is 100-400 nm[12] which can be printed using ink-jet printer with the nozzle diameter about 30-60 µm[20]. Therefore, the particle size of ICPs nanoparticles should be at least in the same order of magnitude to the typical pigment particle size. Due to effects of polymer aggregation, particle sizes bigger than 1000 nm was deemed unsuitable due to the possibility of clogging the print head and rendering the printer useless. Dynamic light scattering was used to determine the particle sizes with the size distribution of all materials used shown in Figure

9.7. The results are shown in both % Number and % Volume (see relevance of these two measurements in Chapter 2 section 2.2.3).

PANI-DBSA-RM solution was found to have a size range lower than 100 nm and PMAS particle size was lower than 160 nm (Figure 9.7 a and 9.7 b, respectively). There was no particle with a size over 160 nm in both PMAS and PANI-DBSA-RM dispersions and both materials were able to be continually printed without blocking the print head. The particle size by Number and Volume % plots were similar for both materials indicating there is no anomalous effects arising from the presence of large particles. However, *s*PANI-DBSA dispersions contain some particles with size over 1000 nm as indicated by the % Volume plot (Figure 9.7 c). Although the dispersions could be printed continuously, once printing was stopped for a few min, the print head became blocked with agglomerated particles. The same trends in particle size were observed for PPy-DS-PVA; hence the quality of PPy-DS-PVA printing was very poor, due to the presence of large particles in the dispersion (Figure 9.7 d).

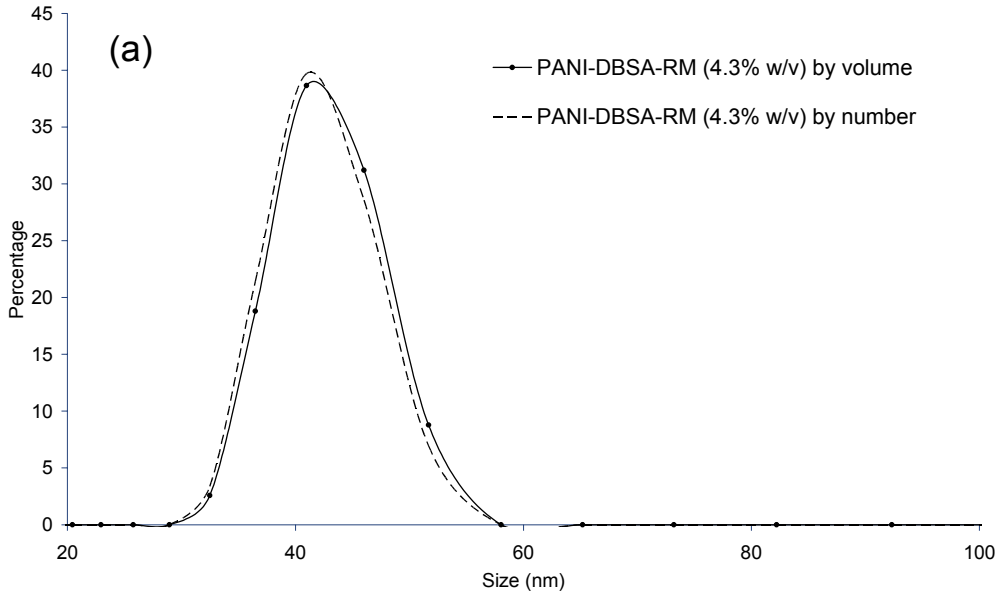

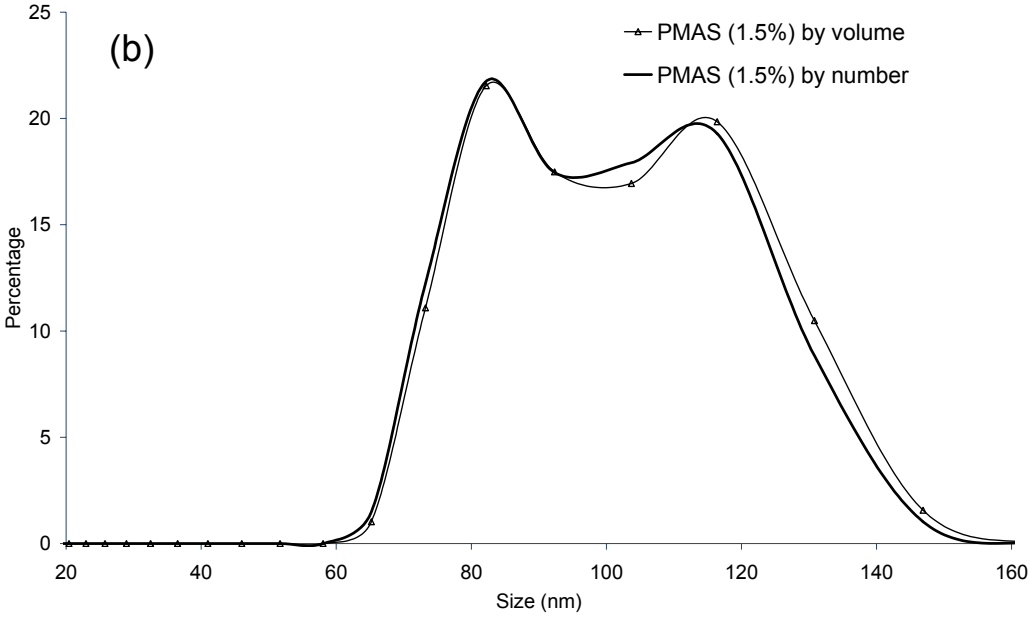
(b)
PMAS (1.5%) by volume
PMAS (1.5%) by number
Percentage
Size (nm)
0
5
10
15
20
25
20
40
60
80
100
120
140
160

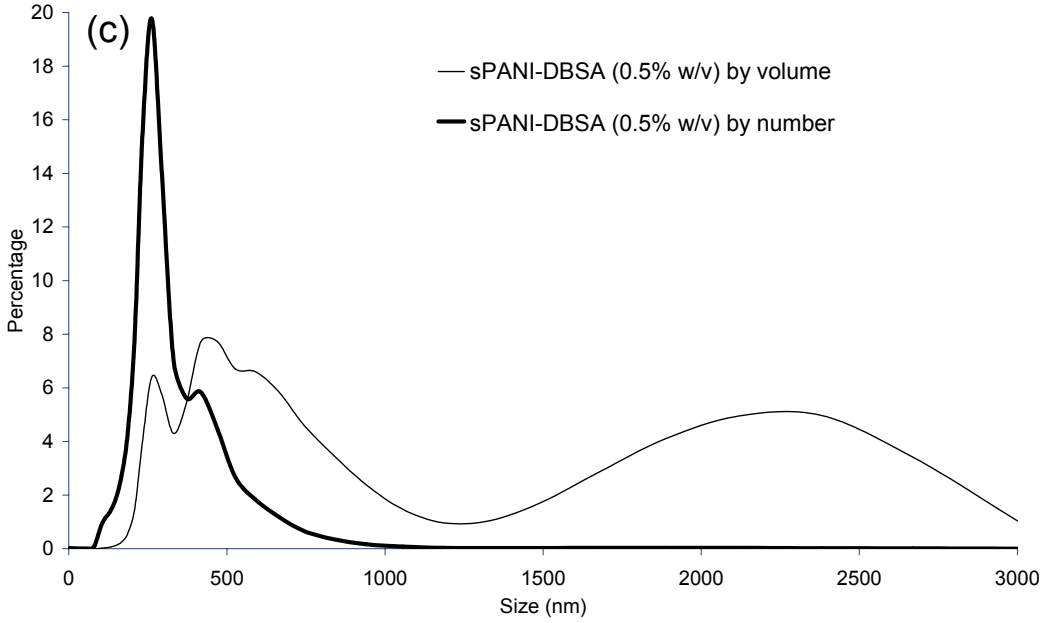
(c)
sPANI-DBSA (0.5% w/v) by volume
sPANI-DBSA (0.5% w/v) by number
Percentage
Size (nm)
0
2
4
6
8
10
12
14
16
18
20
0
500
1000
1500
2000
2500
3000

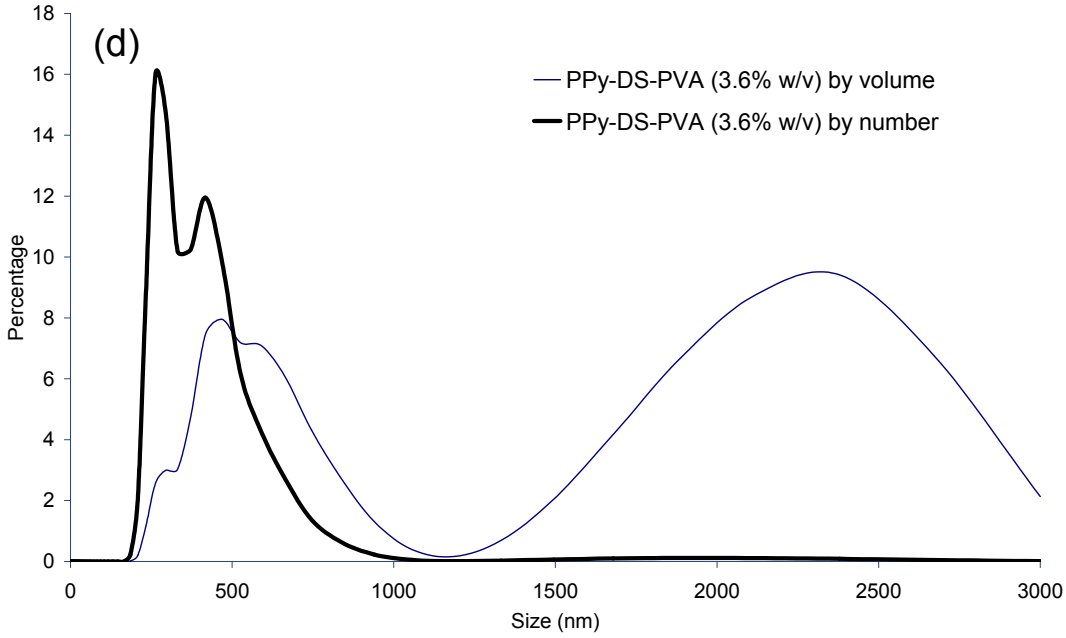

Figure 9.7 Size distribution of all nanodispersions used, indicated by % Number and % Volume: (a) PMAS and PANI-DBSA-RM, (b) *s*PANI-DBSA, and (c) PPy-DS-PVA.

9.3.3.2 Wetting ability and viscosity

As with the hydrophilic/hydrophobic property of the substrate, the wetting ability of the printing materials is also important. This property will drastically affect the printing quality as it affects the spreading and drying behaviour of the ICP nanodispersions on the substrates. The lower the contact angle value the higher the wetting ability of the dispersions. The contact angles of all materials were measured on ITO-coated mylar substrate as shown in Table 9.3.

Table 9.3 Measured contact angle and viscosity values of each of the printing materials used on non UV-treated ITO-coated mylar substrate. The values in brackets represent the concentrations of materials used.

Printing materials (1 µl)	Contact angle (°)	Viscosity (mPa·s)
Water	84±3	0.88
PMAS (0.5 % w/w)	80±1	1.58
PPy-DS-PVA (3.6 % w/w)	68±4	1.50
*s*PANI-DBSA (0.5 % w/w)	11±1	0.99
PANI-DBSA-RM (4.3 % w/w)	11±1	1.35

From contact angle measurement, PANI-DBSA-RM and *s*PANI-DBSA dispersions have the highest wetting ability which may be due to the presence of a large amount of surfactant. Also, it could be seen when printing these materials onto the substrate that they would spread over the surface to a larger extent than PMAS solution which has highest contact angle value.

Viscosity of the dispersions is also another issue as it affects the delivery of the ink. Typically ink viscosity should be between 1 – 30 mPa·s in order to render it printable[8,9]. From Table 9.3, the viscosity of all dispersions tested was found to be in a range that is suitable for printing.

9.3.4 Ink-jet printing of ICP nanodispersions

9.3.4.1 Printing the PPy-DS-PVA nanodispersions

Despite the large particle size observed in the dispersion prepared, PPy-DS-PVA could be printed onto transparencies and plain paper. Only a very light colour could be observed (data not shown) even when printed from concentrated solutions (3.6 % w/w). This is probably the result of the print head acting as a filter for the larger particle sizes and hence only very small particles were actually jetted through the print head. Printing work

on this dispersion was discontinued due to the poor print quality and hence it was not evaluated for biosensing of hydrogen peroxide.

9.3.4.2 Printing the PMAS and PLL solutions

PMAS has been shown previously to be suitable (Chapter 8) as a cast film in a biosensor system. As this polymer is totally soluble in water, and conducting, it was a suitable material for ink-jet printing.

PMAS was printed from the black cartridge of an Epson C45 printer onto paper and ink-jet transparencies. Both 1 % (w/v) and 4 % (w/v) PMAS were printed. The films formed were of good quality, but they were not homogeneous. This could probably be due to its low interaction to the substrate surface as indicated by high contact angle value on the substrate (Table 9.3). Epson ink was added to the 4 % (w/v) PMAS solution at concentrations from 1 % (w/v) to 8 % (w/v) to see if the homogeneity of PMAS films could be improved. A double print was used for each print. The homogeneity of these films improved as the Epson Ink content was increased (Figure 9.8).

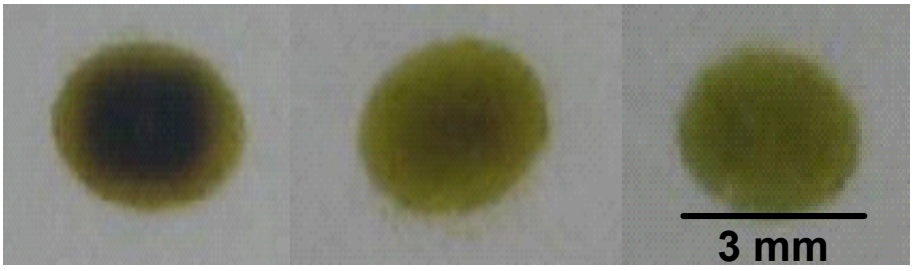

(a) (b) (c)

Figure 9.8 Photographs of Ink-Jet printed PMAS from solutions containing 4 % PMAS and: (a) 0 % Epson Ink, (b) 2 % Epson Ink, and (c) 4 % Epson Ink.

Although the homogeneity of the films increased, the resistance across them also increased as Epson Ink was added (Table 9.4). This is due to the non-conducting nature of the Epson ink.

Table 9.4 Dependence of Epson Ink content on the measured resistance of double printed films of PMAS (4 % w/v (aq)).

% (w/v) Epson Ink	Measured resistance across film (MΩ)
1	20
2	50
4	100
8	120

Although PMAS printed easily the resulting film was soluble in water. For biosensor applications, the film needs to be stable in aqueous solutions, therefore the polymer needs to be complexed with a polycation[21], such as PLL, to form an insoluble film on the substrate as previously shown in Chapter 8, section 8.3.1. As the Epson C45 is a colour printer, it has a multi-print head function. Hence, PMAS can be printed simultaneously with PLL by placing PMAS and PLL in separate compartments. This is important as these materials ideally should not mix before exiting the printer, as on mixing, insoluble fibres with the size over 3000 nm are observed using DLS and so would block the print head.

Internal investigation of the printhead showed that the ink nozzles were completely separated from each other (Figure 9.2). Therefore, it was safe to print two materials that reacted to form large particles from different ink compartments. In Chapter 8, the ratio of PMAS:PLL=1:0.5 was found to be optimal in producing stable and uniform films by evaporative casting. In this work the ratio was varied: 1:1, 1:0.5 and 1:0.25. It was found a

ratio of 1:1 was required to produce a stable uniform film on the substrate. Therefore PMAS (0.5 % w/v), (8 ml), was put in the yellow compartment of the colour cartridge, while PLL (0.5 % w/v) was placed in the magenta compartment (8 ml). A red colour translate to 50 % yellow and 50 % magenta in the printer hence 0.5% (w/v) PMAS and 0.5% (w/v) PLL were printed successfully (Figure 9.9 a).

The prints of the PMAS-PLL films were allowed to dry, before printing subsequent layers. Typically, 8 prints were carried out for any one film. In order to test the solubility, the films were allowed to completely dry, and water was run over the films. When water was run over PMAS only, the film dissolved away immediately. However, with PMAS:PLL at a 1:1 ratio, the films did not dissolve (Figure 9.9 a).

It was shown however, that by reducing the ratio to 1:0.5, the films partially dissolve presumably the uncomplexed PMAS dissolves to leave only the complexed PMAS on the surface. Reducing the ratio further to 1:0.2 results in even more dissolution of PMAS, and a very thin, patchy film is left behind (Figure 9.9 b and 9.9 c).

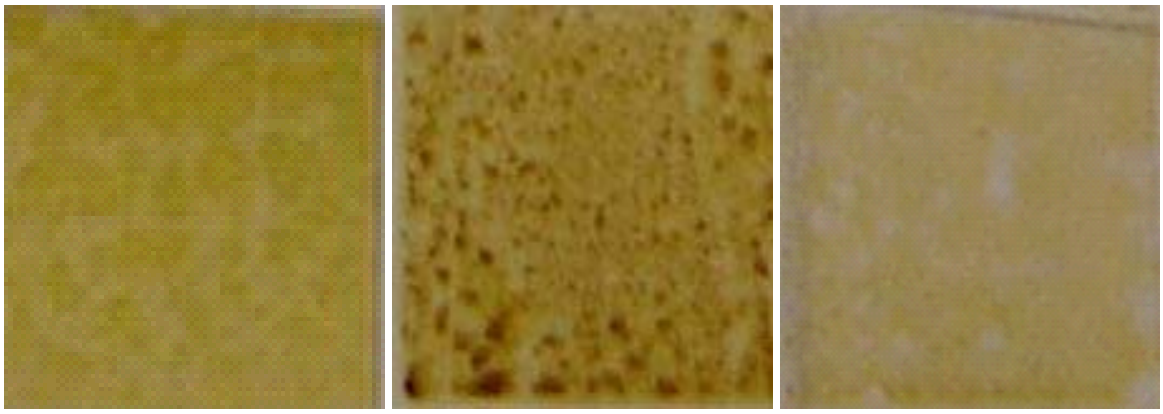

(a) (b) (c)

Figure 9.9 Ink-Jet printed of films (1 X 1 cm^2) on an ink-jet transparencies: (a) PMAS-PLL (1:1) after washing with H_2O, (b) PMAS-PLL (1:0.2) before, and (c) PMAS-PLL (1:0.2) after washing with H_2O.

In order to improve the print quality of PMAS-PLL, ITO-coated mylar was treated using UV-ozone cleaner. The electrochemical window of the UV-treated ITO-coated mylar was found in the same range as those obtained for non UV-treated ITO-coated mylar. Optical microscopy was carried out on PMAS-PLL films that were ink-jet printed (8 prints) on non UV-treated and UV-treated ITO-coated mylar (Figure 9.10 a and 9.10 b, respectively). Ink-jet printing on non UV-treated ITO-coated mylar resulted in films that did not cover the surface area of the ITO adequately (Figure 9.10 a) whereas UV-treated substrate resulted in more homogeneous films that covered a larger portion of the surface of the ITO-coated mylar (Figure 9.10 b). The contact angles of PMAS solution on both substrates were measured. It was found that without UV treatment, the contact angle of PMAS solution (0.5% w/v) had a value of 80±1º. This value decreased to 14±1º after UV treatment of the ITO-coated mylar. This was probably due to the UV-treatment removal of organic impurities on the substrate surface and so increases hydrophilicity. Therefore the UV-treated ITO-coated mylar was the preferred substrate for ink-jet printing.

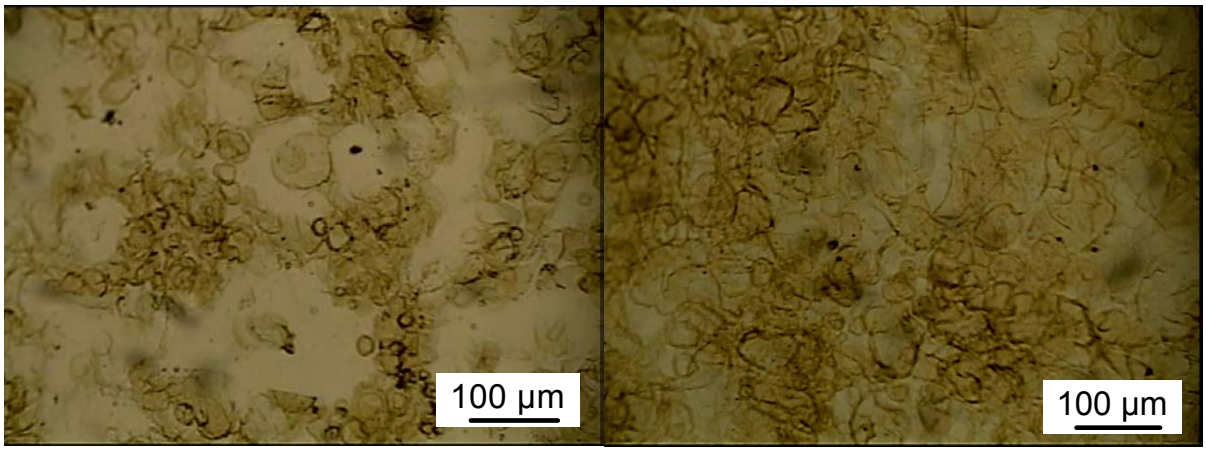

(a) (b)

Figure 9.10 PMAS-PLL (0.5 %) ink-jet printed on (a) non-UV treated ITO and (b) UV treated ITO (10 X Magnification).

PMAS (0.5 %) and PLL (0.5 %) were printed as 1 cm^2 squares on UV treated conducting ITO-coated mylar (8 prints). Cyclic voltammetry was carried out using these films resulting in well defined redox peaks which were stable upon repetitive scans (Figure 9.11 a). In order to evaluate effectiveness of the ink-jet printing, the cast films were also prepared wherein 35 μL was dropped and spread over the 1 cm^2 area. Cyclic voltammograms were subsequently obtained (Figure 9.11 b) and compared to those obtained from ink-jet printing. The CVs of the ink-jet printed films were more defined exhibiting 2 redox transitions between LB and ES at 0.28/-0.02 V (A/A′), and ES to PS at 0.79/0.46V (B/B′). These results are similar to those obtained using PMAS[22] and sulphonic acid ring substituted PANI (SPAN) film[23]. The middle peak at 0.59/0.36 V (C/C′) indicated degradation products from overoxidation of the polymer film at high potential scan. For the cast films (Figure 9.11 b), similar redox processes were observed with the redox couples shown at 0.29/0.06V (A/A′) and 0.75/0.34V (B/B′). However, the CVs were less defined and the middle peak (C/C′) was more pronounced at about 0.59/0.34 V. Film thickness were measured using AFM and found to be 263 nm for ink-jet printed film and greater than 838 nm for evaporative cast film. Although ink-jet printed film were much thinner than the cast film CVs of the ink-jet printed films were comparable in current magnitude to the cast films. This is probably due to the higher surface area of the ink-jet printed films as the multiple prints (8 prints) possibly created multi-thin layer polymeric film on the ITO surface and hence more accessible electron transfer between the electrolyte and the ITO than the dense layer of the evaporative cast films.

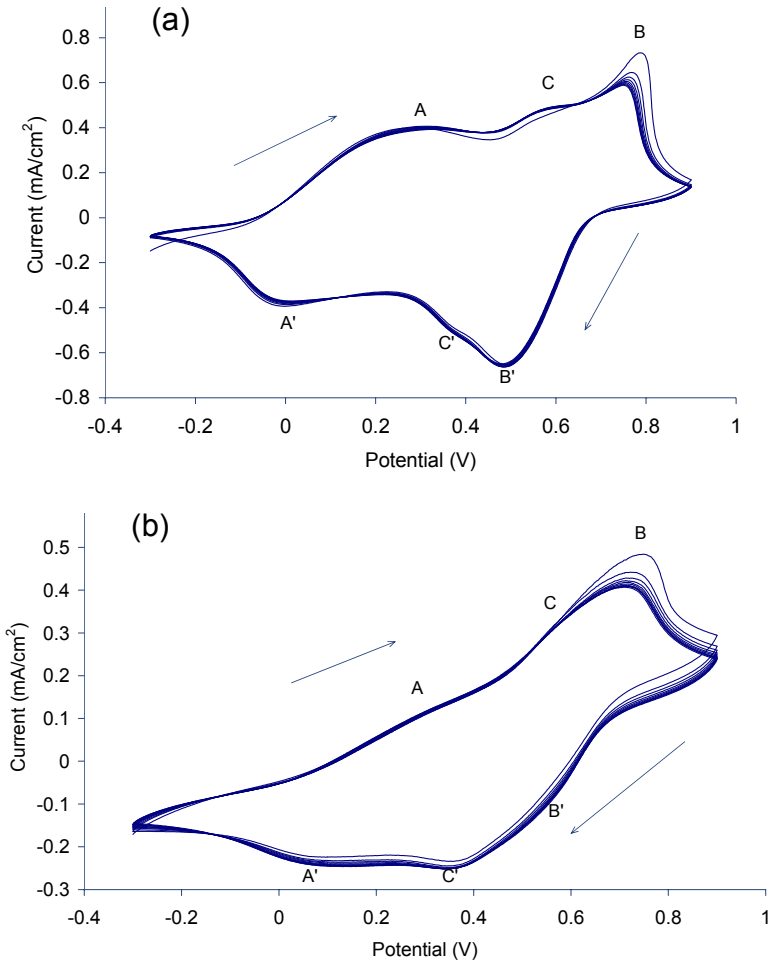

Figure 9.11 Cyclic voltammograms in 0.1 M HCl of: (a) ink-jet printed film (8 prints), and (b) evaporative cast film of PMAS-PLL (35 µL) on UV-treated ITO-coated mylar at 100 mV/s scan rate. Concentrations used: 0.5 % PMAS, 0.5 % PLL. $E_{initial}$ is -0.3 V and arrows indicate direction of potential scan. All potentials are vs. Ag/AgCl (3.0 M NaCl).

UV-visible spectrum of the ink-jet printed PMAS-PLL was compared to the cast film as shown in Figure 9.12. The spectra showed similar electronic properties with characteristic peaks appearing at 340 and 475 nm[24] albeit with lower intensity for the ink-jet printed film which was due to less polymer mass on the substrate.

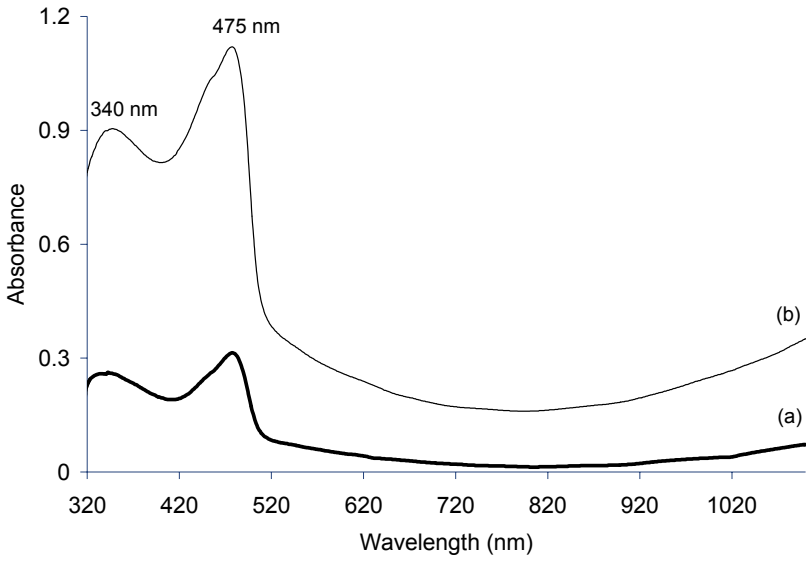

Figure 9.12 UV-visible spectra of (a) ink-jet printed film (8 prints) and (b) evaporative cast film of PMAS-PLL (35 μL/cm^2) on UV-treated ITO-coated mylar. Concentrations used: 0.5 % PMAS, 0.5 % PLL.

During the printing of these reagents, many problems were encountered. Although PMAS printed easily and consistently, its low wetting ability made the full coverage of the printed area difficult. Moreover, PLL constantly blocked the print heads (a problem that destroyed the printer). It is not known exactly why PLL did this, as it is completely soluble in water with pH of 0.5% (w/v) PLL in water 5.5. There may be a compatibility issue with the printer due to its strong cationic properties. As PLL was such a hindrance in the printing process, it was decided that it was not feasible to ink-jet print PLL in this way. As a result, the PMAS-PLL study was abandoned. However, alternative polycations are being investigated to replace PLL for future work.

9.3.4.3 Printing the *s*PANI-DBSA

The supernatant from *nano*PANI-DBSA (*s*PANI-DBSA) was prepared as outlined in Chapter 3 section 3.3.1.3.

The *s*PANI-DBSA (0.5% w/w polymer) was successfully ink-jet printed on UV-treated ITO-coated mylar. Figure 9.13 shows an image of a film taken with a 10x magnification lens. The film appears to almost fully cover the surface of the ITO-coated mylar. The dark spots indicate uncovered areas.

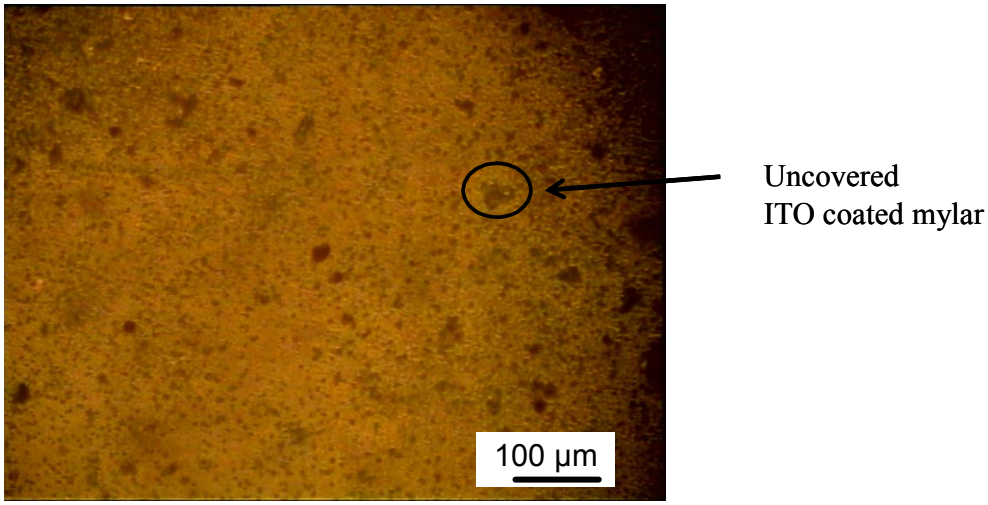

Figure 9.13 Optical Image (10x Magnification) of a *nano*PANI-DBSA ink-jet printed film (8 prints) on UV-treated ITO-coated mylar.

Cyclic voltammograms were obtained using the ink-jet printed film on ITO-coated mylar as the working electrode (Figure 9.14). Two redox couples appeared at 0.27/0.01V and 0.63/0.45V indicating the redox transition from LB to ES (A/A′) and ES to PS (B/B′), respectively (see detail of PANI-DBSA redox transition in Chapter 1 section 1.1.1).

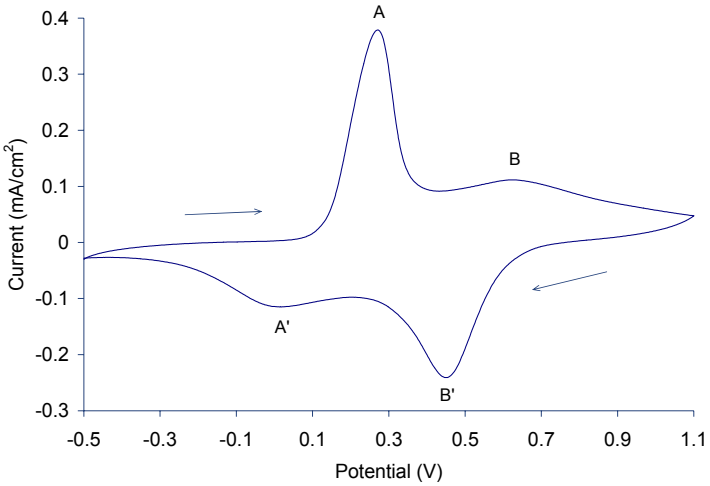

Figure 9.14 Cyclic voltammogram in 0.1 M HCl of: (a) an ink-jet printed of *s*PANI-DBSA (0.5% w/w) film from 8 prints at scan rate 100 mV/s. $E_{initial}$ is -0.3 V and arrows indicate direction of potential scan. All potentials are vs. Ag/AgCl (3.0 M NaCl).

The absorption spectrum of the ink-jet printed *s*PANI-DBSA films are compared with the spectrum of the *s*PANI-DBSA nanodispersions (Figure 9.15). The polaron band in the spectrum of the ink-jet printed film was shifted to higher wavelength compared to the dispersions (from 788 nm to 821 nm, respectively) indicating higher conjugation length[25] which was probably due to the chain interaction during the film formation.

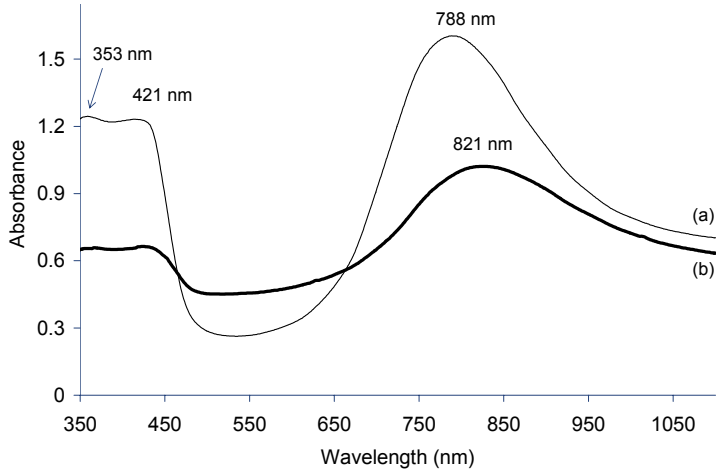

Figure 9.15 UV-visible spectra of: (a) *s*PANI-DBSA dispersions (0.09 g/L), and (b) film from ink-jet printed of *s*PANI-DBSA (8 prints).

The *nano*PANI-DBSA dispersions were shown previously in Chapter 7 to behave as an effective mediator for a biosensor when it was electrochemically cast onto electrodes. The *s*PANI-DBSA dispersion was adjusted to pH 7.0, and HRP was added at the required concentration. The particle size of the dispersion was then remeasured and it was shown that the pH adjustment and addition of HRP did not impact on particle size. The *s*PANI-DBSA-HRP was then prepared on UV-treated ITO electrodes using ink-jet printing. The biosensor performance was evaluated and the film containing HRP showed a higher sensor response than the film without HRP (Figure 9.16) indicating the presence of active HRP in the film.

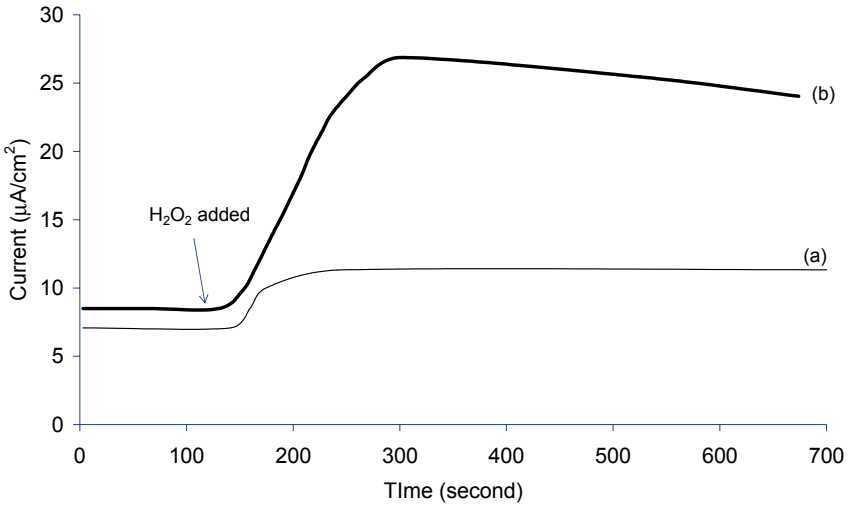

Figure 9.16 Amperometry of ink-jet printed film from *s*PANI-DBSA films containing (a) 0 mg/ml HRP and (b) 5 mg/ml HRP. No. of Prints: 8. Substrate: UV-treated ITO-coated mylar. H_2O_2 concentration: 10 mM.

This material was shown to be promising. However, there were some limitations. The low concentration of polymer made it necessary for multiple printing to be made. An attempt to increase the concentration of polymer in the supernatant failed as the polymer consistently aggregated at higher concentrations. Also since no stabiliser was present in the

dispersion, printing had to be continuous. Only a short down-time would cause blockage of the print head. Moreover, there was a high variability in the particle size within the supernatant. In some batches the particle size was over 1000 nm, a size which eventually blocked the print heads. Although the ink-jet printed films were shown to be sensitive to HRP, the catalytic signal was very low compared with the previous electrodeposited *nano*PANI-DBSA biosensors in Chapter 7. One reason for the lower signals could be the lower polymer concentration in the dispersion (at least ten times). Due to these limitations, the work on these nanodispersions was discontinued.

9.3.4.4 Printing the PANI-DBSA-RM nanodispersions

A rapid mixing method[14] was modified in order to attempt to obtain a dispersion with an even smaller particle size as outlined in Chapter 3 section 3.3.2.

The PANI-DBSA-RM contained 4.26% (w/w) solid with a monodispersed size around 50 nm. The pH was adjusted to 7 before printing onto UV treated ITO-coated mylar (20 prints) to produce smooth films as shown in Figure 9.17.

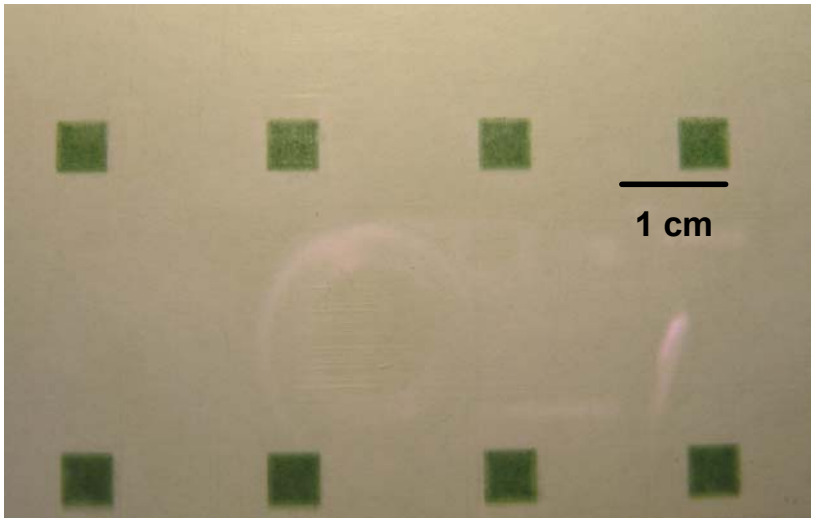

Figure 9.17 Photographs of ink-jet printed films from PANI-DBSA-RM, 20 prints.

The ink-jet printed films dissolved in solution. This solubility was caused by the larger amount of surfactant, DBSA, present in the films. In order to remove excessive surfactant, the films were very gently washed with ethanol. These washed films were then rendered insoluble and electrochemistry was then performed in 0.1 M HCl electrolyte as CV shown in Figure 9.18.

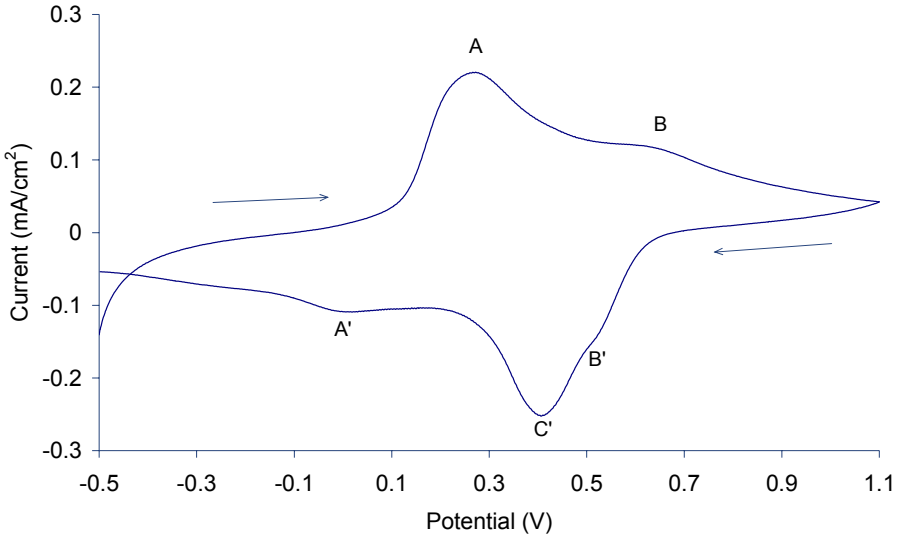

Figure 9.18 Cyclic voltammogram of ink-jet printed films (20 prints) from supernatant PANI-DBSA-RM in 0.1 M HCl at scan rate 20 mV/s. $E_{initial}$ is – 0.5 V and arrows indicate direction of potential scan. All potentials are vs. Ag/AgCl (3.0 M NaCl).

Cyclic voltammograms obtained using these films were found to be similar to the *s*PANI-DBSA films but slightly less defined. Two redox couples appeared at 0.27/0.01 V (A/A′) and 0.62/0.52 V (B/B′) which are due to the switching from LB to ES and ES to PS, respectively. The strong reduction peak (C′) of degradation products, p-benzoquinone and hydroquinone[26], at about 0.41 V appeared in this samples which is possibly due to the small size of the polymer deposited on the surface that formed a thin film which was more easily overoxidised.

UV-visible spectrum of the PANI-DBSA-RM ink-jet printed film is shown in Figure 9.19 and some different features were found with respect to the UV-visible spectrum of the dispersion. The polaron band in the spectrum of the ink-jet printed film was shifted to higher wavelength compared to the dispersions (from 819 nm to 842 nm, respectively) indicating higher conjugation length[25] which was probably due to the chain interaction during the film formation.

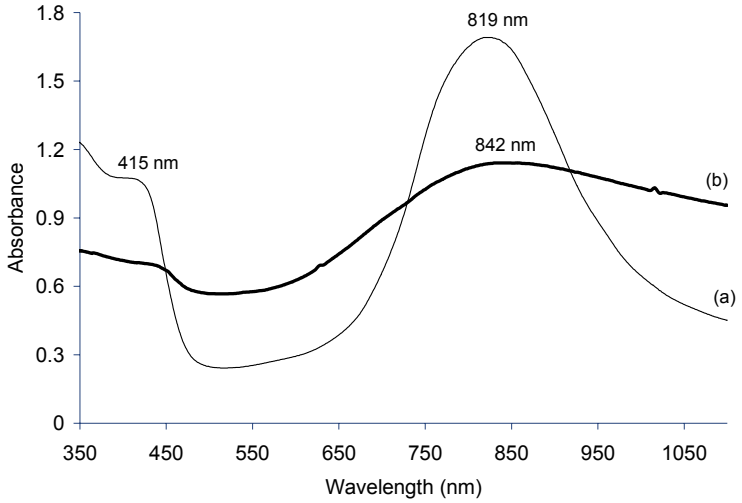

Figure 9.19 UV-visible spectrum of (a) PANI-DBSA-RM nanodispersions (2.13 g/L) and (b) film from ink-jet printed PANI-DBSA-RM (20 prints).

Various concentrations of HRP were prepared in PBS pH 6.4. These solutions (5 μL) were cast on top of the ink-jet printed films, amperometry was conducted on these films where H_2O_2 was added to a stirred solution of buffer where the potential of the film was held at –0.1 V. Typical sensor response appeared to be the same as films from *s*PANI-DBSA (Figure 9.16). The results of varying HRP concentrations are shown in Figure 9.20 and the highest sensor response (30.47 μA/cm^2) obtained from 5 μL of 0.05 mg/ml HRP used. Above this concentration of HRP the responses decreased, possibly due to the

formation of large insulating HRP multilayers which may have reduced the electron transfer kinetics in the PANI film.

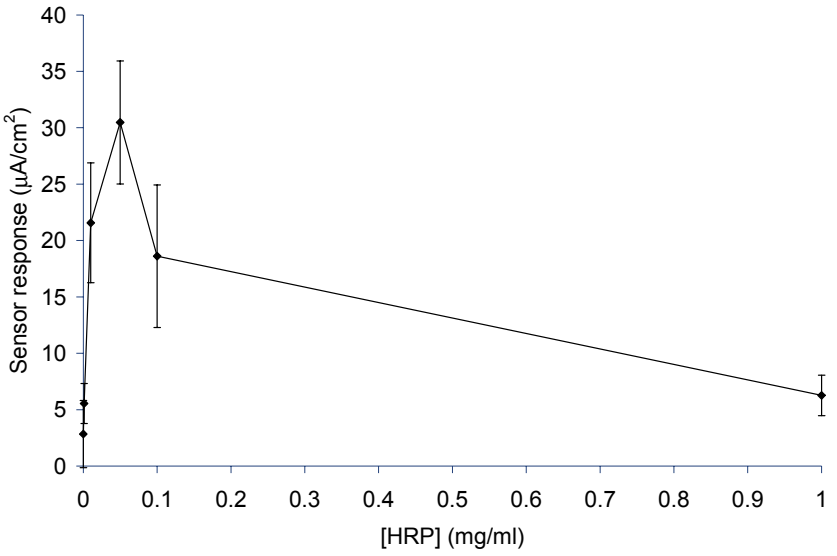

Figure 9.20 Sensor response of ink-jet printed films from PANI-DBSA-RM with 5 μL of HRP cast on top. Potential applied was -0.1 V and 10 mM of H_2O_2 was added.

As an ink-jet printable mediator for a biosensor, the PANI-DBSA-RM material was shown to be the most promising. The small particle size was consistent from batch to batch and it was shown to be about 20-70 nm. Small size and high wetting ability ensured that good printing quality was obtained. The optimum sensor response was high (0.05 mg/ml HRP used). This response was about 10 μA/cm^2 higher than the PMAS-HRP-PLL sensor system in Chapter 8 with about 100 times less HRP being used. Although this ink-jet printed material provided lower sensor responses (on ITO-coated mylar) than the *nano*PANI-DBSA-HRP (on glassy carbon electrode in Chapter 7), it is still a promising material due to its potential for ink-jet printing very thin films from its small particle size. Therefore, ink-jet printing of this material could be a cost effective approach for sensor fabrication that could hold a great deal of potential from a mass production viewpoint.

9.4 Conclusions

An Epson C45 printer is used for piezoelectric ink-jet printing of ICP nanodispersions. The life-time for the Epson printers is not very long, due to clogging with larger particles. Nevertheless, even with 350 sensors produced it is still a low cost approach.

ITO-coated mylar is chosen as the most suitable substrate for printing as it is shown to have the widest potential window range. The hydrophilicity of the mylar is increased from UV-ozone treatment which helps the dispersions spreading in larger area on its surface and continuous film obtained. Moreover, ITO-coated mylar is used in order to directly compare to PMAS-HRP-PLL system in Chapter 8.

From the % Volume particle size data PPy-DS-PVA show large number of large particles over than 1000 nm hence poor printability is obtained from these nanodispersions.

The *s*PANI-DBSA is successfully ink-jet printed. However, catalytic signals to H_2O_2 are very low, compared with the previous PANI-DBSA HRP biosensors (Chapter 7). This is due to the lower concentration of polymer in the supernatant that is used. Moreover, the particle size is difficult to control as the desired size (lower than 1000 nm) is found occasionally which made the printing non-reproducible.

For PMAS-PLL system, PMAS and PLL are printed successfully from different channels but the major drawback is that PLL persistently blocks the print heads and makes the consistent printing impossible. Alternative polycations are being investigated to replace PLL for future work. The resulting films from ratio PMAS:PLL = 1:1 is not dissolved in aqueous electrolyte. Cyclic voltammograms of the ink-jet films are much more defined than

the evaporative cast films and very stable indicating more efficiency of ink-jet printing over casting method.

The most promising material is the PANI-DBSA-RM from the modified rapid mixing method[14]. The particle size is varied from batch to batch around 20-70 nm. The dispersions have high wetting ability as indicated by low contact angle value. The printed films are smooth and homogeneous. Although, they dissolve in the water but the washed film (by ethanol) is stable and shows good sensing performance. At 0.05 mg/ml HRP, the highest sensor response is 30.47 $\mu A/cm^2$ which about 10 $\mu A/cm^2$ higher than the PMAS-HRP-PLL system in Chapter 8 and about 100 times less HRP being used. Some further optimisations that could be carried out to achieve higher sensor response include varying number of prints, using other, more suitable conducting substrates in terms of conductivity and hydrophilic/hydrophobic property such as screen-printed electrodes (SPEs). HRP could also be fabricated using ink-jet printing.

This work has demonstrated the ink-jet printability of conducting polymer nanoparticles and their use as working electrodes for biosensors. These effective low cost sensors can be easily fabricated, its distinct benefit is its amenability to mass production.

9.5 References

1. Kawase, T., Shimoda, T., Newsome, C., Sirringhaus, H., and Friend, R.H., *Thin Solid Films*, 2003. **438-439**: p. 279-287.
2. Sirringhaus, H., Kawase, T., Friend, R.H., Shimoda, T., Inbasekaran, M., Wu, W., and Woo, E.P., *Science*, 2000. **290**(5499): p. 2123-2126.
3. Yoshioka, Y., Calvert, P.D., and Jabbour, G.E., *Macromolecular Rapid Communications*, 2005. **26**(4): p. 238-246.
4. Tzung-Fang Guo, S.-C.C., Seungmoon Pyo, and Yang Yang, *Langmuir*, 2002. **18**(21): p. 8142-8147.
5. Chen, B., Cui, T., Liu, Y., and Varahramyan, K., *Solid-State Electronics*, 2003. **47**(5): p. 841-847.
6. Cui, T.H., Liu, Y., Chen, B., Zhu, M., and Varahramyan, K., *Solid-State Electronics*, 2005. **49**(5): p. 853-859.
7. http://www.epson.co.jp/e/technology/sankei_4.htm, accessed on 10 July 2005.
8. Gans, B.-J.d. and Schubert, U.S., *Macromolecular Rapid Communications*, 2003. **24**(11): p. 659-666.
9. Liu, Z., Su, Y., and Varahramyan, K., *Thin Solid Films*, 2005. **478**(1-2): p. 275-279.
10. http://www.microfab.com/equipment/technotes/technote99-02.pdf, accessed on 30 November 2005.
11. Calvert, P., *Chemistry of Materials*, 2001. **13**(10): p. 3299-3305.
12. Magdassi, S. and Ben Moshe, M., *Langmuir*, 2003. **19**(3): p. 939-942.
13. http://www.sketchpad.net/basics4.htm. accessed on 11 July 2005.
14. Huang, J.X. and Kaner, R.B., *Angewandte Chemie-International Edition*, 2004. **43**(43): p. 5817-5821.
15. http://www.9to6.ie. accessed on 11 July 2005.
16. Killard, A.J., Zhang, S.Q., Zhao, H.J., John, R., Iwuoha, E.I., and Smyth, M.R., *Analytica Chimica Acta*, 1999. **400**: p. 109-119.
17. Killard, A.J., Micheli, L., Grennan, K., Franek, M., Kolar, V., Moscone, D., Palchetti, I., and Smyth, M.R., *Analytica Chimica Acta*, 2001. **427**(2): p. 173-180.
18. Grennan, K., Strachan, G., Porter, A.J., Killard, A.J., and Smyth, M.R., *Analytica Chimica Acta*, 2003. **500**(1-2): p. 287-298.
19. Daniel, H.C., *Quantitative chemical analysis*. 5th ed, ed. W.H.F.a. Company. 1998, New York.
20. Le, H.P., *Journal of Imaging Science and Technology*, 1998. **42**(1): p. 49-62.
21. Tatsuma, T., Ogawa, T., Sato, R., and Oyama, R., *Journal of Electroanalytical Chemistry*, 2001. **501**(1-2): p. 180-185.
22. Tallman, D.E. and Wallace, G.G., *Synthetic Metals*, 1997. **90**(1): p. 13-18, and references cited therein.
23. Li, C.M. and Mu, S.L., *Synthetic Metals*, 2005. **149**(2-3): p. 143-149.
24. Zhou, D.Z., Innis, P.C., Wallace, G.G., Shimizu, S., and Maeda, S.I., *Synthetic Metals*, 2000. **114**(3): p. 287-293.
25. Norris, I.D., Kane-Maguire, L.A.P., and Wallace, G.G., *Macromolecules*, 2000. **33**(9): p. 3237-3243.
26. Chen, W.C., Wen, T.C., and Gopalan, A., *Synthetic Metals*, 2002. **128**(2): p. 179-189.

Conclusions and Future studies

In this thesis, the synthesis of inherent conducting polymers (ICPs) was achieved using various methods such as emulsion polymerisation, use of steric stabiliser and synthesis in the presence of ionic liquid. The nanoparticles obtained were stable in aqueous as dispersions which were more processable. These nanodispersions were further fabricated as mediators for biosensors using electrodeposition, evaporative casting and ink-jet printing and the sensor performance was evaluated.

The *nano*PANI-DBSA with the particle size of 10±2 nm as observed by TEM has been synthesised on a large scale which provided benefits for mass production. The polymer showed typical pH and redox switching and electrochemical properties of PANI. The dispersion of these nanoparticles in aqueous medium showed remarkable stability with small particles suspended in solution for up to 12 months. Their electronic property was stable for up to 8 months and electrochemical property remaining constant for up to 6 months. The conductivity of the *nano*PANI-DBSA was found to be 34±7 S/cm. These nanoparticles proved useful as a mediator in biosensor application when they were fabricated onto the conductive electrode using electrodeposition method as demonstrated in Chapter 7. The nanodomain of these particles contributed to highly ordered nanostructure patterning on the electrode surface. The scan rate study showed that the electrochemical reaction occurring at these nanofilms were surface confined processes. This uniform surface showed improved enzyme deposition characteristics and lower background signal than the electrochemically synthesis of PANI from bulk monomer solutions. Microscopic images showed uniform nanostructured polymeric surfaces which contributed to the

uniform enzyme attachment. The enzyme assay result also confirmed that the horseradish peroxidase (HRP) enzyme immobilised on the polymer film was deposited, approximately as a monolayer, over the surface. The sensors showed about three times higher sensor response to background ratio, at least one order of magnitude quicker response time and about six times lower HRP concentration used under the optimal conditions compared to the sensors fabricated from electropolymerisation of the bulk monomer from previous works of PANI-PVS.

The *nano*PANI-DBSA tended to aggregate and form clusters in concentrated solution. Centrifugation was used to separate the nanoparticles from the agglomerates which precipitate out of the solution. The supernatant (*s*PANI-DBSA) containing the small particles was produced and used as a material for ink-jet printing as outlined in Chapter 9. The enzyme HRP was pre-mixed with the *s*PANI-DBSA nanoparticles and the mixture was fabricated using ink-jet printing. The catalytic signal of the *s*PANI-DBSA/HRP biosensors to H_2O_2 was very low, compared to the *nano*PANI-DBSA/HRP system. This may be due to the lower concentration of PANI in the *s*PANI-DBSA. Moreover, the particle size was difficult to control as the desired size (lower than 1000 nm) was often not achieve and, hence, making the printing non-reproducible. Therefore, no further work from this material has been conducted.

The PANI-DBSA-RM nanoparticles were synthesised as a material to be used for ink-jet printing applications. The PANI-DBSA-RM had a particle size of about 50 nm as observed by TEM and DLS method. These nanoparticles gave good quality ink-jet print on ITO coated mylar substrate. The good adherent films were obtained by washing the excess surfactant using ethanol. HRP was subsequently immobilised onto the polymer film and the sensors tested for amperometric detection of hydrogen peroxide. The biosensing properties

from these ink-jet printed sensors were lower than the sensors from the *nano*PANI-DBSA/HRP system (see Chapter 7) which was possibly due to lower conductivity of the PANI-DBSA-RM nanoparticles. Conductivity of dried PANI-DBSA-RM films was 40±8 mS/cm. However, at 0.05 mg/ml HRP, the highest sensor response was 30.47 $\mu A/cm^2$ which was about 10 $\mu A/cm^2$ higher than the PMAS-HRP-PLL system (as outlined in Chapter 8) and about 100 times less HRP being used. This work has demonstrated the ink-jet printability of conducting polymer nanoparticles and their use as working electrodes for biosensors. These effective low cost sensors can be fabricated easily with the distinct benefit of its amenability to mass production. For future work, the biosensor performance could be improved by some optimisations such as varying the number of prints, using more suitable conducting substrates in terms of conductivity and hydrophilic/hydrophobic properties such as screen-printed electrodes (SPEs). HRP could also be fabricated using ink-jet printing or electrochemical immobilisation.

For future work, synthesis of ICPs nanoparticles to which biomolecules is attached is being interested and the biosensor fabrication from these biomolecules attached ICPs nanoparticles could be performed in a single step. It is anticipated that more efficient electron transfer between ICPs and biomolecules would be achieved and this would make it possible for mass production of sensors using an ink-jet printer.

Carbolan Blue (CB) dye was used as a model compound to incorporate into the PANI-DBSA nanoparticles and it did not hinder the doping and redox switching process. Some different features on UV-visible spectra of the PANI-DBSA-CB nanoparticles compared to the PANI-DBSA indicated the presence of the dye in PANI. The dye was found to have strong interaction with the polymer backbone using Raman spectroscopy and centrifugation test. The PANI-DBSA-CB nanoparticles were electronically stable for up to

8 months and electrochemically stable for up to 6 months. Due to the distinctive colour upon reduction process compare to PANI-DBSA, the PANI-DBSA-CB can be a potential candidate for electrochromic devices. It may be possible to incorporate the others dye molecules or functional groups into PANI using this procedure in future work.

The water soluble polymer, PMAS, was also used to fabricate biosensors. It was made insoluble by complexing with the polycations PLL. HRP was mixed into PMAS-PLL matrix before evaporative cast onto ITO-coated mylar substrate. This biosensor format has proven ability to be easily fabricated from conducting polymer nanoparticles by one-step casting. The scan rate study showed the diffusion limited process dominated in these PMAS-PLL films. The optimum sensor performance was obtained from using surface concentration of 0.11 mg PMAS/cm^2, 0.055 mg PLL/cm^2 and 0.14 mg HRP/cm^2. The optimised sensor had a minimum detectable concentration of 0.01 mM H_2O_2 and a linear range between 0.01 and 0.1 mM H_2O_2 was observed with the sensitivity of 24.9 μA/cm^2 mM^{-1}. The sensor had a high selectivity at a constant potential of -100 mV applied as no significant effect to the catalytic current from the presence of the interference ascorbic acid was observed. It also showed very good long-term stability both being stored in air and in PBS pH 6.4 at 2 ºC. The PMAS-PLL system was also fabricated using ink-jet printing. The CVs from ink-jet printed films were much more defined than the CVs from evaporative casting films indicating electron transfer was enhanced due to better film formation which could lead to better sensor performance. However, the problem with PLL blocking the print head resulted in no further work being pursued. If the problem with PLL could be solved, the ink-jet printed PMAS-HRP-PLL could form a basis for fabrication of a biosensor for hydrogen peroxide. Work is continuing in this area in our laboratory.

PPy nanodispersions were successfully synthesised as outlined in Chapter 4. The use of steric stabiliser (PVA) in the synthesis provided stable nanodispersions with the size decreasing with increasing PVA content. The optimum synthesis temperature was 25 ºC with the optimum ratio of PPy to SDS being 1:0.125. High loading of PPy with small particle sizes and stable nanodispersions was obtained from 0.4 M Py, 2.4% (w/v) PVA and 0.05 M SDS. The PPy-DS-PVA nanoparticles showed reasonable conductivity of 40.1 mS/cm with TEM images showing the segregated nanoparticles with a particle size of 52±5 nm indicating the stabilising efficiency of PVA. The concentrated dispersion (3.6 % w/v) was used in ink-jet printing. The print quality was poor due to the presence of large particles over than 1000 nm as observed by DLS method indicating some aggregation in concentrated solution. No further work on ink-jet printing with this dispersion will be undertaken.

The PTTh nanoparticles dispersed in aqueous media were also synthesised in the presence of surfactant (DBSA) and in IL (emiTFSA). For the synthesis of PTTh-DBSA nanoparticles, the effect of oxidant and surfactant concentrations were studied. The results from UV-Visible and Raman spectroscopy, and OCP and particle size measurements showed the optimal concentration of the oxidant to be 1.0 M and surfactant to be 0.2 M where the TTh monomer concentration was maintained at 0.01 M. The particle size of PTTh-DBSA as observed by TEM varied from small spherical particles (about 30 nm) to irregular clusters and it showed poor dispersion stability as most of the particle precipitated overnight. However, some small particles were able to be suspended in the solution for up to 8 months. The PTTh-DBSA nanoparticles showed poor electroactivity.

The PTTh nanoparticles synthesised in emiTFSA exhibited good electrochemistry with the particle size in the range of about 50 nm to a few hundred nanometers as observed

by TEM. These nanoparticles were dispersed in water by sonication for 2-3 minutes sonication. The effect of oxidant concentrations to UV-Visible and Raman spectra, CVs, and particle size were studied. Raman spectra indicated that a relatively highly doped polymer was obtained. The use of these nanoparticles in photovoltaic devices is being investigated in our laboratory. Ethanol was also used for the synthesis in order to see the effect of the solvent. The PTTh nanoparticles synthesised in ethanol were large and not stable in water.